UNIVERSITY OF CALIFORNIA SAN DIEGO

Porous Silicon Nanomaterials for Bioimaging and Nanomedicine

A dissertation submitted in partial satisfaction of the requirements
for the degree Doctor of Philosophy

in

Nanoengineering

by

Jinyoung Kang

Committee in charge:

Professor Michael J. Sailor, Chair
Professor Jesse V. Jokerst, Co-Chair
Professor Yi Chen
Professor Seth M. Cohen
Professor Liangfang Zhang

2018

The Dissertation of Jinyoung Kang is approved, and it is acceptable in quality and form for publication on microfilm and electronically:

_____

_____

_____

_____

_____

Chair

University of California San Diego

2018

DEDICATION

To my family

TABLE OF CONTENTS

LIST OF FIGURES

LIST OF TABLES

ACKNOWLEDGEMENTS

I would like to express my gratitude to Professor Michael Sailor, for giving me an opportunity to be a part of "Sailor Group", supporting me, believing in me, and teaching me how to be a scientist. Thank you for all your guidance, encouragement and patience in the past five years. I believe what I learned from you will be great value in my future career.

Thanks to my committee members for taking your time on my thesis and helpful advice: Prof. Jesse Jokerst, Prof. Yi Chen, Prof. Seth Cohen, and Prof. Liangfang Zhang.

To all current and former group members – thanks for your support, helpful discussion, and all the good times for chatting, happy hours, and in general. Thanks for the group members who helped me to be familiar with instruments, etching, and lab life when I first joined the group. I will never forget your help. Thanks for the group members who have worked together to keep me moving forward. I hope that I will have the opportunity to work with you in the future. My lab life was happy because of all the group members. I sincerely hope that good luck for your future.

To all collaborators – thanks for all your support, valuable suggestions and encouragement. Thank you for allowing me to use the lab space and to work together. I know it was a marvelous opportunity for me, and I was happy to work together. I wish you all the best in the future. I sincerely hope that I will have the opportunity to work with you in the future.

To all my friends – thank you for always cheering me on. Thank you for spending a lot of time together without being lonely. I will not forget your advice and help.

To my family - thank you for always cheering and encouraging me to focus on my work. Thank you for helping me mentally and physically healthy. I could not have done it without you.

Chapter 2, in full, is a reprint of the material as it appears in Advanced Materials 2016. Jinyoung Kang, Jinmyoung Joo, Ester J. Kwon, Matthew Skalak, Sazid Hussain, Zhi-Gang She, Erkki Ruoslahti, Sangeeta N. Bhatia, Michael J. Sailor. The dissertation author was the primary researcher and author of this material.

Chapter 3, in full, is a reprint of the material as it appears in Journal of the American Chemical Society 2016. Dokyoung Kim, Jonathan M. Zuidema, Jinyoung Kang, Youlin Pan, Lianbin Wu, David Warther, Barry Arkles, Michael J. Sailor. The dissertation author was the primary researcher and author of this material.

Chapter 4, in full, is a reprint of the material as it appears in Advanced Materials 2017. Dokyoung Kim, Jinyoung Kang, Taejun Wang, Hye Gun Ryu, Jonathan M. Zuidema, Jinmyoung Joo, Muwoong Kim, Youngbuhm Huh, Junyang Jung, Kyo Han Ahn, Ki Hean Kim, Michael J. Sailor. The dissertation author was the primary researcher and author of this material.

Chapter 5, in full, is a reprint of the material as it appears in Advanced Materials 2018. Jinyoung Kang, Dokyoung Kim, Junxin Wang, Yunho Han, Jonathan M. Zuidema, Ali Hariri, Ji-Ho Park, Jesse V. Jokerst, Michael J. Sailor. The dissertation author was the primary researcher and author of this material.

VITA

Education:

2007 B.S., Chemical Engineering, Yonsei University, South Korea

2009 M.S., Interdisciplinary Program in Nanomedical Science and Technology, Yonsei University, South Korea

2018 Ph.D., Nanoengineering, University of California San Diego, United States

PUBLICATIONS

1. "Porous Silicon–Graphene Oxide Core–Shell Nanoparticles for Targeted Delivery of siRNA to the Injured Brain" Jinmyoung Joo, Ester J Kwon, **Jinyoung Kang**, Matthew Skalak, Emily J Anglin, Aman P Mann, Erkki Ruoslahti, Sangeeta N Bhatia, Michael J Sailor, *Nanoscale horizons* 1.5 (2016): 407-414.

2. "Self-Sealing Porous Silicon-Calcium Silicate Core–Shell Nanoparticles for Targeted siRNA Delivery to the Injured Brain" **Jinyoung Kang**, Jinmyoung Joo, Ester J. Kwon, Matthew Skalak, Sazid Hussain, Zhi-Gang She, Erkki Ruoslahti, Sangeeta N. Bhatia, Michael J. Sailor, *Advanced Materials* 28.36 (2016): 7962-7969.

3. "Facile Surface Modification of Hydroxylated Silicon Nanostructures Using Heterocyclic Silanes" Dokyoung Kim*, Jonathan M. Zuidema*, **Jinyoung Kang***, Youlin Pan, Lianbin Wu, David Warther, Barry Arkles, Michael J. Sailor, *Journal of the American Chemical Society 138.46 (2016): 15106-15109.* (*These authors contributed equally.)

4. "Two-Photon *In Vivo* Imaging with Porous Silicon Nanoparticles" Dokyoung Kim*, **Jinyoung Kang***, Taejun Wang*, Hye Gun Ryu, Jonathan M. Zuidema, Jinmyoung Joo, Muwoong Kim, Youngbuhm Huh, Junyang Jung, Kyo Han Ahn, Ki Hean Kim, Michael J. Sailor, *Advanced Materials* 29.39 (2017): 1703309. (*These authors contributed equally.)

5. "Antibiotic-loaded nanoparticles targeted to the site of infection enhance antibacterial efficacy" Sazid Hussain*, Jinmyoung Joo*, **Jinyoung Kang**, Byungji Kim, Gary B. Braun, Zhi-Gang She, Dokyoung Kim, Aman P. Mann, Tarmo Mölder, Tambet Teesalu, Santina Carnazza, Salvatore Guglielmino, Michael J. Sailor, Erkki Ruoslahti, *Nature Biomedical Engineering* 2.2 (2018): 95. (*These authors contributed equally.)

6. "Oriented Nanofibrous Polymer Scaffolds Containing Protein-Loaded Porous Silicon Generated by Spray Nebulization" Jonathan M. Zuidema*, Tushar Kumeria*, Dokyoung Kim, **Jinyoung Kang**, Joanna Wang, Geoffrey Hollett, Xuan Zhang, David S. Roberts, Nicole Chan, Cari Dowling, Elena Blanco-Suarez, Nicola J. Allen, Mark H. Tuszynski, Michael J. Sailor, *Advanced Materials* 30.12 (2018): 1706785. (*These authors contributed equally.)

7. "Immunogene therapy with fusogenic nanoparticles modulates macrophage response to Staphylococcus aureus" Byungji Kim*, Hong-Bo Pang*, **Jinyoung Kang**, Ji-Ho Park, Erkki Ruoslahti, Michael J. Sailor, *Nature communications* 9.1 (2018): 1969. (*These authors contributed equally.)

8. "Enhanced Performance of a Molecular Photoacoustic Imaging Agent by Encapsulation in Mesoporous Silicon Nanoparticles" **Jinyoung Kang***, Dokyoung Kim*, Junxin Wang,

Yunho Han, Jonathan M. Zuidema, Ali Hariri, Ji-Ho Park, Jesse V. Jokerst, Michael J. Sailor, *Advanced Materials* (2018): 1800512. (*These authors contributed equally.)

9. "Tracking the Fate of Porous Silicon Nanoparticles Delivering a Peptide Payload by Intrinsic Photoluminescence Lifetime" Yusung Jin*, Dokyoung Kim*, Hajung Roh, Sojeong Kim, Sazid Hussain, **Jinyoung Kang**, Chan-Gi Pack, Jun Ki Kim, Seung-Jae Myung, Erkki Ruoslahti, Michael J. Sailor, Song Cheol Kim, Jinmyoung Joo, *Advanced Materials* 30.35 (2018): 1802878. (*These authors contributed equally.)

10. "Hybrid Polymer/ Porous Silicon Nanofibers for Tunable Release of Functional Nucleic Acids" Jonathan M. Zuidema*, Alessandro Bertucci*, **Jinyoung Kang**, Francesco Ricci, Michael J. Sailor, in preparation (2018) (*These authors contributed equally.)

11. "Tumor-targeted microRNA-silencing Porous Silicon Nanoparticles for Ovarian Cancer Therapy" Alessandro Bertucci*, Kang-Hoon Kim*, **Jinyoung Kang**, Jonathan M. Zuidema, Ester J. Kwon, Dokyoung Kim, Stephen B. Howell, Francesco Ricci, Erkki Ruoslahti, Hyeung-Jin Jang, Michael J. Sailor, in preparation (2018) (*These authors contributed equally.)

12. "Tumor-specific macrophage targeting through recognition of retinoid X receptor beta" Tang Tang*, Yushuang Wei*, **Jinyoung Kang**, Zhi-Gang She, Michael J. Sailor, Erkki Ruoslahti and Hong-Bo Pang, in preparation (2018) (*These authors contributed equally.)

13. "Porous Silicon Nanoparticles for Targeted Nerve Growth Factor Delivery to the Injured Brain" **Jinyoung Kang***, Jonathan M. Zuidema*, Lauren Waggoner, Ester J. Kwon, Michael J. Sailor, in preparation (2018) (*These authors contributed equally.)

14. "PI3Kγ-loaded Porous Silicon Nanoparticles Targeted Tumor Specific Macrophages" **Jinyoung Kang**, Tang Tang, Hong-Bo Pang, Michael J. Sailor, in preparation (2018)

ABSTRACT OF DISSERTATION

Porous Silicon Nanomaterials for Bioimaging and Nanomedicine

by

Jinyoung Kang

Doctor of Philosophy in Nanoengineering

University of California San Diego, 2018

Professor Michael J. Sailor, Chair

Professor Jesse V. Jokerst, Co-Chair

There is increased interest in porous silicon nanomaterials for biomedical applications due to their biodegradability, their biocompatibility, and their intrinsic photoluminescence. This thesis describes cargo loading chemistry, surface chemistry,

molecularly targeted delivery and bioimaging applications using porous silicon nanomaterials.

After a brief introduction to porous silicon materials for biomedical applications, Chapter 2 describes a single-step procedure to simultaneously load and protect a model siRNA therapeutic in porous silicon nanoparticles (pSiNPs). Exogenous calcium ions precipitate with locally generated silicic acid to form calcium silicate, which serves to encapsulate the siRNA payload in pSiNPs. The target gene knockdown efficiency *in vitro* and target tissue accumulation of delivered siRNA *in vivo* are demonstrated.

Chapter 3 presents a facile chemical modification of the surface of the hydroxylated silicon nanostructure. The reaction, a ring-opening heterocyclic silane "click" reaction, is a rapid and efficient means to obtain high surface coverage while preserving the open pore structure and intrinsic photoluminescence of the original silicon nanostructure. This chemistry is sufficiently mild to maintain the activity of payload proteins.

Chapter 4 presents the example of pSiNPs as an imaging agent, which are targeted to tumor tissues *in vivo* using an iRGD peptide targeting probe, and the nanoparticles are imaged by two-photon microscopy. Superior photostability and low systemic toxicity are observed.

Chapter 5 discusses enhanced photoacoustic signals that can be obtained from indocyanine green (ICG) when it is encapsulated in pSiNPs. The photoacoustic response from ICG is enhanced 17-fold when it is sealed in pSiNPs. The substantially improved performance is attributed to the low thermal conductivity of pSiNPs and their ability to protect loaded ICG from photolytic degradation.

CHAPTER 1

Introduction: Porous Silicon Materials for Biomedical Applications

1.1. Porous Silicon Materials

Porous silicon (pSi) materials have attractive properties for biomedical applications, e.g. large surface area, high loading capacity, controllable pore dimension, convenient surface chemistry, biocompatibility, and biodegradability.[1] In particular, biocompatibility and biodegradability are essential properties for the safe application of nanomaterials to biomedical applications. The nano-engineered pSi materials degrade in the organism to the orthosilicic acid [$Si(OH)_4$] form, which is non-toxic and excreted in urine.[2] Moreover, a human has a certain level of Si naturally, and continuously intake Si through our daily food.[3] The nanocrystalline pSi exhibits efficient photoluminescence properties in the near-infrared region by quantum confinement effect.[4-6] Therefore, the intrinsic properties of pSi materials can be applied to diagnose and treat disease by bioimaging and targeted drug delivery with *in vivo* administration.

In this chapter, we describe the cargo loading chemistry and surface chemistry needed to use pSi for biomedical applications and introduce approaches applied to drug delivery and bioimaging applications.

1.2. Cargo Loading Chemistry

In order to use pSi materials for biomedical applications, it is necessary to efficiently load cargo molecules in the pores. For designing an effective drug delivery system, properties of pSi, e.g. pore size, porosity, surface chemistry, and loading method should be carefully considered according to the physical properties of the payload molecules.[7] Furthermore, the loading chemistry should be

sufficiently mild that the activity of the released payload from pSi particles has to be maintained.[8] The loaded drug can be released into the body by pSi degradation or pore diffusion, and the surface characteristics of pSi and the interaction between pSi and payloads influence the drug release profile.[9]

Inorganic pSi nanoparticles are useful for loading and delivering molecules that are easily degradable by enzymes in the body or has low water solubility because it is possible to isolate and protect the payloads from the external environment.[10-13] In addition, since the pore dimension can be easily adjusted, pSi nanoparticles can deliver drugs without limitation of payloads size.[14] Various electrostatic or hydrophobic interactions, physical adsorption, covalent grafting, and pore capping reactions have been utilized for effective drug loading.[15,16] Immersion and impregnation loading methods can be performed using physical adsorption of payloads to the pSi matrix without a harsh chemical environment or higher temperature conditions.[17] Drugs can be loaded by covalent bonding to the pSi surface, and controlled release by cleavage of the linker between drugs and pSi or degradation of "host" pSi matrix.[15] In case of pore capping reaction, drugs can be trapped in the pSi matrix as the pore wall expansion through the oxidation of the pSi skeleton.[8]

Specifically, Chapter 2 provides a method for loading siRNAs in pSi nanoparticles via pore capping reaction.[18] The siRNAs are readily degraded by nuclease in blood serum, thus efficient loading and protection are critical to deliver siRNA to target tissues. As the pSi degrades in the aqueous phase, dissolved silicic acid meets calcium ions, forms calcium silicate precipitates rapidly, blocks the pore,

and traps surrounding siRNA in pSi nanoparticles. It is called the self-sealing chemistry because the source of the capping material is from the local dissolution of pSi itself. Various kinds of hydrophilic payloads including oligonucleotides and small molecules can be loaded in pSi particles using the self-sealing chemistry.

1.3. Surface Chemistry

The pSi requires maintaining physical and chemical properties under the harsh biological conditions for biomedical applications. It can be determined the release rate or locations of the loaded drugs by modifying the rate of pSi degradation or conferring on pSi with functions to be degraded in specific conditions (e.g. pH, enzyme concentration).[19-22] Moreover, target specific accumulation *in vivo* can be obtained by introducing target homing ligands to the pSi surface.[13] Therefore, it is necessary to give various functions to pSi through surface chemistry.

Electrochemically etched pSi has a hydride-terminated surface, which is the starting point for a variety of subsequent reactions. Oxidation and hydrosilylation are two of the most important chemical reactions.[7] By using these reactions, pSi acquires stability and various functional groups to the surface.

Chapter 3 focuses on "ring-opening click reaction", which is facile and effective surface chemistry without byproducts.[23] The ring-opening reaction is faster and surface coverage is greater compared to traditional alkoxysilane chemistry. It is also suitable for biomedical applications because pSi can maintain its original photoluminescence intensity and activity of loaded protein even after the chemical reaction.

1.4. Targeted Drug Deliver Applications

Among the various advantages of pSi, it is most notable that various types of targeting ligands can be conjugated to the pSi surface by the facile surface chemistry. The pSi-based nanomaterial is suitable for drug delivery applications via active targeting because of the ability to easily load and conjugate various kinds of drugs and targeting ligands (e.g. peptides, antibodies, aptamers, small molecules, and proteins).[13] Currently, many promising and successful results using pSi have been reported in the literature to show *in vivo* targeted drug delivery.

Ferrari et al. have reported selective accumulation of pSi microparticles in the bone marrow tissue.[24] The pSi surface was presented E-selectin thioaptamer ligand, which is capable of recognizing E-selectin on endothelium in bone marrow tissue. These aptamer-decorated pSi particles can load anticancer drugs and show higher bone marrow accumulation *in vivo* compared to non-targeted pSi particles. Santos et al. have reported pSi nanoparticles as a cancer theragnostic system, which has iRGD peptides as tumor targeting moieties and ^{111}In radiolabeling as single photon emission computed tomography (SPECT) imaging agent.[25] The pSi-iRGD showed the ability to load antiangiogenic drugs and improved selectivity for metastatic prostate cancer *in vivo*. The recent study has reported that pSi nanoparticles are enabling not only deliver drugs to target site but also obtain therapeutic efficacy *in vivo*. The pSi nanoparticles were synthesized with green fluorescence protein (GFP) against siRNA payloads and conjugated CAQK peptides, which can selectively bind to the injured mouse brain.[26] The injected pSi nanoparticle selectively knockdown

the GFP expression of the injured brain area as well as injured brain selective accumulation.

Future studies are expected to develop pSi-based materials that can be used for clinical translation with a focus on more clinical-oriented programs.

Specifically, Chapter 2 and 4 provide target specific accumulation of pSi *in vivo* by chemically conjugated targeting peptides to the surface. Neuronal tissue targeting peptide (RVG)-conjugated pSi showed payload siRNA delivery to the injured brain area (Chapter 2),[18] and tumor homing peptide (iRGD)-conjugated pSi showed highly selective accumulation in tumor tissue (Chapter 4).[27]

1.5. Bioimaging Applications

Therapy and biomedical imaging are the most intensively studied area of nanoparticles for biomedical applications. Applying pSi as an imaging agent has attracted a lot of attention recently due to the biocompatibility and intrinsic photoluminescence of pSi.[2, 28] The photoluminescence produced by the quantum confinement of the silicon skeleton can be excited by the UV range light and show an emission in the near-infrared region (600-1000 nm).[29,30] Based on this property, Park et al. monitored pSi nanoparticles *in vivo* using its photoluminescence.[2] The passively accumulated pSi nanoparticle in MDA-MB-435 human carcinoma tumors was detected *in vivo*, and the fluorescence intensities of pSi nanoparticle decreased according to the degradation pSi nanoparticles. However, since the quantum yield of pSi is relatively low and the degradation rate *in vivo* is fast, there is a limit to monitor photoluminescence *in vivo* using commercial imaging setup. Joo et al. have

reported gated luminescence imaging of pSi nanoparticles by using a relatively long photoluminescence lifetime of pSi.[31] The gated luminescence images showed a significantly improved signal to noise ratio with minimizing background signal including autofluorescence from mouse skin and tissue. As a result, gated imaging demonstrates 100 times better contrast in major organs after pSi nanoparticle administration compared to commercial fluorescence equipment, IVIS images. Although there has been much progress in monitoring pSi nanoparticles *in vivo*, deep tissue optical imaging is limited by the shallow penetration depth of UV excitation light source.

In chapter 4, we have developed pSi nanoparticles with improved photoluminescence, which can be used as the two-photon *in vivo* imaging agent.[27] The pSi nanoparticles enable relatively deep tissue imaging using two-photon excitation with superior photostability and targeting capability.

On the other hand, many attempts have been made to load or conjugate the imaging agent into the pSi particles for bioimaging applications. The fluorescence dye-conjugated pSi to monitor with the fluorescence imaging equipment, superparamagnetic iron oxide nanoparticles loaded pSi particles to obtain MRI imaging, and radiolabeling onto pSi particles for SPECT imaging have been developed based on pSi materials.[32]

Chapter 5 introduces indocyanine green (ICG) encapsulated pSi nanoparticles as a photoacoustic imaging agent.[33] By sealing ICG in pSi materials with low thermal conductivity, ICG can obtain the insulation effect from surrounding solvent and protection effect from photolytic degradation. As a result, ICG-loaded pSi

nanoparticles showed 17-fold higher photoacoustic response compared to free ICG molecules. This is a good example of the increased sensitivity of the imaging agent using pSi materials.

1.6. References

[1] H. A. Santos, E. Mäkilä, A. J. Airaksinen, L. M. Bimbo, J. Hirvonen, *Nanomedicine* **2014,** *9,* 535.

[2] J.-H. Park, L. Gu, G. Von Maltzahn, E. Ruoslahti, S. N. Bhatia, M. J. Sailor, *Nat Mater* **2009,** *8,* 331.

[3] J. Pennington, *Food Addit Contam* **1991,** *8,* 97.

[4] L. T. Canham, *Appl Phys Lett* **1990,** *57,* 1046;

[5] V. Lehmann, U. Gösele, *Appl Phys Lett* **1991,** *58,* 856;

[6] M. J. Sailor, *Porous silicon in practice: preparation, characterization and applications*, John Wiley & Sons, 2012.

[7] E. J. Anglin, L. Cheng, W. R. Freeman, M. J. Sailor, *Adv Drug Deliv Rev* **2008,** *60,* 1266.

[8] N. L. Fry, G. R. Boss, M. J. Sailor, *Chem Mater* **2014,** *26,* 2758.

[9] N. H. Maniya, S. R. Patel, Z. Murthy, *Rev Adv Mater Sci* **2016,** *44*, 257.

[10] T. Kumeria, S. J. McInnes, S. Maher, A. Santos, *Expert Opin Drug Deliv* **2017,** *14,* 1407.

[11] G. Ahuja, K. Pathak, *Indian J Pharm Sci* **2009,** *71,* 599.

[12] F. Wang, H. Hui, T. J. Barnes, C. Barnett, C. A. Prestidge, *Mol Pharm* **2009,** *7,* 227.

[13] M.-A. Shahbazi, B. Herranz, H. A. Santos, *Biomaterials* **2012,** *2,* 296.

[14] C. Pacholski, M. Sartor, M. J. Sailor, F. Cunin, G. M. Miskelly, *J Am Chem Soc* **2005,** *127,* 11636.

[15] S. M. Haidary, E. P. Corcoles, N. K. Ali, *J Nanomater* **2012,** *18,* 1.

[16] K. Tamarov, S. Näkki, W. Xu, V.-P. Lehto, *J Mater Chem B* **2018,** *6,* 3632.

[17] J. Salonen, A. M. Kaukonen, J. Hirvonen, V.-P. Lehto, *J Pharm Sci* **2008,** *97,* 632.

[18] J. Kang, J. Joo, E. J. Kwon, M. Skalak, S. Hussain, Z. G. She, E. Ruoslahti, S. N. Bhatia, M. J. Sailor, *Adv Mater* **2016,** *28,* 7962.

[19] M. Xue, X. Zhong, Z. Shaposhnik, Y. Qu, F. Tamanoi, X. Duan, J. I. Zink, *J Am Chem Soc* **2011,** *133,* 8798.

[20] W. Xu, R. Thapa, D. Liu, T. Nissinen, S. Granroth, A. Närvänen, M. Suvanto, H. l. A. Santos, V.-P. Lehto, *Mol Pharm* **2015,** *12,* 4038.

[21] E. J. Anglin, M. P. Schwartz, V. P. Ng, L. A. Perelman, M. J. Sailor, *Langmuir* **2004,** *20,* 11264.

[22] Y. Zhu, W. Meng, N. Hanagata, *Dalton Trans* **2011,** *40,* 10203.

[23] D. Kim, J. M. Zuidema, J. Kang, Y. Pan, L. Wu, D. Warther, B. Arkles, M. J. Sailor, *J Am Chem Soc* **2016,** *138,* 15106.

[24] A. P. Mann, T. Tanaka, A. Somasunderam, X. Liu, D. G. Gorenstein, M. Ferrari, *Adv Mater* **2011,** *23,* H278.

[25] C.-F. Wang, M. P. Sarparanta, E. M. Mäkilä, M. L. Hyvönen, P. M. Laakkonen, J. J. Salonen, J. T. Hirvonen, A. J. Airaksinen, H. A. Santos, *Biomaterials* **2015,** *48,* 108.

[26] A. P. Mann, P. Scodeller, S. Hussain, J. Joo, E. Kwon, G. B. Braun, T. Mölder, Z.-G. She, V. R. Kotamraju, B. Ranscht, *Nat Commun* **2016,** *7,* 11980.

[27] D. Kim, J. Kang, T. Wang, H. G. Ryu, J. M. Zuidema, J. Joo, M. Kim, Y. Huh, J. Jung, K. H. Ahn, *Adv Mater* **2017,** *29,* 1703309.

[28] L. Gu, D. J. Hall, Z. Qin, E. Anglin, J. Joo, D. J. Mooney, S. B. Howell, M. J. Sailor, *Nat Commun* **2013,** *4,* 2326.

[29] K.-H. Lin, S.-C. Liou, W.-L. Chen, C.-L. Wu, G.-R. Lin, Y.-M. Chang, *Opt Express* **2013,** *21,* 23416.

[30] C.-C. Tu, Y.-N. Chou, H.-C. Hung, J. Wu, S. Jiang, L. Y. Lin, *Opt Express* **2014,** *22,* 29996.

[31] J. Joo, X. Liu, V. R. Kotamraju, E. Ruoslahti, Y. Nam, M. J. Sailor, *ACS nano* **2015,** *9,* 6233.

[32] D. Ş. Karaman, M. P. Sarparanta, J. M. Rosenholm, A. J. Airaksinen, *Adv Mater* **2018,** 1703651.

[33] J. Kang, D. Kim, J. Wang, Y. Han, J. M. Zuidema, A. Hariri, J. H. Park, J. V. Jokerst, M. J. Sailor, *Adv Mater* **2018,** 1800512.

CHAPTER 2

Self-Sealing Porous Silicon-Calcium Silicate Core-Shell Nanoparticles for Targeted siRNA Delivery to the Injured Brain

2.1. Abstract

A single-step procedure to simultaneously load and protect high concentrations of siRNA in porous silicon nanoparticles (pSiNPs) is presented. Treatment of pSiNPs with an aqueous solution containing siRNA and calcium chloride generates core-shell nanostructures consisting of an siRNA-loaded pSiNP core infiltrated with an insoluble shell of calcium silicate (Ca-pSiNPs). The source of silicate in the shell derives from local dissolution of the pSi matrix, and in solutions containing high concentrations of calcium (II) ion, Ca_2SiO_4 formation occurs primarily at the nanoparticle surface and is self-limiting. The insoluble calcium silicate shell slows the degradation of the pSiNP skeleton and prolongs delivery of the siRNA payload, resulting in more effective gene knockdown *in vitro*. Formation of the calcium silicate shell results in an increase in the external quantum yield of photoluminescence from the porous silicon core from 0.1 to 21 %, presumably due to the electronically passivating nature of the silicate shell. Attachment of two functional peptides that incorporate a sequence derived from the rabies virus glycoprotein (RVG) as a neuronal targeting peptide and myristoylated transportan (mTP) as a cell penetrating moiety to the Ca-pSiNPs yields a construct that shows improved gene silencing *in vitro* and improved delivery *in vivo*.

2.2. Introduction

A significant limitation in efficacy of small molecule, protein, and nucleic acid-based therapeutics is bioavailability. Molecules with low solubility may not enter the blood stream or other bodily fluids at therapeutically effective concentrations,[1–3] and more soluble therapeutics may undergo rapid clearance from the circulatory system by various

biological processes before reaching the intended tissues.[4–6] Loading of therapeutics into porous or hollow nanostructures has emerged as a means to control the concentration–time relationship of drug delivery and improve therapeutic efficacy.[7,8] Much work in nanostructured carriers for drugs has been based on "soft" particles such as liposomes and polymer conjugates,[9,10] or more rigid porous inorganic materials such as mesoporous silicon or silicon oxide.[11–13] Mesoporous silicon and silicon oxide are inorganic and biodegradable materials that have been well studied for drug delivery applications.[8,14–26]

The mechanism of degradation of porous silicon (pSi) involves oxidation of the silicon skeleton to form silicon oxide, followed by hydrolysis of the resulting oxide phase to water-soluble orthosilicic acid ($Si(OH)_4$) or its congeners.[25] To prevent rapid degradation of pSi nanoparticles, various "core–shell" types of structures have been synthesized, where an inner core of a pSi skeleton is surrounded by a shell of more stable silicon oxide,[27,28] titanium oxide,[29–31] carbon,[32–34] or other kinetically stable substances.[35] Core–shell structures are attractive platforms for slow releasing drug delivery formulations because the synthesis of the shell can be performed in concert with drug loading in order to more effectively trap the therapeutic in the nanostructure.[36] Furthermore, the ability of core–shell structures to enhance intensity and persistence of photoluminescence from the luminescent silicon domains in pSi has been demonstrated,[27] which adds imaging and self-reporting drug delivery features to the nanomaterial.

We report here a single-step procedure to simultaneously load and protect high concentrations of siRNA in pSi nanoparticles (pSiNPs) by precipitating an insoluble shell of calcium silicate simultaneous with drug loading (Fig. 2.1). The source of silicate in the shell derives from local dissolution of the pSi matrix, and in solutions containing high

concentrations of calcium (II) ion, we find that Ca_2SiO_4 formation occurs primarily at the nanoparticle surface and is self-limiting. If the calcium ion solution also contains siRNA, the oligocucleotide becomes trapped in the porous nanostructure during shell formation. The insoluble calcium silicate shell slows the degradation of the porous silicon skeleton and the release of siRNA. The porous Si core displays intrinsic photoluminescence due to quantum confinement effects, and we find that the shell formation process leads to an increase in the external quantum yield from 0.1% to 21%, presumably due to the electronically passivating nature of the silicate shell. To demonstrate the potential for gene delivery with this system, we modify the calcium silicate-coated pSiNPs (Ca-pSiNPs) via silanol chemistry to conjugate two functional peptides, one for neuronal targeting and the other for cell penetration. The resulting construct shows significantly improved gene silencing efficacy *in vitro*, and it can be delivered to targeted tissues *in vivo*.

2.3. Results and Discussion

The pSiNPs of average size 180 ± 20 nm (by dynamic light scattering) were prepared as described previously.[37] The siRNA payload was loaded and sealed into the porous nanostructure in one step, by stirring the pSiNPs in an aqueous solution containing the oligonucleotide in the presence of a high concentration (3M) of $CaCl_2$. Control experiments where the same quantity of free siRNA was mixed in a solution 3M in $CaCl_2$, but without added pSiNPs, showed no evidence of precipitate under the reaction conditions. To avoid the possibility of undetectable precipitates of siRNA with Ca^{2+}, the pSiNPs were isolated after reaction by centrifugation and washing three times, first using DI water, then 70% ethanol, and finally absolute ethanol. The mass loading of siRNA was typically 20%,

as determined by difference (free siRNA remaining in the supernatant) and by direct measurent of the quantity of siRNA released from the oligonucleotide-loaded Ca-pSiNPs in RNAse free DI water. The presence of silicon, calcium, and oxygen in the resulting siRNA-loaded, calcium silicate-capped pSiNPs (Ca-pSiNP-siRNA) was confirmed by energy dispersive x-ray (EDX) analysis (Fig. 2.2). No residual chloride was detected. The quantity of oxygen in the pSiNPs increased measurably upon reaction with the Ca^{2+} solution, demonstrating that pSiNPs are oxidized during the reaction. Transmission electron microscope (TEM) images (Fig. 2.3a-c) of empty pSiNP prior to calcium ion treatment, pSiNP after treatment with Ca^{2+} (Ca-pSiNP), and pSiNP after loading of siRNA and treatment with Ca^{2+} (Ca-pSiNP-siRNA) indicated that the reaction with Ca^{2+} generated a distinctive coating (Fig. 2.3bc). Based on the elemental analysis and considering the low solubility of calcium silicate,[38] we propose the capping material to be dicalcium orthosilicate (Ca_2SiO_4) or a mixed phase of calcium orthosilicate, metasilicate, and silicon oxides. No crystalline calcium silicate or silicon oxide phases were observed by powder X-ray diffraction (XRD), but residual crystalline Si was detected in the XRD spectrum (Fig. 2.4a) and in the Raman spectrum (Si-Si lattice mode at 520 cm^{-1}, Fig. 2.4b). The characteristic band for surface Si-O (1020 cm^{-1}) was observed in the FTIR spectrum both before and after Ca^{2+} treatment (Fig. 2.4c). Nitrogen adsorption-desorption isotherm analysis indicated that the total pore volume decreased by 80% (1.36 ± 0.03 cm^3/g to 0.29 ± 0.04 cm^3/g) upon conversion of pSiNP to Ca-pSiNP (Fig. 2.3d). Prior work has shown that oxidation of pSi results in reduction of the pore volume due to swelling of the pore walls as oxygen is incorporated into the silicon skeleton, and this process can result in effective trapping of a payload in the pores.[25, 36]

Optical absorbance measurements, used to measure the amount of elemental silicon in the solution, showed that ~40% of the pSiNPs were degraded within 80 min in a pH 9 buffer when no calcium ion was present. However, in 3M $CaCl_2$ solution (also at pH 9), only ~10% degradation was observed in the same time period (Fig. 2.5a). The calcium silicate shell also impeded release of the siRNA cargo; the Ca-pSiNP-siRNA formulation showed ~5-fold slower release under physiologic conditions (pH 7.4 buffer, 37 °C), compared to a formulation in which siRNA was held in the pSiNPs by electrostatic means (pSiNPs modified with surface amine groups, pSiNP-NH_2, Fig. 2.5b). The Ca-pSiNP-siRNA formulation also showed substantially greater siRNA loading efficiency compared to electrostatically loaded particles (20-25% *vs* 5-8%, respectively). Thus the calcium silicate trapping chemistry effectively encapsulated and slowed release of the siRNA payload, and it protected the pSi skeleton from subsequent oxidation and hydrolysis in aqueous media.

The photoluminescence spectrum obtained at different times during the course of the reaction between pSiNPs and $CaCl_2$ solution showed a gradual increase in intensity (Fig 2.3e). Additionally, the peak wavelength of photoluminescence blue shifted as the reaction progressed. Both of these phenomena (increase in photoluminescence intensity and blue shift of the photoluminescence spectrum) are indicative of the growth of a passivating surface layer on the silicon nanocrystallites.[27, 39, 40] The observed blue shift is typical of a quantum-confined silicon nanoparticle, whose emission wavelength is strongly dependent on size and exhibits a blueshift as the quantum-confined silicon domains become smaller.[38] The photoluminescence emission quantum yield (external) for the pSiNP-calcium silicate core-shell structure (Ca-pSiNP) was 21% (λ_{ex} = 365 nm, Fig. 2.6).

A preliminary *in vitro* cytotoxicity screen on cultured Neuro-2a (mouse neuroblastoma) cells showed no significant cytotoxicity of the Ca-pSiNP formulation at nanoparticle concentrations up to 50 μg/mL (Fig. 2.7), and so the system was loaded with a targeting and a therapeutic payload for gene silencing studies (the loading procedure is described schematically in Fig. 2.8). A small interfering RNA (siRNA) capable of silencing the endogenous gene (peptidylprolyl isomerase B, PPIB) was chosen to test the ability of the calcium silicate chemistry to retain, protect, and deliver a therapeutic payload for *in vivo* studies. The pSiNPs were loaded with siRNA against PPIB (siPPIB) in the presence of 3M $CaCl_2$, which resulted in ~20 wt% siRNA content in the resulting nanoparticle (Ca-pSiNP-siRNA). The morphology of the Ca-pSiNP-siRNA construct appeared similar to the drug-free Ca-pSiNP preparation by TEM (Fig. 2.3c), although the surface charge (zeta potential, Fig. 2.9a) of Ca-pSiNP-siRNA was negative instead of positive. The positive zeta potential of the drug-free Ca-pSiNP preparation is attributed to an excess of Ca^{2+} ions at the particle surface, and the negatively charged siRNA payload neutralizes these charges to the extent that it results in an overall negative zeta potential in the Ca-pSiNP-siRNA construct.

To achieve targeted delivery and intracellular trafficking of the siRNA therapeutic, a tissue targeting peptide and a cell penetrating peptide were then grafted to the calcium silicate shell of the Ca-pSiNP-siRNA construct. A PEG linker was used to attach both of these peptides to improve systemic circulation (Fig. 2.8). First, the chemical coupling agent 2-aminopropyldimethylethoxysilane (APDMES) was grafted to the nanoparticle surface, generating pendant primary amine groups (Ca-pSiNP-siRNA-NH_2).[25] The zeta potential became more positive after the APDMES reaction for either Ca-pSi-NH_2 or Ca-

pSiNP-siRNA-NH_2 formulations due to the primary amine groups on the outermost surface of the nanoparticles (Fig. 2.9a). Functional polyethyleneglycol (PEG) species were then grafted to Ca-pSiNP-siRNA-NH_2 via these primary amines, using a maleimide-poly(ethylene-glycol)-succinimidyl carboxy methyl ester (MAL-PEG-SCM) species.[41] The succinimidyl carboxymethyl ester forms an amide bond with primary amines, and thus provides a convenient means to attach PEG to the aminated nanoparticle. The distal end of the PEG chain contained a second functional group, maleimide. Maleimide forms covalent bonds to thiols, allowing attachment of targeting and cell penetrating peptides. Two peptide species, myr-GWTLNSAGYLLGKINLKALAALAKKIL(GGCC), a myristoylated transportan referred to here as "mTP," and the rabies virus-derived peptide 5FAM-(CCGG)YTIWMPENPRPGTPCDIFTNSRGKRASNG, referred to as "FAM-RVG," were prepared and conjugated to the Ca-pSiNP-siRNA-PEG formulation via reaction of the maleimide group with a cysteine thiol of the relevant peptides. Here, "5FAM" is the fluorescent label 5-carboxyfluorescein, an amine-reactive fluorophore commonly used to label biomolecules ($\lambda_{ex}/\lambda_{em}$ = 495/518 nm).

Cell-penetrating peptides (CPP) such as transportan (TP) have been found to be promising auxiliaries for siRNA delivery. When CPPs are incorporated into nanoparticles, they can increase endocytic escape after internalization to increase the siRNA knockdown efficiency. However, CPPs lack cell-type specificity. To overcome this shortcoming, CPPs have been combined with cell-specific targeting peptides to generate what is known as tandem peptides, and these constructs have been shown to be very efficient siRNA delivery agents.[45] In the present work, the cell-penetrating transportan peptide was attached to a myristoyl group, which contains a hydrophobic 13 carbon aliphatic chain, to enhance the

hydrophobic interaction between the peptide and the lipid bilayer of the cell membrane (mTP).[43] The cell targeting function was accomplished with a peptide sequence from the rabies virus glycoprotein (RVG) that has demonstrated effective neuronal cell targeting efficiency *in vitro* and *in vivo*.[44-46] Attachment of both RVG and mTP peptides to a Ca-pSiNP resulted in a dual peptide nanocomplex, referred to here as "Ca-pSiNP-DPNC." Control nanoparticles containing only mTP or RVG peptides were also prepared, herein designated as Ca-pSiNP-mTP or Ca-pSiNP-RVG, respectively.

Approximately 0.1mg of RVG was conjugated with 1 mg of Ca-pSiNP-siRNA-PEGs, determined by relative fluorescence of the FAM label. In the case of the Ca-pSiNP-siRNA-DPNC construct, approximately 0.04mg of RVG and a comparable amount of mTP was conjugated. The Fourier transform infrared (FTIR) spectrum of Ca-pSiNP-DPNC displayed all the characteristic peaks of Ca-pSiNP-mTP and Ca-pSiNP-RVG (Fig. 2.10). The mean diameter of the Ca-pSiNP-siPPIB-DPNC construct was 220 nm (DLS Z-average, intensity based), representing an increase over the pSiNP starting material of 40 nm. No significant aggregates were observed in the DLS data (Fig. 2.9b).

The Ca-pSiNP-siPPIB-DPNC construct effected knockdown of 52.8% of PPIB gene activity in Neuro-2a cells relative to untreated controls (Fig. 2.11). To eliminate the possibility that gene silencing was caused by toxicity of the nanocomplexes, a similar formulation loaded with a negative control siRNA against the luciferase gene (siLuc) was tested, and it showed no statistically significant difference relative to the untreated control. As additional controls, gene silencing efficiencies of nanoparticles containing only a cell-penetrating or only a cell-targeting peptide were tested (Ca-pSiNP-siPPIB-mTP and Ca-pSiNP-siPPIB-RVG, respectively). Both of these constructs showed some observable

knockdown of PPIB gene expression (27.1-28.9% relative to untreated controls), but the silencing effect was greater with the dual peptide nanoparticle Ca-pSiNP-siPPIB-DPNC ($p < 0.03$) compared with either peptide system individually. In the case of Ca-pSiNP-siPPIB-mTP, the gene knockdown observed *in vitro* is not expected to translate to *in vivo* activity, because the cell penetrating effect of mTP lacks cell-type specificity. On the other hand, silencing by Ca-pSiNP-siPPIB-RVG is attributed to more effective cellular localization *in vitro* due to specific binding of the RVG sequence to Neuro-2a cells. Additional controls using free siPPIB (not contained in a nanoparticle) and siPPIB loaded into bare pSiNPs (no Ca capping chemistry, no targeting peptides, no cell-penetrating peptides) showed no statistically significant knockdown. Furthermore, nano-constructs isolated and stored in ethanol for 7 days at 4 °C still retained their PPIB gene knockdown efficiency (Fig. 2.11).

The present results show better cellular affinity and gene knockdown when the dual peptide nanocomplex (DPNC, containing both mTP and RVG) was used compared with the single peptide conjugated nanoparticles (Ca-pSiNP-siRNA-mTP or Ca-pSiNP-siRNA-RVG). Transmission electron microscope (TEM) data on Ca-pSiNP-DPNC-treated Neuro-2a cells (Fig. 2.12) established that the nanoparticles were indeed internalized and dispersed in the cell cytoplasm after 1 hr incubation. The images are consistent with endosomal uptake of the nanoparticles, although the present studies did not assess the intracellular trafficking or endosomal uptake mechanism(s).

Consistent with its greater knockdown efficiency, confocal microscope images indicated that the Ca-pSiNP-siPPIB-DPNC formulation had greater affinity for Neuro-2a cells than the Ca-pSiNP-siPPIB-RVG formulation (Fig. 2.13). The Ca-pSiNP-siPPIB-

DPNC formulation had approximately half the number of fluorescent FAM marker molecules on its surface compared to Ca-pSiNP-siPPIB-RVG. Even with the lower FAM fluorescence signal per particle, Neuro-2a cells treated with Ca-pSiNP-siPPIB-DPNC showed a larger FAM signal because of the greater cellular affinity of this dual peptide construct relative to the RVG-only formulation. The Ca-pSiNPs are visible in the fluorescence microscope images due to the intrinsic photoluminescence from the quantum-confined Si domains of the nanoparticle. In the case of cells treated with Ca-pSiNP-siPPIB-DPNC, the Si signal is colocalized with the signal from the FAM label on the RVG targeting peptide, and the combined signal is seen in the cytosol, indicative of cellular internalization. The cellular affinity of these two nanoparticle constructs was more accurately quantified by fluorescence-activated cell sorting (FACS) analysis (Fig. 2.14), and the data show that the dual peptide nanoparticle was more efficient at targeting Neuro-2a cells than the nanoparticle that contained only the RVG peptide (51.4 ± 5.6% vs 36.4 ± 5.6 % for Ca-pSiNP-siPPIB-DPNC and Ca-pSiNP-siPPIB-RVG, respectively ($P < 0.04$). Separate fluorescent labels on the RVG peptide and on the siPPIB in the Ca-pSiNP-siPPIB-DPNC established that 65.9 ± 8.7% of the cells contained both RVG and siPPIB (Fig. 2.14d). The results support the hypothesis that conjugating both RVG and mTP to the nanoparticle yields greater cellular affinity, which in turn generates a stronger gene knockdown effect.

Often *in vitro* targeting results are not replicated *in vivo* due to active clearance by the MPS organs and other physiologic factors associated with the complex *in vivo* environment. In order to demonstrate the feasibility of *in vivo* delivery of siRNA by the nanoconstructs, we performed a pilot study involving a penetrating brain injury model in

mice. As having both cell-penetrating and cell-targeting peptides on the same nanoparticle (Ca-pSiNP-siPPIB-DPNC) yielded the strongest gene knockdown *in vitro*, we selected this construct for the *in vivo* gene delivery experiments.

Significant quantities of siRNA accumulated in the site of the brain injury in the mice injected with Ca-pSiNP-siRNA-DPNC (Fig. 2.16). The mice (n = 3) showed 2-fold greater intensity of fluorescence associated with the siRNA payload relative to the fluorescence background in saline-injected control mice, and the ratio of fluorescence at the injured site relative to the uninjured hemisphere was 5.2. There was statistically greater observed efficacy of targeting by the dual peptide Ca-pSiNP-siRNA-DPNC relative to the untargeted nanoparticles Ca-pSiNP-siRNA-PEG ($p < 0.02$). Mice injected with the untargeted Ca-pSiNP-siRNA-PEG construct showed some siRNA fluorescence signal in the brain compared to the uninjected control mice, presumably due to passive leakage into the injury site. Correspondingly, these Ca-pSiNP-siRNA-PEG-injected mice displayed greater fluorescence intensity in the kidney and (to a lesser extent) the liver relative to mice injected with the Ca-pSiNP-siRNA-DPNC constructs. The biodistribution data are thus consistent with the greater ability of the dual-targeted nanoparticles to accumulate in the brain. Mice injected with any of the nanoparticle formulations displayed no overt short-term health effects.

2.4. Conclusions

This work demonstrates a self-sealing chemical procedure that can load oligonucleotides in a biodegradable and intrinsically photoluminescent nanoparticle. Substantial quantities of siRNA can be loaded (> 20% by mass), and the payload is retained

for therapeutically relevant timescales. The calcium silicate shell is readily modified with cell targeting (RVG peptide from rabies virus glycoprotein) and cell-penetrating (myristolated transportan) peptides, and the combination of the two peptides, along with the ability of the calcium silicate chemistry to retain and protect the siRNA payload, yields improved cellular targeting and gene knockdown *in vitro*. The multivalent core-shell nanoparticles circulate to deliver an siRNA payload to a brain injury in live mice, and the dual targeted nanoparticles show improved delivery of siRNA in the *in vivo* brain injury model relative to non-targeted nanoparticles.

2.5. Experimental

Preparation of porous silicon nanoparticles: The pSiNPs were prepared following the published "perforation etching" procedure.[37] A highly boron-doped p^{++}-type silicon wafer (~ 1 mΩ-cm resistivity, 100 mm diameter, Virginia Semiconductor, Inc.) was anodically etched in an electrolyte composed of 3:1 (v:v) of 48% aqueous HF:ethanol. The etching waveform consisted of a square wave in which a lower current density of 46 mA cm^{-2} was applied for 1.818 sec, followed by a higher current density pulse of 365 mA cm^{-2} applied for 0.363 sec. This waveform was repeated for 140 cycles, generating a stratified porous silicon (pSi) film with thin, high porosity "perforations" repeating approximately every 200 nm through the porous layer. The film was removed from the silicon substrate by applying a current density of 3.4 mA cm^{-2} for 250 sec in a solution containing 1:20 (v:v) of 48% aqueous HF:ethanol. The freestanding pSi film was fractured into nanoparticles of mean (Z-average, intensity based) diameter 180 nm (Fig. 2.9b) by immersion in deionized water and ultrasonication for ~12 hr.

Preparation of calcium silicate-coated, siRNA-loaded porous silicon nanoparticles (Ca-pSiNP-siRNA): A stock solution 4 M in calcium chloride ($CaCl_2$) were prepared by adding 2.25 g of solid $CaCl_2$ (MW: 110.98, Anhydrous, Spectrum chemicals) to 5 mL of RNAse-free water. The solution was centrifuged to remove any precipitates and stored at 4 °C before use. For oligonucleotide loading, three kinds of duplexed siRNA constructs for the knockdown of PPIB(1), PPIB(2), and Luciferase was synthesized by Dharmacon Inc. with 3'-dTdT overhangs.[47, 48]: For PPIB gene against siRNA (siPPIB), siPPIB(1) and siPPIB(2) were obtained, respectively, and used 1:1 mixture of siPPIB(1):siPPIB(2) to cover broad range of PPIB gene on the siRNA sequence sense 5'-CAA GUU CCA UCG UGU CAU C dTdT-3' and antisense 5'- GAU GAC ACG AUG GAA CUU G dTdT-3' for siPPIB(1) and sense 5'-GAA AGA GCA UCU AUG GUG A dTdT-3' and antisense 5'-UCA CCA UAG AUG CUC UUU C dTdT-3' for siPPIB(2). Luciferase gene against siRNA (siLuc) was obtained on the siRNA sequence sense 5'-CUU ACG CUG AGU ACU UCG A dTdT-3' and antisense 5'-UCG AAG UAC UCA GCG UAA G dTdT-3'. The pSiNPs (100 μL DI, 1 mg) were mixed with the oligonucleotide solution (150 μL DI, 150 μM in siRNA) and added to the 4 M $CaCl_2$ stock solution (750 μL). The mixture was agitated for 60 min and purified by successive dispersion in/centrifugation from RNAse free deionized water, 70% ethanol, and 100% ethanol. To analyze siRNA loading efficiency, supernatants from each centrifugation step were collected and assayed for free siRNA using a NanoDrop 2000 spectrophotometer (Thermo Scientific, ND-2000). As a control, Ca-pSiNPs without siRNA were prepared in the same manner as described above, but excluding the added siRNA. Mass loading of siRNA was verified by quantification of siRNA released from the oligonucleotide-loaded Ca-pSiNPs, performed in RNAse-free

deionized water and measured using a NanoDrop 2000 spectrophotometer. The two determinations varied by < 10% in the quantity of siRNA loaded.

Conjugation of peptides to Ca-pSiNP: As-prepared Ca-pSiNP-siRNA, Ca-pSiNP or pSiNP samples (1 mg) were suspended in absolute ethanol (1 mL), an aliquot (20 μL) of aminopropyldimethylethoxysilane (APDMES) was added, and the mixture was agitated for 2h. The aminated nanoparticles (Ca-pSiNP-siRNA-NH_2, Ca-pSiNP-NH_2, or pSiNP-NH_2) were then purified three times by centrifugation from absolute ethanol to eliminate unbound APDMES. The solutions (200 μL) of the hetero-functional linkers maleimide-PEG-succinimidyl carboxy methyl ester (MAL-PEG-SCM, MW: 5,000, Laysan Bio Inc., 5 mg/mL in ethanol) or methoxy-PEG-succinimidyl α-methylbutanoate (mPEG-SMB, Mw: 5,000, NEKTAR, 5 mg/mL in ethanol) were added to the aminated nanoparticles (1 mg in 100 μL) and agitated for 2h. Unbound PEG linker molecules were eliminated from the PEGylated nanoparticles (Ca-pSiNP-siRNA-PEG or Ca-pSiNP-PEG) by centrifugation from ethanol three times. For the peptide-conjugated formulations, one of two peptide constructs was used: either mTP, which consists of a myristoyl group (myr) covalently attached by amide bond to the N-terminal glycine residue on the peptide sequence myr-GWTLNSAGYLLGKINLKALAALAKKIL(GGCC), or FAM-RVG, which consists of 5-carboxyfluorescein (5-FAM) attached by amide bond to the N-terminal cysteine residue on the peptide sequence 5-FAM(CCGG)YTIWMPENPRPGTPCDIFTNSRGKRASNG. Both of these constructs were obtained from CPC Scientific Inc. (1 mg/mL in RNAse free water). For Ca-pSiNP-dual peptide nanocomplex (Ca-pSiNP-DPNC or Ca-pSiNP-siRNA-DPNC) synthesis, 50 μL of each peptide solution (mTP and FAM-RVG) was added to 100 μL of Ca-pSiNP-PEG in ethanol, incubated at 4 °C for 4 hours, purified three times by

centrifugation, immersed in ethanol and stored at 4 °C before use. For synthesis of the single peptide conjugated Ca-pSiNP (Ca-pSiNP-siRNA-mTP or Ca-pSiNP-siRNA-RVG) control samples, 100 μL of peptide solution (mTP or FAM-RVG) was added to 100 μL of Ca-pSiNP-siRNA-PEG in ethanol, respectively. The subsequent workup was the same as described above for the Ca-pSiNP-siRNA-DPNC constructs.

Characterization: Transmission electron microscope (TEM) images were obtained with a JEOL-1200 EX II instrument. Scanning electron microscope (SEM) images and energy dispersed x-ray (EDX) data were obtained using an FEI XL30 field-emission instrument. The hydrodynamic size and zeta potential was measured by dynamic light scattering (DLS, Zetasizer ZS90, Malvern Instruments). An Ocean Optics QE-Pro spectrometer was used to obtain steady-state photoluminescence spectra (λ_{ex}: 365 nm) with a 460 nm long-pass emission filter. Quantum yield measurements were performed relative to a Rhodamine 6G in ethanol standard (Q.Y. 95%). All solutions used for quantum yield measurements had optical absorbance values < 0.1 at λ = 365 nm. The photoluminescence intensity in the wavelength range 500 – 980 nm was integrated and plotted *vs* absorbance (Fig. 2.6). Nitrogen adsorption-desorption isotherms were obtained on dry particles at a temperature of 77 K with a Micromeritics ASAP 2020 instrument. Fourier transform infrared (FTIR) spectra were recorded using a Thermo Scientific Nicolet 6700 FTIR instrument. Raman spectra were obtained using a Renishaw inVia Raman microscope with 532 nm laser excitation source.

In vitro experiments: Murine Neuro-2a neuroblastoma cells (ATCC, CCL-131) were cultured in Eagle's Minimum Essential Medium (EMEM) containing 10% fetal bovine serum (FBS). Cytotoxicity of the synthesized nanoparticles was assessed using the

Molecular Probes Live/Dead Viability/Cytotoxicity Kit (Molecular Probes, Invitrogen).[49] This kit uses 2 probes, Calcein AM for live cell staining ($\lambda_{ex}/\lambda_{em}$ = 494/517 nm) and Ethidium homodimer-1 (EthD-1) for dead cell staining ($\lambda_{ex}/\lambda_{em}$ = 528/617 nm). Neuro-2a cells (3000 cells/well) were treated with nanoparticles in triplicate in a 96-well plate. After 48 hrs, each well was washed and treated with the assay solution consisting of 4 μM EthD-1 and 2 μM Calcein AM in Dulbecco's phosphate buffered saline. After 45 min incubation at room temperature in the assay solution, well plates were read with a fluorescence plate reader (Gemini XPS spectrofluorometer, Molecular Devices, inc.) using excitation, emission, and cutoff wavelengths 485/538/515 nm and 544/612/590 nm, respectively. A total of 15 wells per treatment group were evaluated, and plotted as a percentage of untreated control fluorescence intensity.

Neuro-2a cells treated with nanoparticles were visualized with a confocal microscope (Zeiss LSM 710 NLO), using a 40x oil immersion objective. Cells were seeded onto the coverslips (BD Biocoat Collagen Coverslip, 22 mm), incubated with nanoparticles for 2 hrs, washed three times with PBS, fixed with 4% paraformaldehyde, nucleus stained with DAPI and mounted (Thermo Fisher Scientific, Prolong Diamond Antifade Mountant with DAPI). Neuro-2a cells treated with nanoparticles were quantified to demonstrate cellular affinity and siRNA delivery efficiency by FACS analysis (LSR Fortessa).

In order to investigate knockdown efficiency *in vitro*, real-time quantitative reverse transcription polymerase chain reaction (RT-qPCR, Stratagene Mx3005P qPCR system) analysis was performed to examine PPIB mRNA expression. Neuro-2a cells were seeded in 24-well plates (4×10^4 cells per well), and incubated with siRNA-loaded nanoparticles, with concentration corresponding to 100 nM of siRNA. After 48 hrs, cells were harvested

and total RNA was isolated following the manufacturer's protocol (Qiagen, Vlencia, CA). Isolated RNA was transcribed into cDNA following the manufacturer's protocol (Bio-Rad, iScript cDNA Synthesis Kit). Synthesized cDNA was subjected to qPCR analysis using SYBR Green PCR Master Mix. Primer sequences for PPIB as a target mRNA amplification and HPRT as a reference mRNA amplification are described below. PPIB forward: GGAAAGACTGTTCCAAAAACAGTG, PPIB reverse: GTCTTGGTGCTCTCCACCTTCCG; HPRT forward: GTCAACGGGGGACATAAAAG, HPRT reverse: CAACAATCAAGACATTCTTTCCA. All procedures were performed in triplicate.

In vivo experiments: All animal experiments were performed under protocols approved by the MIT Institutional Animal Care and Use Committees (IACUC) and the Sanford Burnham Prebys Medical Discovery Institute Committee on Animal Use and Care. All housing and care of laboratory animals used in this study conformed to the NIH Guide for the Care and Use of Laboratory Animals in Research (see document 180F22) and all requirements and regulations issued by the USDA, including regulations implementing the Animal Welfare Act (P.L. 89-544) as amended (see document 18-F23). The *in vivo* model involved a penetrating brain injury in mice. First, a 5 mm diameter portion of the skull on the right hemisphere of the mouse was removed. Wounds were induced using a 21 gauge needle in a 3x3 grid for a total of 9 wounds, each 3mm deep. After induction of injuries, the skull was replaced (Fig. 2.15). The mice were injected with nanoparticle constructs 6 hours post-injury via the tail vein. To quantify delivery efficiency of the siRNA cargo to the targeted injury site, Dy677-labeled (λ_{em} = 700 nm) siRNA was loaded into Ca-pSiNP-PEG and Ca-pSiNP-DPNC and each of these formulations were injected

into separate mice. After 1 hour of circulation the mice were perfused and the organs harvested.

Fluorescence images of harvested organs were obtained using conventional IVIS 200, xenogen, and Pearl Trilogy, Li-Cor imaging systems.

Statistical analysis: All data in this article are expressed as the means ± standard error of the mean. Significance testing was conducted using two-tailed Student's *t* test. Unless otherwise indicated, $p < 0.05$ was considered statistically significant.

2.6. References

[1] R. H. Muller, C. Jacobs, O. Kayser, *Adv Drug Deliver Rev* **2001,** *47,* 3.

[2] M. Kataoka, K. Sugano, C. D. Mathews, J. W. Wong, K. L. Jones, Y. Masaoka, S. Sakuma, S. Yamashita, *Pharm Res* **2012,** *29,* 1485.

[3] J. E. Kipp, *Int J Pharm* **2004,** *284,* 109.

[4] A. Chonn, S. C. Semple, P. R. Cullis, *J Biol Chem* **1992,** *267,* 18759.

[5] K. F. Pirollo, E. H. Chang, *Trends Biotechnol* **2008,** *26,* 552.

[6] A. Gabizon, D. Papahadjopoulos, *P Natl Acad Sci USA* **1988,** *85,* 6949.

[7] X. W. Lou, L. A. Archer, Z. C. Yang, *Adv Mater* **2008,** *20,* 3987.

[8] E. J. Anglin, L. Y. Cheng, W. R. Freeman, M. J. Sailor, *Adv Drug Deliver Rev* **2008,** *60,* 1266.

[9] Z. Gu, A. Biswas, M. X. Zhao, Y. Tang, *Chem Soc Rev* **2011,** *40,* 3638.

[10] N. Nishiyama, K. Kataoka, *Pharmacol Therapeut* **2006,** *112,* 630.

[11] J. H. Park, L. Gu, G. von Maltzahn, E. Ruoslahti, S. N. Bhatia, M. J. Sailor, *Nat Mater* **2009,** *8,* 331.

[12] E. C. Wu, J. H. Park, J. Park, E. Segal, F. Cunin, M. J. Sailor, *Acs Nano* **2008,** *2,* 2401.

[13] B. Godin, J. H. Gu, R. E. Serda, R. Bhavane, E. Tasciotti, C. Chiappini, X. W. Liu, T. Tanaka, P. Decuzzi, M. Ferrari, *J Biomed Mater Res Part A* **2010,** *94a,* 1236.

[14] H. A. Meng, M. Xue, T. A. Xia, Y. L. Zhao, F. Tamanoi, J. F. Stoddart, J. I. Zink, A. E. Nel, *J Am Chem Soc* **2010,** *132,* 12690.

[15] H. A. Meng, M. Liong, T. A. Xia, Z. X. Li, Z. X. Ji, J. I. Zink, A. E. Nel, *Acs Nano* **2010,** *4,* 4539.

[16] K. Patel, S. Angelos, W. R. Dichtel, A. Coskun, Y. W. Yang, J. I. Zink, J. F. Stoddart, *J Am Chem Soc* **2008,** *130,* 2382.

[17] J. Lu, M. Liong, J. I. Zink, F. Tamanoi, *Small* **2007,** *3,* 1341.

[18] Q. Shabir, A. Pokale, A. Loni, D. R. Johnson, L. T. Canham, R. Fenollosa, M. Tymczenko, I. Rodriguez, F. Meseguer, A. Cros, A. Cantarero, *Silicon* **2011,** *3,* 173.

[19] M. J. Wang, J. L. Coffer, K. Dorraj, P. S. Hartman, A. Loni, L. T. Canham, *Mol Pharmaceut* **2010,** *7,* 2232.

[20] S. Kashanian, F. Harding, Y. Irani, S. Klebe, K. Marshall, A. Loni, L. Canham, D. M. Fan, K. A. Williams, N. H. Voelcker, J. L. Coffer, *Acta Biomater* **2010,** *6,* 3566.

[21] L. T. Canham, C. P. Barrett, T. I. Cox, P. J. Wright, A. P. Bowditch, *US Patent 20,150,352,211,* 2015.

[22] K. Jiang, A. Loni, L. T. Canham, J. L. Coffer, *Phys Status Solidi A* **2009,** *206,* 1361.

[23] D. M. Fan, A. Loni, L. T. Canham, J. L. Coffer, *Phys Status Solidi A* **2009,** *206,* 1322.

[24] J. Salonen, A. M. Kaukonen, J. Hirvonen, V. P. Lehto, *J Pharm Sci-Us* **2008,** *97,* 632.

[25] M. J. Sailor, J. H. Park, *Adv Mater* **2012,** *24,* 3779.

[26] E. Ruoslahti, S. N. Bhatia, M. J. Sailor, *J Cell Biol* **2010,** *188,* 759.

[27] J. Joo, J. F. Cruz, S. Vijayakumar, J. Grondek, M. J. Sailor, *Adv Funct Mater* **2014,** *24,* 5688.

[28] M. Ray, S. Sarkar, N. R. Bandyopadhyay, S. M. Hossain, A. K. Pramanick, *J Appl Phys* **2009,** *105,* 074301.

[29] C. A. Betty, R. Sasikala, O. D. Jayakumar, T. Sakuntala, A. K. Tyagi, *Prog Photovoltaics* **2011,** *19,* 266.

[30] J. L. Li, M. J. Sailor, *Biosens Bioelectron* **2014,** *55,* 372.

[31] G. Jeong, J. G. Kim, M. S. Park, M. Seo, S. M. Hwang, Y. U. Kim, Y. J. Kim, J. H. Kim, S. X. Dou, *Acs Nano* **2014,** *8,* 2977.

[32] C. K. Tsang, T. L. Kelly, M. J. Sailor, Y. Y. Li, *Acs Nano* **2012,** *6,* 10546.

[33] X. T. Zhou, R. Q. Zhang, H. Y. Peng, N. G. Shang, N. Wang, I. Bello, C. S. Lee, S. T. Lee, *Chem Phys Lett* **2000,** *332,* 215.

[34] P. F. Gao, J. W. Fu, J. Yang, R. G. Lv, J. L. Wang, Y. N. Nuli, X. Z. Tang, *Phys Chem Chem Phys* **2009,** *11,* 11101.

[35] J. M. Buriak, *Chem Rev* **2002,** *102,* 1271.

[36] N. L. Fry, G. R. Boss, M. J. Sailor, *Chem Mater* **2014,** *26,* 2758.

[37] Z. T. Qin, J. Joo, L. Gu, M. J. Sailor, *Part Part Syst Char* **2014,** *31,* 252.

[38] O. A. Medinagonzales, R. L. Fox, R. P. Bosshart, *Fert Res* **1988,** *16,* 3.

[39] V. Petrovakoch, T. Muschik, A. Kux, B. K. Meyer, F. Koch, V. Lehmann, *Appl Phys Lett* **1992,** *61,* 943.

[40] A. Sa'ar, *J Nanophotonics* **2009,** *3,* 032501.

[41] J. Joo, X. Y. Liu, V. R. Kotamraju, E. Ruoslahti, Y. Nam, M. J. Sailor, *Acs Nano* **2015,** *9,* 6233.

[42] Y. Ren, S. Hauert, J. H. Lo, S. N. Bhatia, *Acs Nano* **2012,** *6,* 8620.

[43] Y. Ren, H. W. Cheung, G. von Maltzhan, A. Agrawal, G. S. Cowley, B. A. Weir, J. S. Boehm, P. Tamayo, A. M. Karst, J. F. Liu, M. S. Hirsch, J. P. Mesirov, R. Drapkin, D. E. Root, J. Lo, V. Fogal, E. Ruoslahti, W. C. Hahn, S. N. Bhatia, *Sci Transl Med* **2012,** *4,* 147ra112.

[44] L. Alvarez-Erviti, Y. Q. Seow, H. F. Yin, C. Betts, S. Lakhal, M. J. A. Wood, *Nat Biotechnol* **2011,** *29,* 341.

[45] T. L. Lentz, *J Mol Recognit* **1990,** *3,* 82.

[46] P. Kumar, H. Q. Wu, J. L. McBride, K. E. Jung, M. H. Kim, B. L. Davidson, S. K. Lee, P. Shankar, N. Manjunath, *Nature* **2007,** *448,* 39.

[47] V. V. Ambardekar, H. Y. Han, M. L. Varney, S. V. Vinogradov, R. K. Singh, J. A. Vetro, *Biomaterials* **2011,** *32,* 1404.

[48] C. L. Waite, S. M. Sparks, K. E. Uhrich, C. M. Roth, *Bmc Biotechnol* **2009,** *9*, 38.

[49] R. W. Yee, E. G. Norcom, X. P. C. Zhao, *Adv Ther* **2006,** *23,* 511.

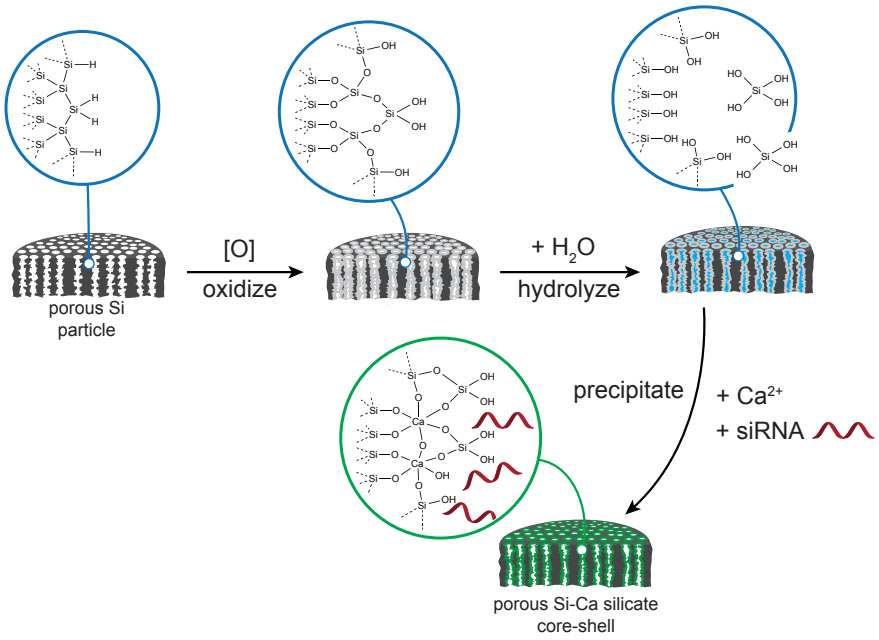

Figure 2.1. Schematic illustration of the mechanistic steps involved in preparation of siRNA-loaded, calcium silicate-coated porous silicon nanoparticles (Ca-pSiNP-siRNA). Mild oxidation (in aqueous media) of porous Si particles generates a thin oxide layer on the Si skeleton. As it forms, the oxide layer becomes hydrated and solublized, releasing $Si(OH)_4$ into solution. High concentrations of Ca^{2+} and siRNA present in the aqueous solution diffuse into the pores, where the Ca^{2+} ions react with the locally high concentration of $Si(OH)_4$, forming a precipitate that traps the siRNA payload within the nanostructure.

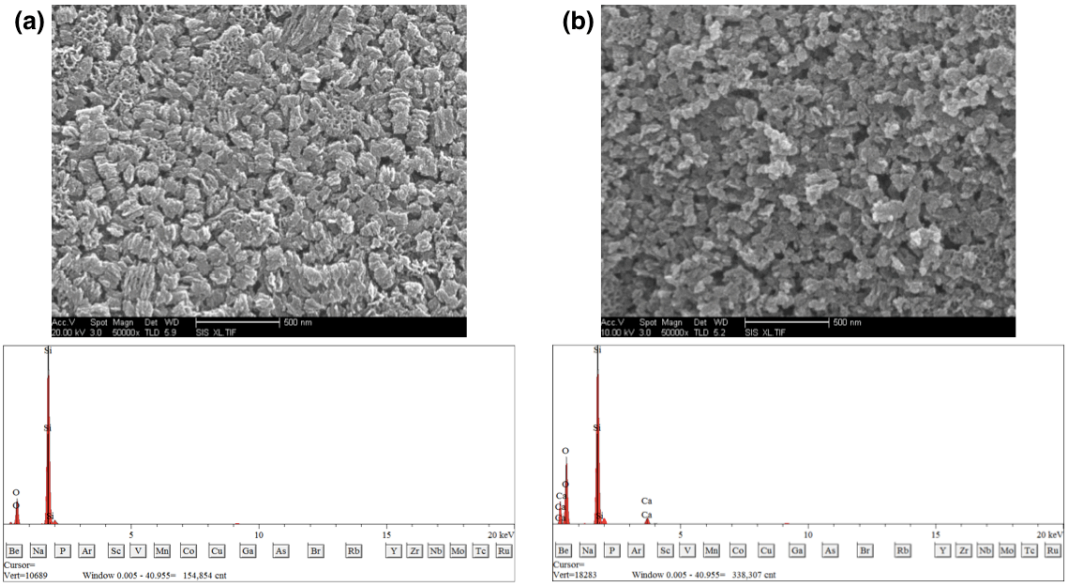

Component	Type	Mole Conc.	Conc.	Units	
O	Calc	42.283	38.350	wt.%	
Si	Calc	38.721	61.650	wt.%	
		100.000	100.000	wt.%	Total

Component	Type	Mole Conc.	Conc.	Units	
O	Calc	66.952	53.143	wt.%	
Si	Calc	31.686	44.150	wt.%	
Ca	Calc	1.362	2.708	wt.%	
		100.000	100.000	wt.%	Total

Figure 2.2. Scanning electron microscope images and elemental (EDX) data of (a) pSiNP and (b) Ca-pSiNP.

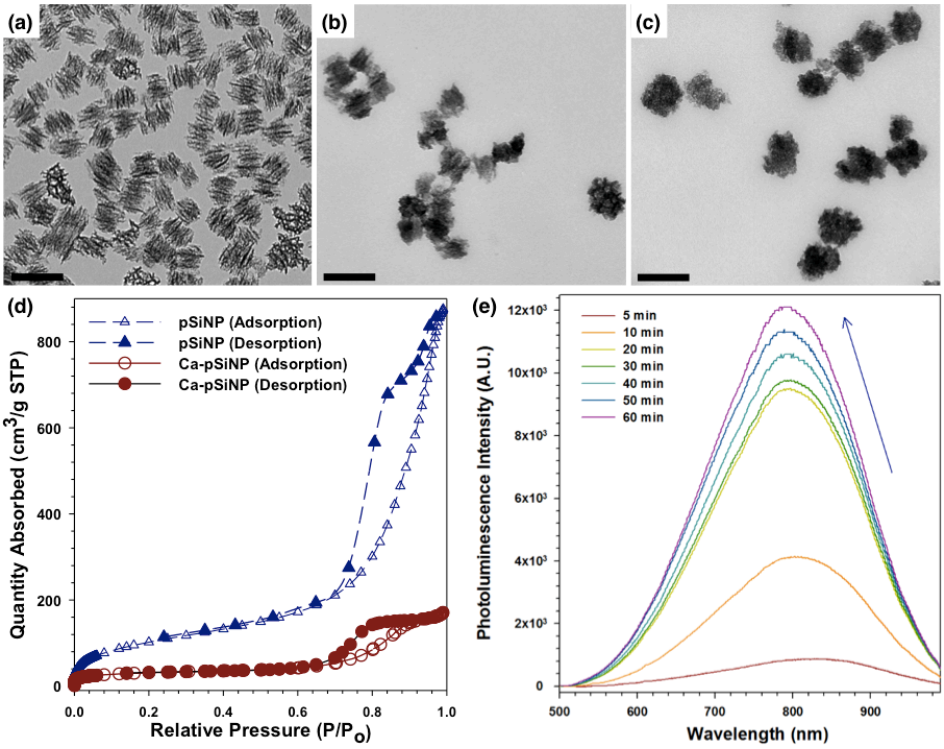

Figure 2.3. Transmission electron microscope (TEM) images of (a) pSiNP, (b) Ca-pSiNP, and (c) Ca-pSiNP-siRNA formulations. Scale bar is 200 nm. (d) Cryogenic nitrogen adsorption-desorption isotherms for pSiNP and Ca-pSiNP formulations. (e) Photoluminescence emission spectra (λ_{ex}: 365nm) obtained during reaction of pSiNP with 3M aqueous $CaCl_2$ solution, used to prepare the Ca-pSiNP formulation. Typical of quantum confinement, as the silicon skeleton becomes thinner the emission spectrum shifts to the blue. The growth of an electronically passivating surface layer and suppression of nonradiative recombination centers is evident in the strong increase in photoluminescence intensity observed as the reaction progresses.

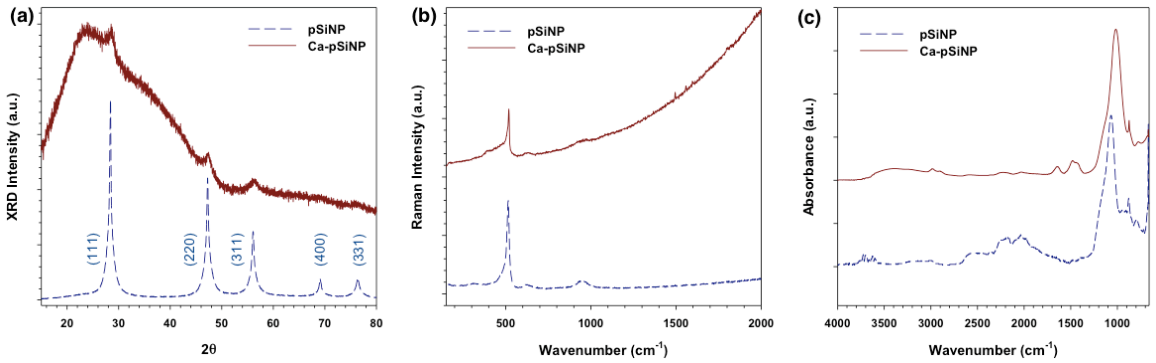

Figure 2.4. (a) Powder X-ray diffraction spectrum of pSiNP (blue dashed line) and Ca-pSiNP (red line), as indicated. Peaks in the diffraction pattern of the Si nanoparticles are labeled with Miller indices, *h k l*, indicating the set of crystalline Si lattice planes responsible for that diffraction peak. (b) Raman spectrum of pSiNP (blue dashed line) and Ca-pSiNP (red line). (c) Diffuse reflectance FTIR spectrum of pSiNP (blue dashed line) and Ca-pSiNP (red line). Spectra are offset along the y-axis for clarity.

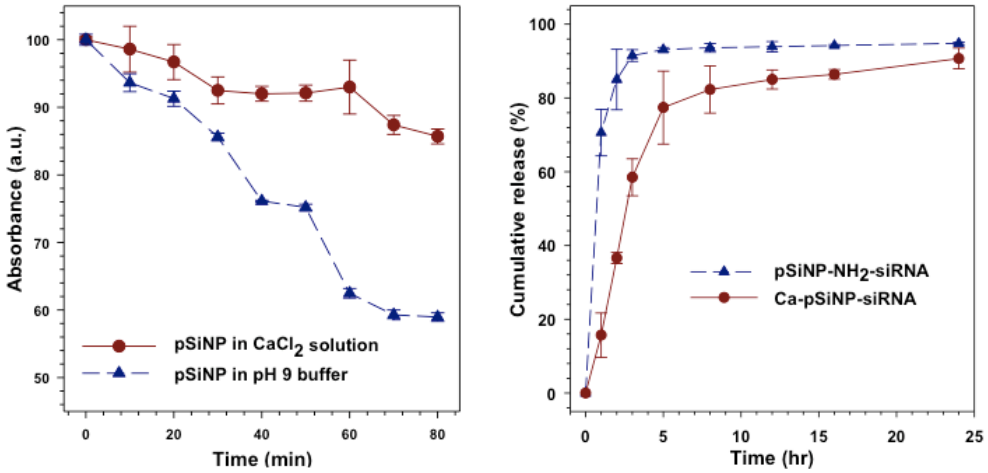

Figure 2.5. (a) UV-Vis absorbance intensity (l = 405 nm) of pSiNP measured as a function of time in pH 9 buffer (blue triangles, dashed line) and pH 9 solution that is 3 M in $CaCl_2$ (red circles, solid line). The loss of absorbance is attributed to degradation of the elemental Si skeleton in the nanoparticle; silicon absorbs 405 nm light strongly, whereas SiO_2 or silicate ions are transparent at this wavelength. (b) Cumulative percent by mass of siRNA released as a function of time at 37 °C in PBS buffer. The pSiNP-NH_2-siRNA formulation was prepared by first grafting of amine to the pore walls of pSiNP using 2-aminopropyldimethylethyoxysilane (APDMES) and then loading siRNA via solution exposure for 2 hrs.

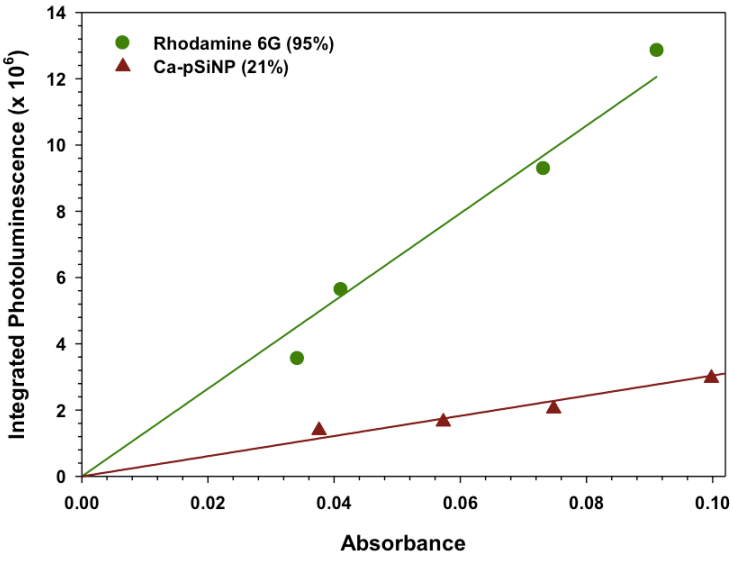

Figure 2.6. Integrated photoluminescence intensity as a function of optical absorbance (365 nm), used to calculate quantum yield of Ca-pSiNP formulation relative to Rhodamine 6G standard. Integrated photoluminescence represents photoluminescence intensity-wavelength curve integrated between 500 - 980 nm. Photoluminescence intensity was measured using a QE-Pro (Ocean Optics) spectrometer, with excitation λ_{ex}= 365 nm and using a 460 nm long-pass emission filter.

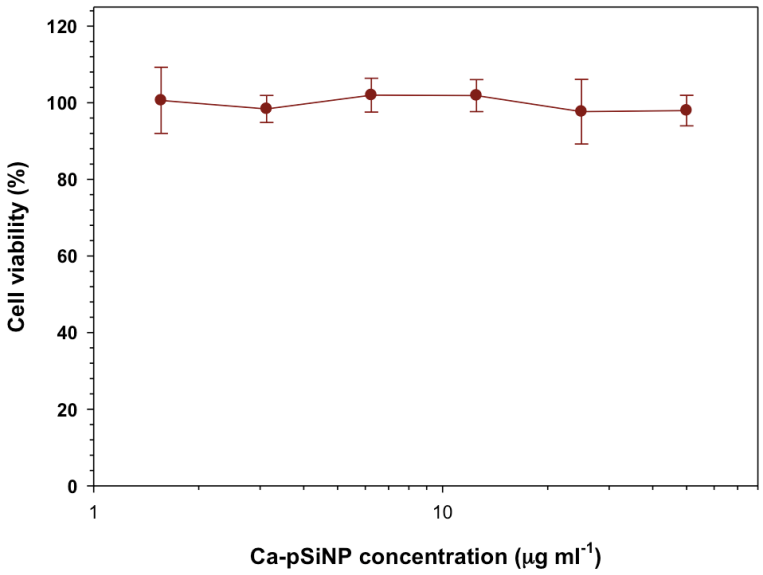

Figure 2.7. Cytotoxicity of Ca-pSiNP construct, quantified by the Calcein AM live/dead assay. Neuro-2a cells were incubated with Ca-pSiNPs in triplicate in a 96-well plate. After 48 hrs, each well was treated with the assay solution, and viability was quantified by measured fluorescence intensity relative to standards.

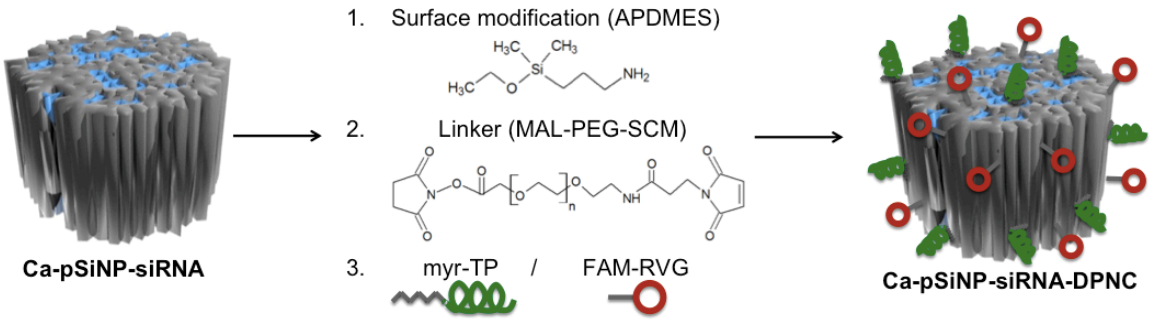

Figure 2.8. Schematic depicting the procedure for PEG modification and conjugation of dual peptides to Ca-pSiNP-siRNA. The coupling agent 2-aminopropyldimethylethoxysilane (APDMES) was grafted to the (calcium silicate and silica) surface of the nanoparticle, generating pendant primary amine groups (Ca-pSiNP-siRNA-NH_2). A functional polyethyleneglycol (PEG) linker was then coupled to the primary amines on the Ca-pSiNP-siRNA-NH_2 nanoparticle, using a maleimide-poly(ethylene-glycol)-succinimidyl carboxy methyl ester (MAL-PEG-SCM) species. The succinimidyl carboxymethyl ester forms an amide bond with primary amines. The distal end of the PEG chain contained a second functional group, maleimide. Maleimide forms covalent bonds to thiols of cysteine, allowing attachment of the neuronal targeting peptide (rabies virus glycoprotein) and cell penetrating peptide (myristoylated transportan).

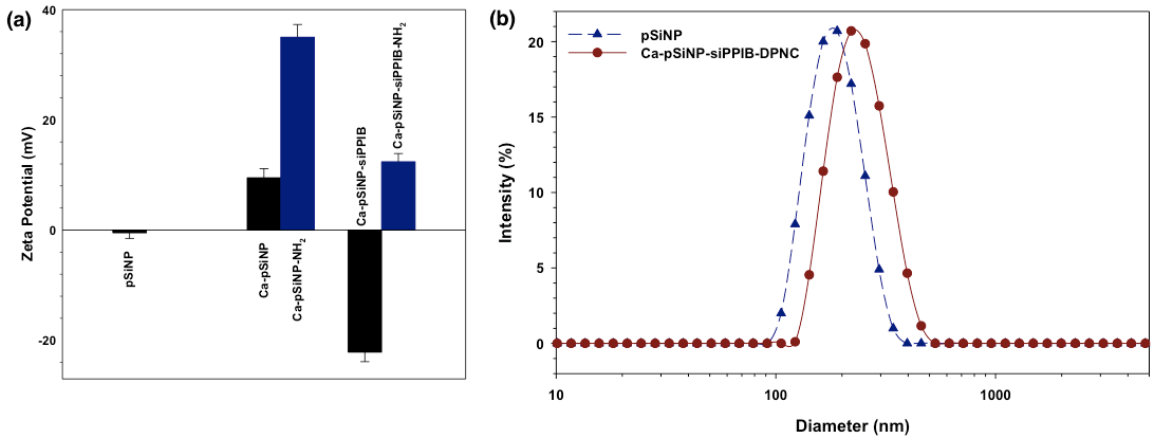

Figure 2.9. (a) Zeta potential of nanoparticles (pSiNP, Ca-pSiNP, Ca-pSiNP-NH_2, Ca-pSiNP-siPPIB, and Ca-pSiNP-siPPIB-NH_2, as described in the text), dispersed in ethanol. (b) Size distribution of pSiNP and Ca-pSiNP-siPPIB-DPNC measured by dynamic light scattering (DLS).

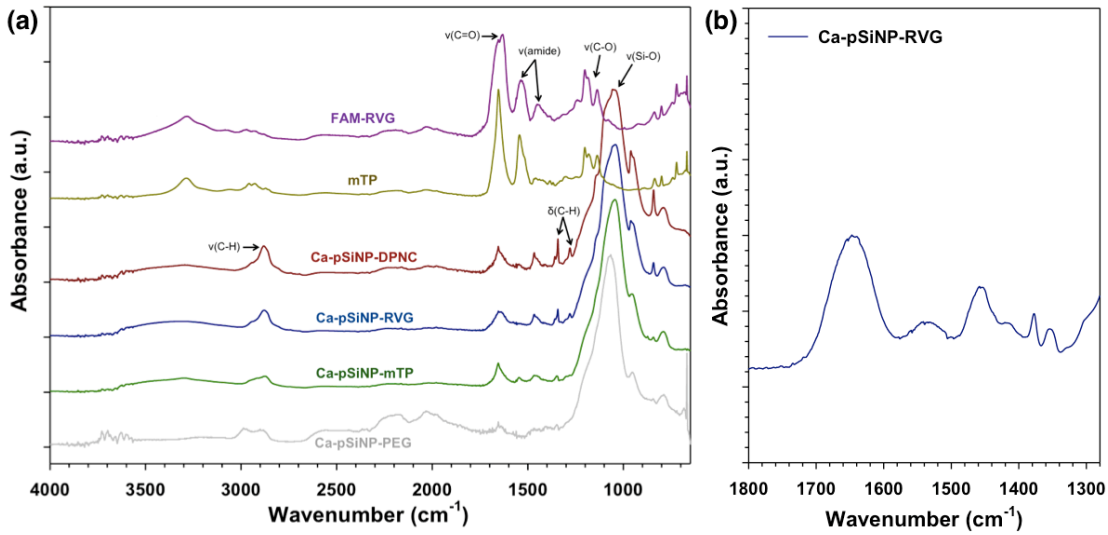

Figure 2.10. (a) ATR-FTIR spectra of nanoparticle formulations (bottom to top) Ca-pSiNP-PEG, Ca-pSiNP-mTP, Ca-pSiNP-RVG, and Ca-pSiNP-DPNC, and peptides (mTP and FAM-RVG). Abbreviations of formulations as described in the text. Spectra are offset along the y-axis for clarity. Assignments of Si-O, C-O, amide and C=O stretching and C-H bending and stretching vibrations are indicated. (Symbols: ν = stretching, δ = bending) (b) Transmission-FTIR spectrum (KBr pellet) of Ca-pSiNP-RVG, expanded in the region 1300-1800 cm^{-1} to clarify the vibration associated with amide bonds (near 1540 cm^{-1}) of the conjugated RVG peptide.

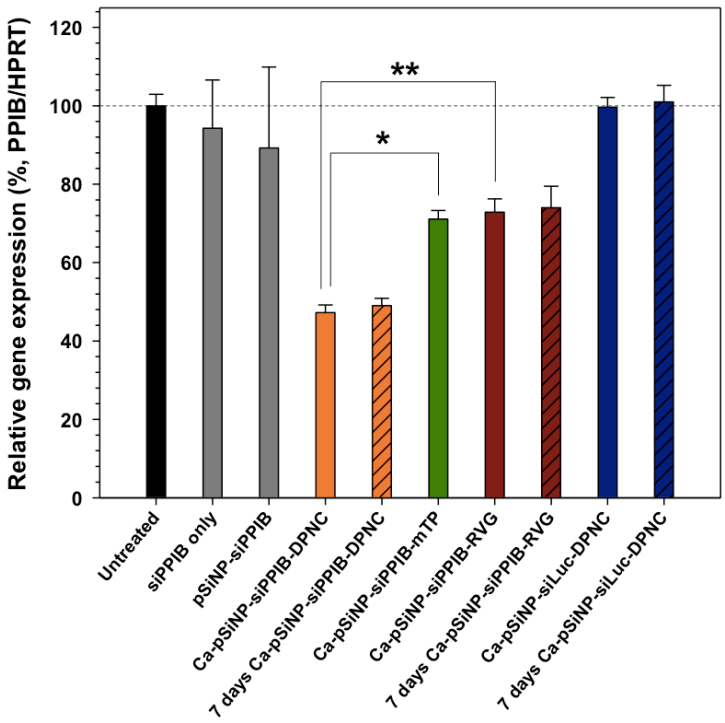

Figure 2.11. The silencing of relative PPIB gene expression in Neuro-2a cells after treatment with siRNA against the PPIB gene (siPPIB), aminated porous Si nanoparticle (pSiNP) loaded with siPPIB (pSiNP-siPPIB), pSiNP-siPPIB construct prepared with a calcium silicate shell and containing both cell-targeting and cell-penetrating peptides on the outer shell in a dual peptide nanocomplex (Ca-pSiNP-siPPIB-DPNC), the pSiNP-siPPIB-calcium silicate shell construct containing only a cell-penetrating peptide on the outer shell (Ca-pSiNP-siPPIB-mTP), the pSiNP-siPPIB-calcium silicate shell construct containing only the cell-targeting peptide on the outer shell (Ca-pSiNP-siPPIB-RVG), and the pSi nanoparticle-calcium silicate shell construct containing a negative control siRNA sequence against luciferase, and containing both the cell-targeting and the cell-penetrating peptides on the outer shell (Ca-pSiNP-siLuc-DPNC). The "7 days" designations indicate that the nanoparticle construct was stored in ethanol at 4°C for 7 days prior to the experiment. The cell penetrating peptide is a myristoylated transportan, and the cell targeting peptide is a domain derived from the rabies virus glycopeptide (RVG) as described in the text. Statistical analyses were performed with Student's *t* test (* $p < 0.01$, ** $p < 0.03$).

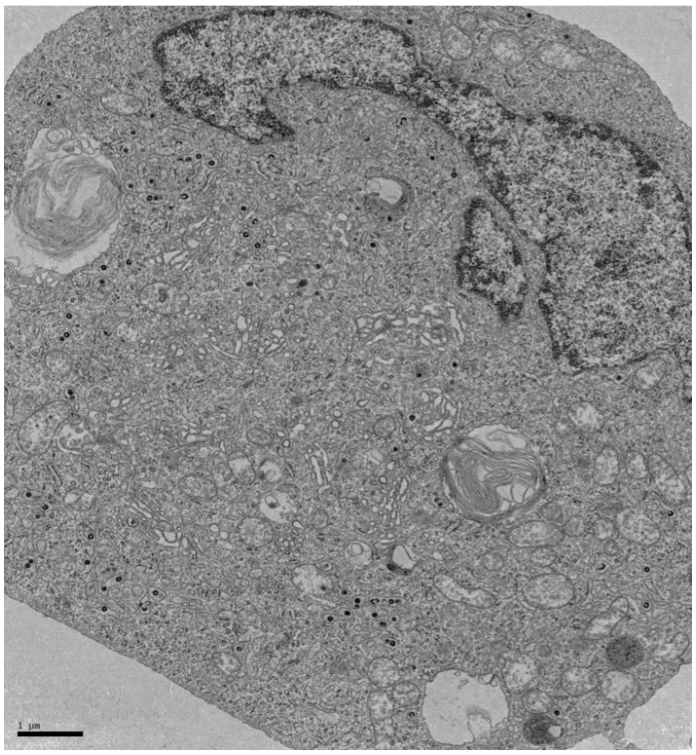

Figure 2.12. TEM image of Neuro-2a cell treated with Ca-pSiNP-DPNC for 1 hr. Ca-pSiNP-DPNCs internalized in the cells are apparent as the small dark dots, which are not present in control images of the same cells (without added Ca-pSiNP-DPNC). Scale bar is 1µm.

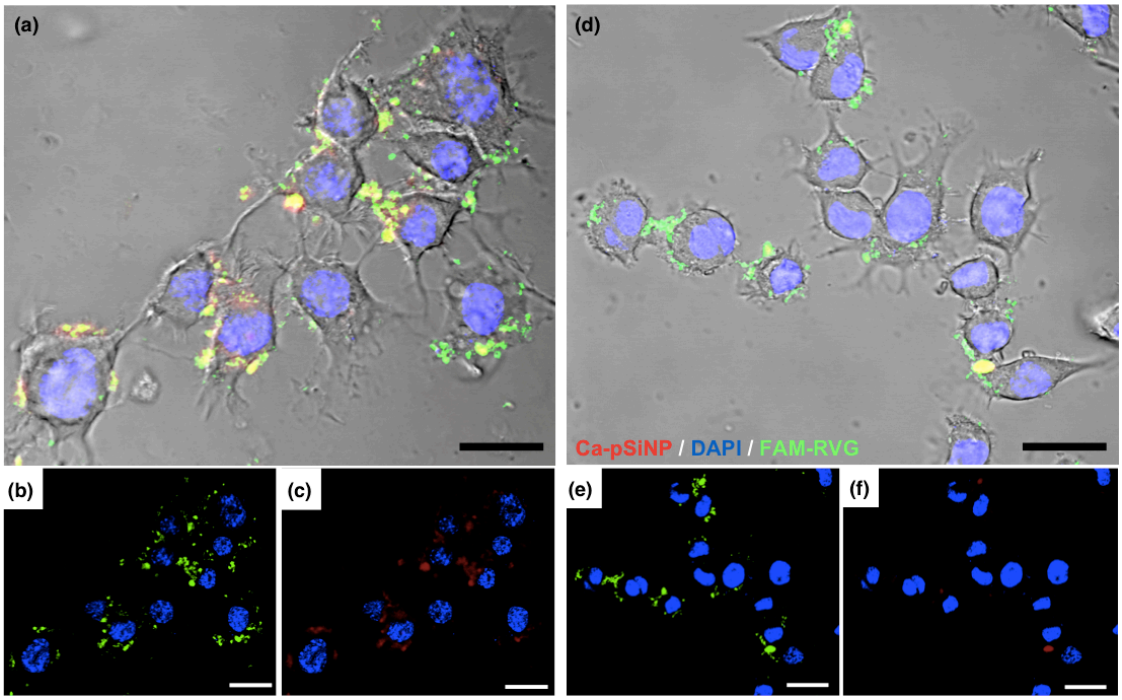

Figure 2.13. Confocal microscope images of Neuro-2a cells treated with (a-c) Ca-pSiNP-siPPIB-DPNC and (d-f) Ca-pSiNP-siPPIB-RVG for 2 hrs at 37°C. The red color represents the signal from intrinsic luminescence of the silicon nanoparticle, blue is from the DAPI nuclear stain, and green is from the FAM tag on the RVG domain. (b, e) Merged images of DAPI and FAM signals. (c, f) Merged image of DAPI and Ca-pSiNP channels. (a,d) Merged images of DAPI, FAM, and Ca-pSiNP channels and bright field image. Yellow in (a) and (d) represents overlap of the silicon and FAM-RVG signals, respectively. Scale bar is 20 μm.

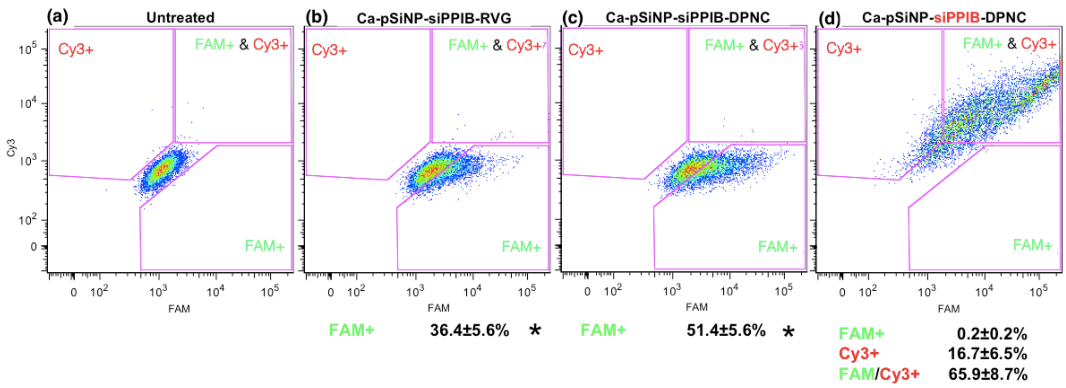

Figure 2.14. FACS analysis of Neuro-2a cells treated with (a) no particles as a control, (b) Ca-pSiNP-siPPIB-RVG, (c) Ca-pSiNP-siPPIB-DPNC, and (d) Cy3-tagged siRNA-loaded Ca-pSiNP-siPPIB-DPNC. The percentages shown below the plots represent quantified proportions of cells transfected with FAM-RVG, Cy3-tagged siRNA, or overlapping of FAM-RVG and Cy3-tagged siRNA, as indicated in the gates displayed. Statistical analyses were performed with Student's *t* test (* $p < 0.04$)

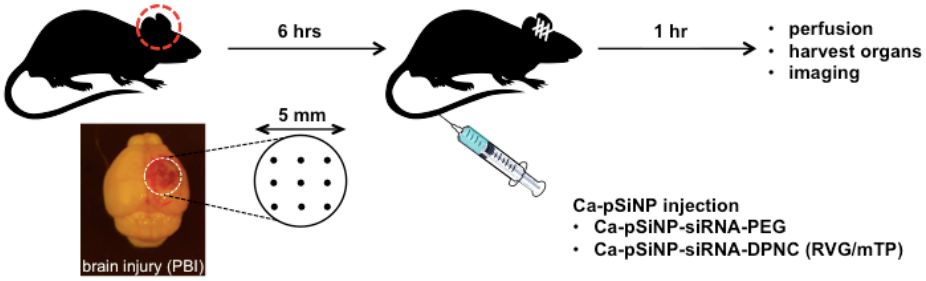

Figure 2.15. Experimental procedure for targeted delivery of siRNA to the injured brain *in vivo*. 6 hrs post-injury, Ca-pSiNP-siRNA-PEG or Ca-pSiNP-siRNA-DPNC were injected. The siRNA in each formulation was labeled with dy677 fluorescent tag. After 1 hr of circulation, the mice were sacrified, perfused, and the organs harvested and imaged.

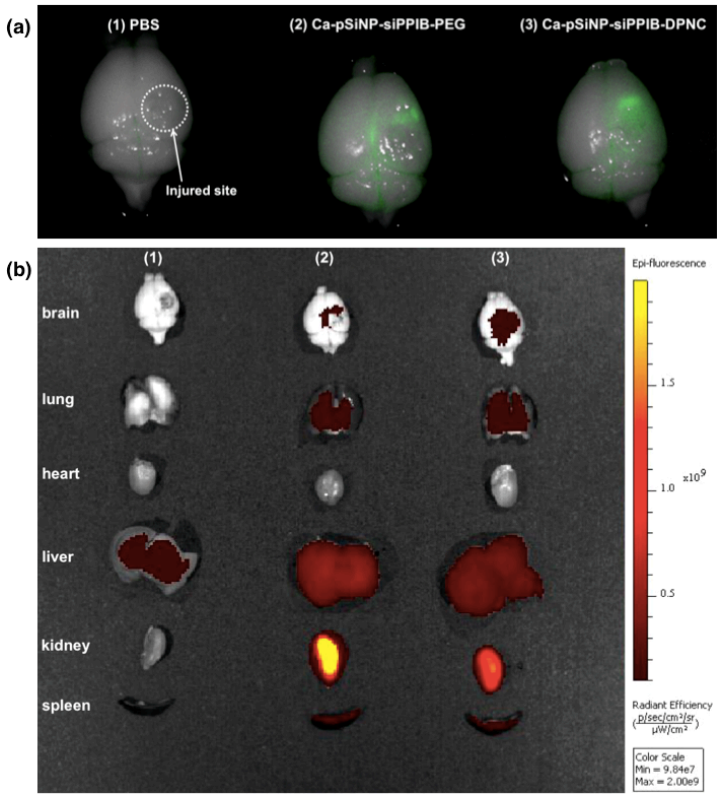

Figure 2.16. *Ex vivo* fluorescence images of harvested organs after intravenous injection of (1) saline as a control, (2) Ca-pSiNP-siRNA-PEG, and (3) Ca-pSiNP-siRNA-DPNC. All siRNA constructs contained covalently attached dy677 fluorophore. (a) Fluorescence image of injured brains obtained using infra-red imaging system Pearl Trilogy (Li-Cor). Green channel in the images corresponds to 700 nm emission from dy677, and the bright field image of the brain tissues is merged with the 700 nm emission. (b) Fluorescence image of whole major organs taken with IVIS (xenogen) imaging system in the Cy5.5 channel ($\lambda_{ex/em}$: 675/694 nm).

Chapter 2, in full, is a reprint of the material as it appears in Advanced Materials 2016. Jinyoung Kang, Jinmyoung Joo, Ester J. Kwon, Matthew Skalak, Sazid Hussain, Zhi-Gang She, Erkki Ruoslahti, Sangeeta N. Bhatia, Michael J. Sailor. The dissertation author was the primary researcher and author of this material.

CHAPTER 3

Facile Surface Modification of Hydroxylated Silicon Nanostructures Using Heterocyclic Silanes

3.1. Abstract

Heterocyclic silanes containing Si−N or Si−S bonds in the ring undergo a ring opening reaction with −OH groups at the surface of porous Si nanostructures to generate −SH or −NH functional surfaces, grafted via O−Si bonds. The reaction is substantially faster (0.5−2 h at 25 °C) and more efficient than hydrolytic condensation of trialkoxysilanes on similar hydroxy-terminated surfaces, and the reaction retains the open pore structure and photoluminescence of the quantum-confined silicon nanostructures. The chemistry is sufficiently mild to allow trapping of the test protein lysozyme, which retains its enzymatic activity upon release from the modified porous nanostructure.

3.2. Introduction

Electrochemical or chemical syntheses of porous silicon (pSi) or silicon nanoparticles usually produce hydrogen-terminated surfaces.[1,2] Driven by the desire for a functional and stable interface, the reactive Si−H surface is often modified postsynthesis using silicon−carbon (Si−C) or silicon−oxygen (Si−O) bond forming reactions.[3] The most common means to functionalize these materials is to graft organotrialkoxy-silanes[4] such as R-Si(OEt)$_3$ or R-Si(OMe)$_3$ to the Si−O modified surfaces.[2,5] These organotrialkoxysilane reagents react with hydroxyl-rich surfaces via hydrolytic condensation, and they provide convenient routes into amine- (R = 3-aminopropyl) or thiol-(R = 3-mercaptopropyl) functionalized surfaces[6,7] that are used in various sensor, energy, and biomedical applications.[1]

Despite their utility, trialkoxysilane reagents have limitations. They can require long reaction times or elevated temperatures to obtain efficient coverage, the alcohol or water

byproducts can be deleterious to the performance of the final product, and they can undergo cross-linking reactions that result in overly thick coatings or clogging of micro- or mesopores.[2,8] Monoalkoxysilanes (such as (3-aminopropyl)-dimethylmethoxysilane) are not susceptible to cross-linking, but their reaction rates, coupling efficiency, and reaction byproducts can still be limiting for many purposes.[2]

In this work, we describe the use of 5-membered heterocyclic compounds containing silicon−sulfur (Si−S) or silicon− nitrogen (Si−N) motifs in the ring, which undergo a facile ring-opening reaction to modify hydroxyls[9−11] at the surface of silicon nanostructures (Fig. 3.1). The reaction is demonstrated on films, microparticles, and nanoparticles of porous silicon (pSi). We refer to the method as a "ring-opening click" reaction due to its combination of simplicity, high yield, wide scope of applicability, lack of byproducts, and use of easily removable solvents.

3.3. Results and Discussion

The pSi used in these experiments was a frame-sheath type of structure, consisting of a crystalline Si framework coated with a hydrophilic, hydroxylated SiO_2 sheath, prepared by treating as-etched pSi with oxidant (deionized water or aqueous hydrogen peroxide) at room temperature. Reaction of dichloromethane (DCM) solutions of the cyclic silanes with the hydroxylated-surface pSi nanoparticles (pSiNPs)[12] proceeded to completion within 1−2 h. The reaction was monitored by observing the change in surface charge on the nanoparticles. The pSiNP starting material displayed a negative ζ-potential (in the range -24 to -28 mV, Fig. 3.2a, Table 3.1) consistent with a hydroxylated surface, and the particles displayed average hydrodynamic diameters of ~200 nm (Fig. 3.2b).

The cyclic azasilanes (butyl-azasilane, diazasilane, and methyl-azasilane) generate primary and secondary amines upon ring-opening, and these reagents increased the ζ-potential of the nanoparticles to between +30 and +35 mV (Fig. 3.2a, Table 3.1). By contrast, ring-opening click of the cyclic thia-silane exposes a thiol functionality, and a decrease in ζ- potential, to −50 mV, was observed from particles subjected to this grafting reaction. The chemistry did not result in a significant increase in nanoparticle size, and no aggregates were observed (Fig. 3.2b). Similar trends were observed when the reaction was performed under mild heating conditions (37 °C) (Fig. 3.3). Transmission electron microscopy (TEM) images indicated that the open pore structure of the nanoparticles was preserved after modification (Fig. 3.2c, Fig. 3.4).

We compared the extent of reaction of cyclic silanes to the extent of reaction of triethoxy-/monoethoxy-silanes[13] with porous Si particles, using ζ-potential, thermogravimetric analysis (TGA), and attenuated total reflectance Fourier transform infrared (ATR-FTIR) spectroscopy. The alkoxy-silane grafting reactions were carried out in either dichloromethane or the more common ethanolic solvent conditions, and the results indicated that the hydrolytic condensation reaction generally required greater time and resulted in lower surface coverage relative to the ring-opening click reaction (Fig. 3.5-3.7). The TGA data indicated the ring-opening reactions gave ~8% attached silane by mass, whereas the alkoxysilane reactions gave 2−4% attached silane by mass (Table 3.2, Fig. 3.8). We attribute the greater efficiency of the heterocyclic coupling reaction primarily to the lower energies of Si−N and Si−S bonds (relative to Si−O) and secondarily to the relief of ring strain from the cyclic reactant. Both of these factors provide a stronger driving force relative to hydrolysis, resulting in faster and more extensive surface coupling.

Next, we investigated the influence of solvent on the extent and rate of the reaction. The changes in ζ-potential were more pronounced in the polar aprotic solvents dichloromethane and dimethyl sulfoxide than in less polar diethyl ether (Fig. 3.9). A 1H NMR study (Fig. 3.10) indicated that the ring-opening click reactions proceed cleanly, with no significant side- products. The ζ-potential values of the pSiNP products displayed little sensitivity to concentration of cyclic silane used in the reaction (Fig. 3.11).

The attenuated total reflectance Fourier-transform infrared (ATR-FTIR) spectrum of the pSi starting material displayed strong bands at 1020 cm^{-1} associated with Si−O stretching modes from the oxide layer of the Si−SiO_2 frame−sheath structure, and stretching and bending modes at 3300 and 1640 cm^{-1}, respectively, assigned to a combination of surface O−H and adsorbed water (Fig. 3.12). After reaction with the cyclic silane reagents, the modified pSi material displayed bands that could be assigned to C−H stretching and bending modes of the grafted reagents. These spectral bands persisted even after extensive rinsing of the materials, indicating that the species were chemisorbed to the pSi surface. The modes associated with surface O−H and adsorbed water on the starting pSi substrate were significantly decreased after the grafting chemistry, indicating high surface coverage of the particle surface including the inner pore walls. Control experiments using samples that were prepared by thermal oxidation of pSi at high temperature (to dehydrate surface Si−OH to Si−O−Si) showed no substantial grafting (Fig. 3.13), demonstrating the importance of surface Si−OH for the reaction to proceed. Additionally, controls using as-prepared pSi samples that contained little surface oxide showed a much lower degree of grafting, and the organosilane species were removed by briefly rinsing the treated surface with ethanolic aqueous HF solution (Fig. 3.14). This type of rinse readily removes Si−O

bonded or physisorbed species, whereas it does not remove Si−C bonded surface species.[2] These results also support the importance of surface Si−OH for the ring-opening click reaction.

Nitrogen adsorption−desorption isotherm analysis of the modified pSiMPs revealed slight decreases in surface area, total pore volume, and average pore diameter relative to the unmodified material (Fig. 3.15, Table 3.3). The BJH surface area and TGA results yielded surface coverage values of 1.1×10^{14} molecules cm^{-2} for thia-silane, and 1.3×10^{14} molecules cm^{-2} for methyl-aza-silane. Powder X-ray diffraction (XRD) measurements showed that the crystallinity of the silicon skeleton was retained in the modified particles; Debye−Scherrer analysis indicated a mean crystallite size of ~2.2 nm, Fig. 3.16). Elemental analysis confirmed the presence of sulfur and nitrogen in the thia-silane and methyl-aza-silane- modified materials, respectively (Table 3.4).

The surface wettability of the modified pSi material was analyzed by water contact angle measurements made on suitably modified pSi films (Fig. 3.17). The products of reaction with thia-silane or diaza-silane, which generate terminal thiol and primary amine moieties, respectively, displayed low contact angles (<16°) characteristic of hydrophilic surfaces. The butyl-aza-silane and methyl-aza-silane reagents generated a more hydrophobic surface (water contact angles of 88° and 73°, respectively), as expected from the more hydrophobic N- methyl and N-butyl terminal species that were generated.[14]

The cyclic thia-silane and aza-silane reagents have an advantage over alkoxysilane reagents in that the thiol or primary amine functional species are only exposed when the reagent undergoes ring-opening with surface −OH groups. The cryptic nature of these functional groups presents the possibility for a one-pot tandem synthesis involving

common thiol- or amine-coupling agents. To demonstrate this feature, we performed the diaza-silane surface modification reaction in a mixture containing succinic anhydride (eq 1).

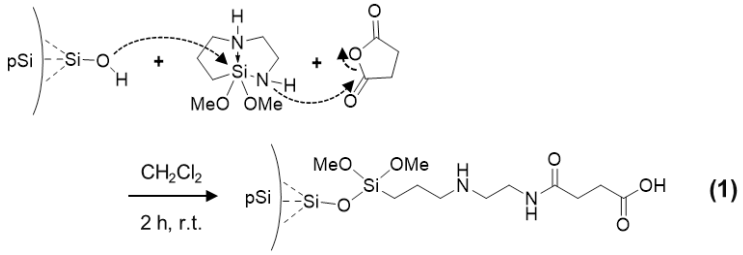

(1)

NMR measurements confirmed that the diaza-silane reagent does not react with succinic anhydride on its own under the reaction conditions used. However, when hydroxylated-surface pSiNPs were present, the ring-opening click reaction generated a primary amine at the surface, which then coupled to succinic anhydride in situ to form the tandem product shown in eq 1. The reaction was confirmed by ζ-potential measurements and ATR-FTIR analysis (Fig. 3.18, 3.19), and the data are consistent with the formation of the expected amide linker and terminal carboxylic acid functionality.

To test the effect of the surface modification on the photoluminescence (PL) of quantum-confined pSi, we prepared a pSiNP formulation that displayed strong PL (λ_{ex} = 365 nm, λ_{em} = 780 nm, external quantum yield ~23%, Fig. 3.2d, 3.20).[15] Silicon quantum dots are useful for bioimaging,[16-19] and there is a need for mild surface modification reactions that do not destroy the PL properties.[20] The surface modification reaction was found to preserve more than 90% of the original PL intensity (based on an equivalent mass of nanoparticles), with no substantial shift in the emission wavelength.

Finally, we tested the compatibility of the surface modification chemistry with a protein payload. pSiNPs have shown utility as delivery vehicles for therapeutic cargos[21-25] that can protect sensitive biologics from denaturing *in vitro* or *in vivo*,[26,27] and there is a

need for chemistries that can be used to attach targeting or biocompatibility agents while preserving the integrity of the therapeutic payload.[28] The model protein lysozyme was used (Table 3.5), and it was loaded into the pSiNPs from aqueous solution (0.1 mg of lysozyme-loaded pSiNPs, mass loading of lysozyme 41%). The particles were separated from the aqueous loading solution by centrifugation, but no attempt was made to remove residual water from the mesopores. The particles were then dispersed into either n-hexane or DCM solutions containing the thia-silane reagent (Fig. 3.21a, 3.22). The surface modification was confirmed by ζ-potential measurements (Table 3.1), where the relatively large positive charge on the lysozyme-loaded particles dropped to negative values after thia-silane grafting due to the generation of surface thiol species. The net change in surface charge was comparable to that observed on empty particles before and after thia-silane modification. The surface chemistry did not significantly impede the rate of lysozyme release from the pSiNPs (Fig. 3.22b); 30−40% of the protein payload was released into 37 °C aqueous PBS solution within 72 h. The rate of lysozyme release did not depend strongly on the solvent used (n-hexane or DCM) for the chemical modification step. However, the modification solvent exerted a strong influence on activity of the released protein; lysozyme released from material modified in DCM retained 98% of its activity, whereas when the chemistry was performed in n-hexane, the released lysozyme showed only 72% activity. This is consistent with control experiments in which lysozyme-loaded pSiNPs were exposed to the two solvents; after removal of the solvents, the lysozyme released into PBS showed 96% and 66% activity for DCM and n-hexane, respectively (Fig. 3.21b). The results demonstrate that the modification chemistry does not react with or

otherwise denature the protein payload, presumably due to the immiscibility of the organic solvents with the hydrated protein payload contained within the particles.

By contrast, when alkoxysilane chemistry (3-mercapto-propyltriethoxysilane, MPTES) was used to modify lysozyme-loaded pSiNPs (using ethanol solvent), the lysozyme released from the MPTES-modified pSiNPs retained only 68 ± 4% activity (Table 3.5). Furthermore, the MPTES chemistry substantially impeded the rate of release of the protein (by a factor of 2 relative to unmodified pSiNPs).

3.4. Conclusion

In summary, ring-opening click chemistry with cyclic silanes provides an efficient, mild, and experimentally convenient method to modify the surface of hydroxylated porous silicon films, microparticles, or nanoparticles. The chemistry proceeds via attack of surface −OH species at the cyclic silane, inducing ring-opening with no byproducts. The room-temperature reaction retains the pore structure and intrinsic photoluminescence of the Si nanomaterial, and it is amenable to tandem functionalization, where a cryptic thiol or primary amine revealed during the ring-opening reaction can couple in situ with a second functional species such as succinic anhydride. This nonaqueous chemistry is sufficiently mild that it does not alter the observed activity of a protein contained within the hydrated porous interior of the material.

3.5. Experimental

Materials. Cyclic thia-/aza-silane reagents; Thia-silane (DMTSCP), Butyl-aza-silane (BADMSCP), Diaza-silane (DMDASCP), and Methyl-aza-silane (MATMSCP) were

supplied by Gelest, Inc. and were used without further purification. Lysozyme activity kit was purchased from Sigma Aldrich (LY0100). PierceTM BCA Protein Assay kit was purchased from Thermo Fisher Scientific (23227). All other chemical reagents were purchased from Aldrich Chemicals, Inc. Single crystal silicon wafers were obtained from Virginia Semiconductor, Inc.

Instrumentation. Etching waveforms were generated in a computer program written in Labview (National Instruments, Inc.), and the electric current was driven by a Keithley 2651A Sourcemeter power supply interfaced to the LabView program. A 50T ultrasonic bath (VWR International) was used for ultrasonic fracture of the pSi films. Particles were collected by centrifugation (Eppendorf Centrifuge Model 5424R). Attenuated total reflectance Fourier transform infrared (ATR-FTIR) spectra were recorded using a Thermo Scientific Nicolet 6700 FTIR instrument fitted with a Smart iTR diamond ATR fixture. All spectra in any given ATR-FTIR plot were measured with the same collection parameters and on comparable quantities of material, in an attempt to make direct comparisons of signal strength between samples. Where multiple spectra are compared, the spectra are offset along the y-axis to improve clarity. Contact angles were measured using a Ramé-Hart DROPimage CA v2.5 instrument. ^{1}H nuclear magnetic resonance (NMR) spectra were recorded on a Varian VX 500 (500 MHz). Dynamic light scattering (DLS) and zeta-potential of nanoparticles were determined using a Malvern Instruments Zetasizer Nano ZS90. Powder x-ray diffraction (XRD) spectra were collected at ambient temperature on a Bruker D8 Advance diffractometer using Cu Kα (λ=1.5418 Å) radiation (40 kV, 40 mA), using a scan speed of 0.1 sec/step, a step size of 0.02° in 2θ, and a 2θ range of 10-80°. An Ocean Optics QE-Pro spectrometer was used to obtain steady-state photoluminescence

spectra (λ_{ex}: 365 nm) with a 510 nm long-pass emission filter. Transmission electron microscope (TEM) images were obtained with a JEOL-1200 EX II 120 kV instrument. Energy dispersive X-ray (EDX) analyses were obtained with an FEI XL30 UHR (Ultra High Resolution) scanning electron microscope fitted with an EDX SDD (Silicon Drift Detector) system by iXRF Systems, inc. for energy dispersive X-ray microanalysis. Nitrogen adsorption-desorption isotherms of the pSi microparticles were recorded at 77 K using a Micro-meritics ASAP 2020 instrument. Prior to the nitrogen adsorption experiment, the pSi microparticles were degassed under vacuum overnight. The surface area of the particles was determined using the BET (Brunnauer-Emmett-Teller) method. Thermogravimetric analysis (TGA) was carried out using a STA 6000 Simultaneous Thermal Analyzer (PerkinElmer) in a nitrogen ambient.

Preparation of porous silicon nanoparticles (pSiNPs). Porous silicon nanoparticles (pSiNPs) were prepared by constant current anodization of heavily boron-doped p-type (<1 mΩ-cm resistivity) single crystal silicon wafers, polished on the (100) face, in aqueous ethanolic hydrofluoric acid electrolytes. CAUTION: HF is highly corrosive to the eyes and skin and proper precautions should be followed when handling. The preparation followed a published "perforated etch" procedure.[12] Prior to preparation of the porous layers, the wafer surfaces were cleaned using a sacrificial etch consisting of electrochemical anodization (60 sec, 46 mA/cm^2) in an electrolyte consisting of 3:1 (v:v) 48% aqueous HF:absolute ethanol, followed by ethanol rinse, then dissolution of the porous film with aqueous KOH (1 M). The wafer was rinsed with water, then ethanol. The perforation etching waveform consisted of a square wave (current density of 46 mA/cm^2 applied for 1.818 sec, current density then raised to 365 mA/cm^2 for 0.363 sec), repeated for 150

cycles. The multilayered porous Si film was removed from the substrate by application of a current pulse of 4 mA/cm^2 for 250 sec in an electrolyte consisting of 1:29 (v:v) of 48% aqueous HF:absolute ethanol. The freestanding films (~60 mg) were fractured by ultrasound in deionized water (DI H_2O, 7 mL) for 20 hr, and allowed to oxidize in this aqueous phase for 6 weeks at room temperature (25 °C). The resulting porous silicon nanoparticles were collected using centrifugation (15,000 rpm, 15 min) and washed 3 times with ethanol. The hydroxylated surface functionality (Si-OH, Si-O-Si) was confirmed by ATR-FTIR.

Preparation of porous silicon microparticles (pSiMPs). Porous Si microparticles (pSiMPs) were prepared in a manner similar to the nanoparticles. Prior to preparation of the porous layers, the wafer surfaces were cleaned using a sacrificial etch consisting of electrochemical anodization (300 sec, 87.1 mA/cm^2) in an electrolyte consisting of 3:2 (v:v) 48% aqueous HF:absolute ethanol, followed by ethanol rinse, then dissolution of the porous layer with aqueous KOH (1 M). The wafer was rinsed with water followed by ethanol and the cell was re-filled with fresh electrolyte consisting of 3:2 (v:v) 48% aqueous HF:absolute ethanol. The sample was then etched using an etching waveform consisting of a square wave (current density of 87.1 mA/cm^2 applied for 120 sec, current density then raised to 174.2 mA/cm^2 for 0.636 sec, and finally current density set to zero for 30 sec). This waveform was repeated for 70 cycles, generating a "perforated" porous Si film with alternating layers of high and low porosity. The porous film was removed from the substrate by application of 4.36 mA/cm^2 for 500 sec in an electrolyte composed of 1:29 (v:v) of 48% aqueous HF:absolute ethanol. The freestanding porous Si film was then fractured by ultrasonication (50T, VWR International) for 90 min in ethanol (7 mL), and

the resulting colloidal dispersion of porous silicon microparticles was allowed to settle at room temperature overnight. The upper 30% portion of the colloidal dispersion was discarded, and the remaining portion was filtered through filter paper (Whatman, Cat. No. 1002-070). The filter paper was dried, and the brown colored particles (~500 mg) were collected from the paper. For the hydroxylated-surface porous silicon microparticle preparation, the collected particles (~200 mg) were transferred to deionized water (10 mL) and incubated for 12 hr at 70 °C. The resulting microparticles were collected by centrifugation (15,000 rpm, 15 min) and washed 3 times with ethanol. The hydroxylated surface functionality (Si-OH, Si-O-Si) was confirmed by ATR-FTIR on the isolated pSiMPs. The particles displayed a mean particle size of ~5 μm in scanning electron microscope (SEM) images.

Preparation of porous silicon films (pSi films). Porous Si films were prepared in a manner similar to the particles, except they were not removed from the Si substrate. Prior to preparation of the porous layers, the wafer surfaces were cleaned using a sacrificial etch consisting of electrochemical anodization (60 sec, 50 mA/cm^2) in an electrolyte consisting of 3:1 (v:v) 48% aqueous HF:absolute ethanol, followed by ethanol rinse, then dissolution of the porous film with aqueous KOH (1 M). The wafer was rinsed with water, then ethanol. Samples were then prepared by etching at constant current density of 50 mA/cm^2 for 600 sec for the 50–60% porosity samples. Porosity was verified using the Spectroscopic Liquid Infiltration Method (SLIM) measurement.[29] To generate the hydroxylated (Si-OH, Si-O-Si) porous Si films, as-etched porous Si chips (Si-H surface) were incubated in H_2O_2 (aqueous, 30% by mass) for 1 hr at room temperature. To generate the dehydrated (Si-O-Si) porous Si film, as-etched porous Si chips were inserted into a tube furnace (ThermoScientificTM,

MiniMite TF55035A) and the temperature was ramped from room temperature to 800 °C at a rate of 10 °C/min. The temperature was held at 800 °C for 2 h, and then the furnace was allowed to cool to room temperature for ~2 h prior to removal of the samples. The tube furnace reaction was carried out in ambient air.

Coupling reaction of pSiMPs/pSiNPs with cyclic-silanes. The pSiMPs/pSiNPs were twice suspended in dichloromethane (DCM) and isolated by centrifugation (15,000 rpm, 15 min) in order to remove protic solvents such ethanol and water. After the washing steps, the pSiMPs (~10 mg) or pSiNPs (~1 mg) were suspended in DCM (400 μL), an aliquot of cyclic-silane reagent (100 μL) was added, and the mixture was agitated for 2 h. The resulting particles were then washed 2 times by centrifugation (15,000 rpm, 15 min) from DCM.

Coupling reaction of pSi micro-/nano-particle with trialkoxy-/mono-alkyoxysilanes. The coupling reactions with trialkyoxy-/monoalkyoxy-silanes were carried out by suspending the pSiMPs (~10 mg) or pSiNPs (~1 mg) in ethanol (950 μL), adding an aliquot of trialkoxysilane (50 μL), and then agitating the mixture for 1–12 h. The resulting particles were then washed 2 times by centrifugation (15,000 rpm, 15 min) from ethanol to remove unreacted reagent. NOTE: Significant aggregations were observed at higher concentration of alkyoxisilane (data not shown).

Coupling reaction of pSi films with cyclic silane. The pSi films, of typical dimensions 1.2 cm in diameter and 20 microns thick, still attached to the silicon substrate, were immersed in a solution containing DCM (800 μL) and the cyclic-silane reagent (200 μL), and the mixture was agitated for 2 h. The chip was rinsed with DCM and ethanol several times and then dried in a stream of dry nitrogen. To remove traces of physically

absorbed reagent, chips were further rinsed by immersion in ethanol, which was then subjected to ultrasonication (50T ultrasonic bath, VWR International) for 1 min.

One-pot (tandem) reaction of pSiNPs with cyclic silane and succinic anhydride. The pSiNPs were washed with dichloromethane (DCM) two times using centrifugation (15,000 rpm, 15 min) to remove protic solvents such as ethanol and water. After the washing steps, the pSiNPs (~1 mg) were suspended in DCM (400 μL) containing succinic anhydride (Sigma-Aldrich, 2 mg/mL or 5 mg/mL), an aliquot of cyclic-silane reagent (100 μL) was added, and the mixture was agitated for 2 h. The resulting particles were then washed 2 times by centrifugation (15,000 rpm, 15 min) from DCM to remove unreacted reagent.

Photoluminescence study. The pSiNPs were dispersed in ethanol, and photoluminescence intensity was measured using a thermoelectrically cooled CCD spectrometer (OceanOptics QEPro) using a 365 nm LED light source and 370 nm bandpass filter for excitation, and a 510 nm longpass optical filter prior to the spectrometer. The integrated photoluminescence intensity was obtained in the wavelength range of 500–980 nm. Plotted values represent average values (n=4) with error bars representing 1 standard deviation.

NMR study of cyclic-silane grafting reactions. The pSiNPs (~1 mg) were suspended in $CDCl_3$ (400 μL), the cyclic-silane reagent (50 μL) was added, and the mixture was agitated for 2 h. The supernatant was colleted by centrifugation (15,000 rpm for 15 min), and 1H proton NMR was immediately measured. For the control experiment, ethanolic $CDCl_3$ (ethanol: $CDCl_3$=1:10, v/v) was used.

Lysozyme loading into pSiNPs. Lysozyme (pI of 11.35) was loaded into the pSiNPs by electrostatic adsorption. The enzyme was dissolved in 1X PBS (pH 7.4) at a

concentration of 10 mg/mL. The as-sonicated pSiNPs were then dispersed into this solution at a concentration of 1 mg/mL. The mixed solution was then spun on a rotating microcentrifuge tube mixer for 18 hr. Loading and release of lysozyme was determined from 0.1 mg of pSiNPs. Total lysozyme loading and release was determined with the PierceTM BCA protein assay kit. Protein loading percent, defined as; "((mass protein)/(mass protein+mass pSiNP))*100" was found to be 41% using this method (n=3).

Coupling of cyclic-silane to exterior of lysozyme-containing pSiNPs. The lysozyme-loaded pSiNPs (~1 mg, hydroxylated-surface) were isolated from the aqueous solution by centrifugation. They were not dried, but were washed with dichloromethane (200 μL) 2 times by centrifugation (15,000 rpm, 15 min). The resulting pSiNPs were suspended in dichloromethane (200 μL) or n-hexane (200 μL), an aliquot of cyclic-silane reagent (5 μL) was added, and the mixture was agitated for 10 min. The resulting pSiNPs were then washed 2 times with dichloromethane (200 μL) and 2 times with ethanol (200 μL) by centrifugation (15,000 rpm, 15 min) to remove unreacted reagent.

Quantification of activity of lysozyme released from lysozyme-containing pSiNPs. 0.1 mg of lysozyme-loaded pSiNPs (mass loading of lysozyme 41%, or 76 μg) were dispersed in PBS at an initial concentration of 1 mg/mL. The volume of PBS was maintained constant for the remainder of the time points. The pSiNP solutions were incubated at 37°C and the supernatant was collected by centrifgation after 24, 48, and 72 hours of release. The amount of active lysozyme released at each time point was determined using the standard protocol for the lysozyme activity kit. Active lysozyme causes a decrease in optical absorbance (at a wavelength of 450 nm) over the 5-minute

assay period, and the absorbance values were correlated to quantity of active lysozyme via a calibration curve made from assaying known concentrations of active lysozyme.

Calculation of surface coverage. Surface coverage of the grafted species was determined as molecules per area, where the number of molecules on the surface was determined by TGA measurement of the relevant surface-grafted particles (Table 3.2) and the area of the surface was determined from the BET surface area measurement of the particles (Table 3.3). We assumed the molecular weight of the surface-grafted reagent in its ring-opened form (Si-OH terminal).

Calculation of nanostructure crystallite size. The average crystallite size for the Si domains in the pSiMPs was calculated using the powder x-ray diffraction (XRD) data of Fig. 3.15 and the Debye-Scherrer formula; $D_P=0.94\lambda/(\beta\cos\theta)$ where D_P = average crystallite size, β = line broadening (FWHM) in radians, θ = Bragg angle, and λ = X-ray wavelength (1.5418 Å). Each number (β, θ) was derived from the XRD analysis program JADE (Materials Data, Inc.).

3.6. References

[1] L. Canham, *Handbook of porous silicon,* Springer, **2014.**

[2] M. J. Sailor, *Porous silicon in practice: preparation, characterization and applications,* John Wiley & Sons, **2012.**

[3] J. M. Buriak, *Chem Rev* **2002,** *102,* 1271.

[4] R. M. Pasternack, S. Rivillon Amy, Y. J. Chabal, *Langmuir* **2008,** *24,* 12963.

[5] J. Riikonen, M. Salomäki, J. van Wonderen, M. Kemell, W. Xu, O. Korhonen, M. Ritala, F. MacMillan, J. Salonen, V.-P. Lehto, *Langmuir* **2012,** *28,* 10573.

[6] A. J. Nijdam, M. M.-C. Cheng, D. H. Geho, R. Fedele, P. Herrmann, K. Killian, V. Espina, E. F. Petricoin III, L. A. Liotta, M. Ferrari, *Biomaterials* **2007,** *28,* 550.

[7] R. L. Williams, M. J. Hadley, P. J. Jiang, N. A. Rowson, P. M. Mendes, J. Z. Rappoport, L. M. Grover, *J Mater Chem B* **2013,** *1,* 4370.

[8] R. G. Acres, A. V. Ellis, J. Alvino, C. E. Lenahan, D. A. Khodakov, G. F. Metha, G. G. Andersson, *J Phy Chem C* **2012,** *116,* 6289.

[9] B. Arkles, Y. Pan, G. L. Larson, D. H. Berry, Cyclic azasilanes: Volatile coupling agents for nanotechnology. In *Silanes and other coupling agents;* Mittal, K. L., Ed.; CRC Press: Boca Raton, FL, 2004; Vol. 3, p 179.

[10] L. Ju, N. C. Strandwitz, *J Mater Chem C* **2016,** *4,* 4034.

[11] A. F. Maddox, J. G. Matisons, M. Singh, J. Zazyczny, B. Arkles, *MRS Online Proc Libr* **2015,** *1793,* 35.

[12] Z. Qin, J. Joo, L. Gu, M. J. Sailor, *Part Part Syst Charact* **2014,** *31,* 252.

[13] J. Joo, X. Liu, V. R. Kotamraju, E. Ruoslahti, Y. Nam, M. J. Sailor, *ACS nano* **2015,** *9,* 6233.

[14] L. De Stefano, G. Oliviero, J. Amato, N. Borbone, G. Piccialli, L. Mayol, I. Rendina, M. Terracciano, I. Rea, *J R Soc Interface* **2013,** *10,* 20130160.

[15] J.-H. Park, L. Gu, G. Von Maltzahn, E. Ruoslahti, S. N. Bhatia, M. J. Sailor, *Nat Mater* **2009,** *8,* 331.

[16] M. Gongalsky, L. Osminkina, A. Pereira, A. Manankov, A. Fedorenko, A. Vasiliev, V. Solovyev, A. Kudryavtsev, M. Sentis, A. Kabashin, *Sci Rep* **2016,** *6,* 24732.

[17] L. A. Osminkina, V. A. Sivakov, G. A. Mysov, V. A. Georgobiani, U. A. Natashina, F. Talkenberg, V. V. Solovyev, A. A. Kudryavtsev, V. Y. Timoshenko, *Nanoscale Res Lett* **2014,** *9,* 463.

[18] X. Cheng, S. B. Lowe, S. Ciampi, A. Magenau, K. Gaus, P. J. Reece, J. J. Gooding, *Langmuir* **2014,** *30,* 5209.

[19] J. Liu, F. Erogbogbo, K.-T. Yong, L. Ye, J. Liu, R. Hu, H. Chen, Y. Hu, Y. Yang, J. Yang, *ACS nano* **2013,** *7,* 7303.

[20] G. E. Kotkovskiy, Y. A. Kuzishchin, I. L. Martynov, A. A. Chistyakov, I. Nabiev, *Phys Chem Chem Phys* **2012,** *14,* 13890.

[21] D. Liu, L. M. Bimbo, E. Mäkilä, F. Villanova, M. Kaasalainen, B. Herranz-Blanco, C. M. Caramella, V.-P. Lehto, J. Salonen, K.-H. Herzig, *J Controlled Release* **2013,** *170,* 268.

[22] E. Tasciotti, X. Liu, R. Bhavane, K. Plant, A. D. Leonard, B. K. Price, M. M.-C. Cheng, P. Decuzzi, J. M. Tour, F. Robertson, *Nat Nanotechnol* **2008,** *3,* 151.

[23] J. Henstock, L. Canham, S. Anderson, *Acta biomater* **2015,** *11,* 17.

[24] L. Canham, Porous silicon for medical use: from conception to clinical use. In *Porous Silicon for Biomedical Applications;* H.A. Santos, Ed.; Elsevier: Cambridge, 2014; p 3.

[25] K.-T. Yong, W.-C. Law, R. Hu, L. Ye, L. Liu, M. T. Swihart, P. N. Prasad, *Chem Soc Rev* **2013,** *42,* 1236.

[26] C.-C. Wu, Y. Hu, M. Miller, R. V. Aroian, M. J. Sailor, *ACS nano* **2015,** *9,* 6158.

[27] T. Tanaka, L. S. Mangala, P. E. Vivas-Mejia, R. Nieves-Alicea, A. P. Mann, E. Mora, H.-D. Han, M. M. Shahzad, X. Liu, R. Bhavane, *Cancer Res* **2010,** *70,* 3687.

[28] J. Salonen, Drug Delivery With Porous Silicon. In *Handbook of Porous silicon;* L. T. Canham, Ed.; Springer: Switzerland, 2014; p 909 2017, 1.

[29] E. Segal, L. A. Perelman, F. Cunin, F. Di Renzo, J. M. Devoisselle, Y. Y. Li, M. J. Sailor, *Adv Funct Mater* **2007,** *17,* 1153.

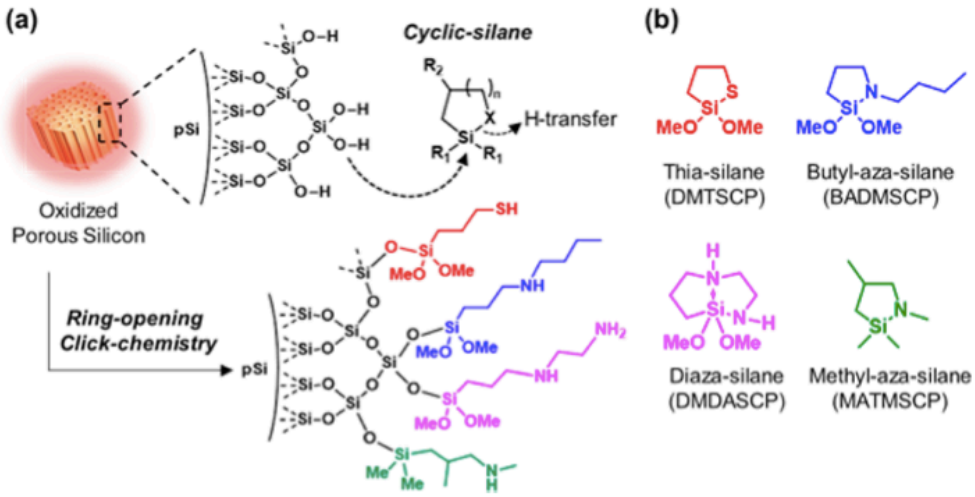

Figure 3.1. (a) Schematic illustration of the ring-opening click-reaction of cyclic-silanes with the silanol-terminated pore walls of oxidized porous silicon (pSi). (b) Structures of the reagents used in this study: thia-silane (DMTSCP, 2,2-dimethoxy-1-thia-2-silacyclopentane), butyl-aza-silane (BADMSCP, N-n-butyl-aza-2,2-dimethoxy-silacyclo-pentane), diaza-silane (DMDASCP, 2,2-dimethoxy-1,6-diaza-2-silacy-clooctane), and methyl-aza-silane (MATMSCP, N-methyl-aza-2,2,4-trimethyl-silacyclopentane). R_1 = OMe, Me. R_2 = H, Me.

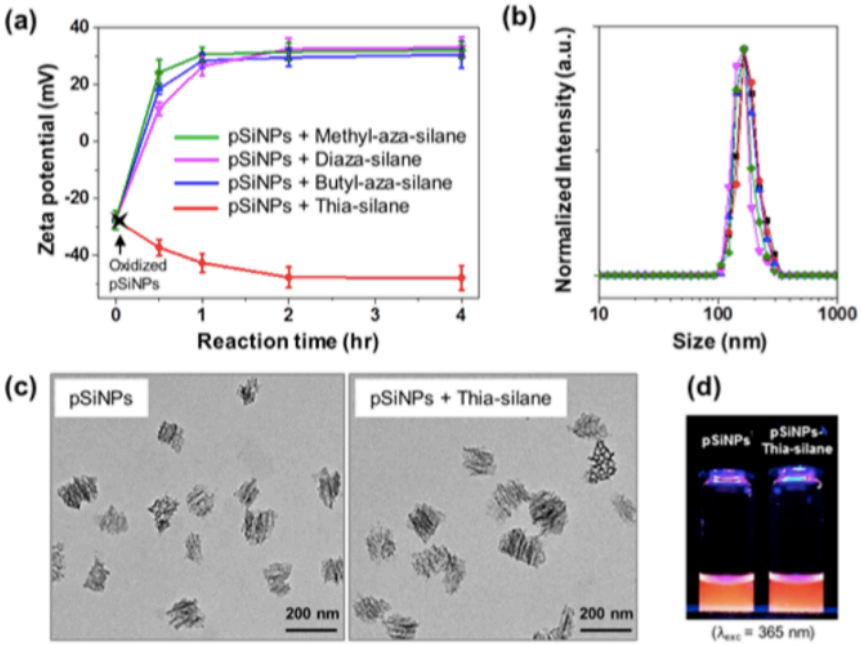

Figure 3.2. (a) ζ-potential and (b) mean hydrodynamic diameter (intensity distribution) of surface-oxidized pSiNPs, measured by dynamic light scattering (DLS), as a function of time of reaction with the indicated cyclic silanes (diluted 1:4 v:v into dichloromethane) at 25 °C. Particles were isolated at the indicated time points, rinsed, and redispersed in deionized water for the measurement. Means and standard deviations calculated from triplicate measurements. (c) Transmission electron microscopy (TEM) images of pSiNPs before and after reaction with thia-silane at 25 °C for 2 h. (d) Photograph of nanoparticles from (c) dispersed in ethanol and viewed under 365 nm illumination.

Table 3.1. Measured size (z-average) and zeta potential (parentheses) values for porous silicon nanoparticles (pSiNPs) and products of reactions with the indicated silane reagents. The intensity-based size distribution of each sample is represented in Figures 2b and S1. The size and zeta potential values were measured in deionized water (DI H_2O) after reaction and workup to remove unreacted reagent. The standard deviations are calculated from 3 replicate measurements. The zeta potential and size of the pSiNP starting material (prior to surface modification) were -27.6 ± 3.4 mV and 188.9 ± 8.1, respectively for Sets 1-5. The zeta potential and size of the pSiNP starting material (prior to surface modification) were -24.5 ± 6.2 mV and 235.8 ± 8.9, respectively for Sets 6-8. PDI values: < 0.3.

Set 1	**r.t. (25 ºC), DCM**	**30 min**	**1 h**	**2 h**	**4 h**
Temperature dependence[a, b]	pSiNP + Thia-silane	185.1± 5.5 (-37.3 ± 2.9)	190.6 ± 7.4 (-42.7 ± 3.2)	192.1 ± 11.1 (-47.8 ± 3.6)	190.4 ± 10.0 (-47.9 ± 4.2)
	pSiNP + Butyl-aza-silane	187.2 ± 8.8 (18.5 ± 1.9)	193.4 ± 9.1 (28.5 ± 2.5)	191.1 ± 8.2 (29.6 ± 3.2)	189.3 ± 9.1 (30.6 ± 4.7)
	pSiNP + Diaza-silane	188.3 ± 10.2 (11.5 ± 3.4)	193.9 ± 10.8 (26.5 ± 3.3)	190.6 ± 12.8 (32.6 ± 3.8)	192.1 ± 11.2 (33.1 ± 3.7)
	pSiNP + Methyl-aza-silane	184.6 ± 7.7 (24.3± 4.5)	198.2 ± 13.9 (30.6 ± 2.5)	193.6 ± 6.9 (31.6 ± 3.1)	194.6 ± 9.3 (32.1 ± 3.0)
	Heat (37 ºC), DCM	**30 min**	**1 h**	**2 h**	**4 h**
	pSiNP + Thia-silane	190.6 ± 14.4 (-40.2 ± 4.9)	212.5 ± 7.5 (-42.7 ± 4.2)	208.3 ± 5.2 (-45.8 ± 5.1)	198.4 ± 10.6 (-46.1 ± 6.2)
	pSiNP + Butyl-aza-silane	200.2 ± 4.7 (28.1 ± 4.7)	214.3 ± 8.8 (38.5 ± 2.5)	215.9 ± 7.7 (39.6 ± 5.2)	207.6 ± 9.8 (40.1 ± 5.7)
	pSiNP + Diaza-silane	206.8 ± 7.8 (21.5 ± 2.2)	208.6 ± 13.4 (36.5 ± 4.3)	205.6 ± 5.4 (42.6 ± 5.8)	206.4 ± 8.8 (43.1 ± 6.7)
	pSiNP + Methyl-aza-silane	189.1 ± 5.9 (22.3 ± 4.5)	205.4 ± 10.9 (32.6 ± 2.5)	205.9 ± 11.9 (38.6 ± 3.1)	199.0 ± 7.7 (40.5 ± 4.3)
Set 2	**r.t. (25 ºC), DCM**	**1 h**	**2 h**	**4 h**	**-**
Control experiments[a, b]	pSiNPs + APTES	(-2.5 ± 5.1)	(4.2 ± 5.3)	(6.4 ± 6.1)	-
	pSiNPs + APDMES	(-1.6± 7.2)	(5.5 ± 7.4)	(6.5 ± 6.7)	-
	pSiNPs + MPTES	(-29.9 ± 7.3)	(-32.4 ± 5.9)	(-35.2 ± 6.3)	-
	r.t. (25 ºC), EtOH	**1 h**	**2 h**	**4 h**	**-**
	pSiNPs + APTES	(9.06 ± 3.1)	(13.8 ± 4.4)	(16.5 ± 2.9)	-
	pSiNPs + APDMES	(-6.5 ± 5.2)	(3.3 ± 4.3)	(10.5 ± 4.1)	-
	pSiNPs + MPTES	(-34.6 ± 3.3)	(-39.3 ± 3.8)	(-39.8 ± 4.5)	-
Set 3	**r.t. (25 ºC) / 2 h**	**DCM**	**DMSO**	**Ether**	**-**
Solvent dependence[b]	pSiNP + Thia-silane	(-47.6 ± 5.2)	(-46.7 ± 4.1)	(-38.3 ± 3.3)	-
	pSiNP + Butyl-aza-silane	(29.6 ± 4.2)	(24.0 ± 5.5)	(12.2 ± 4.6)	-
	pSiNP + Diaza-silane	(33.1 ± 5.1)	(22.5 ± 4.3)	(14.1 ± 3.7)	-
	pSiNP + Methyl-aza-silane	(31.6 ± 3.9)	(25.8 ± 4.1)	(9.9 ± 2.5)	-

Table 3.1. Measured size (z-average) and zeta potential (parentheses) values for porous silicon nanoparticles (pSiNPs) and products of reactions with the indicated silane reagents. (Continued)

Set 4	**r.t. (25 ºC) / 2 h, DCM**	**0 µL : 100 µL**	**100 µL : 100 µL**	**400 µL : 100 µL**	**900 µL : 100 µL**
Concentration dependence[b,c]	pSiNP + Thia-silane	(-38.9 ± 8.2)	(-39.0 ± 6.1)	(-46.0 ± 7.2)	(-39.7 ± 3.1)
	pSiNP + Butyl-aza-silane	(20.6 ± 9.1)	(30.1 ± 4.5)	(29.6 ± 7.4)	(16.5± 4.2)
	pSiNP + Diaza-silane	(17.8 ± 7.7)	(33.3 ± 5.8)	(32.6 ± 4.1)	(21.4 ± 5.1)
	pSiNP + Methyl-aza-silane	(0.4 ± 7.2)	(20.2 ± 4.8)	(31.6 ± 5.3)	(15.7 ± 2.6)
Set 5	**r.t. (25 ºC)**	**1 h**	**2 h**	**4 h**	**8 h**
Oxidation dependence[a,d]	pSiNPs (-10.6 ± 4.6)	(-16.4 ± 5.2)	(20.2 ± 6.1)	(29.8 ± 3.8)	(30.1 ± 5.7)
	pSiNPs (-21.9 ± 6.2)	(22.3 ± 7.6)	(26.5 ± 5.9)	(30.6 ± 5.6)	(31.1 ± 6.7)
	pSiNPs (-39.1 ± 5.4)	(-12.5 ± 6.5)	(3.9 ± 7.2)	(12.6 ± 6.7)	(21.6 ± 8.5)
Set 6	**r.t. (25 ºC) / DCM / 2 h**				
In situ functionalization[e]	pSiNP starting material for Sets 6-8: 235.8 ± 8.9 (-24.5 ± 6.2)				
	No succinic anhydride with diaza-silane: 233.5 ± 10.5 (32.6 ± 8.5)				
	2 mg/mL succinic anhydride with diaza-silane: 245.9 ± 14.3 (15.8 ± 6.2)				
	5 mg/mL succinic anhydride with diaza-silane: 252.7 ± 17.0 (8.8 ± 4.1)				
	5 mg/mL succinic anhydride without diaza-silane: 242.8 ± 9.2 (-24.5 ± 3.2)				
Set 7	**r.t. (25 ºC) / 2 h**	**Rxn in DCM**	**Rxn in *n*-Hex**	**-**	**-**
Lysozyme-pSiNPs[b]	Lyso-pSiNPs	(22.1 ± 8.1)	(35.1 ± 5.9)	-	-
	Lyso-pSiNPs + Thia-silane	(-2.8 ± 6.9)	(-3.2 ± 7.4)	-	-
Set 8	**r.t. (25 ºC) / 2 h**	**Rxn in EtOH**	**-**	**-**	**-**
Lysozyme-pSiNPs[b]	Lyso-pSiNPs	(31.7 ± 3.6)	-	-	-
	Lyso-pSiNPs + MPTES	(24.0 ± 8.1)	-	-	-

[a]Reactions were run for the times indicated across the top of the column header.

[b]Reagent abbreviations: APTES, 3-(aminopropyl)triethoxysilane; APDMES, 3-(aminopropyl)dimethylethoxysilane; MPTES, 3-(mercaptopropyl)triethoxysilane, DCM, dichloromethane; DMSO, dimethylsulfoxide; Ether, diethylether; n-Hex, n-hexane. Chemical structures of the cyclic silanes are given in Figure 1 of the main text.

[c]Set 4, concentration dependence: reagent concentrations given across the columns are X µL : Y µL, where X is volume of DCM (0–900 µL), and Y is the volume of the indicated cyclic silane reagent.

[d]Set 5, oxidation dependence: This set tested the effect of the degree of oxidation of the porous silicon nanoparticles (pSiNPs) on the efficiency of the coupling reaction with butyl-aza-silane. Three types of frame-sheath pSiNPs were prepared, by varying the duration of the sheath-forming water oxidation step: reaction times for the pSiNP samples with initial zeta potential -10.6 ± 4.6, -21.9 ± 6.2, and -39.1 ± 5.4 were 1, 20, and 40 days, respectively. The pSiNPs (~1 mg) were suspended in DCM (400 µL) and an aliquot of butyl-aza-silane (100 µL) was added, and the mixture was agitated for 1–8 h.

[e]Set 6, Tandem functionalization: The pSiNPs (~1 mg) were suspended in DCM (400 µL) containing succinic anhydride (2 mg/mL or 5 mg/mL), and aliquot of diaza-silane (100 µL) was added. The mixture was agitated for 2 h.

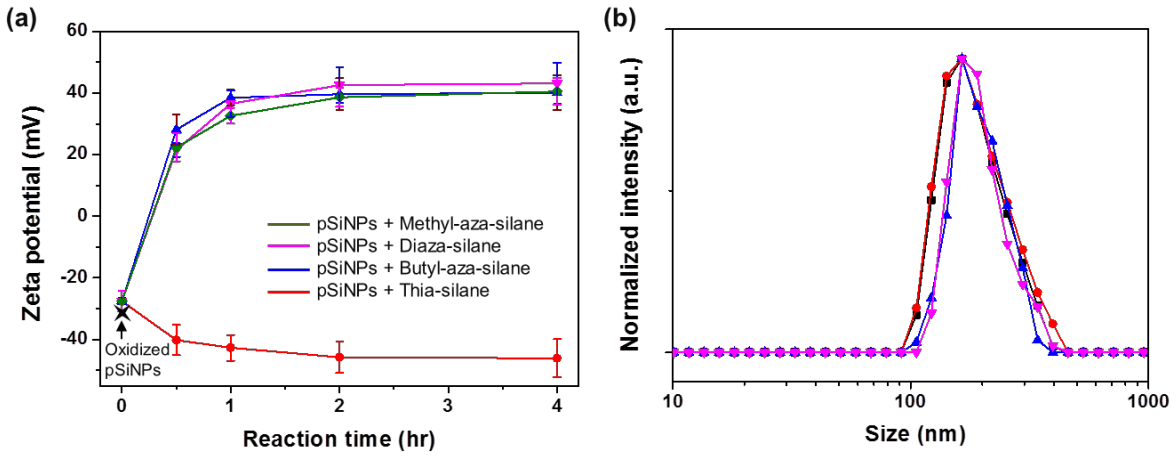

Figure 3.3. (a) Zeta potential and (b) Size distribution of porous silicon nanoparticles (pSiNPs) as a function of time of reaction with the indicated cyclic silanes in dichloromethane (DCM) at 37 °C, measured by dynamic light scattering (DLS). The pSiNPs were reacted with cyclic silanes (100 µL) diluted in DCM (400 µL). Particles were isolated at the indicated time points, rinsed, and re-dispersed in deionized water (DI H_2O) for the measurement. The size distribution was measured after 4 hr reaction. Mean values and standard deviations are calculated from 3 replicate measurements.

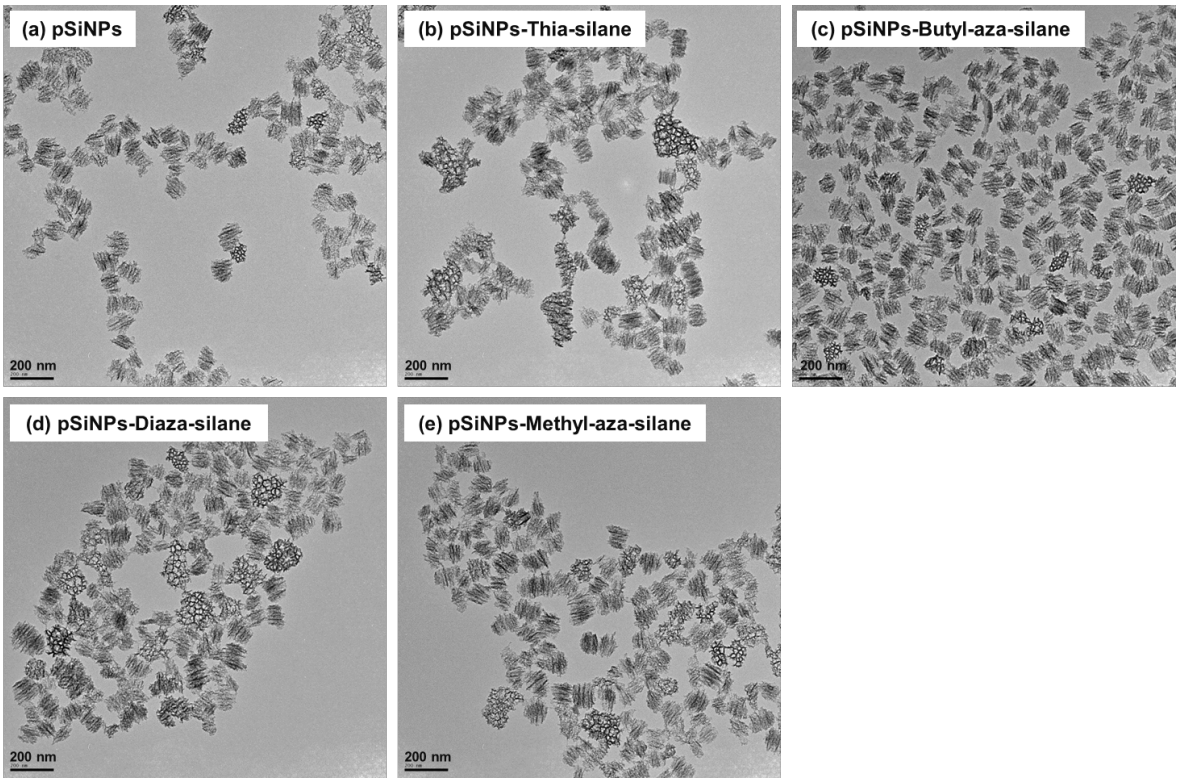

Figure 3.4. Transmission electron microscope (TEM) images of (a) porous silicon nanoparticles (pSiNPs), after reaction with (b) thia-silane, (c) butyl-aza-silane, (d) diaza-silane, and (e) methyl-aza-silane at 25 °C for 2 h. Samples were isolated by centrifugation and rinsing as described in the experimental section.

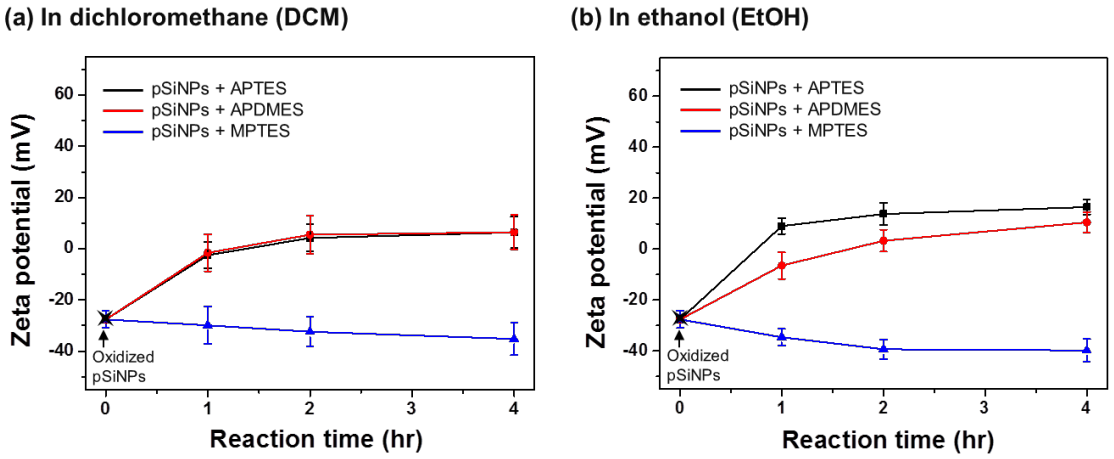

Figure 3.5. Zeta potential of porous silicon nanoparticles (pSiNPs), as a function of time of reaction with the indicated alkoxysilane reagents in (a) dichloromethane (DCM) and (b) ethanol (EtOH) at 25 °C. Particles were isolated at the indicated time points, rinsed, and re-dispersed in deionized water (DI H_2O) for the measurement. Reaction conditions were similar to those used in Figure 2a in the main text: the pSiNPs (2.5 mg/mL) were reacted in a solution containing 100 μL of alkoxysilane diluted into 400 μL of DCM (a) or 50 μL of alkoxysilane diluted into 950 μL of EtOH (b). Triethoxy- and monoethoxy-silanes are: APTES, 3-(aminopropyl)triethoxysilane; APDMES, 3-(aminopropyl)dimethylethoxysilane; MPTES, 3-(mercaptopropyl)triethoxysilane. The means and standard deviations are calculated from 3 replicate measurements.

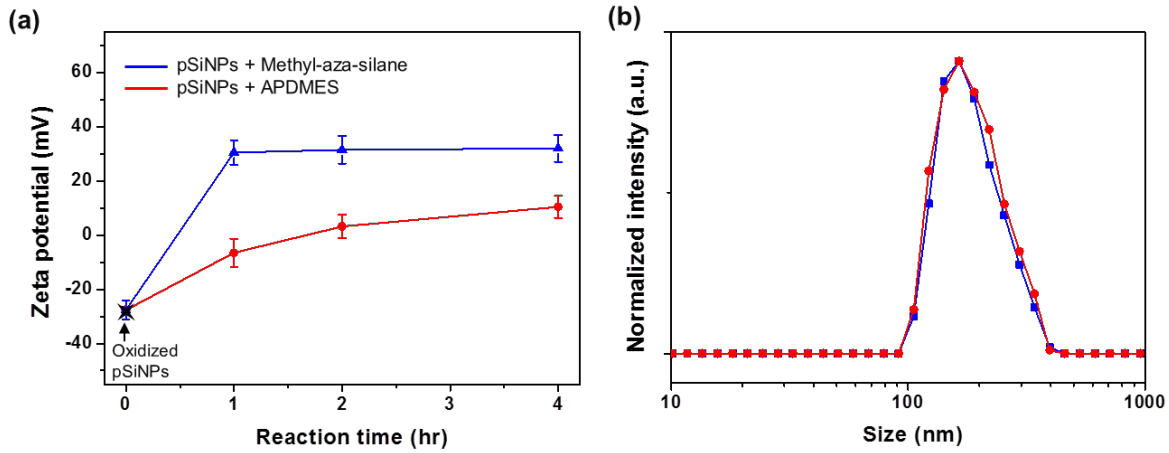

Figure 3.6. Dynamic light scattering (DLS) data showing (a) zeta potential and (b) size distribution of porous silicon nanoparticles (pSiNPs) as a function of time of reaction with the indicated silanes at 25 °C. The pSiNPs were reacted with the cyclic methyl-aza-silane (100 µL) dissolved in dichloromethane (DCM, 400 µL), or with APDMES (50 µL) dissolved in ethanol (EtOH, 950 µL). Particles were isolated at the indicated time points, rinsed, and re-dispersed in deionized water (DI H_2O) for the DLS measurement. The size distribution was measured after 4 h of reaction. Mean values and standard deviations are calculated from 3 replicate measurements.

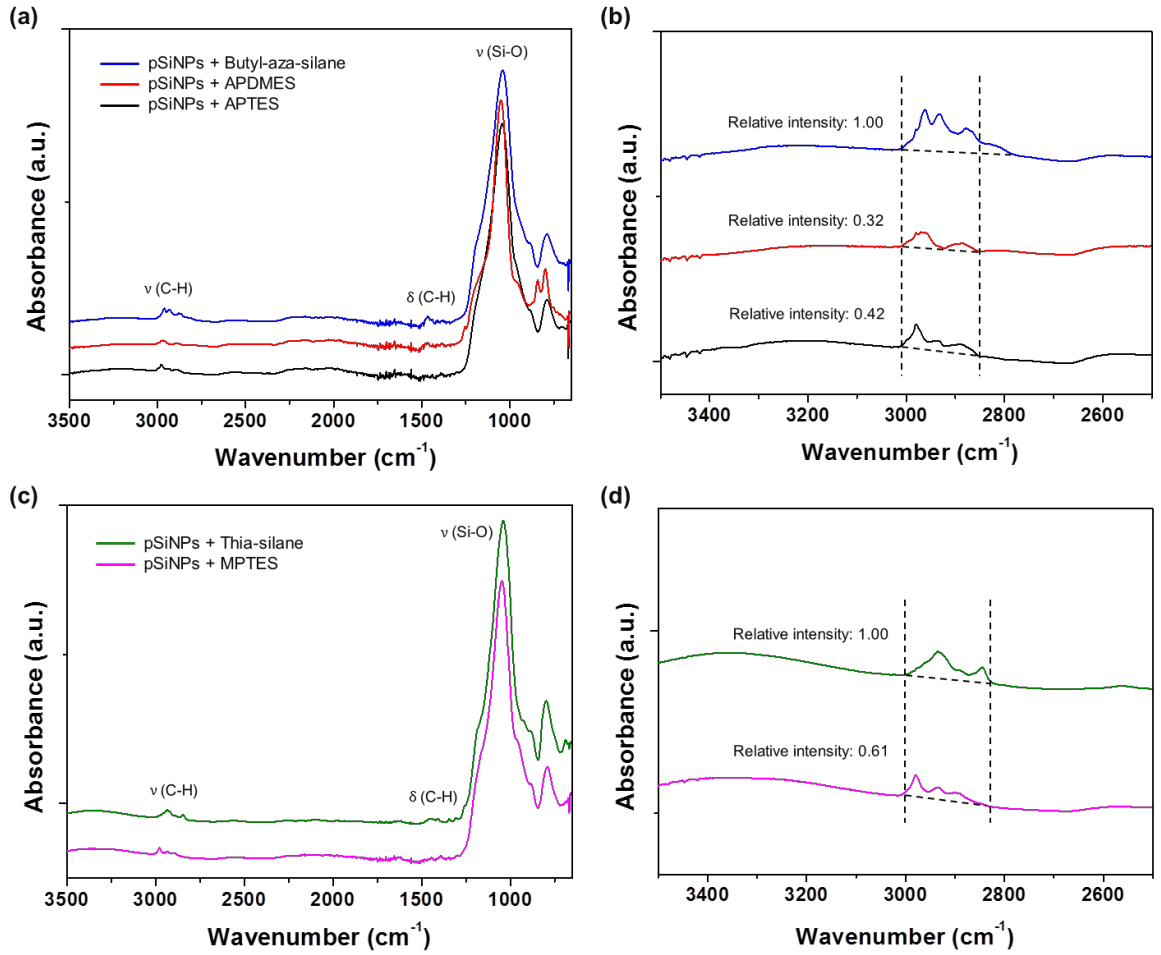

Figure 3.7. Attenuated total reflectance Fourier-transform infrared (ATR-FTIR) spectra of reaction products of porous silicon microparticles (pSiMPs) with the indicated silanes. Cyclic silane chemisty was carried out at 25 °C for 2 h in dichloromethane (DCM), and alkoxysilane chemistry was carried out at 25 °C for 12 h in ethanol (EtOH). (a, b) Amine derivatives: Butyl-aza-silane, APDMES (3-aminopropyl-dimethylethoxysilane), APTES (3-aminopropyl-triethoxysilane). (c, d) Thiol derivatives: Thia-silane, MPTES (3-mercaptopropyl-triethoxysilane). The numbers in graphs (b) and (d) represent the relative area of the curves integrated in the wavenumber ranges indicated. Assignments of stretching modes (C-H, and Si-O) and bending modes (C-H) are as indicated. Symbols: ν=stretching, δ=bending. Prior to the ATR-FTIR measurement, the particles were fully dried in vacuum for 2 days (after removal of unreacted silane and workup).

Table 3.2. Thermogravimetric analysis (TGA) data of porous Si microparticles (pSiMPs) and the products resulting from reaction with cyclic silanes (Set 1) and alkyoxysilanes (Set 2). Cyclic silane chemistry was carried out at 25 °C for 2 h in dichloromethane (DCM), and alkoxysilane chemistry was carried out at 25 °C for 12 h in ethanol (EtOH). The particles were dried in vacuum for 2 days prior to analysis (after removal of unreacted silane and workup). Mass change (%) is change in mass at 800°C relative to the same sample at 30°C. Net mass change (%) is the change in mass of the modified particles relative to unmodified particles. The diaza-silane product was prepared from a 10% cyclohexane solution.

Set 1	**pSi microparticle**	**pSi microparticle + Thia-silane**	**pSi microparticle + Butyl-aza-silane**
Mass (at 30 °C)	6.0614 mg	5.7888 mg	7.1532 mg
Mass (at 800 °C)	5.9262 mg	5.1913 mg	6.4301 mg
Mass change (mg)	-0.1352 mg	-0.5975 mg	-0.7231 mg
Mass change (%)	-2.23%	-10.32 %	-10.11 %
Net mass change (%)	-	8.09%	7.88%
	-	**pSi microparticle + Diaza-silane**	**pSi microparticle + Methyl-aza-silane**
Mass (at 30 °C)	-	5.3532 mg	7.4357 mg
Mass (at 800 °C)	-	5.0701 mg	6.6728 mg
Mass change (mg)	-	0.2831 mg	0.7629 mg
Mass change (%)	-	-5.29 %	-10.26 %
Net mass change (%)	-	3.06%	8.03%
Set 2	-	**pSi microparticle + MPTES**	**pSi microparticle + APTES**
Mass (at 30 °C)	-	3.9974 mg	6.1442 mg
Mass (at 800 °C)	-	3.7552 mg	5.8566 mg
Mass change (mg)	-	0.2422 mg	0.2876 mg
Mass change (%)	-	-6.06 %	-4.68 %
Net mass change (%)	-	3.83%	2.45%

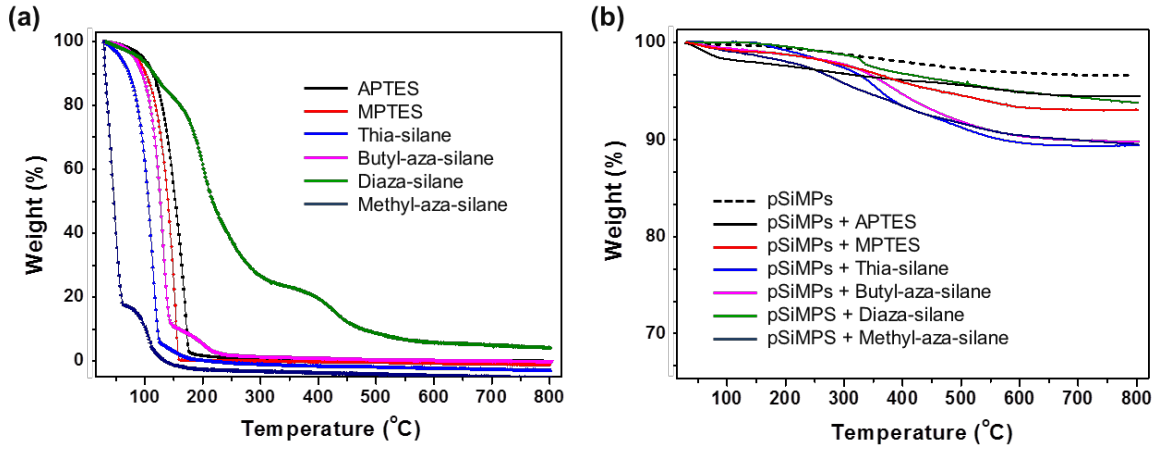

Figure 3.8. Thermogravimetry curves measured for (a) silane reagent starting materials as indicated, and (b) products resulting from reaction of porous silicon microparticles (pSiMPs) with the indicated silane reagents. Cyclic silane chemistry was carried out at 25 °C for 2 h in dichloromethane (DCM), and alkoxysilane chemistry was carried out at 25 °C for 12 h in ethanol. Prior to the thermogravimetry measurement, the particles were fully dried in vacuum for 2 days (after removal of unreacted silane and workup). These TGA results provide direct evidence of conjugation to the particles, because the attached ligands are removed gradually from the products as the temperature increases to 800 °C, while the reagent starting materials evaporate cleanly below 200 °C (with the exception of the diaza silane reagent).

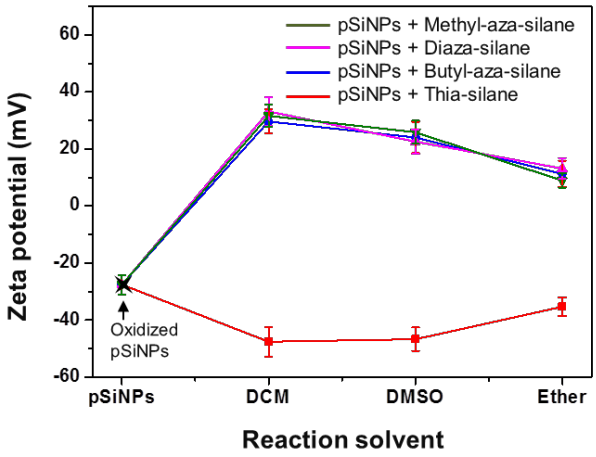

Figure 3.9. Zeta potential of porous silicon nanoparticles (pSiNPs) functionalized with the indicated cyclic silane (100 µL) as a function of the solvent (400 µL) in which the functionalization reaction was run. All reactions were carried out for 2 h at 25 °C. Solvents used: DCM = dichloromethane, DMSO = dimethylsulfoxide, Ether = diethylether. Particles were isolated after the 2 h functionalization reaction, rinsed with pure solvent, and re-dispersed in deionized water (DI H_2O) for the measurement. Mean values and standard deviations are calculated from 3 replicate measurements.

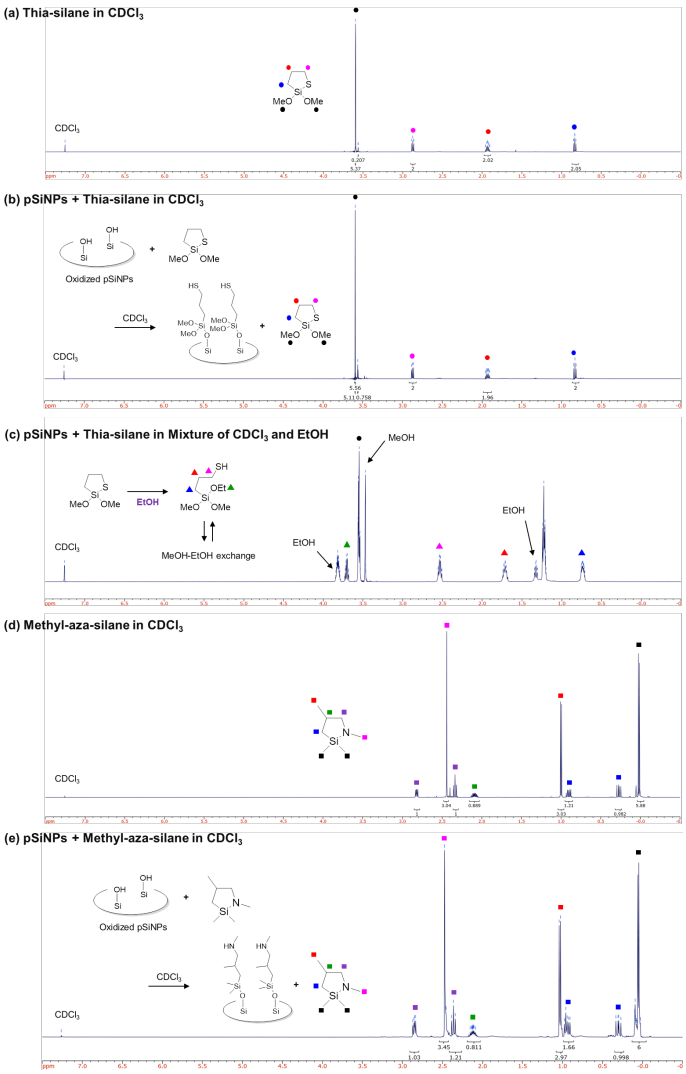

Figure 3.10. ^{1}H NMR spectra investigating the possibility of byproduct formation in the ring-opening click reaction of cyclic silanes with porous silicon nanoparticles (pSiNPs). The particles were reacted with the cyclic silane in $CDCl_3$ at 25 °C for 2 h, and then the particles were removed from the solution by centrifugation prior to NMR analysis. Thus only the soluble silane starting material or soluble byproducts can be detected in this experiment. (a) pure thia-silane in $CDCl_3$. (b) Thia-silane after reaction with oxidized pSiNPs. No reaction byproducts were detected by NMR. (c) Control experiment where oxidized pSiNPs reacted with thia-silane in a mixture of ethanol (EtOH) and $CDCl_3$ (1:10, EtOH:$CDCl_3$, by volume). Ethanol induces a ring-opening reaction with cyclic silanes and generates methanol (MeOH) as a byproduct. The NMR spectrum of the cyclic-silane changes substantially when it undergoes ring-opening, and a peak assigned to the MeOH byproduct is also observed. (d) pure methyl-aza-silane reagent in $CDCl_3$. (e) Methyl-aza-silane after reaction with oxidized pSiNPs in $CDCl_3$ at 25 °C for 2 h. The spectrum matches that of the pure methyl-aza-silane reagent and no reaction byproducts were detected by NMR. Insets: proposed reactions with spectral assignments as indicated with the colored shapes.

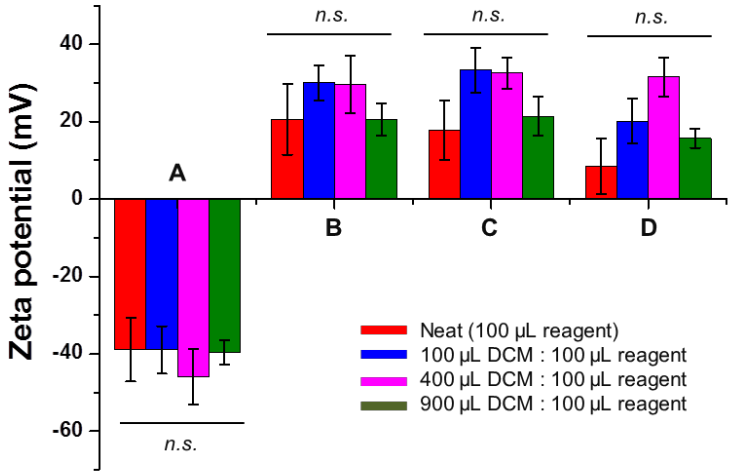

Figure 3.11. Measured zeta potential of porous silicon nanoparticles (pSiNPs) (-27.6 mV, ~1 mg) after reaction with cyclic silanes (100 µL) at different concentrations for 2 h at 25 °C. The colored bars indicate different dilutions of the neat cyclic silane reagent with dichloromethane (DCM) solvent. Concentration of pSiNPs in each of these dilutions is ~1 mg. A; pSiNPs + thia-silane, B; pSiNPs + butyl-aza-silane, C; pSiNPs + diaza-silane, D; pSiNPs + methyl-aza-silane. The values were measured after reaction, separation by centrifugation, rinsing, and then re-dispersion of the particles in deionized water (DI H_2O). The standard deviations are calculated from 3 replicate measurements.

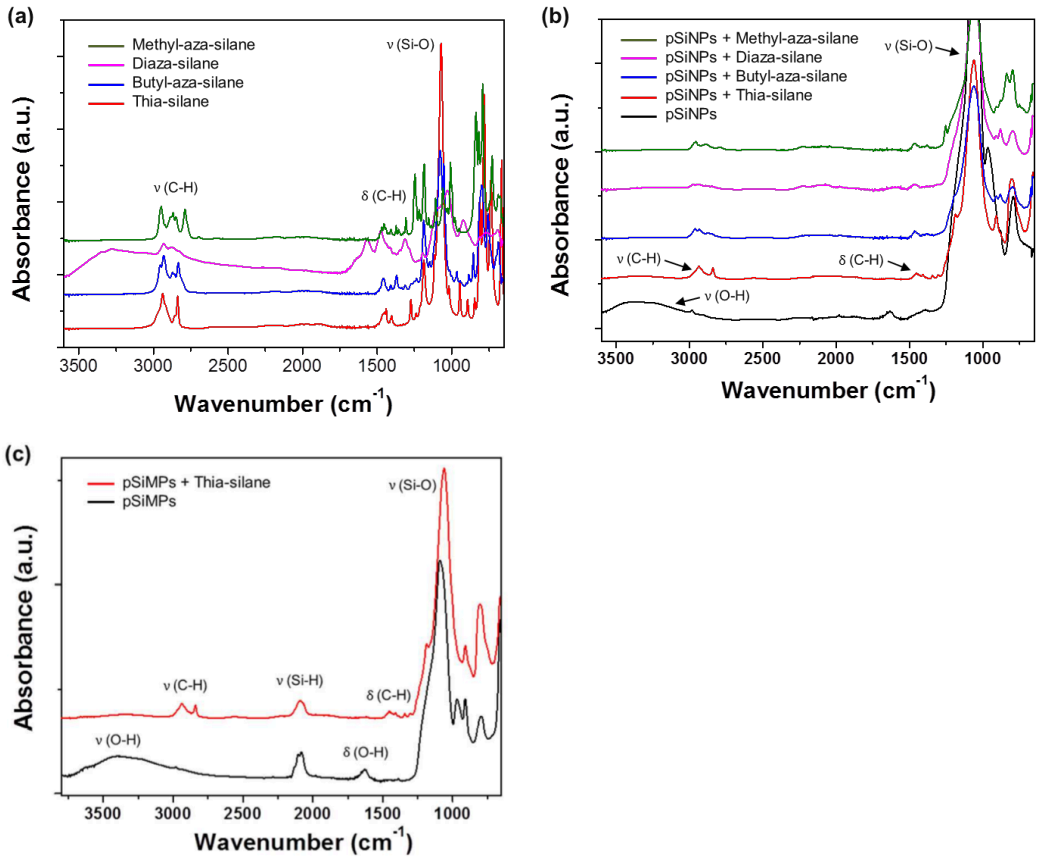

Figure 3.12. Attenuated total reflectance Fourier-transform infrared (ATR-FTIR) spectra of cyclic silane reagents and products of their reaction with porous Si nanoparticles (pSiNPs) or porous Si microparticles (pSiMPs). (a) Cyclic silane reagents, measured as the neat liquids. (b) Porous Si nanoparticles (pSiNPs) and products resulting from reaction of pSiNPs with the indicated cyclic silane reagents at 25 °C for 2 h (after removal of unreacted silane and workup). (c) Porous Si microparticles before (pSiMPs) and after (pSiMPs + thia-silane) reaction with cyclic thia-silane reagent. Note compared to the nanoparticle formulations, the oxidized microparticles retain some surface Si-H species that are detected in the ATR-FTIR spectrum. Assignments of stretching modes (O-H, C-H, and Si-O) and bending modes (C-H) are indicated. Symbols: ν=stretching, δ=bending. Prior to the ATR-FTIR measurement, the particles were fully dried in vacuum for 2 days. The spectra indicate the particles contain substantial surface hydroxyl species prior to reaction with the cyclic silane reagents.

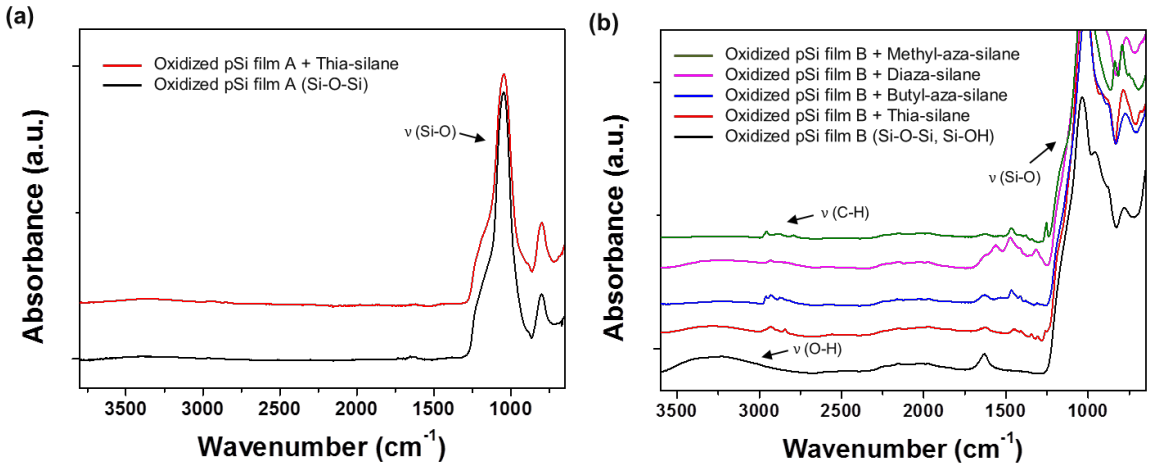

Figure 3.13. Attenuated total reflectance Fourier-transform infrared (ATR-FTIR) spectra of porous Si films subjected to different oxidation conditions and the products of reaction with cyclic silane reagents. The porous Si samples used in these experiments were films, still attached to the silicon chip substrate for convenience in handling. (a) Product resulting from reaction of porous SiO_2 film (prepared by oxidation of porous Si film at 800°C for 2 h in air, denoted as "Oxidized pSi film A") before and after reaction with thia-silane (at 25 °C for 2 h, followed by workup to remove unreacted reagent). The result indicates no substantial reactivity of this dehydrated Si-O-Si surface toward the cyclic silane reagent. (b) Products resulting from reaction of hydroxylated-surface pSi films (prepared by oxidation of pSi film in aqueous hydrogen peroxide, denoted as "Oxidized pSi film B") with the indicated silane reagents (at 25 °C for 2 h, followed by workup to remove unreacted reagent). The milder oxidation process for "Oxidized pSi film B" generates surface hydroxyl species that are reactive toward the cyclic silanes. Assignments of stretching modes (O-H, C-H, and Si-O) are indicated. Initial porosity of all porous Si films was 50–60%.

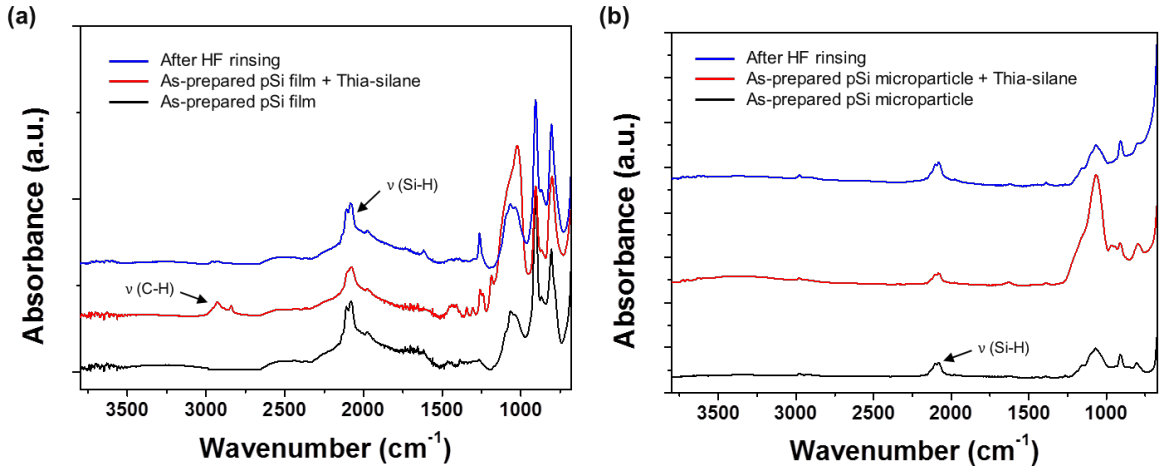

Figure 3.14. Attenuated total reflectance Fourier-transform infrared (ATR-FTIR) spectra of as-prepared porous Si (pSi) materials. (a) Product resulting from reaction of as-etched pSi film with thia-silane (at 25 °C for 2 h, followed by workup to remove unreacted reactant). The porous Si samples used in these experiments were films, still attached to the silicon chip substrate for convenience in handling. The "after HF rinsing" trace corresponds to the spectrum of the sample after rinsing with aqueous ethanolic HF to remove physically absorbed reactant and freely accessible oxide at the surface. (b) as-etched pSi microparticles (containing no oxide sheath, but detached from the Si wafer substrate), the product resulting from treatment of the as-etched pSi microparticles with thia-silane (at 25 °C for 2 h, followed by workup to remove unreacted reagent), and after rinsing of the modified material with an ethanolic aqueous HF solution. Assignments of stretching modes (C-H and Si-H) are indicated. Prior to the ATR-FTIR measurement, the particles were dried in vacuum for 2 days.

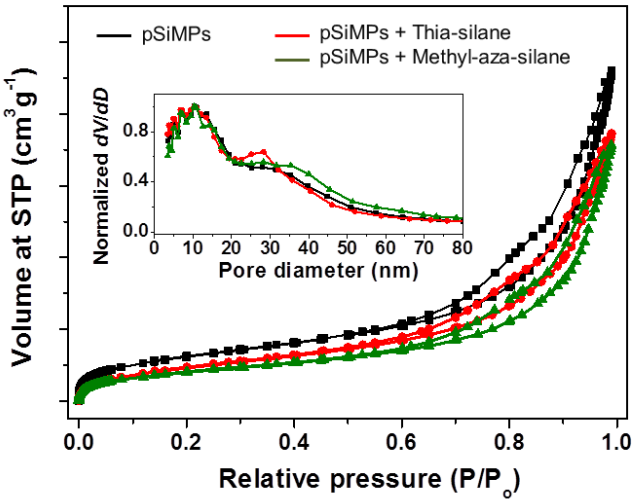

Figure 3.15. Isothermal curves and pore size distribution (inset) of the oxidized pSiMP starting material and the products of reaction with thia-silane and methyl-aza-silane, as indicated.

Table 3.3. Nitrogen adsorption analysis of the pSi microparticles (pSiMPs), and resulting products with thia-silane and methyl-aza-silane. BJH pore volumes represent average pore diameter. Prior to the nitrogen adsorption experiment, the particles were degassed under vacuum overnight.

	BET Surface area (m^2 g^{-1})	**BJH pore volume (cm^3 g^{-1})**	**BJH pore size (nm)**
pSi microparticle	397.86	1.33	15.51
pSi microparticle + Thia-silane	300.57	1.09	13.16
pSi microparticle + Methyl-aza-silane	301.30	1.10	13.06

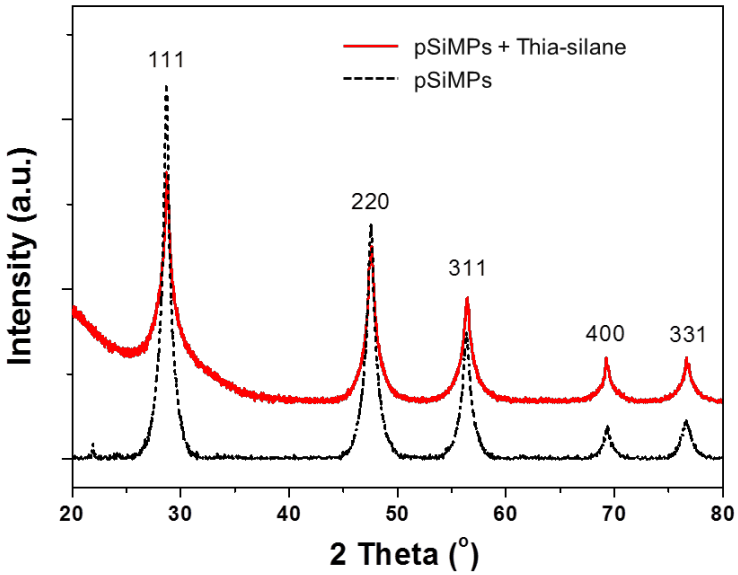

Figure 3.16. Powder X-ray diffraction (XRD) spectrum of porous silicon microparticles (pSiMPs) before (black dashed trace) and after (red solid trace) reaction with thia-silane reagent (at 25 °C for 2 h, followed by workup to remove unreacted reagent). Peaks in the diffraction pattern of the pSiMPs are assigned Miller indices (h k l) of the reflection, indicating the set of crystalline Si lattice planes responsible for that diffraction peak. Prior to the XRD measurement, the particles were fully dried in vacuum for 2 days. Debye-Scherrer method used to calculate nanostructure crystallite size is described in the supplemental experimental section.

Table 3.4. Elemental composition analysis of pSi microparticle (pSiMPs) starting material and the coupling products with thia-silane and methyl-aza-silane. Elemental analyses derived from energy-dispersive X-ray (EDX) analysis in an FEI XL30 UHR (Ultra High Resolution) scanning electron microscope. The particles were fully dried in vacuum for 2 days prior to analysis (after removal of unreacted silane and workup).

Sets	Component	Type	Mole Conc.	Conc.	Units
pSi microparticles	O	Calc.	22.130	22.130	-
	Si	Calc.	77.870	77.870	-
	Total	-	100.000	100.000	wt.%
pSi microparticles + thia-silane	C	Calc.	15.434	10.880	-
	O	Calc.	36.050	29.983	-
	Si	Calc.	45.653	57.053	-
	S	Calc.	2.863	2.085	-
	Total	-	100.000	100.000	wt.%
pSi microparticles + methyl-aza-silane	C	Calc.	16.780	9.089	-
	O	Calc.	27.314	19.708	-
	Si	Calc.	53.733	68.060	-
	N	Calc.	2.173	3.143	-
	Total	-	100.000	100.000	wt.%

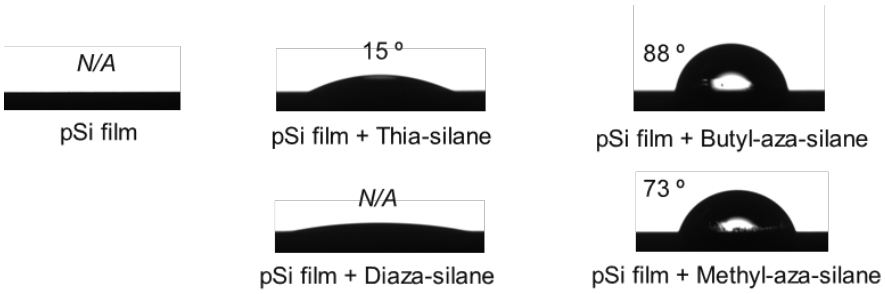

Figure 3.17. Measured water contact angles and water drop images of the oxidized porous silicon film surface and the products resulting from reaction with thia-silane, butyl-aza-silane, diaza-silane, and methyl-aza-silane, as indicated. Water contact angle standard error is ± 5° from 3 replicate measurements. Initial porosity of all pSi films was 50–60%.

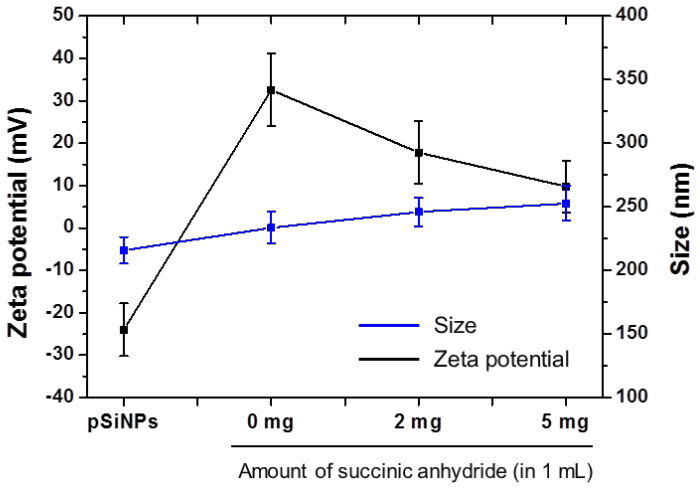

Figure 3.18. Zeta-potential (black line) and mean hydrodynamic diameter (blue line, z-average value) of porous silicon nanoparticles (pSiNPs), with diaza-silane (100 μL) and succinic anhydride (0, 2, 5 mg/mL) in dichloromethane (DCM, 400 μL) after reaction at 25 °C for 2 h. Particles were isolated at the indicated time points, rinsed, and re-dispersed in deionized water (DI H_2O) for the measurement. Mean values and standard deviations are calculated from 3 replicate measurements.

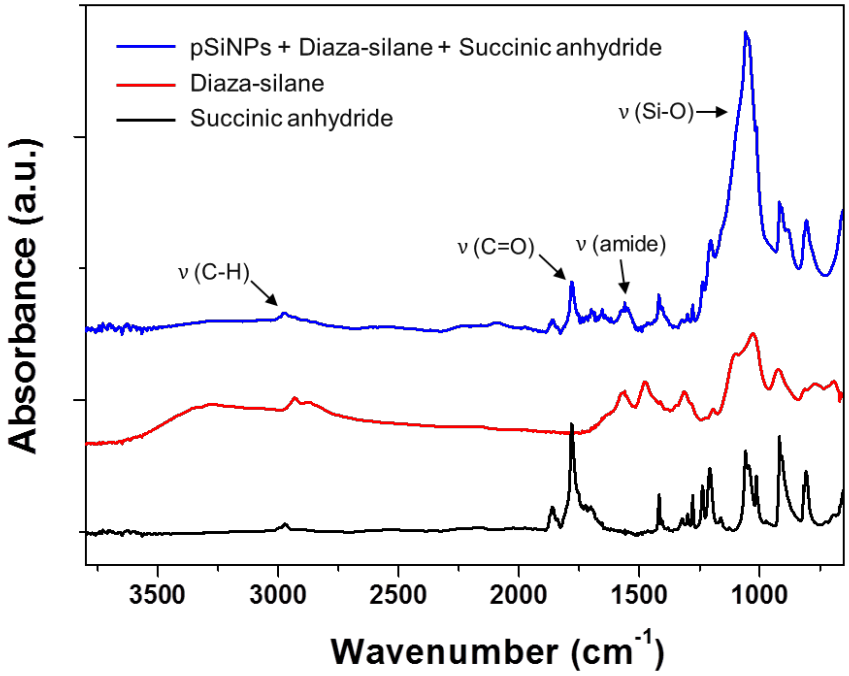

Figure 3.19. Attenuated total reflectance Fourier-transform infrared (ATR-FTIR) spectra of the starting reagents succinic anhydride and diaza-silane, and the product resulting from the reaction of porous silicon nanoparticles (pSiNPs) in dichloromethane (400 µL) solution containing diaza- silane (100 µL) and succinic anhydride (5 mg/mL) after reaction at 25 °C for 2 h, followed by workup to remove unreated reagents. Assignments of stretching modes: aliphatic C-H (2971 cm^{-1}), carboxylic C=O (1779 cm^{-1}), amide II (1560 cm^{-1}), Si-O (1056 cm^{-1}) are as indicated. Prior to the ATR-FTIR measurement, the particles were fully dried in vacuum for 2 days.

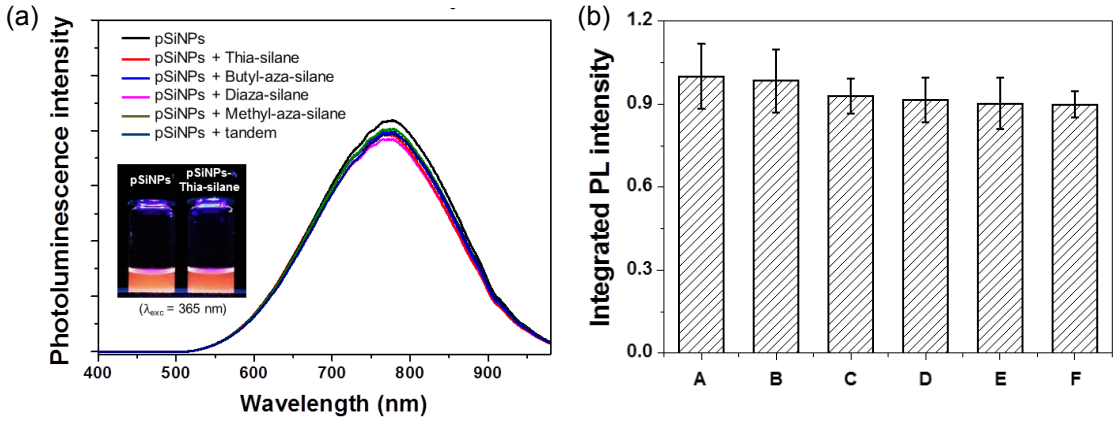

Figure 3.20. (a) Photoluminescence (PL) emission spectra (λ_{exc}=365 nm) of the pSiNP starting material and the products of reaction with thia-silane, butyl-aza-silane, diaza-silane, methyl-aza-silane, and the tandem reagent consisting of diaza-silane and succinic anhydride (eq. 1). The photoluminescence spectra were measured in ethanol. Inset photo was taken under UV illumination (365 nm). (b) Normalized photoluminescence intensity (integrated intensity in the wavelength range 500–980 nm, excitation wavelength 365 nm) for porous silicon nanoparticles (pSiNPs) and various reaction products with cyclic silanes. (A) porous silicon nanoparticles (pSiNPs) before reaction, (B) after reaction with thia-silane, (C) after reaction with butyl-aza-silane, (D) after reaction with diaza-silane, (E) after reaction with methyl-aza-silane, and (F) after reaction with diaza-silane and succinic anhydride mixture. The standard deviations are calculated from 4 replicate measurements.

Table 3.5. Data used to determine percent activity of lysozyme released from lysozyme-loaded porous silicon nanoparticles (pSiNPs) with or without the indicated surface chemistry. Non-modified and reagent-modified pSiNPs are compared, as is the solvent used in the coupling reaction (n-hexane or dichloromethane or ethanol). Where applicable, lysozyme was loaded prior to the modification reaction. The lysozyme activity assay (active protein released) was compared to the BCA protein assay (total protein released) to determine the percent activity of loaded lysozyme from control and functionalized pSiNPs.

Set 1	**Thia-silane in *n*-hexane (*n*-Hex)**			
Release time	Without thia-silane		With thia-silane	
	Active Lysozyme (μg)	Total Lysozyme (μg)	Active Lysozyme (μg)	Total Lysozyme (μg)
24 h	11.97 ± 2.08	19.83 ± 1.37	13.82 ± 0.89	19.51 ± 0.32
48 h	4.29 ± 0.59	5.62 ± 1.19	5.17 ± 0.47	6.93 ± 1.64
72 h	4.50 ± 0.87	5.97 ± 0.72	4.24 ± 0.51	5.60 ± 0.31
Total	20.75 ± 2.85	31.42 ± 2.10	23.23 ± 1.49	32.04 ± 1.19
% Activity	-	66 ± 4.7	-	72 ± 1.9
Comments	40% of protein was released in 72 h. Difference in % activity of protein released from capped or non-capped particles is not significant. Mass loading of lysozyme typically 76 μg in 0.1 mg of lysozyme-loaded porous Si nanoparticles (41%)			
Set 2	**Thia-silane inn dichloromethane (DCM)**			
Release time	Without thia-silane		With thia-silane	
	Active Lysozyme (μg)	Total Lysozyme (μg)	Active Lysozyme (μg)	Total Lysozyme (μg)
24 h	13.53 ± 1.44	13.91 ± 1.27	14.45 ± 0.69	14.24 ± 1.19
48 h	5.97 ± 0.72	6.21 ± 0.63	5.73 ± 0.64	6.56 ± 1.67
72 h	6.10 ± 0.36	6.27 ± 2.28	6.14 ± 0.45	6.01 ± 0.10
Total	25.58 ± 0.66	26.40 ± 3.32	26.32 ± 1.71	26.82 ± 0.53
% Activity	-	96 ± 5.3	-	98 ± 4.7
Comments	34% of protein was released in 72h. Difference in % activity of protein released from capped or non-capped particles is not significant			
Set 3	**MPTES chemistry in ethanol (EtOH)**			
Release time	Without MPTES		With MPTES	
	Active Lysozyme (μg)	Total Lysozyme (μg)	Active Lysozyme (μg)	Total Lysozyme (μg)
24 h	24.08 ± 0.8	29.93 ± 0.8	4.38 ± 0.4	9.50 ± 0.7
48 h	5.37 ± 1.0	6.77 ± 0.2	4.44 ± 0.6	4.38 ± 0.1
72 h	5.00 ± 0.4	5.85 ± 0.1	3.41 ± 0.9	4.20 ± 0.1
Total	34.45 ± 2.1	42.55 ± 0.8	12.23 ± 0.4	18.07 ± 0.8
% Activity	-	81 ± 3.3	-	68 ± 4.0
Comments	54% of protein was released from particles without chemistry and 23% of protein was released from particles with MPTES chemistry in 72 h. % activity of protein released from MPTES modified particles is significantly less than control particles.			

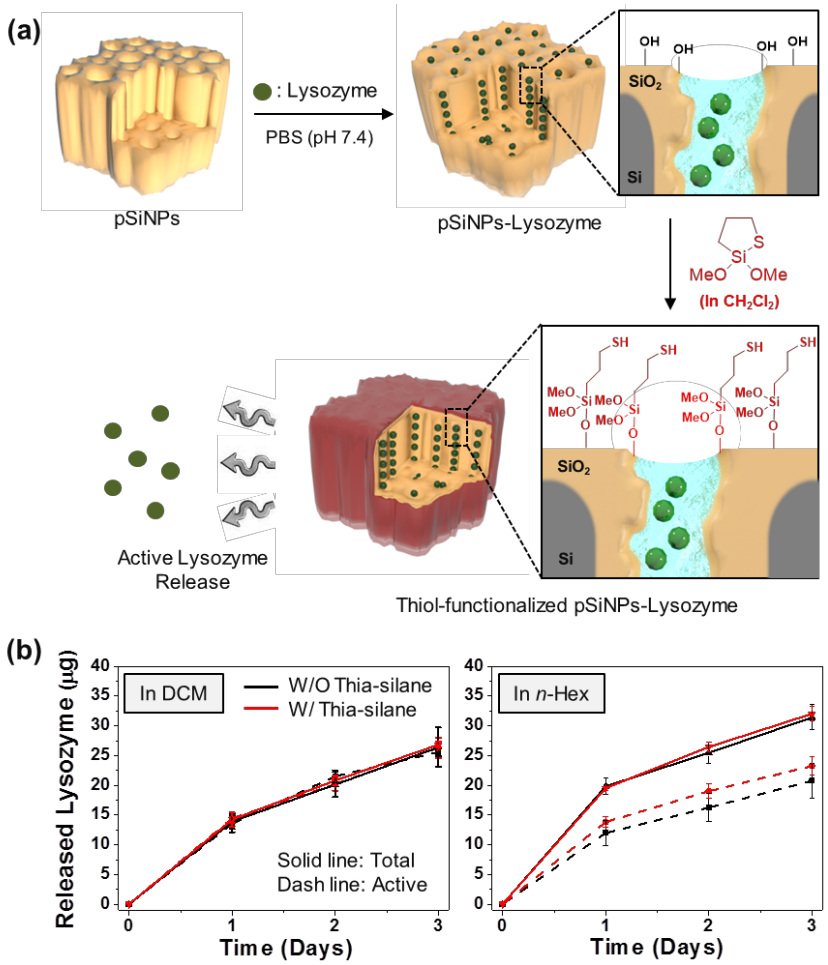

Figure 3.21. (a) Procedure used to load lysozyme into pSiNPs and modify the resulting particles using the ring-opening click reaction. The pSiNPs are loaded with lysozyme from aqueous solution, and the click reaction is run in DCM or n-hexane to decorate the outer perimeter of the nanoparticles. Immersion in aqueous buffer at 37 °C induces slow release of the protein payload. (b) Micrograms of total lysozyme released (BCA assay) from unmodified pSiNPs (black line) and thia-silane functionalized pSiNPs (red line). Dashed lines show micrograms of active lysozyme released (lysozyme activity assay). Total protein loaded was ~76 μg. "In DCM" and "In n-Hex" denote solvent in which the ring-opening click reactions were run. Release experiments were performed in PBS buffer at 37 °C.

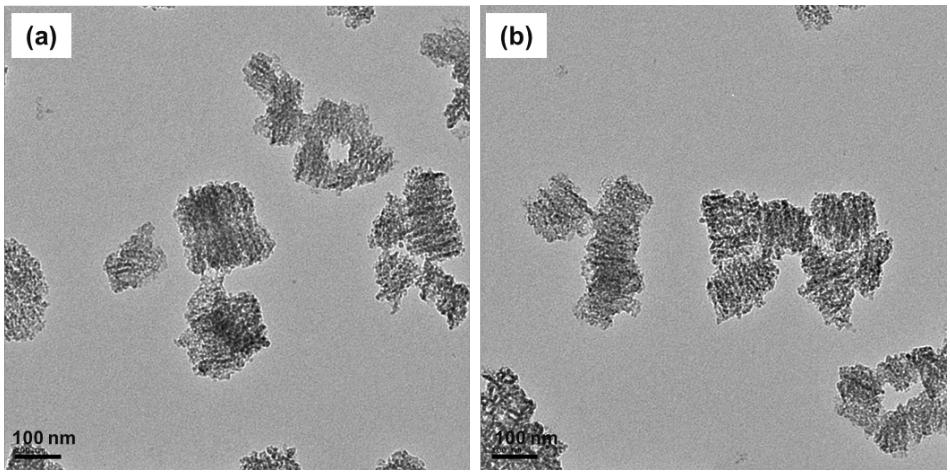

Figure 3.22. Transmission electron microscope (TEM) images of lysozyme-loaded porous silicon nanoparticles (pSiNPs), before (a) and after (b) reaction with thia-silane reagent. Scale bar is 100 nm.

Chapter 3, in full, is a reprint of the material as it appears in Journal of the American Chemical Society 2016. Dokyoung Kim, Jonathan M. Zuidema, Jinyoung Kang, Youlin Pan, Lianbin Wu, David Warther, Barry Arkles, Michael J. Sailor. The dissertation author was the primary researcher and author of this material.

CHAPTER 4

Two-photon *In Vivo* Imaging with Porous Silicon Nanoparticles

4.1. Abstract

A major obstacle in luminescence imaging is the limited penetration of visible light into tissues and interference associated with light scattering and autofluorescence. Near-infrared (NIR) emitters that can also be excited with NIR radiation via two-photon processes can mitigate these factors somewhat because they operate at wavelengths of 650–1000 nm where tissues are more transparent, light scattering is less efficient, and endogenous fluorophores are less likely to absorb. This study presents photolytically stable, NIR photoluminescent, porous silicon nanoparticles with a relatively high two-photon-absorption cross-section and a large emission quantum yield. Their ability to be targeted to tumor tissues *in vivo* using the iRGD targeting peptide is demonstrated, and the distribution of the nanoparticles with high spatial resolution is visualized.

4.2. Introduction

Photoluminescence (PL) is a versatile tool in chemical, biological, and biomedical science as it enables operationally simple, cost-effective, noninvasive, sensitive, and rapid visualization of organisms at a subcellular level with high resolution.[1-3] Accordingly, various kinds of photoluminescent organic/inorganic labels have been developed for the detection and imaging of analytes, biological systems, diseased tissues, or events.[4-6] For imaging tissues by laser-scanning confocal fluorescence microscopy, typical exogenous luminescent probes offer imaging depths of only a few tens of micrometers, owing to the scattering of light and interference of tissue autofluorescence from intrinsic fluorophores such as riboflavin, flavoproteins, and nicotinamide adenine dinucleotide.[7,8] Two-photon microscopy (TPM) provides a means to increase penetration depth and improve spatial

resolution due to the reductions in tissue autofluorescence and scattering associated with the longer wavelengths of both the exciting and emitting photons.[9,10] Thus, TPM has been employed as a minimally invasive tool for numerous short-term and long-term animal studies.[11]

Semiconductor nanocrystals have been harnessed as one or two-photon imaging agents to monitor cellular trafficking, tumor microenvironments, and tissue vasculature.[12-16] These materials typically show remarkable photostability compared with organic dyes, and some display sufficient two-photon absorption cross-sections (TPACS, δ) to be of use in two-photon imaging schemes.[17,18] Silicon-based nanocrystals have emerged as promising substitutes for toxic cadmium or lead-based semiconductor nanocrystals;[19-21] the aqueous degradation product of mesoporous silicon is principally $Si(OH)_4$, which is the form of silicon naturally present in tissues of the body.[22] As nanoparticles, the mesoporous form of silicon has been shown to be useful for drug delivery applications, where the 50–80% void volume leads to relatively high capacity for protein, small molecule, or nucleic acid payloads (typical mass loadings in the range of 10–20%).[23-25] The utility of porous silicon nanoparticles (pSiNPs) has been enhanced by the incorporation of tissue-specific targeting elements, which can reduce the overall dose needed to effect productive therapeutic or imaging results *in vivo*.

One-photon photoluminescence from quantum-confined pSiNPs has been effectively harnessed for bioimaging due to their tissue-penetrating near-infrared (NIR) emission,[26-29] although applications are limited by the short wavelengths needed for efficient excitation (300 - 450 nm). Imaging silicon nanoparticles (both porous and solid forms) via two-photon excitation has been reported.[30-33] While this has the potential to

provide tissue images at greater depths and at higher resolution, no live animal imaging results with intravenously administered silicon nanoparticles have yet been reported, presumably due to their relatively low TPACS and low accumulation in the imaged tissues. Here we demonstrate the utility of pSiNPs for *in vivo* two-photon imaging by optimizing the pSiNP size to maximize TPACS and by adding a peptide targeting group to selectively accumulate the nanoparticles in tumor tissues.

4.3. Results and Discussions

The pSiNPs were prepared from highly doped p-type single-crystal silicon wafers in aqueous ethanolic electrolytes containing HF (hydrofluoric acid), using an electrochemical perforation etch followed by liftoff, ultrasonic fracture, aging, and isolation as previously described.[34] The perforation etch yields pSi particles with well-controlled particle size and distribution. In the present case, we prepared two size classes for comparison, one of nominal hydrodynamic diameter 60 nm and the other of nominal diameter 230 nm, denoted as 60 nm pSiNPs and 230 nm pSiNPs, respectively (measured by dynamic light scattering (DLS); Fig. 4.1a-c and Fig. 4.3-4.4). The ultrasonic fracture process generated a native oxide on the porous Si skeleton (Fig. 4.1a), and this SiO_2 sheath imparted a negative zeta potential (−37.4 ± 3.8 mV; Table 4.1) to the nanoparticles. The samples displayed bands in the infrared spectrum consistent with a hydroxylated silicon oxide (Si–O stretching mode at 1020 cm^{-1} and O–H stretching and bending modes at 3300 cm^{-1} and 1640 cm^{-1}, respectively; Fig. 4.4). The X-ray photoelectron spectra (XPS) were consistent with the existence of a surface oxide layer on the nanoparticles (Fig. 4.1d). Raman spectroscopy (Si lattice mode at 515 cm^{-1}; Fig. 4.4) and powder X-ray diffraction (XRD) (Fig. 4.4) analysis showed the

pSiNPs retained a crystalline silicon skeleton, although there was a broadening of the peaks associated with crystalline silicon post-ultrasonication. The ultrasonication process also induced a decrease in the total pore volume and average pore diameter as measured by nitrogen absorption–desorption isotherm analysis, consistent with the growth of a SiO_2 sheath on the surface of the pore walls (Fig. 4.5 and Table 4.2).

The growth of the SiO_2 sheath activated PL from the nanoparticles (Fig. 4.1e); the increase in the PL signal is attributed to passivation of nonradiative surface defects by the oxide layer. The PL (λ_{ex} = 365 nm) from the 60 nm pSiNPs became detectable after 12 h of ultrasonic fracture, and the intensity of PL maximized at an emission wavelength of 780 nm after ≈48 h of ultrasonication (Fig. 4.1e and Fig. 4.6). The PL intensity was observed to decrease after 48 h of ultrasonication (Fig. 4.6), presumably due to degradation and dissolution of the nanoparticles. The radiative recombination of electron–hole pairs confined in crystalline silicon domains is reported to occur at dimensions smaller than 5 nm, approximately the exciton diameter for crystalline silicon.[35] The calculated crystallite size in the skeleton of the 60 nm pSiNPs, determined using the Debye–Scherrer formula from powder XRD data, was 1.5 nm (see Fig. 4.4 and the formula in the Experimental section). Thus, the nanoparticles can be considered to consist of an ensemble of quantum-confined domains dispersed in the nanoparticle skeleton. Using rhodamine 6G as a standard, the 60 nm pSiNPs showed a quantum yield of 22.3% (Fig. 4.7), substantially greater than the 9.4% quantum yield of the larger 230 nm pSiNP preparation (Fig. 4.8).[30] The reason for the greater quantum yield of the smaller pSiNPs is not clear at this time, but it may be due to the presence of fewer quantum-confined domains in a given nanoparticle that can undergo proximal quenching. Alternatively, the smaller nanoparticles may possess a more complete

passivating oxide shell.[36] As expected for quantum-confined silicon,[35] the PL emission lifetime for both nanoparticle formulations was on the timescale of microseconds (PL half-life measured at λ_{em} = 780 nm of 106 and 121 μs for 230 nm pSiNPs and 60 nm pSiNPs, respectively; Fig. 4.9 and Table 4.3).

We next determined the two-photon transition probability of the pSiNPs using luminescence correlation spectroscopy. We scanned the excitation wavelength range from 750 to 1050 nm and collected emission signals in the wavelength range 560–740 nm to avoid interference of the excitating photons with the pSiNP emission spectrum (Fig. 4.1e). For a process in which excitation results from simultaneous absorption of two photons, the luminescence emission intensity is expected to depend quadratically on average excitation power P_{ex}, or $I_{PL} = (P_{ex})^2 \times \Delta t \times C$, where I_{PL} is the amount of photoluminescence light detected, Δt is the duration of the pulsed excitation, and C represents constants associated with the experimental setup.[37] The measurements were carried out by varying the incident power and recording the corresponding emission intensities for two separate excitation wavelengths, 800 and 850 nm. A log–log plot of emission intensity versus incident power yielded a slope of ≈2.0, as expected for a two-photon absorption process (Fig. 4.10a). Under two-photon excitation conditions (λ_{ex} = 850 nm), strong PL was only observed at the focal point of the exciting beam, in contrast to the PL observed along the entire beam path for one-photon excitation (λ_{ex} = 365 nm) (Fig. 4.10b).

The TPACS (δ) of the 60 nm pSiNPs were determined in the excitation range 750–1050 nm using rhodamine 6G as a reference (Fig. 4.10c).[38,39] The maximum TPACS from 60 nm pSiNPs was found to be 5.57 GM (Göeppert-Mayer, 1 GM = 10^{-50} cm^4 s^{-1} per

photon), and it occurred at an excitation wavelength of λ_{ex} = 800 nm (Fig, 4.10d; for calculation see the Experimental Section). The TPACS of the 60 nm pSiNPs was substantially larger than the corresponding TPACS of the 230 nm pSiNPs at λ_{ex} = 800 nm (5.57 GM vs 1.86 GM for 60 nm and 230 nm pSiNPs, respectively; Fig. 4.10e). For comparison, the maximum TPACS for rhodamine 6G in this wavelength range is 55 GM (at λ_{ex} = 750 nm).[39] However, the 60 nm pSiNPs showed superior photostability compared with the organic dye when subjected to two-photon excitation; negligible emission changes were observed with 20 mW of laser excitation (λ_{ex} = 850 nm) over a period of 60 min, whereas rhodamine 6G showed a 40% loss in intensity under the same conditions (Fig. 4.10f). The resilience demonstrated by the pSiNPs is important for biological imaging applications where longer measurement timescales might be needed and where chromophore photostability can be a limiting factor, such as assaying protein activity, monitoring cellular redox potentials, tracking cell migration, and quantifying accumulation or clearance of probes in tissues.

We next evaluated the nanoparticles as two-photon imaging agents in a tissue-specific targeting application. For this study we chose the tumor-homing peptide iRGD (sequence: CRGD-KGPDC), for two main reasons: 1) it is known to provide selective targeting to (neuropilin-positive) tumor cells;[40] and 2) it has also been shown to be highly effective in targeting pSiNPs to tumors in a mouse xenograft model.[41] Due to their superior two-photon cross-section, these studies used the 60 nm, rather than the 230 nm pSiNP formulation. The peptide was attached to the pSiNPs via a bifunctional poly(ethylene-glycol) (PEG) linker (Fig. 4.11a) as follows (Fig. 4.12): a cysteine thiol on

the peptide was coupled to a maleimide group on one end of the PEG linker; the other end of the linker contained a succinimidyl valerate group, which was coupled to a free amine on the pSiNP surface. The free amine groups on the pSiNP surface were previously generated by hydrolytic condensation of 2-aminopropyldimethylethoxysilane (APDMES). The mean hydrodynamic diameter of the resulting construct (named, "60 nm pSiNP-iRGD") increased from the original 60 to 90 nm (mean *z*-average, intensity based), indicating that the conjugation chemistry placed an ≈15 nm corona around the pSiNP core. The polydispersity index measured by DLS was <0.2, indicating that there was no substantial aggregate formation caused by the conjugation chemistry (Fig. 4.12). The PL intensity of the pSiNP-iRGD construct under two-photon excitation (λ_{ex} = 850 nm, power = 20 mW) was similar to the pSiNP starting material, and it similarly showed good stability during 60 min of exposure to the excitation source (Fig. 4.12). The longer-term stability of the nanoparticle construct was assessed in a simple pH 7.4 buffer solution maintained at 37 °C, using one-photon photoluminescence measurements. Under UV excitation (λ_{ex} = 365 nm), the 60 nm pSiNP-iRGD construct lost ≈20% of its PL intensity within 1 h, 50% within 2 h, and PL was near zero after 24 h (Fig. 4.13).

When incubated with HeLa cells, *in vitro* cellular TPM images indicated significant uptake of the 60 nm pSiNP-iRGD (Fig. 3.11b and Fig. 4.14). The nanoparticles localized to the cytosol of the cells and displayed a greater level of cellular uptake relative to untargeted control pSiNPs, consisting of bare pSiNPs (containing just a simple oxide coating) or where the PEG-linker was present but the peptide was replaced with a methoxy group ("pSiNP-mPEG").

We next performed a series of experiments to determine if normal tissues would interfere with the two-photon imaging modality used to detect the pSiNPs. For this evaluation we dissected individual organs (brain, kidney, lung, spleen, and liver) from mice and then incubated them (2 h, 37 °C) in phosphate-buffered saline (PBS) control or in a solution of untargeted, oxide-coated 60 nm pSiNPs (10 mg mL^{-1}). Both one-photon (confocal laser scanning microscope, CLSM) and two-photon images were obtained (Fig. 4.15). Whereas control tissue samples incubated in buffer only displayed minimal PL signals in the observation channel in either one-photon or two-photon imaging modalities, all organs incubated with pSiNPs displayed strong PL signals (Fig. 4.16). The signals were more pronounced in the near-surface region of the organs, though the two-photon images showed stronger signals from the pSiNPs at depths >30 μm into the tissues relative to one-photon CLSM, as can be expected from the greater penetration depth of the two-photon imaging modality (Fig. 4.15-4.16).

Finally, we evaluated the ability of the targeted pSiNPs to image a near-surface tumor by TPM, using a mouse xenograft tumor model and the 60 nm pSiNPs-iRGD formulation as the imaging agent. Tumor-bearing mice were prepared by subcutaneous inoculation of HeLa cells in the dermal layer (>200 μm depth) of the right hind limb (Fig. 4.11c; see the Experimental section). Prior to imaging, the morphological properties of the tumor (Fig. 4.11b, right) and normal (Fig. 4.11b, left) tissue regions were evaluated using optical coherence tomography (OCT).[42,43] The angiographic OCT images revealed randomly distributed, undefined blood vessels in the region surrounding the tumor nodule, and the cross-sectional *y*–*z* axis-scanned OCT images provided in-depth information on the

tissues: epidermal layer (0–50 μm from skin surface) and dermal layer (below 50 μm) (Fig. 4.17).

TPM images were then monitored in the region of the tumor nodule. The 60 nm pSiNP-iRGD construct (20 mg kg^{-1}) was administered via intravenous tail-vein injection and monitoring commenced 25 min postinjection, to ensure sufficient time for blood circulation. The data showed substantial two-photon signals in the dermal layers (125–155 μm) compared with the PBS-injected control, indicative of accumulation of the nanoparticles in the tumor region (Fig. 4.11d and Fig. 4.18). The two-photon emission signal was relatively stable throughout the 1 h monitoring period. The depth dependence of the TPM signal was assessed from the superficial dermal layer (100–150 μm from the skin) to the internal dermal layer (200–250 μm from the surface) at regular intervals (15 μm) in the tumor region, for a period of 60 min post-injection (Fig. 4.11e and Fig. 4.19). The PL emission signal was recorded in two wavelength channels: 400–430 nm, the region where the second harmonic generation (SHG) signal from collagen fibers in the dermal layer appears;[44] and 560–740 nm, the emission window for the 60 nm pSiNP-iRGD construct. Images were acquired under the same two-photon excitation conditions (λ_{ex} = 850 nm, power = 50 mW). The SHG signal from collagen was strong in the superficial dermal layer (blue channel in Fig. 4.11e), and the signal from the nanoparticles was strongest in the zone between 170 and 215 μm from the skin surface (internal dermal layer, red channel in Fig. 4.11e). The *z*-stacked TPM images of normal and tumor regions at 140–215 μm depths, obtained before injection and after injection of the 60 nm pSiNP-iRGD construct, showed selective accumulation of the nanoparticles. Control injections of PBS showed no significant interference from biological tissues (Fig. 4.11f and Fig. 4.19-4.20).

The *in vivo* TPM imaging capability of pSiNPs was compared to the standard two-photon absorber rhodamine 6G. Both probes were injected locally into the dermis near the tumor (at a depth of ≈200 μm from the surface). We chose a localized injection because systemically administered rhodamine 6G shows no organ or tumor specificity. For TPM images of approximately comparable intensity (Fig. 4.21), the pSiNP dose needed to be much larger (40 μg) relative to rhodamine 6G (20 ng). This reflects the substantially lower two-photon absorption cross-section (Fig. 4.10) and the lower emission quantum yield (Fig. 4.7) of the pSiNPs relative to rhodamine 6G. Thus although the present *in vivo* TPM results demonstrate that the combination of NIR emission and NIR two-photon excitation can substantially improve the image quality relative to one-photon, UV excitation, the pSiNPs are substantially weaker than a standard molecular TPM probe. The low toxicity of the silicon system, its ability to carry therapeutic payloads, and its ability to selectively and multivalently target tissues offer substantial advantages to motivate further studies to improve the two-photon cross-section of the silicon nanomaterial.

Distribution and histological studies of the organs collected from the same mice (n = 4) 60 min postinjection were analyzed by *ex vivo* TPM imaging and hematoxylin/eosin staining. In the TPM images, substantially higher PL intensity was observed in the tumor (hind limb) in comparison with the main organs (brain, kidney, liver, and lung) and PBS-injected control mice (n = 4) (Fig. 4.11gh and Fig. 4.22). The biodistribution data are consistent with the selective homing property previously seen for peptide-targeted pSiNP formulations.[41,45,46] Histopathology showed no significant toxicity in the tissues relative to the control (Fig. 4.23).

4.4. Conclusions

This study represents the first example of two-photon imaging of pSiNPs in live animals, and it demonstrates a potential application in selective tumor imaging. The tumor imaging demonstration presented in this work highlights two advantages of pSiNPs as imaging agents: their multivalent targeting capability for selective tissue homing and their low systemic toxicity. The 60 nm pSiNP formulation showed higher quantum yield (22.3%) and greater two-photon absorption cross-section (5.57 GM at 800 nm, 4.29 GM at 850 nm) relative to larger pSiNPs. While the two-photon absorption cross-section is modest relative to standard molecular two-photon imaging agents such as rhodamine 6G, the photostability under excitation conditions was found to be substantially greater.

4.5. Experimental

Materials: All chemical reagents were purchased from Aldrich Chemicals, Inc. Single crystal silicon wafers were obtained from Virginia Semiconductor, Inc. Maleimide-PEG-succinimidyl valerate (MAL-PEG-SVA, MW: 5,000) and methoxy-PEG-succinimidyl valerate (mPEG-SVA, MW: 5,000) were purchased from Laysan Bio Inc. iRGD peptides (sequence: CRGDKGPDC) were obtained from CPC Scientific Inc. Iminobenzo[*g*]coumarin was synthesized by H. G. Ryu at Department of Chemistry, POSTECH.[48]

Instrumentation: Etching waveforms were generated in a computer program written in Labview (National Instruments, Inc.), and the electric current was driven by a Keithley 2651A Sourcemeter power supply interfaced to the LabView program. A 50T ultrasonic bath (VWR International) was used for ultrasonic fracture of the pSi films.

Particles were collected by centrifugation (Eppendorf Centrifuge Model 5424R). Attenuated total reflectance Fourier transform infrared (ATR-FTIR) spectra were recorded using a Thermo Scientific Nicolet 6700 FTIR instrument fitted with a Smart iTR diamond ATR fixture. All spectra in a given ATR-FTIR plot were measured with the same collection parameters and on comparable quantities of material, in an attempt to make direct comparisons of signal strength between samples. Where multiple spectra are compared, the spectra are offset along the y-axis to improve clarity. Hydrodynamic size and zeta-potential of nanoparticles were determined by dynamic light scattering (DLS) using a Malvern Instruments Zetasizer Nano ZS90. Powder x-ray diffraction (XRD) spectra were collected at ambient temperature on a Bruker D8 Advance diffractometer using Cu Kα (λ=1.5418 Å) radiation (40 kV, 40 mA), a scan speed of 0.1 sec/step, a step size of 0.02° in 2Θ, and a 2Θ range of 10–80°. An Ocean Optics QE-Pro spectrometer fitted with a 510 nm long-pass emission filter was used to obtain steady-state photoluminescence spectra (λ_{exc}: 365 nm). Transmission electron microscope (TEM) images were obtained with a JEOL-1200 EX II 120 kV instrument. Nitrogen adsorption-desorption isotherms of the pSiNPs were recorded at 77 K using a Micromeritics ASAP 2020 instrument. Prior to the nitrogen adsorption experiment, the pSiNPs were degassed under vacuum overnight. The surface area of the particles was determined using the BET (Brunnauer-Emmett-Teller) method. X-ray Photoelectron Spectroscopy (XPS) of samples was performed at the Korea Basic Science Institute (KBSI) using a K-Alpha^{TM} (ThermoFisher Scienfitic^{TM}) spectrometer with a focused monochromatic Al-Kα source operating at 12 kV and 20 mA, and with samples maintained in ultrahigh vacuum (base pressure of 10^{-10} torr). The samples were prepared by deposition of a suspension of pSiNPs onto a Cu substrate immediately

prior to the XPS measurements. The measurements were obtained over an area of 1 mm^2 on the Cu substrate.

Preparation of pSiNPs (60 nm Size): pSiNPs were prepared by electrochemical etching of highly doped p-type single-crystal silicon wafers in an electrolyte consisting of 3:1 (*v:v*) 48% HF:absolute ethanol. CAUTION: HF is highly toxic and corrosive and contact with skin should be avoided. Procedures involving HF should always be carried out in a fume hood configured to handle HF and the operator should wear appropriate protective gloves, gown, and face shield. The synthetic procedure is outlined in Fig. 4.2. The Si wafers were contacted on the backside with a strip of Al foil. Prior to preparation of the porous layers, the wafer surfaces were cleaned using a sacrificial etch consisting of electrochemical anodization (60 s, 50 mA cm^{-2}) in an electrolyte consisting of 3:1 (*v:v*) 48% aqueous HF:absolute ethanol, followed by ethanol rinse, then dissolution of the porous film with aqueous KOH (2 M). The wafer was rinsed with water and then with ethanol. A perforation etching waveform[34] was used to prepare the porous layers, which consisted of a current density pulse of 50 mA cm^{-2} of 0.60 s duration, followed by a current density pulse of 400 mA cm^{-2} of 0.363 s duration. This waveform was repeated for 500 cycles, generating a porous nanostructure consisting of ≈60-nm-thick porous silicon layers separated by high porosity ("perforation") layers (Fig. 4.2). The pSi layer was removed from the silicon substrate by application of a current pulse of 4 mA cm^{-2} for 250 s in a solution containing 1:20 (*v:v*) aqueous HF:absolute ethanol (lift-off step). The freestanding films (≈63 mg) were fractured by ultrasound in deionized water (DI H_2O, 6 mL) for 48 h and aged for 24 h at room temperature (25 °C). The resulting surface-oxidized porous Si-SiO_2 frame-sheath nanoparticles were filtered twice through a syringe filter (first through

Millipore, Millex syringe filter unit, 220 nm model #SLGP033RS, then a 100 nm model #SLVV033RS) and used without further purification. The concentration of the resulting pSiNP solution was ≈10 mg mL^{-1} in DI H_2O (5 mL), yield: 80%. The duration of ultrasonication used in the above description was determined by a systematic optimization study, where nanoparticle size was analyzed as a function of time (12–60 h) of ultrasonication. The average size and size distributions were monitored by DLS and confirmed by transmission electron microscopy (TEM). The nanoparticle size became smaller over time, and the 48 h ultrasonication time was found to yield particles with average hydrodynamic diameters of ≈60 nm.

Preparation of pSiNPs (230 nm Size): The preparation followed a similar procedure as for the 60-nm formulation described in the main text, except the perforation etching waveform consisted of a current density pulse of 50 mA cm^{-2} of 1.818 sec duration, followed by a current density pulse of 400 mA cm^{-2} of 0.363 sec duration, and the waveform was repeated for only 150 cycles. The multilayered porous Si film (~60 mg) was removed from the substrate and fractured into nanoparticles as described above, except the ultrasonic fracture was performed for 20 hr, and the resulting nanoparticles were allowed to oxidize in this aqueous phase for 6 weeks at room temperature (25 °C). The resulting nanoparticles were collected by centrifugation (15,000 rpm, 15 min) and washed 3 times with ethanol.[2]

Calculation of nanostructure crystallite size: The average crystallite size for the Si domains in the pSiNPs was calculated using the powder x-ray diffraction (XRD) data of Fig. 4.4 and the Debye-Scherrer formula; $D_p=0.94\lambda/(\beta\cos\theta)$ where D_p=average crystallite size, β=line broadening (FWHM) in radians, θ=Bragg angle, and λ=X-ray wavelength

(1.5418 Å). Each number (β, θ) was derived using the XRD analysis program JADE (Materials Data, Inc.).

Time-gated photoluminescence study of pSiNPs: A custom-built time-domain imaging system was used to acquire photoluminescence decay and time-gated images. A LED source (λ_{exc}=365 nm, Ocean Optics) was used as the excitation source at a repetition rate of 10 Hz, which was externally synchronized and triggered with a function generator (Keithley3390, 50 MHz arbitrary waveform generator). Time-resolved images and spectral data were obtained with an intensified CCD camera (iSTAR 334T, Andor Technology Ltd.). Andor SOLIS software was used to program delays and timing pulses and to analyze images including signal-to-noise (SNR).[3] SNR was calculated using the equation: $SNR=(Mean_{signal}-Mean_{background})/Mean_{background}$, where $Mean_{signal}$ is the average intensity measured during the relevant excitation window and $Mean_{background}$ is the average intensity with excitation off. For *in vitro* comparison images, aliquots (in DI H_2O) of pSiNPs (60-nm size, 1 mg mL^{-1}), pSiNPs (230-nm size, 1 mg mL^{-1}), rhodamine 6G (1 μM), and iminobenzo[*g*]coumarin (1 μM) were placed in separate cuvettes next to each other and imaged simultaneously. To obtain time-gated images, fixed time delays (1 μs or 5 μs after termination of the excitation pulse) were used and emission signals were acquired for a subsequent 150 μs. The signals (sample, background) were accumulated 10 times during 3 s. To obtain spectral decay curves, initial (steady-state) intensity (I_0) was determined during 30 μs prior to shutting off the LED source. The PL intensity (I) was then measured for a duration of 30 μs at the relevant time post-excitation. The source off-data acquisition delay was then incremented by 10 μs for a total of 500 μs. A value of $T_{1/2}$ (effective τ) was calculated by determining the time at which the area under the decay curve was half of the

total area. Time-resolved photoluminescence decay curves were then generated by plotting I/I_0 in 10 μs steps, for each respective wavelength, over the total 500 μs PL lifetime decay.[49,50]

Two-photon microscope setup and data processing: A custom-built two-photon microscope with a wavelength-tunable Ti-Sapphire laser (Chameleon Ultra II, Coherent) at 140 fs pulse width and 80 MHz pulse repetition rate and conventional upright-microscope body (BX51, Olympus, Japan) was used.[51] XY-raster scanning was achieved using X-Y galvanometric scanners (6215H, Cambridge Technology, USA), and three dimensional (3D) two-photon imaging was performed using a 20× objective lens (XLUMPLFLN-20XW, 1.0 NA, water immersion, Olympus, Japan) and piezo-z objective translator (P-725.4CL, PI, Germany). Laser power was measured with a power meter (S310C, Thorlabs, Inc., USA) at the objective lens back pupil to account for beam clipping and transmittance losses. The measured power was assumed to be equal to the laser power at the focal plane in the sample. Two-photon microscope (TPM) images were acquired using photon-counting photomultiplier tubes (PMTs, H7421-40P, Hamamatsu, Japan) and processed with MATLAB software. The laser power was measured at the surface of sample using power meter (S310Cm)

Assessment of photo-stability under two-photon laser irradiation conditions: The pSiNPs (60-nm size, 1 mg mL^{-1}, 50 μL) and rhodamine 6G (1 μM, 50 μL) were loaded in single-well glass slides (CITOGLAS, Cat# 2306-0001, Citotest, China) and covered with a glass cover slip. The edges of the cover slip were coated with a transparent nail polish to prevent evaporation of solvent and the slide was mounted on a vibration isolation table. Excitation wavelength was tuned to 850 nm (4 mW laser power at focal plane) for all

samples and the emission spectra were collected in the wavelength range 560–740 nm. Two-photon intensities were acquired as a function of time for 60 min. Data were acquired and averaged from five different depths in the sample, using a z-step increment of 5 μm with a low scanning speed (0.15 frames sec^{-1}).

Grafting of PEG-iRGD to pSiNPs: The 60 nm pSiNPs were separated from the stock solution of pSiNPs prepared above by centrifugation (15 000 rpm, 15 min) using a centrifugal filter (Millipore, MRCF0R100). The as-collected pSiNP pellet (1 mg) was resuspended in ethanol (1 mL), aminopropyldimethylethoxysilane (APDMES, 20 μL) was added, and the mixture was agitated for 4 h. The aminated nanoparticles (pSiNP-NH_2) were then purified three times by centrifugation from ethanol to eliminate unbound APDMES. Then a solution (200 μL) of one of the desired heterofunctional linkers maleimide-PEG-succinimidyl valerate (MAL-PEG-SVA, MW: 5000, 5 mg mL^{-1} in ethanol) or methoxy-PEG-succinimidyl valerate (mPEG-SVA, MW: 5000, 5 mg mL^{-1} in ethanol) was added to the aminated nanoparticles (1 mg in 800 μL) and agitated for 2 h. The resulting PEGylated nanoparticles (pSiNP-PEG or pPSiNP-mPEG) were isolated and purified by centrifugation/resuspension in fresh ethanol three times. For the peptide-conjugated (targeted) formulations, iRGD peptide (sequence CRGDKGPDC, cyclized between the two cysteine residues, 100 μL, 1 mg mL^{-1} in DI H_2O) was added to 100 μL of pSiNP-PEG in ethanol, incubated at 4 °C for 4 h, purified three times by centrifugation, dispersed in PBS (pH 7.4, 100 μL), and stored at 4 °C before use.

Photoluminescence Study of pSiNPs: Nanoparticles (either the 60 nm or the 230 nm sizes) were dispersed in ethanol, and photoluminescence intensity was measured using a cooled CCD (charge coupled device) spectrometer (OceanOptics QEPro) using a 365 nm

LED (light-emitting diode) light source, a 370 ± 20 nm bandpass filter for excitation, and a 510 nm longpass emission filter. The integrated photoluminescence intensity was obtained in the wavelength range 500–980 nm. Plotted values represent average values (n = 4) with error bars representing 1 standard deviation. For the experiments where PL intensity of pSiNPs was monitored as a function of time during aqueous dissolution, particles were dispersed in PBS (pH 7.4, 0.5 mg mL^{-1}) and incubated at 37 °C. The PL intensity was measured at each time point, and particles were transferred to fresh PBS using centrifugation (15 000 rpm, 15 min) through a centrifugal filter (Millipore, MRCF0R100).

Measurement of Two-Photon Cross-Sections of pSiNPs: The two-photon cross-section (δ) was determined using the femtosecond fluorescence measurement technique. Nanoparticles were dispersed in DI H_2O and the two-photon-induced luminescence intensity was measured against a rhodamine 6G standard (QY = 0.95). 100 μL (1 mg mL^{-1}) of each sample was loaded in single-well glass slides (CITOGLAS, Cat# 2306-0001, Citotest, China) and covered with a glass cover slip. The edges of the cover slip were coated with a transparent nail polish to prevent evaporation of solvent before mounting the slide on the vibration isolation table. The intensities of the two-photon-induced luminescence spectra of the reference and of pSiNPs were measured under the same excitation conditions. The two-photon cross-sections were calculated using the relationship $\delta_s = \delta_r(S_s\Phi_r n_r c_r)/(S_r\Phi_s n_s c_s)$, where the subscripts s and r stand for the sample and reference molecules, respectively; S is the integrated fluorescence intensity at focal plane; Φ is the fluorescence quantum yield; n is the overall fluorescence collection efficiency of the experimental apparatus; c is the number density of the molecules in solution, based on a mass estimation; and δ_r is the two-photon cross-section of the reference sample. The two-

photon absorption cross-section (TPACS, GM) was calculated using the relationship GM= $\delta_{max}\Phi$; where Φ is the fluorescence quantum yield of the nanoparticles.[38,39,47]

Cell preparation and cellular TPM imaging: Roswell Park Memorial Institute (RPMI) medium, fetal bovine serum (FBS), penicillin-streptomycin (PS), phosphate buffered saline (PBS), and trypsin-EDTA were purchased from Hyclone (GE Healthcare Life Sciences, USA). HeLa human cervical cancer cells were obtained from the Korean Cell Line Bank. HeLa cells were maintained in RPMI, supplemented with 10% (*v/v*) FBS and 1% (*w/v*) PS at 37 °C in a humidified atmosphere of 5% CO_2 in air. Cells were passaged when they reached approximately 80% confluence. Cells were separately seeded onto four cell culture dishes at a density of 1×10^5 cells and incubated overnight at 37 °C under 5% CO_2. Four groups of HeLa cells were prepared and treated with a given nanoparticle formulation (20 μg per well) or PBS for 30 min. Following incubation, the cells were washed three times with phosphate-buffered saline (PBS) and fixed with 4% paraformaldehyde (PFA) for 10 min. The TPM images were obtained using an excitation wavelength of 850 nm with 10 mW laser power (measured at the the objective lens back pupil to account for transmittance losses), and the PL intensity was collected in the wavelength range 560–740 nm. 3D volumetric scanning was performed at a scanning speed of 0.04 frames sec^{-1}, and a stepwise increment of 1 μm in the *z*-direction. PL intensities were quantified using the representative plane image showing cell adhesion to the culture dish.

Animal preparation and ethical conduct of research: Animal models were bred at the animal facility in the POSTECH Biotech Center under specific pathogen-free (SPF) conditions and they had access to food and water *ad libitum*. All animal experimental

procedures were conducted in accordance with institutional guidelines and regulations and approved by the Institutional Animal Care & Use Committee at POSTECH (IACUC, approval number POSTECH-2015-0030-C1).

Preparation of Mouse Xenograft Tumor Model and In Vivo TPM Imaging: All animal experimental procedures were conducted in accordance with institutional guidelines and regulations and approved by the Institutional Animal Care & Use Committee at POSTECH (approval number POSTECH-2015-0030-C1). Hairless mice (SKH1-HrHr, 6 weeks, female) were anesthetized via inhalation of a gas mixture of 1.5% *v/v* isoflurane (Terrell, Piramal, USA) and medical grade oxygen, and then HeLa cells (5×10^6 cells) were subcutaneously (SC) injected at the right side of the hind limb (dermis layer). TPM imaging was performed 10 d after SC injection of the HeLa cells; tumor growth sufficient for the experiment was confirmed by naked eye and by OCT. The prepared mouse was placed on a custom-made hind limb holder, which was configured to maintain constant temperature and to provide positioning via a motorized *X–Y* translational stage. The 60 nm size pSiNP-iRGD formulation (20 mg kg^{-1}) was intravenously injected via tail vein. *In vivo* TPM images were obtained with 850 nm excitation (50 mW laser power), and PL intensity was quantified in the wavelength range 560–740nm. 3D volumetric scanning was performed at 0.4 frames per second and a stepwise increment of 3 μm in the *z*-direction. For the control experiment, TPM imaging was performed under the same experimental conditions after intravenous tail-vein injection of PBS (200 μL) instead of pSiNPs. Time-lapse images were acquired for 60 min with a time interval of 6 min under constant experimental conditions.

Tissue preparation and ex vivo OPM/TPM imaging: Hairless mice (SKH1-Hr^{Hr}, 6

weeks, female) were anesthetized via inhalation of a gas mixture of 1.5% *v/v* isoflurane (Terrell™, Piramal, USA) and medical grade oxygen, and then sacrificed by cervical dislocation. Main organs (brain, kidney, lung, spleen, and liver) were dissected from the mice (n=4) after perfusion to eliminate blood from the tissues. The prepared tissue samples were dipped into a solution of the pSiNPs (60-nm size, 10 mg mL^{-1} in DI H_2O) at 37 °C for 60 min and then washed three times with phosphate-buffered saline (PBS) prior to mounting on glass slides. One-photon confocal scanning laser microscopy (CSLM) and two-photon microscopy (TPM) imaging was performed in the same tissue regions, using a stepwise *z*-direction increment of 3 μm. Excitation wavelength was tuned to 488 nm and 850 nm for CLSM and TPM images, respectively, using similar excitation laser powers (50 mW at the focal plane) and scanning speed of 0.4 frames sec^{-1}. PL intensity was quantified in the wavelength range 560–740 nm.

Optical coherence tomography (OCT) setup, data processing, and in vivo imaging: A custom-built optical coherence tomography (OCT) setup, described previously, was used.[52] A wavelength-swept light source (SSOCT-1310, AXSUN Technologies), having a center wavelength at 1310 nm (107 nm bandwidth) with 50 kHz sweeping speed was used. The imaging depth range was 6 mm in air. Light from the source was split into a 95:5 ratio; 95% of light toward the interferometry setup, 5% toward a fiber Bragg grating (FBG) to generate an external trigger signal for data acquisition. In the interferometer, light was split into the sample and reference arms with 80:20 couplers (FiberAll, Korea). In the sample arm, light was collimated to 1.8 mm in diameter with a fiber collimator (HPUCO-13A-1300/1550-S-11AS, OZ optics), and passed through a 2D galvanometric scanner (GVS012, Thorlabs, Inc., USA) and an objective lens (LSM03, Thorlabs, Inc., USA), then

focused at the sample. The detecting window was slanted at 8° to avoid strong specular reflection. Reflected light from the sample and reference arms were combined and detected with two balanced photodetectors (PDB410C, Thorlabs, Inc., USA) in a polarization dispersed detection setup. Signals from the detectors were digitized with a two-channel data acquisition board (Alazartech, Inc., Canada) after passing through low pass filters (81 MHz cut-off frequency, Mini-circuits). The resulting data were post-processed to obtain both OCT intensity and angiographic images. OCT intensity images were obtained in 3D by acquiring multiple cross-sectional images in the y-z plane with a stepwise increment in the x-direction. Angiographic OCT images were obtained using a complex differential variance algorithm.[53,54] The differential variance of the complex data in 10 sequential images was calculated at each y-position. The signal-to-noise ratio of the system was 103.2 dB and the frame rate was 100 frames sec^{-1}. *In vivo* OCT imaging of the xenograft tumor-bearing mouse (hind limb region) was performed with 5 × 5 × 2.25 mm field-of-view in the x-, y-, and z-direction, respectively. The anesthetized mouse test subject was placed on a custom-made heating plate to maintain body temperature, and the tumor region of the hind limb was immobilized using a custom-made clamp (see *in vivo* TPM imaging section). *In vivo* OCT images were collected in the y-z direction.

In vivo two-photon induced PL intensity analysis of pSiNPs compared to rhodamine 6G: pSiNPs (100 μL, 0.4 mg mL^{-1}) and rhodamine 6G (100 μL, 0.4 μM) were subcutaneously (SC) injected into the hind limb of the mouse, adjacent to the tumor, and immediately imaged in the dermis (up to 250 μm depth from the surface). Two-photon imaging was performed using 850 nm excitation wavelength, with 50 mW laser power. 3D volumetric scanning was conducted at a scanning speed of 0.04 frames sec^{-1}, and a stepwise

increment of 5 μm in the *z*- direction. TPM images were spectrally resolved into 2 channels (400–430 nm; blue, 560–740 nm; red), the PL intensity was analyzed in the red channel (560–740 nm). PL intensities were quantified by using the averaged pixel intensities in the X-Y plane images showing cell adhesion along the *z*-direction in the dermis. The experiment was replicated in a second mouse and gave similar results.

Determination of biodistribution of in vivo-administered pSiNP-iRGD by TPM: After acquisition of the *in vivo* TPM images, mice were anesthetized *via* inhalation of a gas mixture of 1.5% *v/v* isoflurane (Terrell™, Piramal, USA) and medical grade oxygen, and sacrificed by cervical dislocation. The main organs (brain, kidney, lung, spleen, and liver) and tumor (hind limb) were dissected from the mice (n=4) after perfusion to eliminate blood from the organs. Dissected organs were washed three times with phosphate-buffered saline (PBS) and individually mounted on a slide glass. The experimental conditions were the same as with the *ex vivo* TPM imaging experiments described above.

Histological examination of tissue samples: The fixed tissues were cryo-protected in 30% DNase & RNase-free sucrose (Sigma, MO, US) until they were wholly submerged. The tissues were then carefully molded with OCT compound (Optimal Cutting Temperature compound: 10% *w/w* polyvinyl alcohol, 25% *w/w* polyethylene glycol, and 85.5% *w/w* inactive species; Leica, Wetzlar, Germany), and placed on dry ice to freeze the OCT compound. The frozen tissue block was adhered to the sample holder of a cryotome cryostat (Leica, model# CM3000, Wetzlar, Germany), and maintained at -28 °C until the temperature of the frozen tissue block equilibrated with the temperature of the cryostat. Tissue sections of 18 μm thickness (30 μm for tumor) were prepared using a high profile microtome blade in the cryostat. The sections were transferred to gelatin-coated slides

(Marienfeld, Lauda-Königshofen, Germany) and stored at -80 °C. Prepared slides were dried for 30 minutes in air at room temperature (25 °C), followed by hydration in deionized water (DI H_2O) for 20 min. The slides were again transferred to fresh DI H_2O and incubated for 10 minutes for better permeability of the staining reagents. The tissue sections were then stained in Hematoxylin solution (Sigma, Lot# MHS1 SIGMA, USA) for 15 min, and rinsed several times using tap water. After checking for a faint blue color, the sections were stained with Eosin (Sigma, Lot# R03040, USA) for 30 sec, and then rinsed using a mixture of ethanol (Merck, USA) and water (ethanol:DI H_2O = 7:3 by volume), then pure ethanol, sequentially. The slide was dipped into xylene (Duksan, Ansan, Korea) for 10 sec twice to remove water, and 3 drops of histomount (National Diagnostics, GA, USA) were added to the surface of the tissue sample. The resulting slides were dried for 1 day in air at room temperature (25 °C). H&E staining images were obtained using an optical microscope (BH-2, Olympus, Tokyo, Japan).

4.6. References

[1] Y. Yang, Q. Zhao, W. Feng, F. Li, *Chem Rev* **2013,** *113,* 192.

[2] K. P. Carter, A. M. Young, A. E. Palmer, *Chem Rev* **2014,** *114,* 4564.

[3] H. Xiang, J. Cheng, X. Ma, X. Zhou, J. J. Chruma, *Chem Soc Rev* **2013,** *42,* 6128.

[4] E. A. Owens, M. Henary, G. El Fakhri, H. S. Choi, *Acc Chem Res* **2016,** *49,* 1731.

[5] J. V. Jokerst, S. S. Gambhir, *Acc Chem Res* **2011,** *44,* 1050.

[6] P. Zrazhevskiy, M. Sena, X. Gao, *Chem Soc Rev* **2010,** *39,* 4326.

[7] W. R. Zipfel, R. M. Williams, R. Christie, A. Y. Nikitin, B. T. Hyman, W. W. Webb, *Proc Nat Acad Sci USA* **2003,** *100,* 7075.

[8] S. Huang, A. A. Heikal, W. W. Webb, *Biophys J* **2002,** *82,* 2811.

[9] W. R. Zipfel, R. M. Williams, W. W. Webb, *Nat Biotechnol* **2003,** *21,* 1369.

[10] C. Xu, W. Zipfel, J. B. Shear, R. M. Williams, W. W. Webb, *Proc Nat Acad Sci USA* **1996,** *93,* 10763.

[11] K. W. Dunn, T. A. Sutton, *ILAR J* **2008,** *49,* 66.

[12] J. H. Yu, S.-H. Kwon, Z. Petrášek, O. K. Park, S. W. Jun, K. Shin, M. Choi, Y. I. Park, K. Park, H. B. Na, N. Lee, D. W. Lee, J. H. Kim, P. Schwille, T. Hyeon, *Nat Mater* **2013,** *12,* 359.

[13] X. Gao, Y. Cui, R. M. Levenson, L. W. K. Chung, S. Nie, *Nat Biotechnol* **2004,** *22,* 969.

[14] H. Wang, T. B. Huff, D. A. Zweifel, W. He, P. S. Low, A. Wei, J.-X. Cheng, *Proc Nat Acad Sci USA* **2005,** *102,* 15752.

[15] J. Kim, Y. Piao, T. Hyeon, *Chem Soc Rev* **2009,** *38,* 372.

[16] A. Fu, W. Gu, C. Larabell, A. P. Alivisatos, *Curr Opin Neurobiol* **2005,** *15,* 568.

[17] D. R. Larson, W. R. Zipfel, R. M. Williams, S. W. Clark, M. P. Bruchez, F. W. Wise, W. W. Webb, *Science* **2003,** *300,* 1434.

[18] G. D. Scholes, G. Rumbles, Nature Materials 2006, 5, 683.

[19] K. T. Yong, W. C. Law, R. Hu, L. Ye, L. W. Liu, M. T. Swihart, P. N. Prasad, *Chem Soc Rev* **2013,** *42,* 1236.

[20] A. M. Derfus, W. C. W. Chan, S. N. Bhatia, *Nano Lett* **2004,** *4,* 11.

[21] H. S. Choi, J. V. Frangioni, *Mol Imaging* **2010,** *9,* 291.

[22] J. R. Henstock, L. T. Canham, S. I. Anderson, *Acta biomater* **2015,** *11,* 17.

[23] E. Tasciotti, X. W. Liu, R. Bhavane, K. Plant, A. D. Leonard, B. K. Price, M. M. C. Cheng, P. Decuzzi, J. M. Tour, F. Robertson, M. Ferrari, *Nat Nanotechnol* **2008,** *3,* 151.

[24] L. Canham, in *Handbook of Porous Silicon* (Ed: L. Canham), Springer International Publishing, Switzerland, **2014**, p. 909.

[25] J. Salonen, in *Handbook of Porous Silicon* (Ed.: L. Canham), Springer International Publishing, Switzerland, **2014**, p. 909.

[26] C. M. IHessel, E. J. Henderson, J. G. C. Veinot, *Chem Mater* **2006,** *18,* 6139.

[27] M. B. Gongalsky, L. A. Osminkina, A. Pereira, A. A. Manankov, A. A. Fedorenko, A. N. Vasiliev, V. V. Solovyev, A. A. Kudryavtsev, M. Sentis, A. V. Kabashin, V. Y. Timoshenko, *Sci Rep* **2016,** *6,* 24732.

[28] C. M. Hessel, D. Reid, M. G. Panthani, M. R. Rasch, B. W. Goodfellow, J. W. Wei, H. Fujii, V. Akhavan, B. A. Korgel, *Chem Mater* **2012,** *24,* 393.

[29] X. G. Li, Y. Q. He, S. S. Talukdar, M. T. Swihart, *Langmuir* **2003,** *19,* 8490.

[30] J.-H. Park, L. Gu, G. von Maltzahn, E. Ruoslahti, S. N. Bhatia, M. J. Sailor, *Nat Mater* **2009,** *8,* 331.

[31] G. S. He, Q. D. Zheng, K. T. Yong, F. Erogbogbo, M. T. Swihart, P. N. Prasad, *Nano Lett* **2008,** *8,* 2688.

[32] X. S. Xu, S. Yokoyama, *Appl Phys Lett* **2011,** *99,* 251105.

[33] M. Nayfeh, O. Akcakir, J. Therrien, Z. Yamani, N. Barry, W. Yu, E. Gratton, *Appl Phys Lett* **1999,** *75*, 4112.

[34] Z. T. Qin, J. Joo, L. Gu, M. J. Sailor, *Part Part Syst Charact* **2014,** *31*, 252.

[35] S. Ilya, V. Jan, L. Jan, *Nanotechnology* **2017,** *28,* 072002.

[36] A. Sa'ar, *J Nanophotonics* **2009,** *3,* 032501.

[37] P. E. Hänninen, M. Schrader, E. Soini, S. W. Hell, *Bioimaging* **1995,** *3,* 70.

[38] A. Fischer, C. Cremer, E. H. K. Stelzer, *Appl Opt* **1995,** *34,* 1989.

[39] N. S. Makarov, M. Drobizhev, A. Rebane, *Opt Express* **2008,** *16,* 4029.

[40] K. N. Sugahara, T. Teesalu, P. P. Karmali, V. R. Kotamraju, L. Agemy, D. R. Greenwald, E. Ruoslahti, *Science* **2010,** *328,* 1031.

[41] J. Joo, X. Liu, V. R. Kotamraju, E. Ruoslahti, Y. Nam, M. J. Sailor, *ACS Nano* **2015,** *9,* 6233.

[42] T. E. de Carlo, A. Romano, N. K. Waheed, J. S. Duker, *Int J Retina Vitreous* **2015,** *1,* 5.

[43] B. Kim, T. J. Wang, Q. Li, J. Nam, S. Hwang, E. Chung, S. Kim, K. H. Kim, *J Biomed Opt* **2013,** *18,* 080502.

[44] X. Chen, O. Nadiarynkh, S. Plotnikov, P. J. Campagnola, *Nat Protoc* **2012,** *7,* 654.

[45] J. Kang, J. Joo, E. J. Kwon, M. Skalak, S. Hussain, Z.-G. She, E. Ruoslahti, S. N. Bhatia, M. J. Sailor, *Adv Mater* **2016,** *28,* 7962.

[46] A. P. Mann, P. Scodeller, S. Hussain, J. Joo, E. Kwon, G. B. Braun, T. Molder, Z.-G. She, V. R. Kotamraju, B. Ranscht, S. Krajewski, T. Teesalu, S. Bhatia, M. J. Sailor, E. Ruoslahti, *Nat Commun* **2016,** *7,* 11980.

[47] C. S. Lim, H. J. Kim, J. H. Lee, Y. S. Tian, C. H. Kim, H. M. Kim, T. Joo, B. R. Cho, *ChemBioChem* **2011,** *12,* 392.

[48] D. Kim, S. Sambasivan, H. Nam, K. H. Kim, J. Y. Kim, T. Joo, K. H. Lee, K. T. Kim, K. H. Ahn, *Chem Commun* **2012,** *48,* 6833.

[49] D. L. Fisher, J. Harper, M. J. Sailor, *J Am Chem Soc* **1995,** *117,* 7846.

[50] J. H. Song, M. J. Sailor, *J Am Chem Soc* **1997,** *119,* 7381.

[51] B. Jeong, B. Lee, M. S. Jang, H. Nam, S. J. Yoon, T. Wang, J. Doh, B. G. Yang, M. H. Jang, K. H. Kim, *Opt Express* **2011,** *19,* 13089.

[52] Y. Yoon, Q. Y. Li, V. H. Le, W. H. Jang, T. J. Wang, B. Kim, S. Son, W. K. Chung, C. Joo, K. H. Kim, *Opt Express* **2015,** *23,* 12874.

[53] A. S. Nam, I. Chico-Calero, B. J. Vakoc, *Biomed Opt Express* **2014,** *5,* 3822.

[54] B. Kim, S. H. Lee, C. J. Yoon, Y. S. Gho, G. O. Ahn, K. H. Kim, *Biomed Opt Express* **2015,** *6,* 2512.

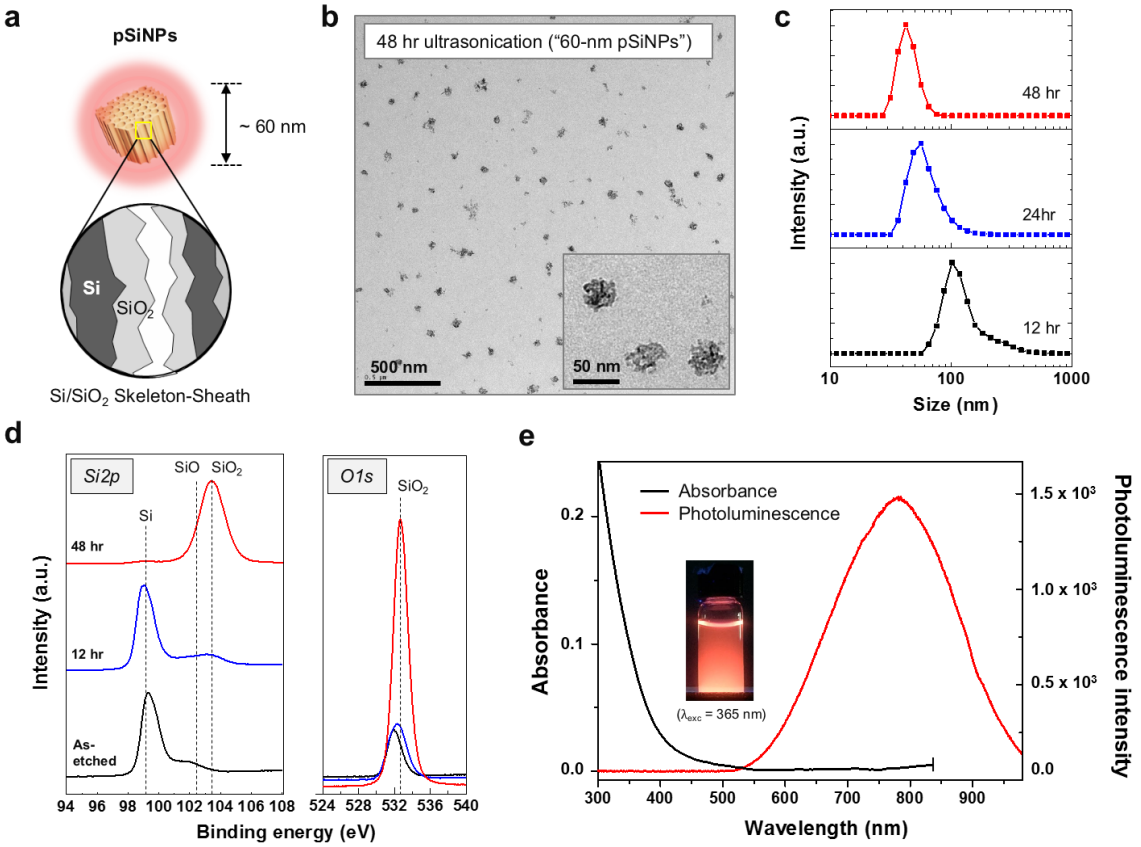

Figure 4.1. Preparation and characterization of 60 nm pSiNPs. a) Schematic illustration of the skeleton-sheath Si-SiO_2 structure of the porous silicon nanoparticles used in this study. b) Transmission electron microscope (TEM) images of the pSiNPs. These particles were prepared by ultrasonication in deionized water for 48 h. c) Mean hydrodynamic diameter (intensity distribution) of nanoparticles that were ultrasonicated for the indicated time periods, measured by dynamic light scattering (DLS). Particles were isolated at the indicated time points, rinsed, and redispersed in deionized water (DI H_2O) for the measurement. d) X-ray photoelectron spectra (XPS) in the Si2p and O1s regions of nanoparticles that were ultrasonicated for the indicated time periods. "As-etched" refers to the as-etched pSi film, prior to ultrasonication. Assignments: SiO/SiO_2 at 102–104 eV (Si2p) and 532.5 eV (O1s). e) Absorbance and photoluminescence emission spectra of the 60 nm pSiNP formulation. Photoluminescence measured in ethanol using ultraviolet excitation (λ_{ex} = 365 nm). The inset photograph obtained under UV illumination (365 nm).

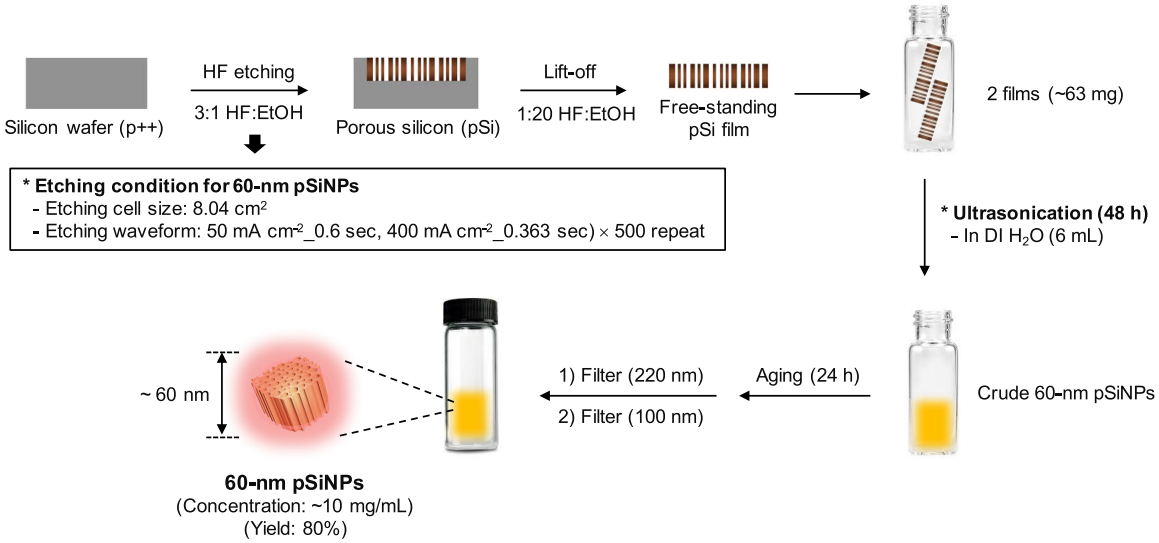

Figure 4.2. Schematic illustration of pSiNP preparation. The detailed procedure is described in the Experimental section.

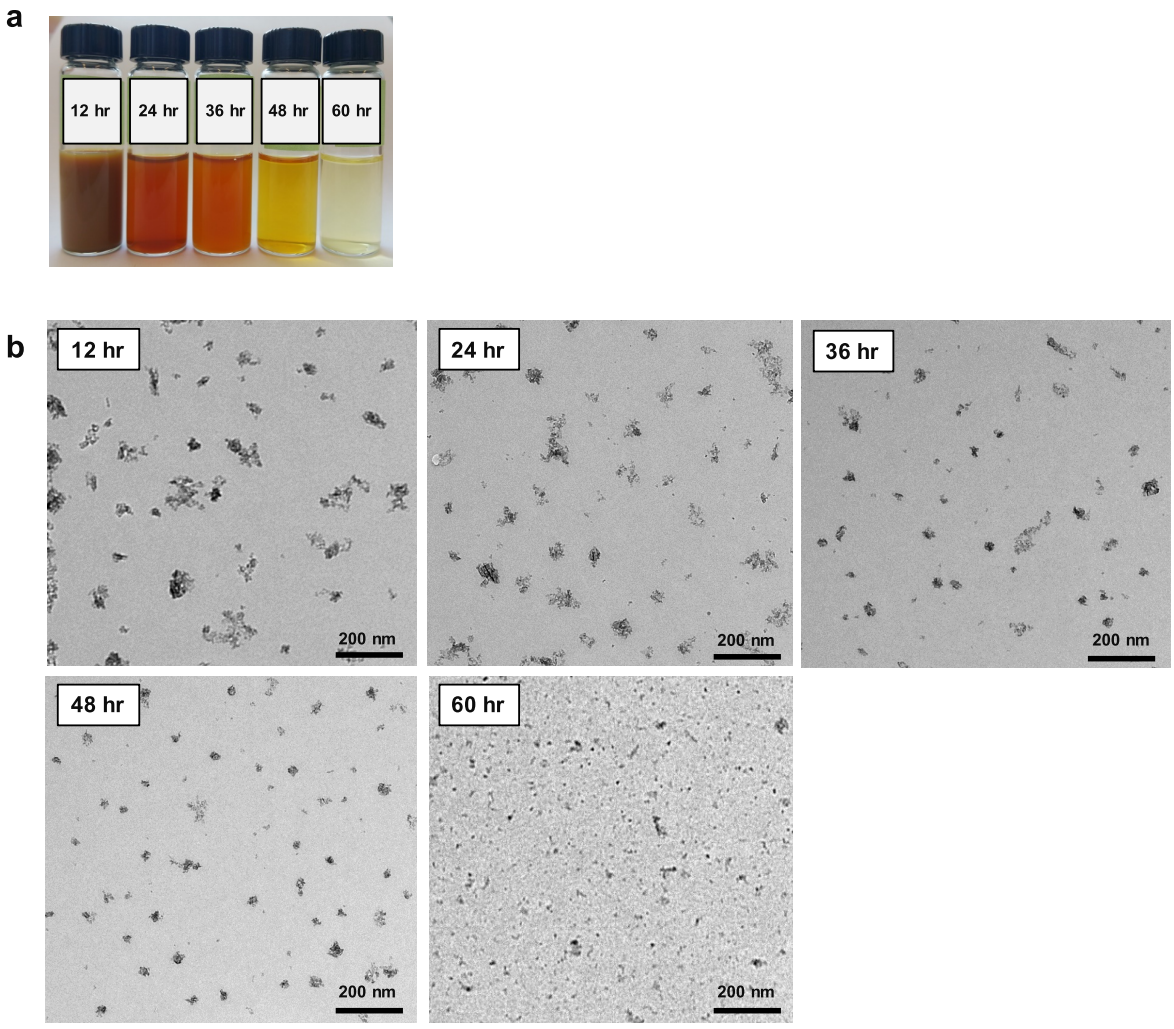

Figure 4.3. Characterization of nanoparticles subjected to ultrasonic fracture conditions for the indicated times. (a) bright field image of vials after ultrasonication for the indicated times. Volume of DI H_2O is 6 mL. (b) Transmission electron microscope (TEM) images of nanoparticles isolated after ultrasonication for the indicated times.

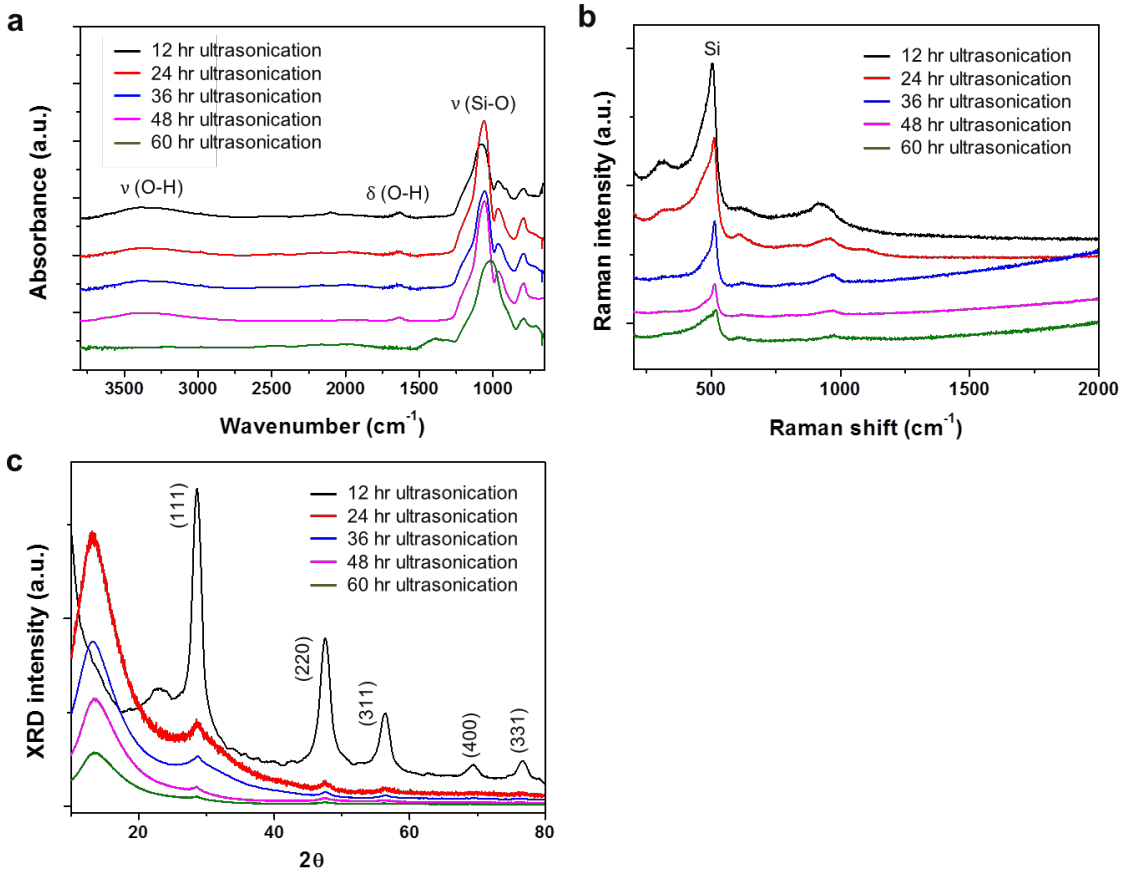

Figure 4.4. Spectroscopic characterization of nanoparticles subjected to ultrasonic fracture conditions for the indicated times. (a) Attenuated total reflectance Fourier-transform infrared (ATR-FTIR) spectra. Assignments of stretching modes (O-H and Si-O) and bending modes (O-H) are as indicated. Symbols: υ=stretching, δ=bending. (b) Raman spectra. Si lattice mode at ~510 cm^{-1}. (c) Powder X-ray diffraction (XRD) spectra. Miller indices (*h k l*) of the relevant crystalline Si reflections are indicated. The nanoparticles were isolated at the indicated time points by centrifugation (15,000 rpm, 15 min) using centrifugal filter units (Millipore, MRCF0R100), and the resulting particles were rinsed with ethanol three times. Prior to the measurements, the nanoparticles were fully dried in vacuum for 2 days.

Table 4.1. Hydrodynamic size and zeta-potential of 60-nm and 230-nm pSiNP preparations. The hydrodynamic size and zeta-potential were measured in deionized H_2O by dynamic light scattering (DLS). Various conditions are shown. Those highlighted in green indicate the conditions used to prepare the "60-nm" and "230-nm" pSiNP formulations used in this work. The standard deviations are calculated from 3 replicate measurements. Polydispersity index (PDI) values: < 0.3.

Etching condition	Ultrasonication time (hr)	Size (nm)	Zeta-potential (mV)
50 mA cm^{-2}_0.6 sec, 400 mA cm^{-2}_0.363 sec	12	218 ± 10	-24.4 ± 4.7
* 500 repeats (*pSiNPs, 60 nm*)	24	99 ± 13	-30.3 ± 4.2
	36	81 ± 10	-36.8 ± 6.7
	48	63 ± 6	-37.4 ± 3.8
	60	23 ± 8	-43.8 ± 6.2
50 mA cm^{-2}_1.8 sec, 400 mA cm^{-2}_0.363 sec	24	230 ± 10	-27.6 ± 3.4
* 150 repeats (*pSiNPs, 230 nm*)	48	123 ± 13	-45.5 ± 5.5

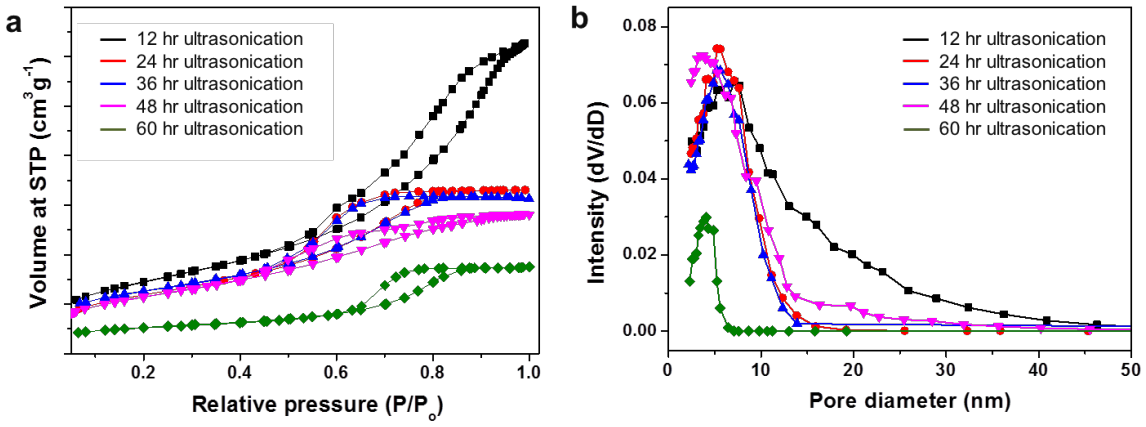

Figure 4.5. Nitrogen adsorption measurements of nanoparticles subjected to ultrasonic fracture conditions for the indicated times. (a) Isothermal curves. (b) Pore size distribution. The nanoparticles were isolated at the indicated time points using centrifugation (15,000 rpm, 15 min) with centrifugal filter units (Millipore, MRCF0R100), and the resulting particles were rinsed with ethanol three times. Prior to the nitrogen adsorption experiment, the nanoparticles were degassed under vacuum overnight.

Table 4.2. Nitrogen adsorption analysis of 60-nm and 230-nm pSiNP preparations. BJH pore size represents average pore diameter. Samples were degassed under vacuum overnight prior to the nitrogen adsorption experiment. Various conditions are shown. Those highlighted in green indicate the conditions used to prepare the "60-nm" and "230-nm" pSiNP formulations used in this work.

Etching condition	Ultrasonication time (hr)	BET surface Area (m^2g^{-1})	BJH pore volume (cm^3g^{-1})	BJH pore size (nm)
50 mA cm^{-2}_0.6 sec, 400 mA cm^{-2}_0.363 sec * 500 repeats (*pSiNPs, 60 nm*)	12	534	0.96	17.52
	24	433	0.49	5.79
	36	457	0.49	5.11
	48	532	0.53	5.08
	60	189	0.25	2.93
50 mA cm^{-2}_1.8 sec, 400 mA cm^{-2}_0.363 sec * 150 repeats (*pSiNPs, 230 nm*)	24	500	2.21	19.46
	48	469	0.46	5.94

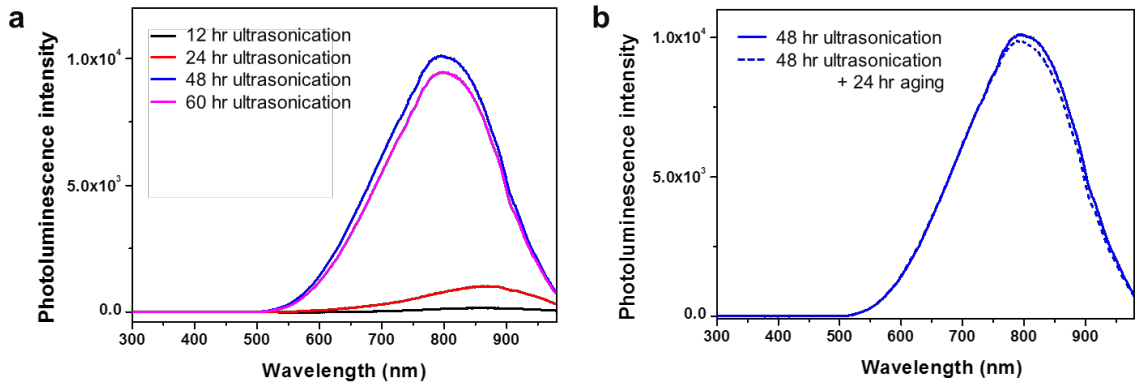

Figure 4.6. Steady-state photoluminescence spectra of nanoparticles subjected to ultrasonic fracture conditions for the indicated times. (a) Photoluminescence (PL) emission spectra (λ_{ex} =365 nm). The nanoparticles were isolated at the indicated time points by centrifugation (15,000 rpm, 15 min) with centrifugal filter units (Millipore, MRCF0R100), and the resulting particles were rinsed with ethanol three times. The PL spectra were measured from cuvettes containing the nanoparticle samples dispersed in ethanol. (b) PL emission spectra of sample after 48 hr ultrasonication, compared to an equivalent sample that was subsequently subjected to 24 hr aging at 25 °C.

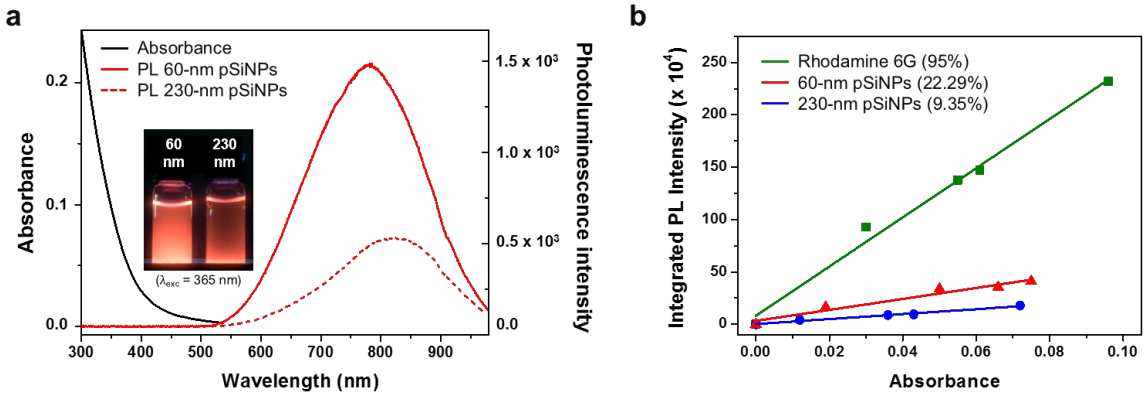

Figure 4.7. Comparison of photoluminescence (PL) efficiency of the two pSiNP types used in this study (nominal sizes 60 nm and 230 nm). (a) Absorbance and PL emission spectra of pSiNPs (size: 60 nm) and pSiNPs (size: 230 nm). Spectra were measured on nanoparticles dispersed in ethanol and excited with ultraviolet illumination (λ_{ex}=365 nm). Inset photo was obtained with UV illumination (365 nm). The sample preparation conditions are given in the Experimental section. (b) Integrated PL intensity as a function of optical absorbance (λ_{abs}=365 nm), used to calculate quantum yield of the 60-nm and the 230-nm pSiNPs, relative to rhodamine 6G standard. Integrated PL represents the integration of the PL intensity *vs* wavelength curve between 500 and 980 nm. PL intensity was measured using a QE-Pro (Ocean Optics) spectrometer, with UV excitation (λ_{ex}=365 nm) and using a 460 nm long-pass emission filter.

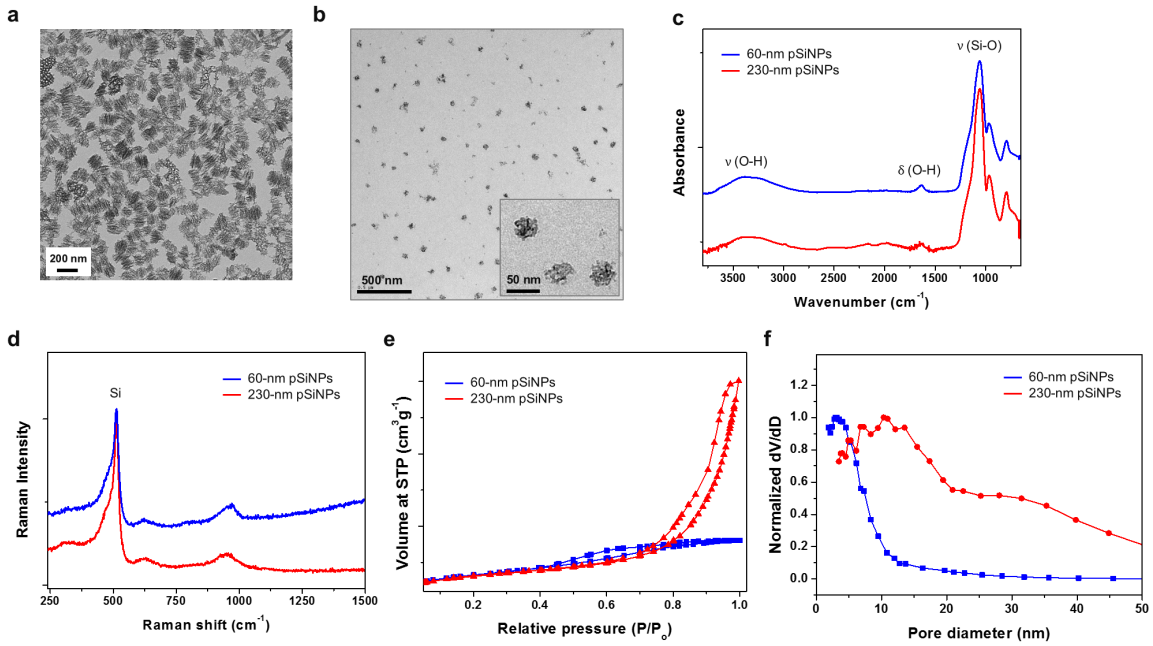

Figure 4.8. Characteristics of the two pSiNP types used in this study (nominal sizes 60 nm and 230 nm). (a) Transmission electron microscope (TEM) image of 230-nm pSiNPs. (b) Transmission electron microscope (TEM) image of 60-nm pSiNPs. (c) Attenuated total reflectance Fourier-transform infrared (ATR-FTIR) spectra comparing 230-nm and 60-nm pSiNPs. Assignments of stretching modes (O-H and Si-O) and bending modes (O-H) are as indicated. Symbols: υ=stretching, δ=bending. (d) Raman spectra comparing 230-nm and 60- nm pSiNPs. The Si lattice mode appears at ~505 cm^{-1}. Prior to the measurement of (a–d), the nanoparticles were fully dried in vacuum for 2 days. (e) Isothermal curves of 230-nm and 60- nm pSiNPs. (f) Pore size distribution 230-nm and 60-nm pSiNPs. Prior to the nitrogen adsorption experiments, the nanoparticles were degassed under vacuum overnight.

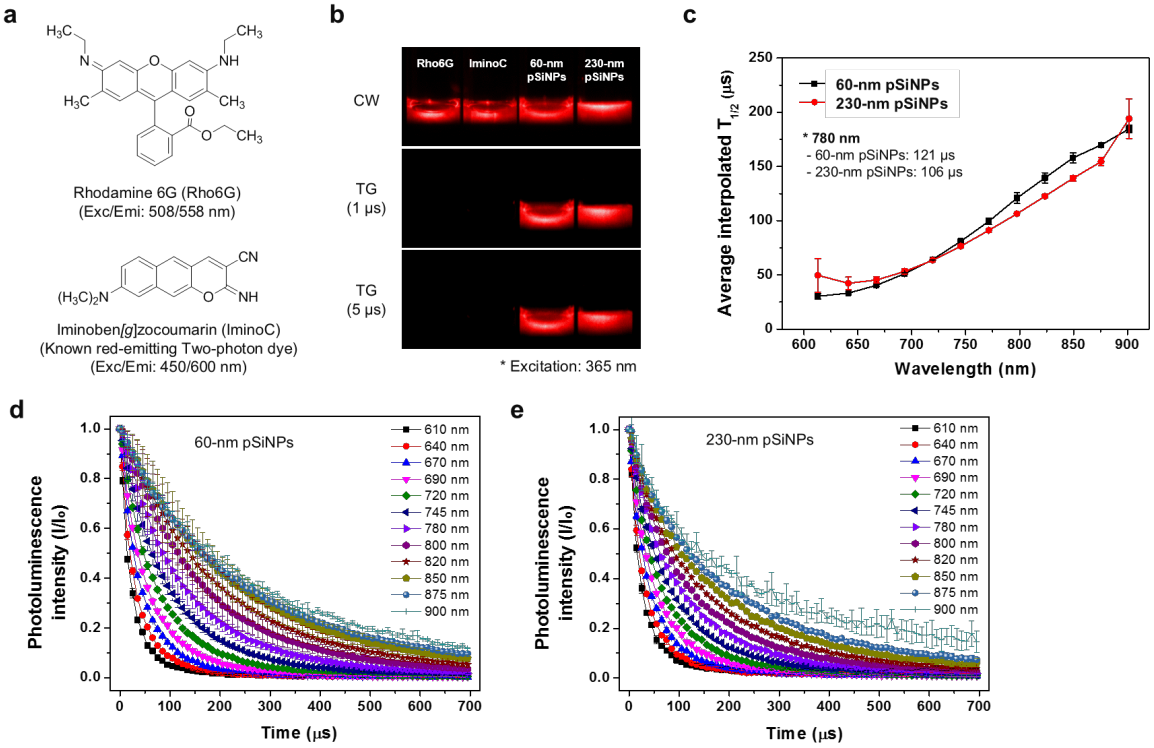

Figure 4.9. Photoluminescence emission lifetime analysis of the two pSiNP types used in this study (nominal sizes 60 nm and 230 nm). (a) Molecular structure of rhodamine 6G (Rho6G) and Iminobenzocoumarin (IminoC) standards, representing well-known red-emitting two-photon excitable dyes. (b) Photoluminescence (PL) emission images under continuous wave (CW) excitation (λ_{ex} = 365 nm) and time-gated (TG) excitation (λ_{ex} = 365 nm, 1–µs or 5–µs delays). Each sample was prepared in DI H_2O. Concentration of the molecular dyes (Rho6G and IminoC) was 10 µM. (c) Analyzed PL emission lifetimes of 230-nm and 60-nm pSiNPs. (d) PL intensity decays of 60-nm pSiNPs, measured at the indicated wavelengths (λ_{ex} = 365 nm). I_0 = initial intensity. (e) PL intensity decays of 230-nm pSiNPs, measured at the indicated wavelengths (λ_{ex} = 365 nm). The 230-nm and 60-nm pSiNPs were dispersed in DI H_2O for experiments (d) and (e).

Table 4.3. Photoluminescence lifetime signal-to-noise ratio (SNR) analysis. SNR values were analyzed in continuous wave (CW) or time-gated (TG) emission modes (see details in Experimental section). SNR values were compared with known two-photon excitable red-emitting dye standards: rhodamine 6G and iminobenzo[*g*]coumarin (see structures in Fig. 4.9). Background (baseline) signal level was considered the noise value.

	Rhodamine 6G	Iminobenzocoumarin	pSiNPs (60 nm)	pSiNPs (230 nm)
CW	1247.9	1229.0	1251.1	1453.2
TG (1 μs)	14.6	37.3	1530.3	1510.3
TG (5 μs)	8.0	21.8	946.6	920.1

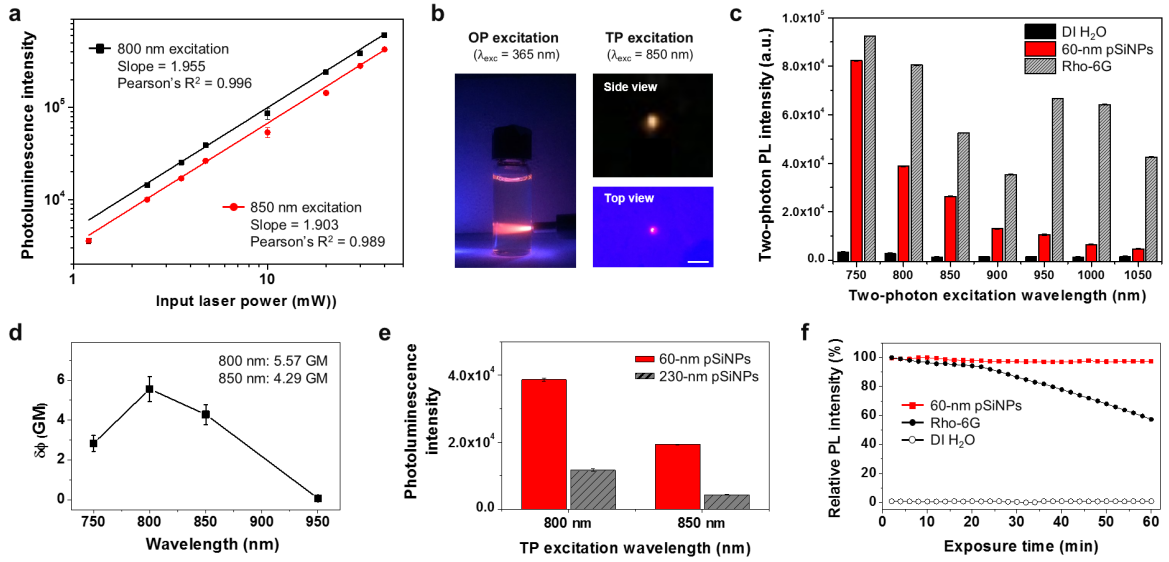

Figure 4.10. Two-photon photoluminescence characteristics of 60 nm pSiNPs. a) Log–log plot showing laser power dependence of the photoluminescence intensity from 60 nm pSiNPs dispersed in DI H_2O. The pSiNPs were cited using a Ti:sapphire laser emitting at 800 nm (black squares) or 850 nm (red circles), and photoluminescence intensity was collected in the wavelength range 560–740 nm (see the Experimental section). b) Photographs showing illumination of a dispersion of 60 nm pSiNPs in DI H_2O using one-photon excitation (λ_{ex} = 365 nm, light comes from right) and focused two-photon excitation (λ_{ex} = 850 nm, power = 100 mW). Scale bar is 1.0 mm. c) Two-photon photoluminescence intensity as a function of λ_{ex} for 60 nm pSiNPs, rhodamine 6G, and DI H_2O control. The pSiNP and rhodamine 6G samples were dissolved in DI H_2O. Samples were excited at the indicated two-photon excitation wavelength and the photoluminescence intensity was quantified in the range 560–740 nm. The same laser power (4.8 mW) was applied for each measurement. d) Two-photon absorption cross-sections (GM) of 60 nm pSiNPs in DI H_2O as a function of excitation wavelength. The error bars represent standard deviation calculated from triplicate measurements (see details in the Experimental section). e) The two-photon-induced photoluminescence intensity of 60 nm pSiNPs and 230 nm pSiNPs in DI H_2O, measured at excitation wavelengths of 800 and 850 nm, as indicated. The same laser power (4.8 mW) was applied, and the photoluminescence intensity was quantified by integration over the wavelength range 560–740 nm. Standard deviations calculated from triplicate measurements. Each sample contained the same concentration of pSiNPs (1 mg mL^{-1}) or rhodamine 6G (1 μm). f) Comparison of photostability of 60 nm pSiNPs and Rho-6G in DI H_2O under two-photon excitation conditions (λ_{ex} = 850 nm, laser power = 20 mW). Relative photoluminescence intensity was monitored for 60 min at 2 min intervals. The PL signal was collected over the wavelength range 560–740 nm.

Figure 4.11. *In vitro* and *in vivo* two-photon microscope images of porous Si nanoparticles selectively targeted to tumor tissues. (a) Schematic illustration depicting the structure of the 60 nm pSiNP-iRGD construct used (iRGD-specific targeting peptides attached to the pSiNP via 5 kDa PEG linkers, "pSiNP-iRGD"). (b) *In vitro* TPM images of HeLa cells treated with targeted and control 60 nm pSiNPs (20 μg per well) after 30 min incubation at 37 ∞C. The designation "pSiNP" represents control 60 nm pSiNPs containing only a native oxide surface chemistry. The designation "pSiNP-mPEG" represents control pSiNPs containing the 5 kDa PEG linkers, but each PEG is terminated with a methoxy group instead of the targeting peptide. Laser power 10 mW at the focal plane. (c) Photograph of xenograft tumor in the hind limb of a mouse, obtained under ambient light, showing the regions where the *in vivo* TPM images were collected for normal (blue, left) and tumor (red, right) tissue samples. (d) Intensity of signals extracted from TPM images of live animals, obtained in the tumor region for mice injected with 60 nm pSiNP-iRGD (20 mg kg^{-1}, $n = 4$) or with PBS control ($n = 4$), monitored as a function of time postinjection. Time point 0 represents measurements made on animals prior to injection. Laser power ≈50 mW at the focal plane. The intensity data were derived from the TPM images at a depth of 140 μm from the epidermal surface of the animal (along the *z*-direction), and the inset images correspond to the same depth, obtained 60 min postinjection. Scale bar is 35 μm. (e) *In vivo* TPM images of tumor region acquired at the indicated depths, 60 min postinjection of 60 nm pSiNP-iRGD (20 mg kg^{-1}). Laser power ≈50 mW at the focal plane. The images shown are representative images out of 30 sectional images obtained from depths in the range 100–250 μm. The red and blue signals were collected in the wavelength range 560–740 and 400–430 nm, respectively, corresponding to the pSiNP and the collagen signals, respectively. (f) Sections from *in vivo* TPM images from normal and tumor regions, obtained at a depth of 140–215 μm prior to injection (control) and 60 min postinjection of either PBS or 60 nm pSiNP-iRGD. (g) *Ex vivo* TPM images of organs harvested from animals that were sacrificed 60 min postinjection of 60 nm pSiNP-iRGD (tail-vein injection, 20 mg kg^{-1}). The images shown are representative images obtained at a depth of 45–165 μm. h) Biodistribution of pSiNP-iRGD derived from measured PL intensity from the *ex vivo* TPM images of panel (g). The percentages represent relative PL intensity from each organ after baseline subtraction; baseline values for each organ were obtained from the PBS-injected controls. All TPM images were obtained with 850 nm excitation, and emission intensity was measured in the wavelength range 560–740 nm.

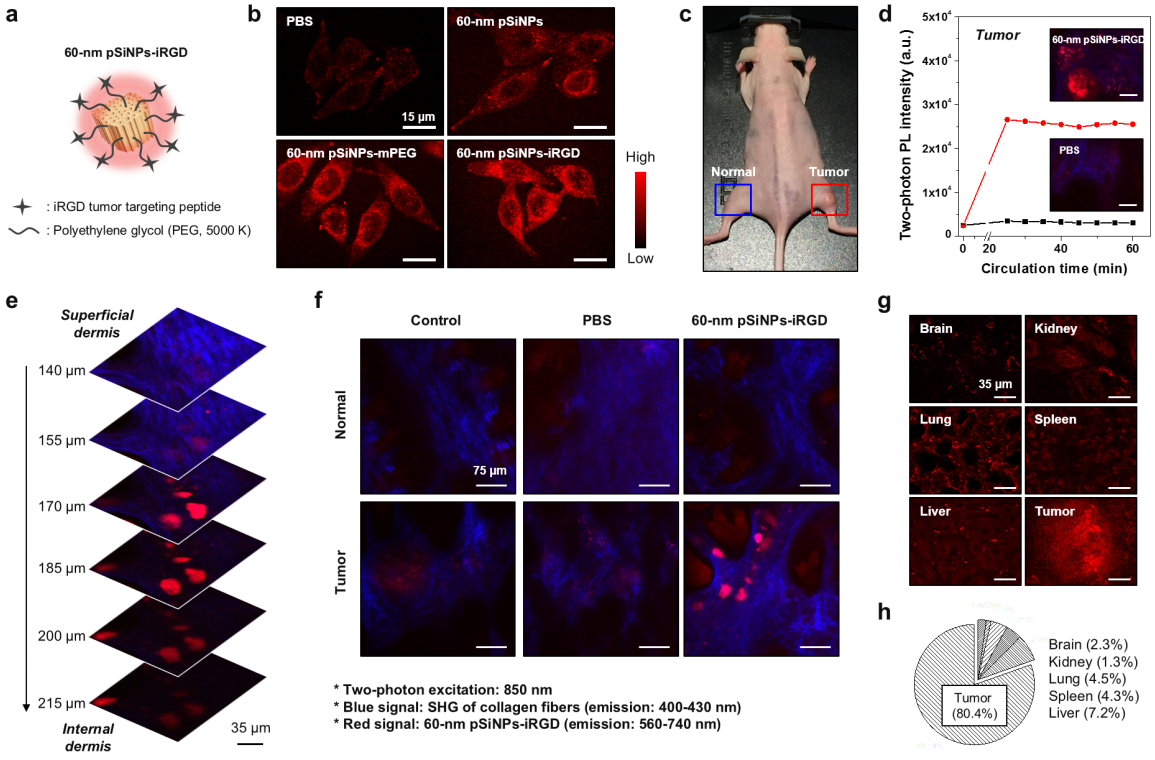
a
60-nm pSiNPs-iRGD
: iRGD tumor targeting peptide
: Polyethylene glycol (PEG, 5000 K)
b
PBS
60-nm pSiNPs
15 μm
60-nm pSiNPs-mPEG
60-nm pSiNPs-iRGD
High
Low
c
Normal
Tumor
d
Tumor
60-nm pSiNPs-iRGD
PBS
Two-photon PL intensity (a.u.)
Circulation time (min)
e
Superficial dermis
140 μm
155 μm
170 μm
185 μm
200 μm
215 μm
Internal dermis
35 μm
f
Control
PBS
60-nm pSiNPs-iRGD
Normal
Tumor
75 μm
* Two-photon excitation: 850 nm
* Blue signal: SHG of collagen fibers (emission: 400-430 nm)
* Red signal: 60-nm pSiNPs-iRGD (emission: 560-740 nm)
g
Brain
Kidney
35 μm
Lung
Spleen
Liver
Tumor
h
Tumor (80.4%)
Brain (2.3%)
Kidney (1.3%)
Lung (4.5%)
Spleen (4.3%)
Liver (7.2%)

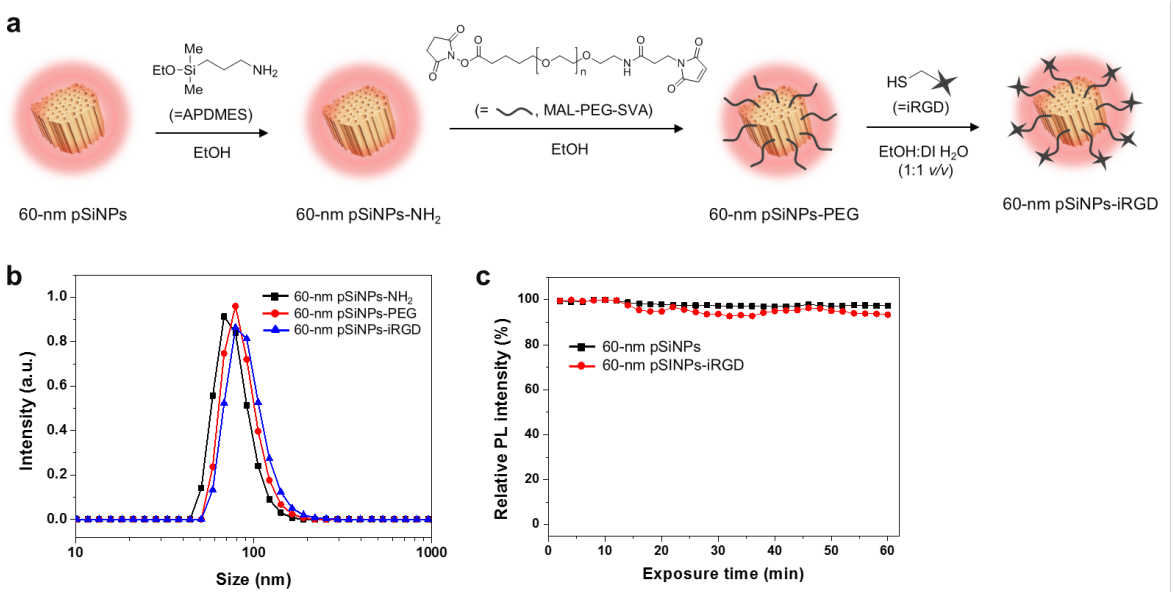

Figure 4.12. Chemistry and characterization of 60-nm pSiNP-iRGD formulation. (a) Schematic depicting the preparation method for 60-nm pSiNP-iRGD (see details in Experimental section). (b) Mean hydrodynamic diameter (intensity distribution) of 60-nm pSiNP-NH_2, 60- nm pSiNP-PEG, and 60-nm pSiNP-iRGD, measured by dynamic light scattering (DLS). Each nanoparticle sample was isolated, rinsed with ethanol and then re-dispersed in ethanol for the measurement. Means and standard deviations calculated from triplicate measurements. (c) Photostability comparison of 50-nm pSiNP-iRGD with 60-nm pSiNP formulations in DI H_2O under two-photon excitation conditions (λ_{ex} = 850 nm, laser power 20 mW). Relative photoluminescence intensity was monitored for 60 min at 2-min intervals. The PL intensity was integrated over the wavelength range 560–740 nm.

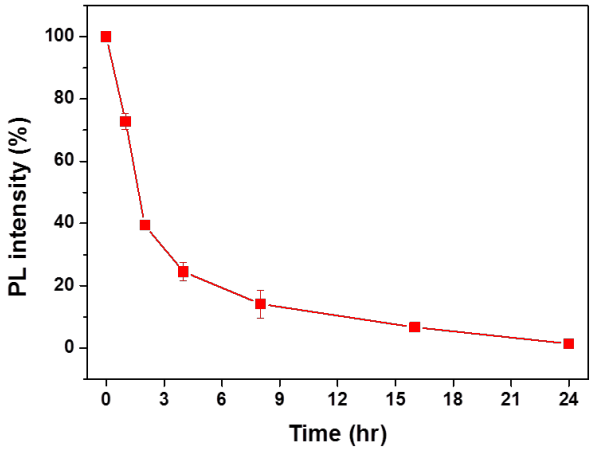

Figure 4.13. Loss of photoluminescence intensity from 60-nm pSiNPs as a function of time incubated in phosphate-buffered saline (PBS) solution (pH 7.4) at 37 °C. Nanoparticle solutions (0.5 mg mL^{-1}) were removed from the incubator and the integrated PL intensity was quantified in the wavelength range 500–980 nm (λ_{ex} = 365 nm) at the indicated time points. After each spectral acquisition, the nanoparticles were removed from the PBS solution by centrifugation and then re-dispersed in fresh PBS (see details in the Experimental section).

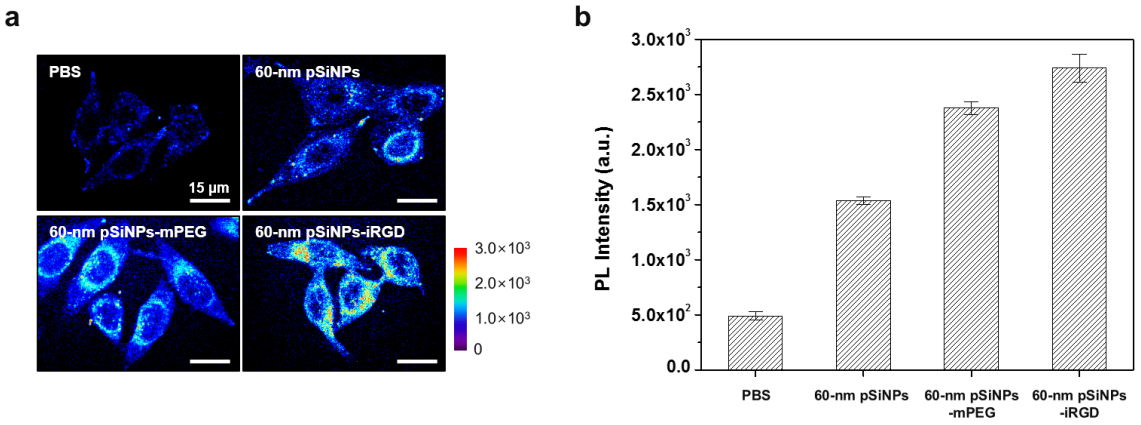

Figure 4.14. Two-photon microscope (TPM) images of HeLa cells treated with 60-nm pSiNPs *in vitro*. (a) PL intensity-mapping TPM images of HeLa cells treated with 60-nm pSiNP, 60-nm pSiNP-mPEG, and 60-nm pSiNP-iRGD (corresponding to images in Fig. 4.11b), obtained by averaging of all the data pixels. The intensity-mapped (panel a) and pseudo color-mapped (Fig. 4.11b) images were processed using MATLAB software. (b) Relative PL intensity from intensity-mapped TPM images. The error bars indicate ± SD.

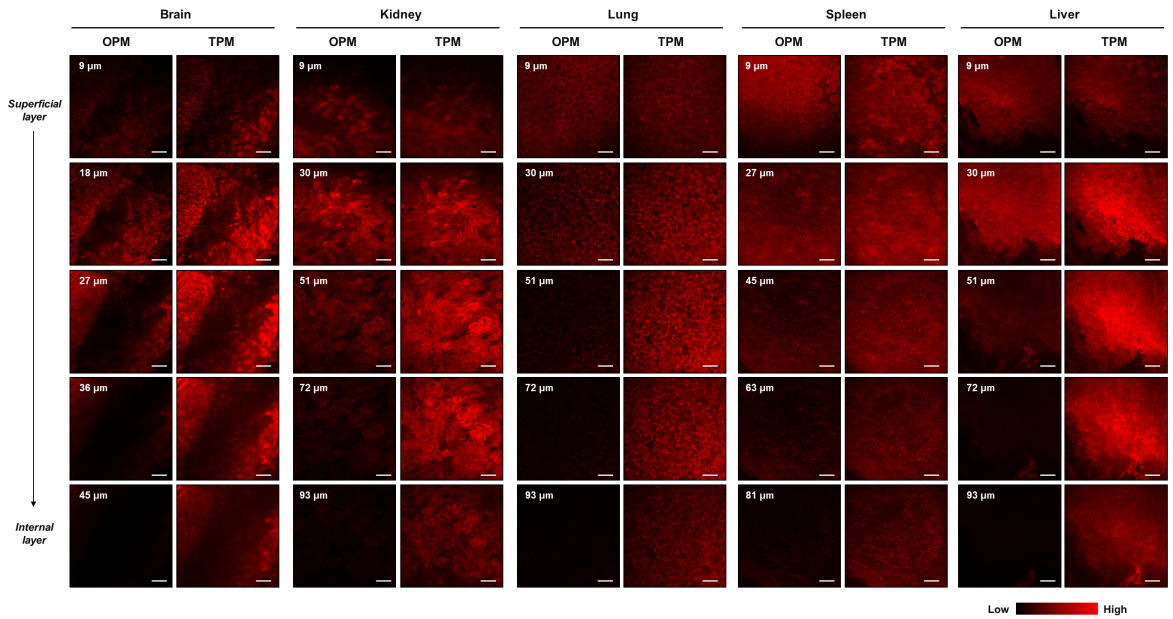

Figure 4.15. Comparison of one-photon and two-photon microscope (OPM and TPM, respectively) images of mouse organs treated with 60-nm pSiNPs. Sacrificed mouse organs (as indicated) were immersed in a DI H_2O solution of 60-nm pSiNPs (10 mg mL^{-1}) for 2 hr at 37 C. After incubation, the organs were washed several times with PBS solution. One-photon images were obtained with a confocal laser scanning microscope (CLSM) using an excitation wavelength of 488 nm, and PL intensity was collected in the wavelength range 560–740 nm. Two-photon microscope (TPM) images were obtained using an excitation wavelength of 850 nm, with power of 65 mW, and PL intensity was collected in the wavelength range 560–740 nm. Scale bar for all images is 50 µm. Pseudo-color mapping is in red.

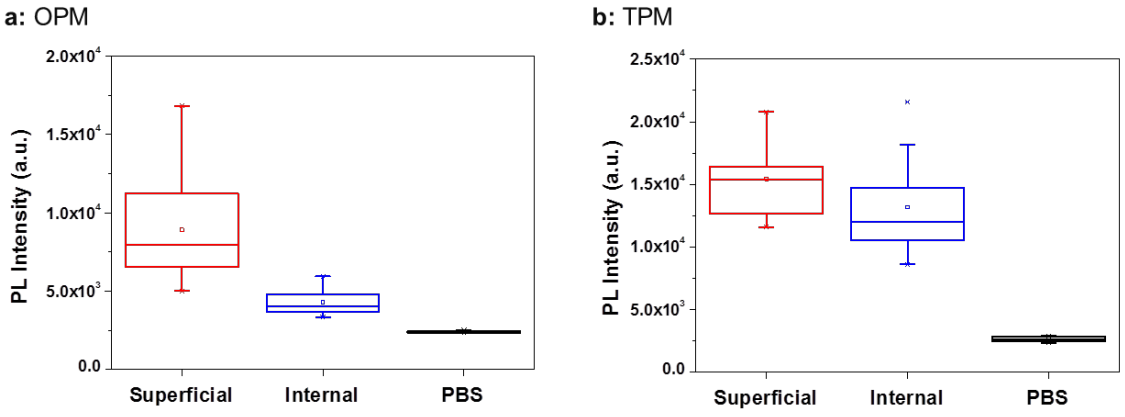

Figure 4.16. Quantified intensity of photoluminescence (PL) from one-photon (OPM) and two-photon microscope (TPM) images of mouse organs treated with 60-nm pSiNPs. (a) Relative photoluminescence (PL) intensity of one-photon microscope (OPM) images from Fig. S12, obtained by collecting and averaging all the data pixels. (b) Relative PL intensity of two-photon microscope (TPM) images from Fig. S12, obtained by collecting and averaging all the data pixels. The average PL intensities were derived from the OPM/TPM images from superficial (~30 μm from surface) and internal (deeper than 30 μm) depths, respectively. PBS is control organs treated with phosphate-buffered saline alone.

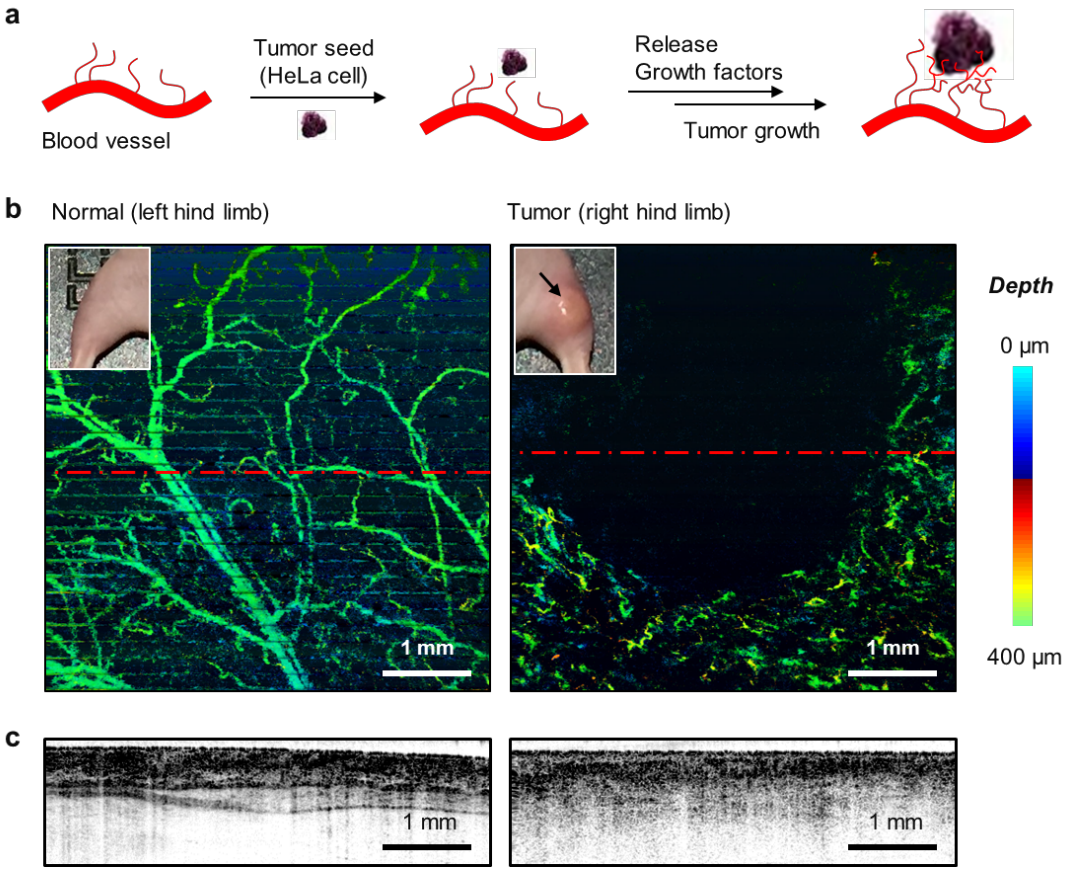

Figure 4.17. Characterization of tumor in xenograft mouse model. (a) Schematic illustration of blood vessel generation in xenograft tumor mouse model. An injected tumor seed (HeLa cells) in the dermal layer of the hind limb skin of a mouse releases growth factors that induce growth of blood vessels. The tumor-associated vessels show a disorganized and undefined arteriole morphology, lacking in organized large blood vessels. (b) Projected angiographic optical coherent tomography (OCT) images in *en face* (x-y axis) of hind limbs of control (normal, left hind limb) and tumor (right hind limb image) regions, as indicated. The color-mapping angiographic OCT images reveal depth-dependent vascular structures in the hind limb skin at depths ranging from the skin surface to 400 μm (z-direction). (c) Cross-sectional (y-z axis) OCT images of normal and tumor region obtained from sections indicated by the red dashed lines in panel b, respectively. In contrast with the normal hind limb, the tumor region presents a vague layered structure associated with the intradermal tumor.

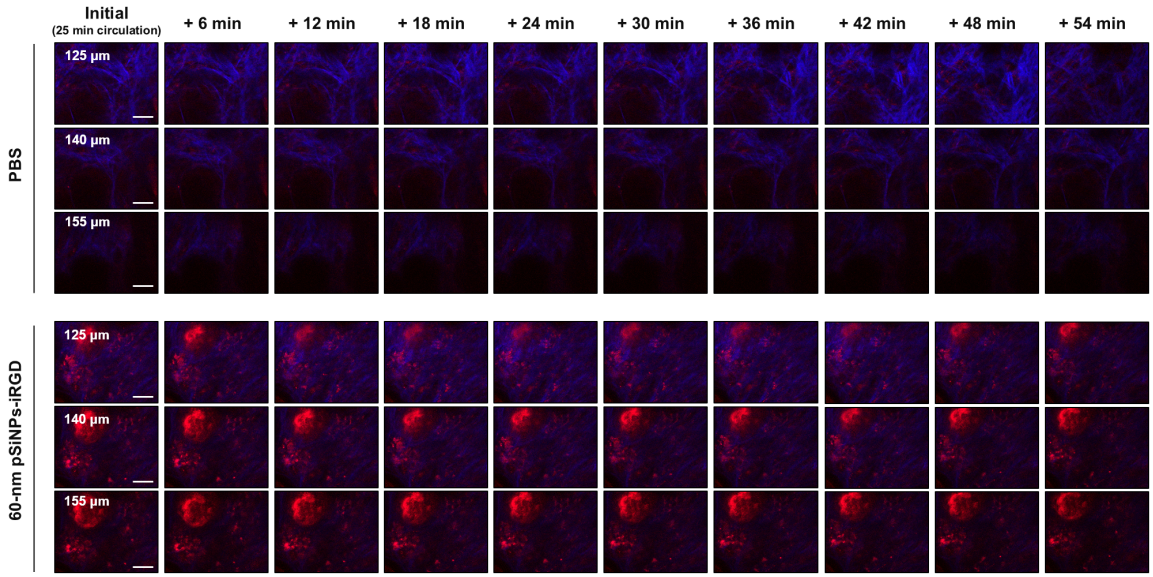

Figure 4.18. *In vivo* time-lapse two-photon microscope (TPM) images of mouse treated with 60-nm pSiNP-iRGD formulation. TPM images obtained in the tumor region, beginning 25 min after intravenous injection of the 60-nm pSiNP-iRGD (20 mg kg^{-1}) formulation. Images were obtained using an excitation wavelength of 850 nm, with power of ~50 mW, and PL intensity was collected in the wavelength range 560–740 nm. The images were acquired at depths of 150–200 µm from the skin surface. "Initial" represents images obtained 25 min after intravenous injection via tail-vain, and succeeding images were acquired at the indicated time points post-initial. Scale bar for all images is 35 µm.

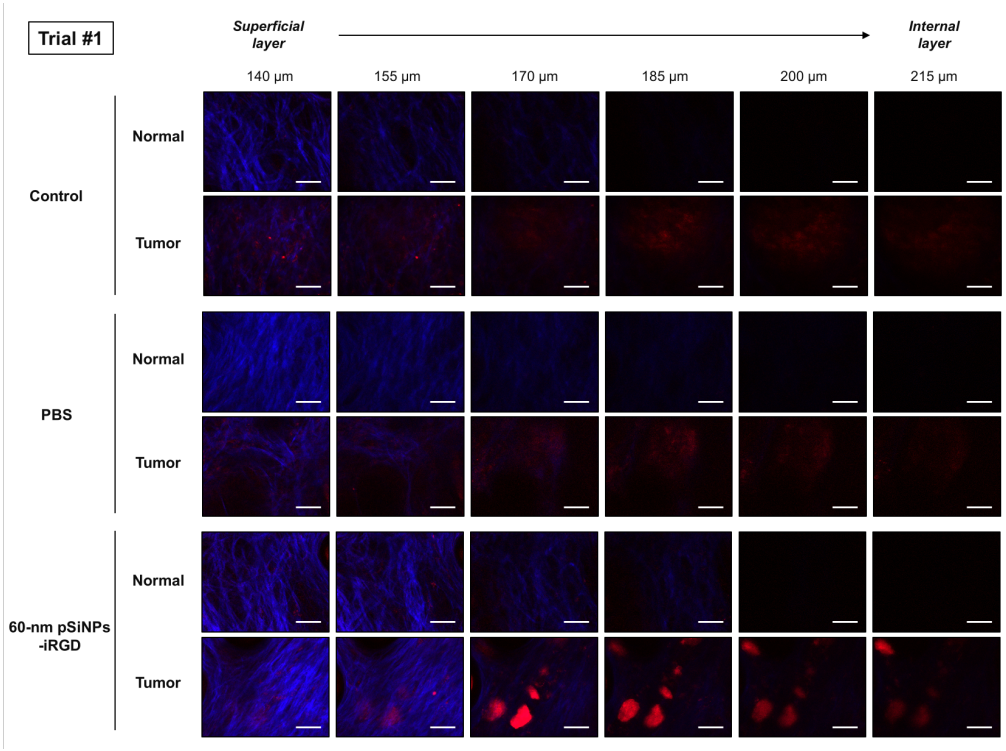

Figure 4.19. Two-photon microscope (TPM) images of normal and tumor region of live mouse injected with 60-nm pSiNP-iRGD formulation. "Control" denotes set of *in vivo* TPM images of normal and tumor region of the mouse obtained prior to injection; "PBS" denotes images of the corresponding tissue regions obtained after intravenous injection of phosphate-buffered saline; and pSiNP-iRGD (60 nm) denotes set of images of the corresponding tissue regions obtained 1 hr after injection (20 mg kg^{-1}) of the pSiNP-iRGD (60 nm) construct. TPM Images were obtained using an excitation wavelength of 850 nm, with laser power of ~50 mW, at the depths indicated (relative to the skin surface). PL intensity was collected in the wavelength range 560–740 nm (red channel) and 400–430 nm (blue channel). The blue channel corresponds to the SHG signal from collagen in the dermal layer (see text). Scale bar is 35 µm for all images.

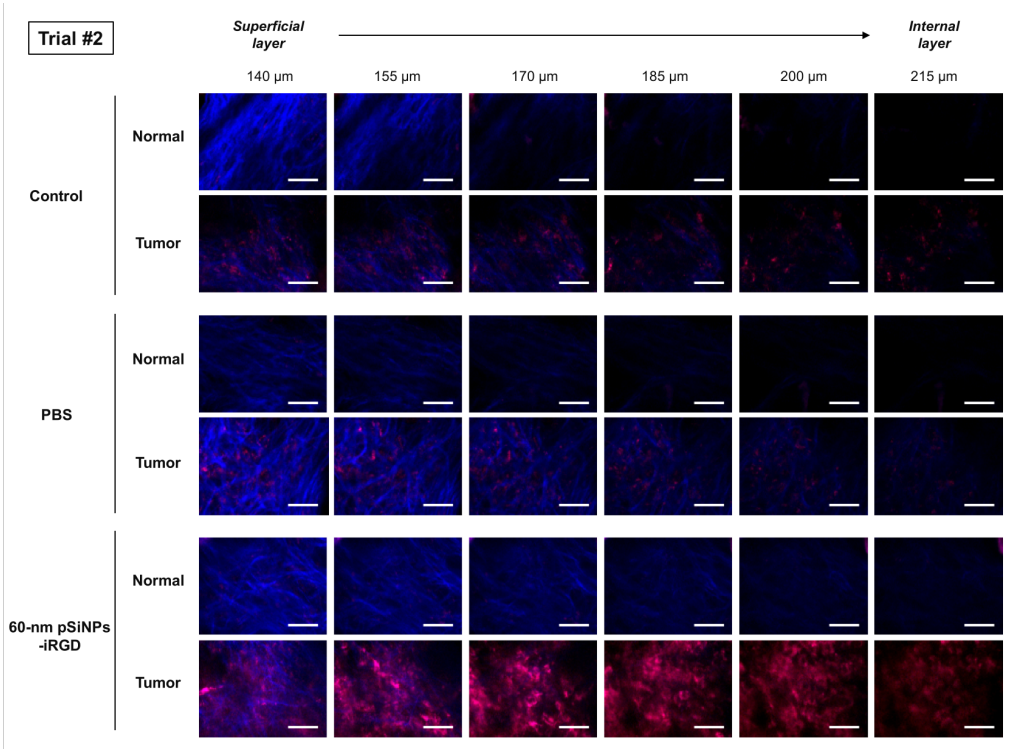

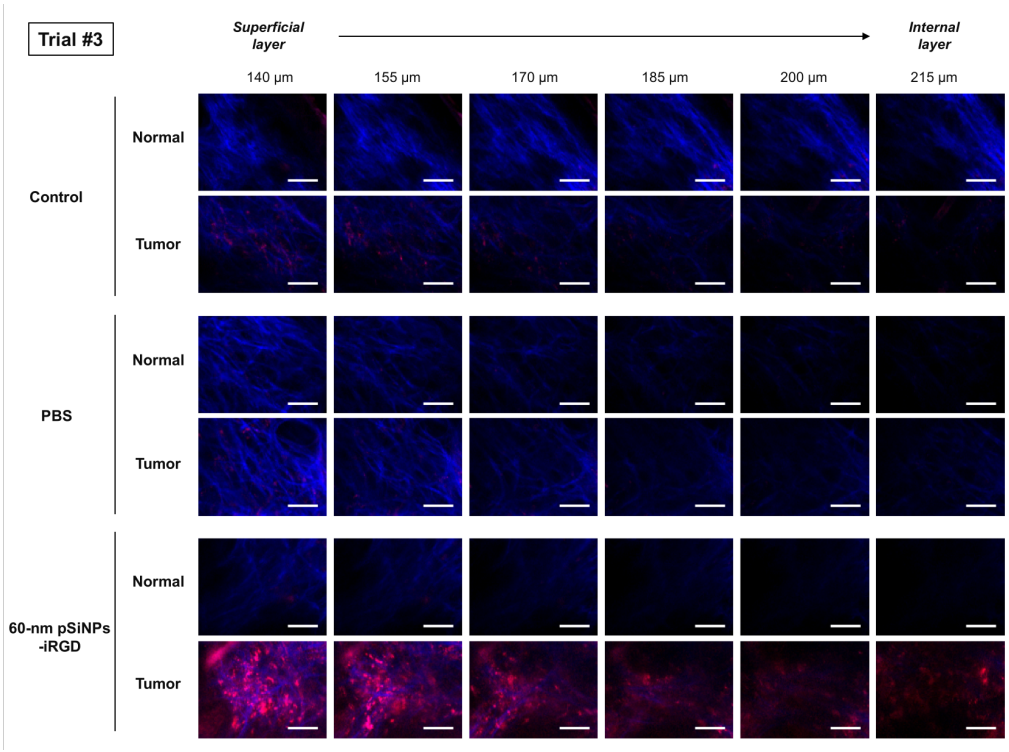

Figure 4.19. Two-photon microscope (TPM) images of normal and tumor region of live mouse injected with 60-nm pSiNP-iRGD formulation. (Continued)

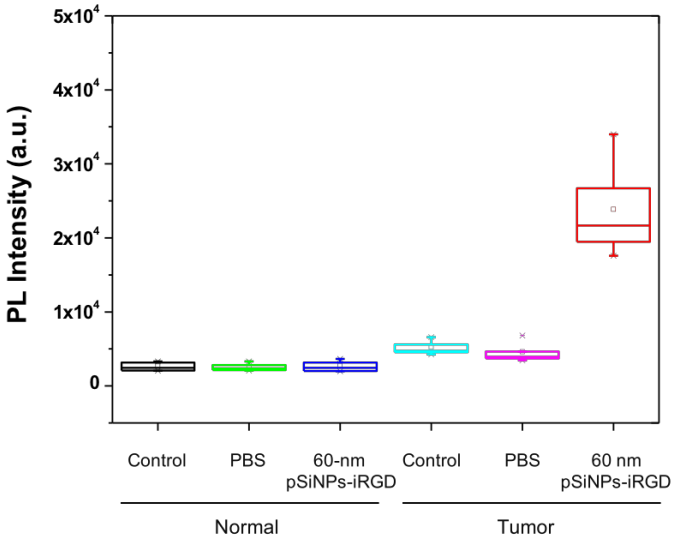

Figure 4.20. Relative intensity of photoluminescence quantified from the *in vivo* TPM images of treated mice. Relative photoluminescence (PL) intensity obtained from the TPM images of Fig. 4.19, integrated over the wavelength range 560–740 nm. "Control", "PBS" and "pSiNP-iRGD" as defined in Fig. 4.19. n=4 mice for each category.

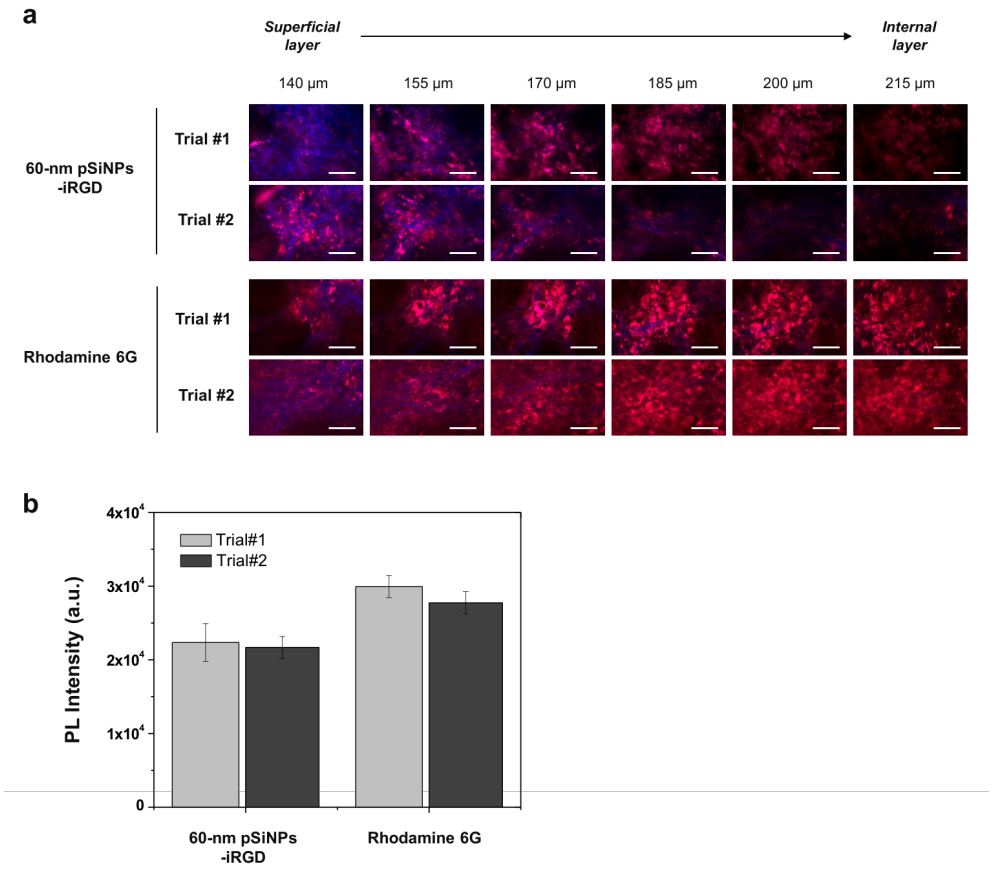

Figure 4.21. Two-photon microscope (TPM) images and relative intensity of photoluminescence quantified from the *in vivo* TPM images of pSiNPs or rhodamine 6G treated mice. (a) Two-photon microscope images of tumor region of mouse injected with 60- nm pSiNPs and rhodamine 6G. The images were obtained after subcutaneous (SC) injection of pSiNPs (100 µL, 0.4 mg mL^{-1}) and rhodamine 6G (100 µL, 0.4 µM) into the dermis in the hind limb of the mouse, adjacent to the tumor. The images were recorded within 5 min of injection. TPM Images were obtained using an excitation wavelength of 850 nm, with laser power of ~50 mW, at the depths indicated (relative to the skin surface). PL intensity was collected in the wavelength range 560–740 nm (red channel) and 400–430 nm (blue channel). The blue channel corresponds to the SHG signal from collagen in the dermal layer (see text). Scale bar is 35 µm for all images. Trial #1 and Trial #2 each correspond to a separate tumor-bearing mouse. (b) Relative intensity of photoluminescence intensity from the *in vivo* two-photon images from panel a.

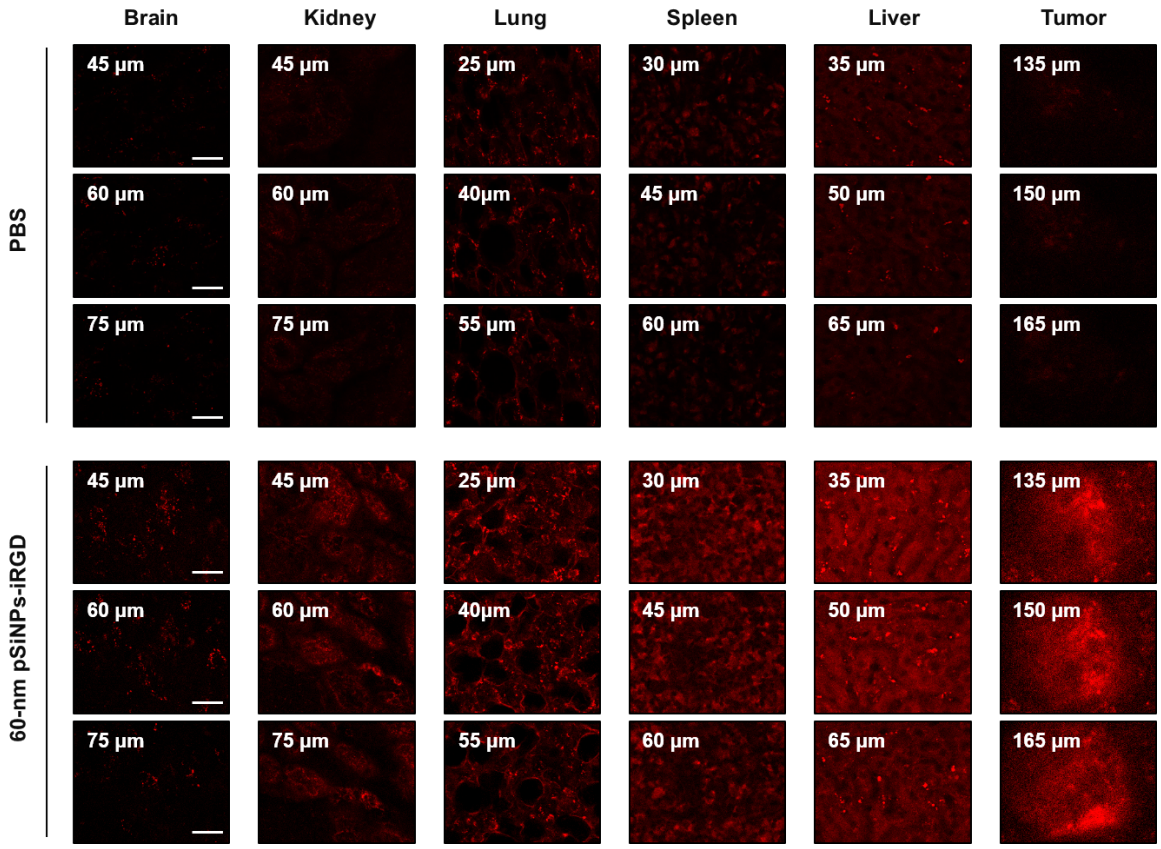

Figure 4.22. Two-photon microscope (TPM) images of tissues harvested from mouse injected with 60-nm pSiNP-iRGD formulation. Animals were sacrificed 1 hr after administration of the 60-nm pSiNP-iRGD construct (intravenous tail-vein, 20 mg kg^{-1}). TPM images were acquired from the perfused organs using an excitation wavelength of 850 nm, with laser power of ~50 mW, at the depths indicated (relative to the tissue surface). PL intensity was collected in the wavelength range 560–740 nm. Scale bar is 35 µm for all images. "PBS" and pSiNP-iRGD images were obtained from two different mice and are representative of replicate measurements made on four separate animals.

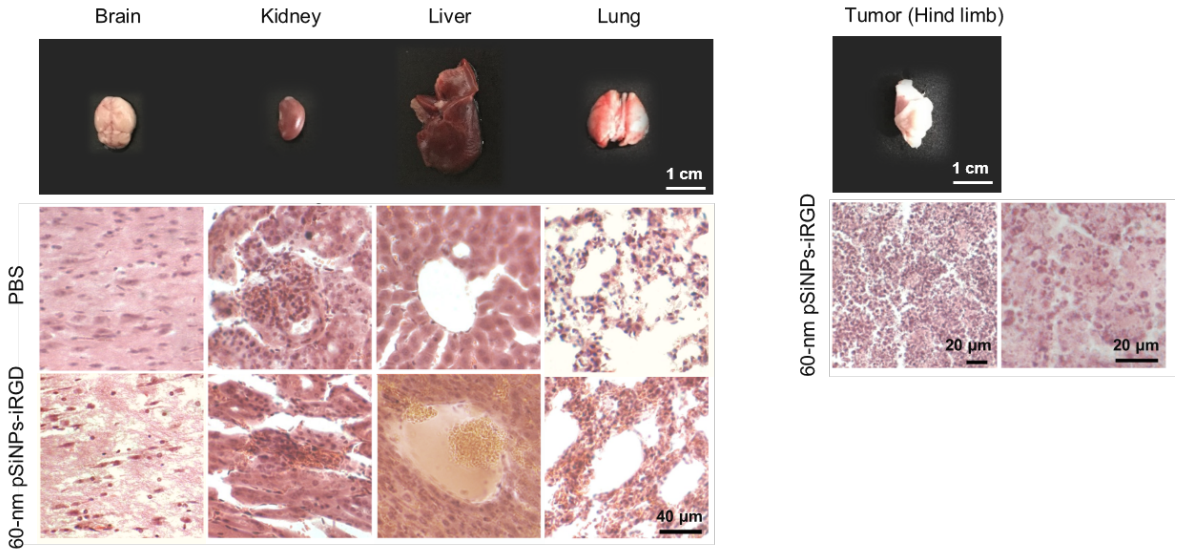

Figure 4.23. Histological examination of main organs (brain, kidney, liver, lung) and tumor (hind limb). Main organs were dissected from mice after intravenous injection of phosphate-buffered saline (PBS, 200 μL) or 60-nm pSiNP-iRGD (20 mg kg^{-1}) (intravenous injection via tail-vein), and stained with haematoxylin and eosin (H&E). The examination indicates no abnormalities or inflammation of the organs occurred during the 1-hr particle treatment period. The stained sections were histopathologically evaluated by Dr. Junyang Jung (Department of Anatomy and Neurobiology, Kyung Hee University, Korea) and are representative of four animals for each set.

Table 4.4. Measured zeta-potentials of pSiNP-iRGD and intermediate constructs. DLS size distribution is given in Fig. 4.12. Zeta-potential values were measured in DI H_2O. The standard deviations are calculated from 3 replicate measurements. PDI values: < 0.3.

	60-nm pSiNP-NH_2	60-nm pSiNP-PEG	60-nm pSiNP-iRGD	60-nm pSiNP-mPEG
Zeta-potential (mV)	+31.1 ± 2.1	+32.0 ± 1.8	+42.2 ± 3.9	+39.0 ± 4.1

Chapter 4, in full, is a reprint of the material as it appears in Advanced Materials 2017. Dokyoung Kim, Jinyoung Kang, Taejun Wang, Hye Gun Ryu, Jonathan M. Zuidema, Jinmyoung Joo, Muwoong Kim, Youngbuhm Huh, Junyang Jung, Kyo Han Ahn, Ki Hean Kim, Michael J. Sailor. The dissertation author was the primary researcher and author of this material.

CHAPTER 5

Enhanced Performance of a Molecular Photoacoustic Imaging Agent by Encapsulation in Mesoporous Silicon Nanoparticles

5.1. Abstract

Photoacoustic (PA) imaging allows visualization of the physiology and pathology of tissues with good spatial resolution and relatively deep tissue penetration. The method converts near-infrared (NIR) laser excitation into thermal expansion, generating pressure transients that are detected with an acoustic transducer. Here, we find that the response of the PA contrast agent indocyanine green (ICG) can be enhanced 17-fold when it is sealed within a rigid nanoparticle. ICG encapsulated in particles composed of porous silicon (pSiNP), porous silica, or calcium silicate all show greater PA contrast relative to equivalent quantities of free ICG, with the pSiNPs showing the strongest enhancement. A liposomal formulation of ICG performs similar to free ICG, suggesting that a rigid host nanostructure is necessary to enhance ICG performance. The improved response of the nanoparticle formulations is attributed to the low thermal conductivity of the porous inorganic hosts and their ability to protect the ICG payload from photolytic and/or thermal degradation. The translational potential of ICG-loaded pSiNPs as photoacoustic probes is demonstrated via imaging of a whole mouse brain.

5.2. Introduction

Photoacoustic (PA) imaging is a promising biomedical tool that addresses the resolution and depth limits of optical imaging.[1–3] In PA imaging, laser pulses are directed at tissues containing a molecular or nanoparticle chromophore with a strong optical absorbance at the laser wavelength, typically in the near-infrared (NIR) region of the spectrum. Nonradiative relaxation converts the optical excitation into a thermoacoustic wave[1,4,5] which is detected with audio transducers and reconstructed into a 3D image.[6]

Since light is used only to excite the target molecules and the generated acoustic waves are less efficiently scattered than photons in biological tissues, images can be obtained at greater depths and with higher spatial resolution than can be achieved with more conventional fluorescence imaging.

Materials exhibiting a high extinction coefficient at NIR wavelengths and efficient conversion of optical excitation into heat are used as contrast agents for PA imaging.[7–9] One of the more common PA imaging agents is indocyanine green (ICG), an FDA-approved fluorophore with a strong NIR absorbance. One of the challenges of organic imaging agents such as ICG is photochemical degradation, which irreversibly reduces the PA response and limits the quality of images that can be obtained. Metallic nanoparticles with strong plasmon bands in the NIR have been proposed to address this challenge because they are substantially more stable toward photolytic degradation. Another potential advantage of using nanoparticles as PA contrast agents is that they can incorporate affinity agents such as peptides, aptamers, or antibodies[10,11] to better target the tissues of interest. The PA response of a nanoparticle contrast agent has been found to increase substantially if it is thermally isolated from the surrounding aqueous matrix, because this generates a larger temperature differential immediately after the laser pulse. Thus core–shell nanoparticles composed of gold nanorod cores and silica shells show increased image contrast relative to "bare" gold nanorods.[12] In this study, we reasoned that the same approach may be applicable to molecular contrast agents, and sought to improve the PA response of ICG by trapping it in a nanoparticle of relatively low thermal conductivity. We further reasoned that ICG would be less susceptible to photolytic degradation when trapped in a nanoparticle host. Porous silicon, porous silica, and calcium silicate materials were tested as hosts for

ICG. All three materials have low thermal conductivity and have been studied extensively as *in vivo* biomaterials due to their low toxicity and superior biocompatibility[13–15] relative to metallic nanoparticles—an important consideration in translation to human diagnostic applications.[16–18]

5.3. Results and Discussions

For the porous silicon nanoparticles (pSiNPs), ICG was trapped within the porous matrix using a calcium silicate capping chemistry previously developed for oligonucleotide payloads.[19] The pSiNPs were prepared by electrochemical anodization of highly doped p-type single-crystal silicon wafers in an aqueous ethanolic electrolyte containing hydrofluoric acid and ultrasonic fracture of the resulting porous silicon layer (see the Experimental Section).[20] ICG was then loaded and sealed into the pSiNPs by means of calcium silicate precipitation chemistry to generate the Ca-pSiNP-ICG composites (Fig. 5.1).[19] TEM images of the pSiNPs prior to loading displayed the open pore structure characteristic of this material, with pore diameters on the order of 20 nm (Fig. 5.1b). After the loading and sealing process, the pores in the Ca-pSiNP-ICG composite appeared to be filled (Fig. 5.1c), consistent with prior results.[19] Residual nanocrystalline Si was evident in the Raman spectrum from the observation of a lattice mode[21] at 510 cm^{-1}, although this band was somewhat broadened on the low energy side relative to the pSiNP starting material (Fig. 5.2a), indicative of some loss of crystallinity. The presence of crystalline silicon was confirmed by powder X-ray diffraction (XRD) measurements (Fig. 5.2b). The Ca-pSiNP-ICG nanoparticles had an average particle size of (170 nm by dynamic light scattering, Table 5.1) that was somewhat larger than the pSiNP starting material, and

nitrogen adsorption measurements indicated a decrease in surface area associated with the pore filling and sealing process (Fig. 5.3). The Ca- pSiNP-ICG nanoparticles readily dispersed in water or ethanol and displayed the distinctive green color of ICG compared to the brownish appearance of pSiNPs (Fig. 5.1d). Bands characteristic of ICG were observed in the optical absorbance spectrum (λ_{abs} = 790 nm) and also in the Fourier transform infrared (FTIR) spectrum (Fig. 5.3). The mass loading of ICG was determined by thermogravimetric analysis (TGA) to be 11%, (Fig. 5.3). The fluorescence from ICG (λ_{em} = 820 nm) was quenched by 60% in the Ca-pSiNP-ICG formulation. This can be attributed to energy transfer quenching by the silicon skeleton of the pSiNPs (Fig. 5.4), although we cannot rule out a contribution from self-quenching due to aggregation of the dye within the pSiNPs.[22,23] The electrospray ionization mass spectrum of the material released from Ca-pSiNP-ICG into aqueous solution displayed a parent ion at m/z = 751 (Fig. 5.5), confirming the presence of ICG in the nanoparticles.

The photoacoustic response of Ca-pSiNP-ICG was compared to free ICG (15−150 μg mL^{-1}) by scanning tubes containing solutions of the relevant contrast agent with 790 nm pulsed laser irradiation. The effective concentration of ICG in the Ca-pSiNP-ICG samples was 15 ± 5 μg mL^{-1} (Fig. 5.1 and Fig. 5.6). The Ca-pSiNP-ICG formulation produced a photoacoustic signal that was significantly ($p < 0.01$) greater than for samples containing comparable or even much larger concentrations of free ICG. The signal was 8-fold larger than that from a solution of free ICG at a concentration of 10 μg mL^{-1} (Fig. 5.7), and the signal was also significantly ($p < 0.01$) stronger than that observed from the highest concentration of free ICG studied (150 μg mL^{-1}). The PA measurements were replicated on four independent Ca-pSiNP-ICG preparations (Fig. 5.8).

To evaluate the factors involved in enhancing the PA signal, we prepared and tested three other nanoparticle types containing encapsulated ICG: a porous calcium silicate nanoparticle (CaS-ICG), a microporous silica nanoparticle sealed with calcium silicate (Ca-Silica-ICG), and a liposomal nanoparticle (Lip-ICG) (Table 5.1). The ICG was incorporated into each of the nanoparticles during their synthesis. The CaS-ICG nanoparticles were prepared by mixing ICG and $CaCl_2$ solution (2 M) with silicic acid (see the Experimental Section and Fig. 5.9). The Ca-Silica-ICG samples were prepared by mixing commercial microporous silica nanoparticles (pore size <2 nm) with ICG and $CaCl_2$ solution (Fig. 5.10). These nanoparticles displayed different pore dimensions and ICG loading efficiency, but they had average diameters similar to the pSiNPs used in this work (between 120 and 200 nm, Table 5.1). For this comparison, the concentration of each nanoformulation was adjusted to display a similar optical absorbance at 790 nm (the absorbance band of ICG), which was approximately equal to the absorbance displayed by free ICG at a concentration of 10 μg mL^{-1} (Fig. 5.11a). All three of the inorganic nanoparticle samples (Ca-pSiNP-ICG, CaS-ICG, and Ca-Silica-ICG) displayed substantially larger photoacoustic signals relative to free ICG (Fig. 5.11bc). On the basis of SNR values (normalized to the absorbance value at 790 nm), the photoacoustic generation efficiencies were between 5- and 17-fold greater than for free ICG, with the Ca-pSiNP-ICG material showing the largest efficiency (Table 5.1).

In contrast to the behavior of the relatively rigid inorganic nanoparticles, a “softer” nanoparticle based on a liposome (Lip-ICG) showed no enhancement of the photoacoustic signal from encapsulated ICG. The Lip-ICG formulation was prepared by extrusion through polycarbonate membranes containing 100 nm pores as described previously.[24] In

order to make a direct comparison, Lip-ICG and Ca-pSiNP-ICG nanoparticles were prepared of comparable size (Table 5.1 and Fig. 5.11a), and their concentrations were adjusted to yield comparable optical absorbance at λ = 788 nm (Fig. 5.11b). Photoacoustic signals recorded using λ = 788 nm pulsed laser irradiation (Fig. 5.12) showed six fold lower response from the Lip-ICG sample relative to Ca-pSiNP-ICG. The response of the liposomal formulation was thus quite similar to the response of a comparable concentration of free ICG.

The poor PA imaging performance of the liposomal formulation relative to the inorganic nanoparticles was consistent with steady-state laser heating measurements. In these experiments, the samples were continuously irradiated with a high power laser (power density 1.1 W cm^{-2}) emitting at λ = 808 nm and the temperature was recorded as a function of time (Fig. 5.13). The Ca-pSiNP-ICG and Lip-ICG samples were dispersed in 20% ethanol (in DI water) and the concentrations adjusted such that the optical absorbance at λ = 808 nm was comparable for each sample (Fig. 5.13c). Irradiated Ca-pSiNP- ICG rapidly attained a steady state temperature that was 47 °C greater than the sample in the dark (ambient temperature was ≈25°C), it was stable under irradiation, and it maintained a constant elevated temperature for the duration of the experiment (Fig. 5.13b). By contrast, Lip-ICG displayed a lower level of steady-state heat generation, and the initial elevation in tem- perature decreased rapidly with increasing irradiation time. The behavior of the Lip-ICG formulation is consistent with a photobleaching process, and it was mirrored by the behavior of free ICG (Fig. 5.13c).[25,26] Free ICG is known to be photolytically unstable under laser irradiation,[27,28] and oxidized porous Si has previously been shown to protect a trapped fluorescent molecular payload from the photobleaching process.[29] In order to

quantify this in the present system, we monitored fluorescence intensity from free ICG and from Ca-pSiNP-ICG during irradiation with λ = 790 nm pulsed laser light as a function of time. Fluorescence from free ICG lost >10% of its intensity during 5 min of irradiation, while the fluorescence spectrum from nanoparticle-encapsulated ICG did not change substantially under these conditions (Fig. 5.14). We conclude that the more rigid, sealed pSiNPs effectively protect loaded ICG from photobleaching, and postulate that this results in a more constant response and a higher steady-state temperature elevation upon sustained laser irradiation. While the greater photostability that ICG exhibits when it is loaded into Ca-pSiNP-ICG might contribute to the large photoacoustic signal enhancement seen with this nanoparticle host, it is likely that other factors are involved as well. For example, the relative rigidity of a solid porous host is expected to inhibit rotations, vibrations, and Brownian motion of dye molecules trapped within, and this could influence PA performance.

Control experiments were performed to test if trapping of the ICG payload within the porous nanoparticle was a necessary condition for the high PA response observed. For these experiments we blocked the empty pore openings of the pSiNPs via thermally induced silane dehydrocoupling of octadecylsilane (H3Si-C18H37).[30] Spectroscopic measurements combined with centrifugation indicated that the resulting particle (C18-pSiNP) effectively excluded ICG, and photoacoustic measurements on a mixture of C18-pSiNP and free ICG showed no signal enhancement relative to free ICG alone (Fig. 5.15), establishing that PA signal enhancement is not caused simply by proximity of the pSiNPs to ICG. A second control experiment was performed in which the empty pSiNP surface was modified with primary amines using the (3-aminopropyl)-dimethylmethoxysilane

coupling agent, and ICG was loaded onto the resulting positively charged surface *via* electrostatic interaction (pSiNP-NH_2-ICG). This experiment was performed to test if the dye payload must be sealed within a rigid host in order to exhibit PA signal enhancement. The rationale for these experiments was that a surface-adsorbed dye would be in contact with the liquid phase and so would experience better thermal coupling to the solution. Thus the pSiNP-NH_2-ICG construct received no calcium silicate sealing chemistry. These samples showed no enhancement in the PA signal relative to a comparable concentration of free ICG (Fig. 5.15), indicating that simple adsorbtion of ICG onto the surface of the nanoparticle is not sufficient to achieve PA contrast enhancement.

The porous silicon-based host contained an additional feature that may contribute to heating that is not seen with the simpler oxide-based hosts: it contains elemental silicon. This material displayed pronounced quenching of fluorescence from the ICG payload (Fig. 5.4) that was not observed with the other nanoparticle hosts. Prior studies of porous silicon have shown that it can act as an efficient quencher of fluorescence from a proximal organic dye.[23,31] Silica and calcium silicate, being insulators, do not have a high density of electronic states available to quench fluorescence in a similar manner. For the silicon-containing nanoparticle, fluorescence quenching provides an additional means to channel the excited state of an emissive molecular guest into a nonradiative (thermal) pathway, and this nonradiative quenching process may be responsible for the slightly greater signals generated by the pSiNP constructs relative to the porous silica-based nanoparticles. In addition, the efficient quenching of fluorescence by the silicon host may limit photo-oxidation of the dye by intercepting its excited state before it has time to generate singlet oxygen or participate in other photochemical degradation pathways.

Taken together, the above results suggest that photoacoustic signal enhancement of a molecular dye contrast agent is a general characteristic of the rigid porous inorganic host, which we postulate to arise from two complementary factors: First, the relatively low thermal conductivity of the porous silicon, silica and calcium silicate host materials[32–35] allows the particles to better retain heat generated during the laser pulse, yielding a larger temperature differential and resulting in a stronger photoacoustic signal. A similar effect has been invoked to explain the improved PA signals seen from gold nanorods that have been encapsulated in silica shells.[12] Second, as seen previously with thermally oxidized porous Si,[29] encapsulation of the dye in a relatively oxygen-impermeable structure shuts down photobleaching processes that degrade the free dye.

Finally, we demonstrated the feasibility of the use of the nanoparticle-based photoacoustic imaging agent in tissues using *ex vivo* mouse brains (fixed in 1% agarose gel, n = 3 per each group). We injected aliquots of Ca-pSiNP-ICG and ICG (at equivalent concentrations, based on the ICG absorbance at λ = 790 nm) at the lambda point of each brain, which is the location of some of the largest blood vessels in this organ (Fig. 5.16). Ca-pSiNP-ICG, ICG, and phosphate buffered saline (PBS)-injected brains were positioned in a water tank ≈1 cm beneath the acoustic transducer and imaged. Strong photoacoustic signals were detected in the Ca-pSiNP-ICG injected brains in the region emanating from the injection point, and signals from deeper in the tissues were also visible (Fig. 5.17). By contrast, only weak signals were detected in brains injected with free ICG. The presence of ICG in both brain samples was verified by its characteristic photoacoustic spectrum, obtained from brain coronal cross sections (Fig. 5.18). The corresponding photoacoustic spectrum from the control (PBS-injected) brain was featureless. The *ex vivo* photoacoustic

data validate that the Ca-pSiNP-ICG construct is an effective PA contrast agent for imaging of tissues, and that the substantial improvement in contrast afforded by the nanoparticle host *in vitro* is also apparent in animal tissue imaging.

5.4. Conclusion

The calcium silicate sealing chemistry used in this study to trap ICG in the Ca-pSiNP-ICG formulation has been used previously to load siRNA as a potential drug payload, and this chemistry allows conjugation of polyethylene glycol linkers and peptide-based targeting groups to a pSiNP host, which have shown selective homing and delivery of the payload to injured brain tissues from systemic circulation.[19] The results of the present work showing that this nanoparticle can stabilize a photolytically unstable dye, maintain a large photothermal temperature differential, and significantly enhance the performance of a photoacoustic imaging agent in animal tissues establishes the feasibility of expanding this selective tissue targeting system into photoacoustic imaging and photothermal therapy applications.

5.5. Experimental

Materials: All chemical reagents were purchased from Aldrich Chemicals, Inc. Single crystal silicon wafers were obtained from Virginia Semiconductor, Inc. Indocyanine green (ICG) was purchased from Sigma-Aldrich Inc. (United States Pharmacopeia (USP) reference standard). Solid $CaCl_2$ was purchased from Spectrum Chemicals, Inc. 1,2-dimyristoyl-sn-glycero-3-phosphocholine (DMPC) and 1,2-distearoyl-sn-glycero-3-phosphoethanolamine-N-[methoxy(polyethylene glycol)-2000] (ammonium salt) (DSPE-

PEG(2000) methoxy) were purchased from Avanti Polar Lipids, Inc. Sephadex G-50 beads were purchased from GE Healthcare Life Sciences, Inc. 100 kDa dialysis tubing (biotech cellulose ester membrane) was purchased from Spectrum Lab, Inc. Amicon 100 kDa centrifugal filter units were purchased from Millipore Sigma, Inc. 120 nm microporous silica nanospheres were purchased from Nanocomposix, Inc.

Preparation of Porous Silicon Nanoparticles: The pSiNPs were prepared following the published "perforation etching" procedure with slight modification.[20] A highly boron-doped p++-type single-crystal silicon wafer (1 mΩ cm resistivity, 100 mm diameter, Virginia Semiconductor, Inc.) was anodically etched in an electrolyte consisting of 3:1 (*v:v*) of 48% aqueous hydrofluoric acid (HF): absolute ethanol. Prior to preparation of the pSi layer, the silicon wafer was etched a thin porous layer called "sacrificial layer" with 3:1 (*v:v*) 48% aqueous HF:ethanol and removed with aqueous potassium hydroxide (KOH, 2 M). The etching waveform consisted of a lower current density 50 mA cm^{-2} of 1.2 s, followed by a higher current density 400 mA cm^{-2} of 0.363 s. This waveform was repeated for 500 cycles, generating a pSi film with "perforations" as cleavage points during ultrasonication repeating approximately every 120 nm. The etched pSi layer was collected from the silicon substrate by applying 4 mA cm^{-2} current density for 250 s in a solution containing 1:20 (*v:v*) aqueous HF:ethanol. The collected pSi films were fractured into nanoparticles in deionized water (DI H_2O, 6 mL) for 24 h. The pSiNPs were purified three times by centrifugation (14,000 rpm, 20 min).

Preparation of ICG-Loaded Inorganic Nanoparticles (Ca-pSiNP-ICG, Ca-Silica-ICG, CaS-ICG, and pSiNP-NH_2-ICG): ICG was loaded into the pSiNPs following the published "self-sealing chemistry" procedure with slight modification.[19] The pSiNPs (1

mg in 100 μL ethanol) were mixed with ICG solution (2 mg mL^{-1} in DI water, 150 μL), DI water (250 μL) and aqueous $CaCl_2$ solution (2 M, 500 μL). The mixture was subjected to ultrasonication (50T ultrasonic bath, VWR International) in an ice water bath for 30 min. The ICG-loaded pSiNPs (Ca-pSiNP-ICG) were purified by three sequential centrifugation steps (14,000 rpm, 20 min), where the supernatant was discarded and the pellet was redispersed in DI water, 70% ethanol, and finally 100% ethanol. The control calcium silicate-sealed pSiNPs (Ca-pSiNP) were prepared without ICG following the above procedure but omitting ICG from the reaction. The Ca-Silica-ICG and CaS-ICG samples were prepared in the same manner, but commercial silica nanoparticles (1 mg in 100 μL ethanol) or silicic acid was added to the reaction mixture instead of pSiNPs. The silicic acid used in this preparation was synthesized by dissolution of 1 mg pSiNP in aqueous KOH (50 μL, 2 M) and filtration of the solution through an Amicon centrifugal filter unit (100 kDa cutoff) prior to use. The aminated pSiNPs (pSiNP-NH_2-ICG) were prepared by mixing pSiNPs (1 mg in 1 mL ethanol) with 12 μL of (3-aminopropyl)-dimethylmethoxysilane for ≈3 h. The mixture was purified three times by centrifugation (14,000 rpm, 20 min) from ethanol to remove excess reagents. The aminated pSiNPs (1 mg in 850 μL ethanol) were mixed with ICG solution (2 mg mL^{-1} in ethanol, 150 μL) and agitated for 2 h. The resulting pSiNP-NH_2-ICG construct was purified three times by centrifugation (14,000 rpm, 20 min) from ethanol to eliminate excess ICG.

Preparation of ICG-Loaded Liposome Nanoparticle (Lip-ICG): ICG was loaded into liposomes following the published procedure with slight modification.[24] Lipid stock solution was prepared with concentration of 10 mg mL^{-1} in chloroform and ICG was dissolved in methanol with 1 mg mL^{-1}. The lipid film was prepared with a mixture of 30.8

mg DMPC, 6.7 mg DSPE-PEG (2000) Methoxy, and 148.6 μg ICG (molar ratio DMPC:DSPE-PEG:ICG = 250:12.5:1) and the solvents were evaporated in a vacuum desiccator. The lipid film was hydrated with DI water (20 mL) and subsequently extruded through a 100 nm pore-size polycarbonate membrane at 40 °C. Lip-ICG was purified using Sephadex G-50 beads in a 100 kDa dialysis tube overnight under continuous water elution to remove free ICG not encapsulated by liposome. The purified Lip-ICG was concentrated with a 100 kDa centrifugal filter to prepare the final concentration (40–80 μg mL^{-1}). Loaded ICG content was measured by UV–vis absorbance and calculated based on a standard curve.

Characterization: Transmission electron microscopy (TEM) images were obtained with a JEOL-1200 EX II instrument. The hydrodynamic size and zeta potential was measured using dynamic light scattering (DLS, Zetasizer ZS90, Malvern Instruments). FTIR spectra were obtained with a Thermo Scientific Nicolet 6700 FTIR instrument. Raman spectra were recorded using a Renishaw inVia Raman microscope with 532 nm laser excitation source. Powder XRD spectra were obtained at ambient temperature on a Bruker D8 Advance diffractometer using Cu Kα (λ = 1.5418 Å) radiation (40 kV, 40 mA), a scan speed of 0.1 s per step, a step size of 0.02° in 2θ, and a 2θ range of 10°–80°. TGA was carried out using an STA 6000 Simultaneous Thermal Analyzer (PerkinElmer) in a nitrogen ambient. Electrospray ionization mass spectrometry was performed using a nanoACQUITY UPLC-TripleTOF 5600. Optical absorbance spectra were acquired using a Molecular Devices Spectra Max spectrophotometer or a Nanodrop2000 (Thermo Fisher Scientific) instrument. Fluorescence spectra were obtained using a Molecular Devices Spectra Max GEMINI XPS.

Photoacoustic Imaging: The photoacoustic instrument was a Vevo 2100 commercial photoacoustic scanner (Visualsonics) described previously.[36] The system consisted of a flashlamp-pumped Q-switched Nd:YAG laser with optical parametric oscillator and second harmonic generator operating at 20 Hz between 680 and 970 nm with a 1 nm step size and a pulse of 4–6 nm. The peak energy was 45 ± 5 mJ at 20 Hz at the source. The laser was coupled into 21 to 30 MHz centered transducers (LZ250 and LZ400). The full field of view of the transducer was 14–23 mm wide. The acquisition rate was 5 frames s^{-1}.

A total volume of 17 μL of each sample was placed in polyethylene tubing (Harvard apparatus) with an outer diameter of 1.27 mm and an inner diameter of 0.85 mm, and the tubing was fixed in a custom-built phantom holder.[37] The phantom holder incorporated 16 equally spaced holes with diameters ranging from 1.7 to 2.5 mm. The samples were positioned 1 cm beneath the acoustic transducer for optimal signal collection. The laser energy was calibrated and optimized using a built-in energy meter prior to measurements. The samples were typically scanned with 100% laser energy and the signal was amplified between 10 to 40 dB for optimal visualization. We also performed 3D scans to image all parts of the tubing using 790 or 788 nm excitation; photoacoustic spectra were collected in the wavelength range from 680 to 970 nm.

For *ex vivo* experiments, mice were sacrificed after blood perfusion with PBS, and fixed in 4% paraformaldehyde for 24 h. Then, 15 μL of PBS, free ICG or Ca-pSiNP-ICG solution was injected twice at the lambda point of the brain at an interval of 15 min. 25 mL of 1% agarose gel was poured into a 100 mm well plate and allowed to cool to make a bottom layer. Each brain was placed on top of the cooled agarose gel, and another 25 mL of

1% agarose gel was poured over the tissue carefully, to avoid bubble formation. The prepared agarose-fixed tissues were positioned 1 cm from the transducer in a water tank to obtain the photoacoustic images.

Measurement of Thermal Profile under Continuous Laser Exposure: Temporal heating profiles were obtained under continuous laser exposure, on samples consisting of 200 μL of free ICG or Ca-pSiNP-ICG in 1:1 (by volume) ethanol:DI water. For comparison with the liposomal formulations, Lip-ICG or Ca-pSiNP-ICG samples were prepared in solutions composed of 1:4 (by volume) ethanol:DI water. Samples were placed in 96-well plates and exposed for 300 s to an NIR light source (1.1 W cm^{-2}, BWF2 808 nm diode laser, B & W TEK Inc.). The temperature during laser irradiation was recorded using an infrared camera (FLIR SC305, FLIR Systems, Inc.).

Measurement of Stability of Fluorescence from ICG Formulations under Laser Irradiation: Ethanol mixtures of free ICG (20 μg mL^{-1}), or Ca-pSiNP-ICG containing an equivalent quantity of ICG, were diluted with deionized water to form a 1:1 (by volume) ethanol:DI mixture. The resulting samples were placed in cuvettes and excited with λ = 790 nm light from a tripled YAG-pumped optical parametric oscillator (Opolette 355, Opotek Inc.), operating at 20 Hz with nominal pulse width 8 ns and an average power density of 0.3 mW (≈0.5 cm diameter expanded beam). Fluorescence spectra were obtained every 10 s for a period of 5 min using a cooled CCD (charge coupled device) spectrometer (QE Pro, Ocean Optics) fitted with an 800 nm long-pass emission filter.

5.6. References

[1] P. Beard, *Interface Focus* **2011,** *1,* 602.

[2] E. Z. Zhang, J. G. Laufer, R. B. Pedley, P. C. Beard, *Phys Med Biol* **2009,** *54,* 1035.

[3] V. Ntziachristos, D. Razansky, *Chem Rev* **2010,** *110,* 2783.

[4] C. Kim, C. Favazza, L. H. V. Wang, *Chem Rev* **2010,** *110,* 2756.

[5] H. D. Lu, B. K. Wilson, A. Heinmiller, B. Faenza, S. Hejazi, R. K. Prud'homme, *ACS Appl Mater Interfaces* **2016,** *8,* 14379.

[6] M. H. Xu, L. H. V. Wang, *Rev Sci Instrum* **2006,** *77*.

[7] D. Wu, L. Huang, M. S. Jiang, H. B. Jiang, *Int J Mol Sci* **2014,** *15,* 23616.

[8] L. H. V. Wang, S. Hu, *Science* **2012,** *335,* 1458.

[9] K. Y. Pu, A. J. Shuhendler, J. V. Jokerst, J. G. Mei, S. S. Gambhir, Z. N. Bao, J. H. Rao, *Nat Nanotechnol* **2014,** *9,* 233.

[10] J. Weber, P. C. Beard, S. E. Bohndiek, *Nat Methods* **2016,** *13,* 639.

[11] J. J. Li, F. F. Cheng, H. P. Huang, L. L. Li, J. J. Zhu, *Chem Soc Rev* **2015,** *44,* 7855.

[12] Y. S. Chen, W. Frey, S. Kim, P. Kruizinga, K. Homan, S. Emelianov, *Nano Lett* **2011,** *11,* 348.

[13] H. Zhang, D. R. Dunphy, X. Jiang, H. Meng, B. Sun, D. Tarn, M. Xue, X. Wang, S. Lin, Z. Ji, *J Am Chem Soc* **2012,** *134,* 15790.

[14] L. T. Canham, in *Porous Silicon for Biomedical Applications*, (Ed: H. A. Santos), Woodhead Publishing, Cambridge, UK 2014, pp. 3–20.

[15] C. Wu, J. Chang, W. Fan, *J Mater Chem* **2012,** *22,* 16801.

[16] H. S. Choi, W. Liu, P. Misra, E. Tanaka, J. P. Zimmer, B. I. Ipe, M. G. Bawendi, J. V. Frangioni, *Nat Biotechnol* **2007,** *25,* 1165.

[17] C.-H. Su, H.-S. Sheu, C.-Y. Lin, C.-C. Huang, Y.-W. Lo, Y.-C. Pu, J.-C. Weng, D.-B. Shieh, J.-H. Chen, C.-S. Yeh, *J Am Chem Soc* **2007,** *129,* 2139.

[18] N. Pernodet, X. Fang, Y. Sun, A. Bakhtina, A. Ramakrishnan, J. Sokolov, A. Ulman, M. Rafailovich, *Small* **2006,** *2,* 766.

[19] J. Kang, J. Joo, E. J. Kwon, M. Skalak, S. Hussain, Z. G. She, E. Ruoslahti, S. N. Bhatia, M. J. Sailor, *Adv Mater* **2016,** *28,* 7962.

[20] Z. T. Qin, J. Joo, L. Gu, M. J. Sailor, *Part Part Syst Charact* **2014,** *31,* 252.

[21] B. Li, D. Yu, S.-L. Zhang, *Phys Rev B* **1999,** *59,* 1645.

[22] S. Letant, J. Vial, *J Appl Phys* **1997,** *82,* 397.

[23] E. C. Wu, J.-H. Park, J. Park, E. Segal, F. Cunin, M. J. Sailor, *ACS Nano* **2008,** *2,* 2401.

[24] H. J. Yoon, H. S. Lee, J. Y. Lim, J. H. Park, *ACS Appl Mater Interfaces* **2017,** *9,* 5683.

[25] V. Saxena, M. Sadoqi, J. Shao, *J Pharm Sci* **2003,** *92,* 2090.

[26] L. Hou, J. Fang, W. Wang, Z. Xie, D. Dong, N. Zhang, *J Mater Chem B* **2017,** *5,* 3348.

[27] J. F. Bringley, T. L. Penner, R. Z. Wang, J. F. Harder, W. J. Harrison, L. Buonemani, *J Colloid Interface Sci* **2008,** *320,* 132.

[28] Y. W. Wang, Y. Y. Fu, Q. L. Peng, S. S. Guo, G. Liu, J. Li, H. H. Yang, G. N. Chen, *J Mater Chem B* **2013,** *1,* 5762.

[29] W. J. Xu, J. Riikonen, T. Nissinen, M. Suvanto, K. Rilla, B. J. Li, Q. Wang, F. Deng, V. P. Lehto, *J Phys Chem C* **2012,** *116,* 22307.

[30] D. Kim, J. Joo, Y. L. Pan, A. Boarino, Y. W. Jun, K. H. Ahn, B. Arkles, M. J. Sailor, *Angew Chem, Int Ed* **2016,** *55,* 6423.

[31] L. Gu, M. Orosco, M. J. Sailor, *Phys Status Solidi A* **2009,** *206,* 1374.

[32] H.-P. Ebert, F. Hemberger, *Int. J Therm Sci* **2011,** *50,* 1838.

[33] N. Koshida, T. Nakajima, M. Yoshiyama, K. Ueno, T. Nakagawa, H. Shinoda, *MRS Online Proc Libr* **2011,** *536,* 105.

[34] A. I. Boukai, Y. Bunimovich, J. Tahir-Kheli, J.-K. Yu, W. A. Goddard III, J. R. Heath, *Nature* **2008,** *451,* 168.

[35] N. Koshida, in *Handbook of Porous Silicon*, (Ed: L. T. Canham), Springer, Cham, Switzerland 2014, 207.

[36] J. Wang, F. Chen, S. J. Arconada-Alvarez, J. Hartanto, L.-P. Yap, R. Park, F. Wang, I. Vorobyova, G. Dagliyan, P. S. Conti, *Nano Lett* **2016,** *16,* 6265.

[37] S. J. Arconada-Alvarez, J. E. Lemaster, J. Wang, J. V. Jokerst, *Photoacoustics* **2017,** *5,* 17.

[38] D. Baciu, J. Simitzis, Journal of Optoelectronics and *Adv Mater* **2007,** *9,* 3320

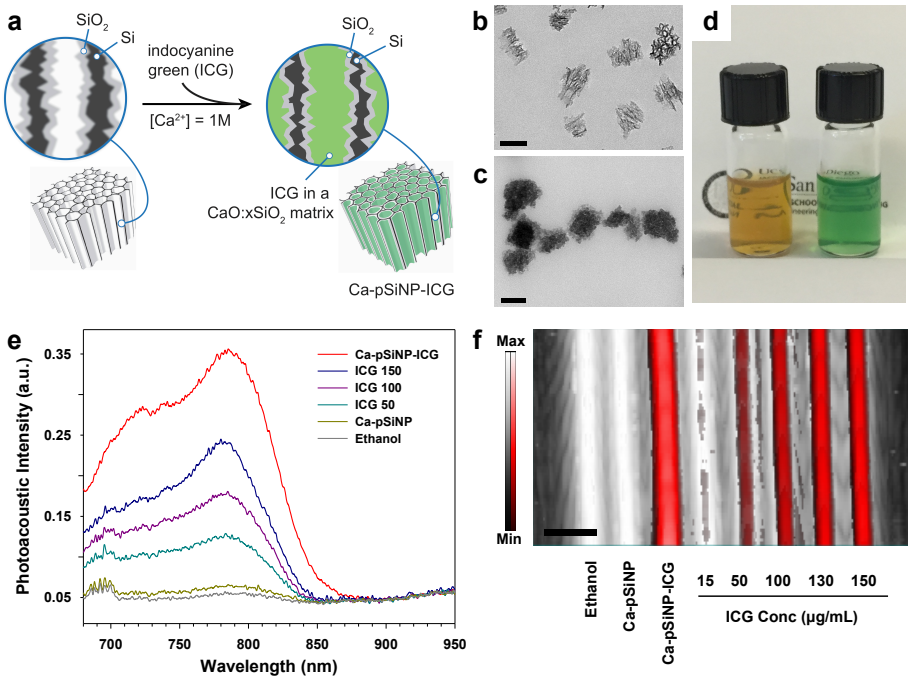

Figure 5.1. Preparation and properties of ICG-containing porous Si nanoparticles. (a) Procedure used to simultaneously load and seal ICG into the pores of porous silicon nanoparticles (pSiNPs). When pSiNP is incubated in a solution containing ICG and a high concentration of aqueous calcium ion, silicon from the dissolving nanoparticle is locally converted to calcium silicate, sealing the pores and trapping ICG in the nanostructure. The resulting composite of calcium silicate, porous silicon, and indocyanine green is designated Ca-pSiNP-ICG. (b) Transmission electron microscopy (TEM) image of the pSiNP starting material, prior to loading. (c) TEM image of Ca-pSiNP-ICG. Scale bars are 100 nm. (d) Photograph of pSiNPs (left) and Ca-pSiNP- ICG (right) dispersed in ethanol (1 mg mL^{-1}, based on particle mass). (e) Comparative photoacoustic spectra of ethanol solutions of Ca-pSiNP-ICG, free ICG at concentrations of 150, 100, and 50 μg mL^{-1} as indicated, control Ca-pSiNPs that did not contain any loaded ICG, and pure ethanol. The traces represent intensity of the photoacoustic signal as a function of probe laser wavelength. (f) Photoacoustic image overlaid on the ultrasound image with a maximum intensity projection. Tubes contain (from left to right): pure ethanol solvent, Ca-pSiNP, Ca-pSiNP-ICG, and various concentrations of ICG as indicated. All solutions made from ethanol. The black to white and red to white intensity bars correspond to ultrasound and photoacoustic intensity, respectively. Scale bar is 3 mm. The concentration of ICG in the Ca-pSiNP-ICG samples of (e) and (f), quantified by the characteristic optical absorbance of ICG at λabs = 790 nm, corresponds to 15 ± 5 μg mL^{-1}.

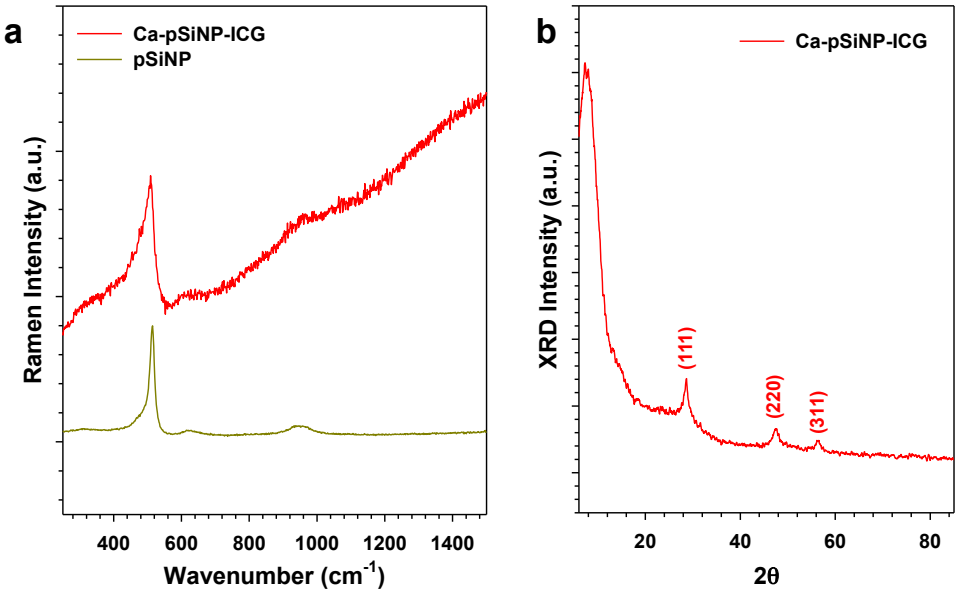

Figure 5.2. (a) Raman spectrum of Ca-pSiNP-ICG and pSiNP. (b) Power X-ray diffraction spectrum of Ca-pSiNP-ICG and pSiNP. The crystalline Si lattice planes based on Miller indices, *h k l*, are labeled in the diffraction pattern.

Table 5.1. Summary of properties and relative photoacoustic efficiency of ICG contrast agents studied.

	Absorbance[a]	Size, nm[b]	Mass loading of ICG (%)[c]	PA efficiency[d]
ICG 20 µg/mL	0.7416	N/A	N/A	1
Ca-pSiNP-ICG	0.3518	168	11.0	17
Ca-Silica-ICG	0.3753	146	2.6	15
CaS-ICG	0.4524	194	16.5	5
Lip-ICG	0.6563	121	57.7	1

[a] Optical absorbance measured at λ = 790 nm in ethanol (DI water for Lip-ICG). ICG content in each nanoparticle was determined from the optical absorbance at 790 nm. Empty nanoparticles displayed negligible absorbance at this wavelength.

[b] Average nanoparticle diameter, obtained from DLS measurement. Errors ± 5%

[c] Mass loadings determined from TGA analysis (Ca-pSiNP-ICG and Ca-Silica-ICG) or by optical absorbance (CaS-ICG and Lip-ICG).

[d] Relative photoacoustic generation efficiency defined as ratio of SNR to absorbance at λ = 790 nm, normalized to the measured value for free ICG in 20 µg/mL ethanol solution.

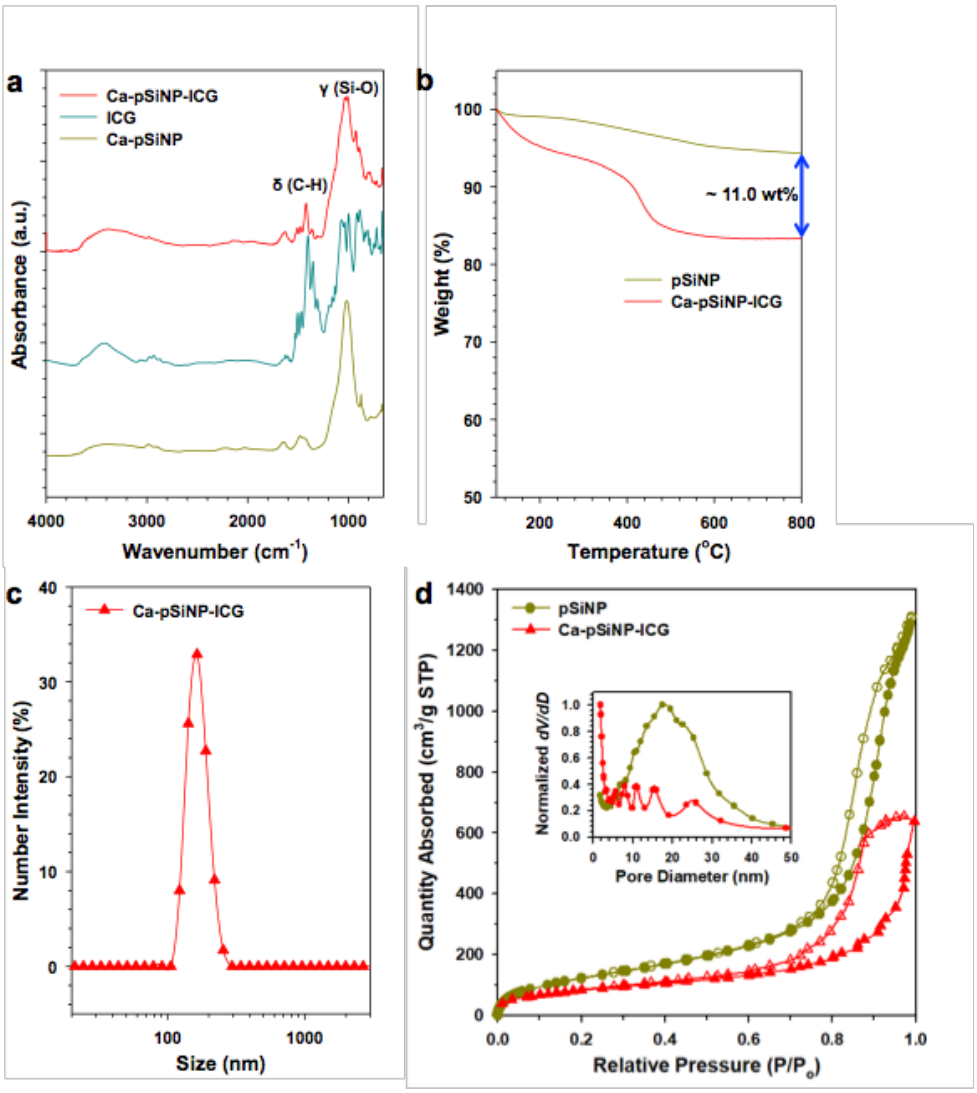

Figure 5.3. (a) ATR-FTIR spectra of Ca-pSiNP-ICG, ICG, and Ca-pSiNP (top to bottom). Si-O stretching (1000 cm^{-1}) and C-H bending (1420 cm^{-1}) modes are assigned (Symbol: ν = stretching, δ = bending). Spectra are offset along the y-axis for clarity. (b) Thermogravimetric analysis (TGA) data of pSiNP and Ca-pSiNP-ICG. The particles were fully dried for 4 h in a vacuum oven prior to analysis. The weight change (%) is plotted from 100 to 800 °C. The difference of net weight change between pSiNP and Ca-pSiNP-ICG is ~11 %, as indicated in the graph. (c) Size distribution of Ca-pSiNP-ICG in ethanol measured by dynamic light scattering (DLS). (d) Cryogenic nitrogen adsorption-desorption isotherms and pore size distribution (inset) of pSiNP starting material and Ca-pSiNP-ICG as indicated.

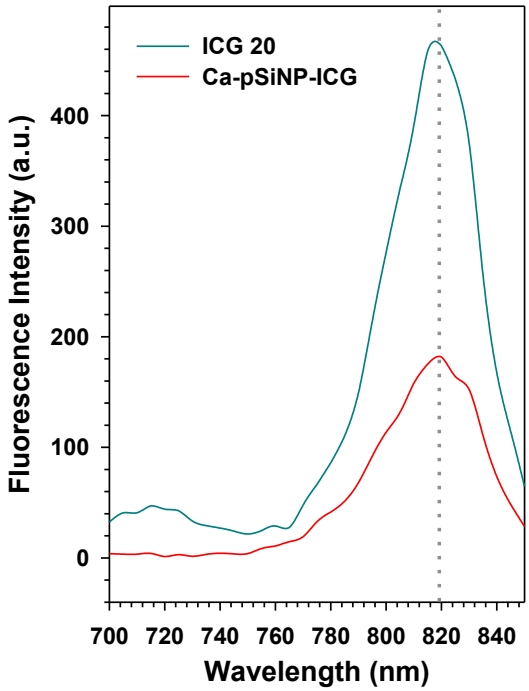

Figure 5.4. Fluorescence spectra of free ICG (ICG 20) and Ca-pSiNP-ICG in ethanol. The concentration of ICG in the ICG 20 sample was 20 μg/mL, and the concentration of the Ca-pSiNP-ICG sample was adjusted such that it displayed the same optical absorbance value at λ_{abs} = 790 nm. The emission spectra show maxima at λ_{em} = 820 nm, indicated by the gray dotted line.

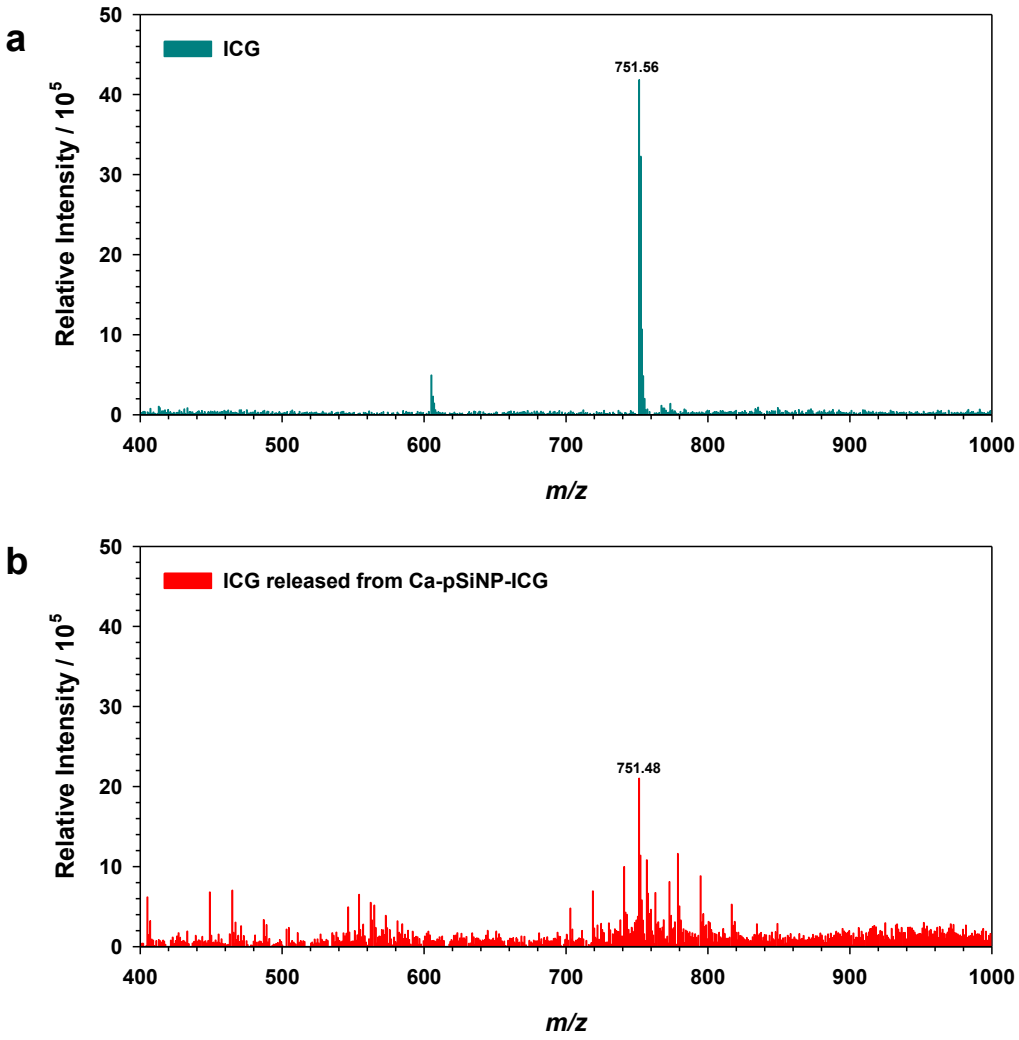

Figure 5.5. The electrospray ionization mass spectrometry (ESI-MS) of (a) ICG and (b) ICG released from Ca-pSiNP-ICG. Ca-pSiNP-ICG was dispersed in DI water (1 mg/mL) for 24 h to dissolve the pSiNP host and release loaded ICG, and the supernatant was collected by centrifugation (14,000 rpm, 20 min). The supernatant was diluted with methanol (10 % DI water in methanol), and the ESI-MS spectrum was obtained in negative ion mode. The characteristic mass of the parent ion at m/z = 751 was observed in both ICG control (a) and in the supernatant (b).

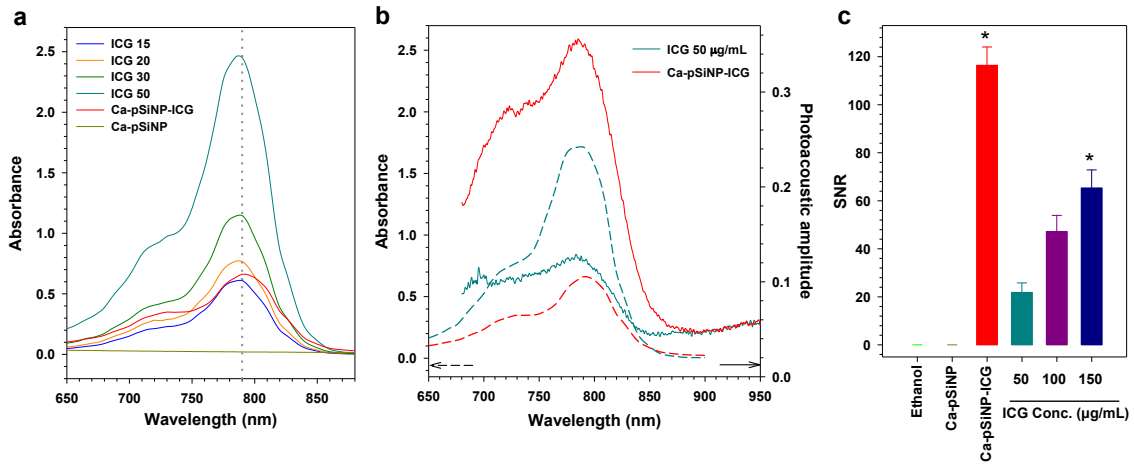

Figure 5.6. Photoacoustic performance of Ca-pSiNP-ICG relative to controls. (a) Optical absorbance spectra (in ethanol) of free ICG, Ca-pSiNP-ICG, and Ca-pSiNP (control containing no ICG). The number designations after "ICG" in the legend indicates the concentration of ICG in the solution (15, 20, 30, 50 µg/mL). Ca-pSiNP has no absorbance at 790 nm, which is indicated with gray dotted line. (b) UV-Vis absorbance (dashed line) and photoacoustic amplitude (solid line) spectra of ICG (50 µg/mL, cyan color) and Ca-pSiNP-ICG (red color). The absorption at 790 nm is obtained (a) prior to acquisition of the photoacoustic spectra. (c) SNR of photoacoustic signal from ethanol, Ca-pSiNP, Ca-pSiNP-ICG, and ICG 50, 100, 150 µg/mL (*p < 0.01). SNR obtained using Image J software.

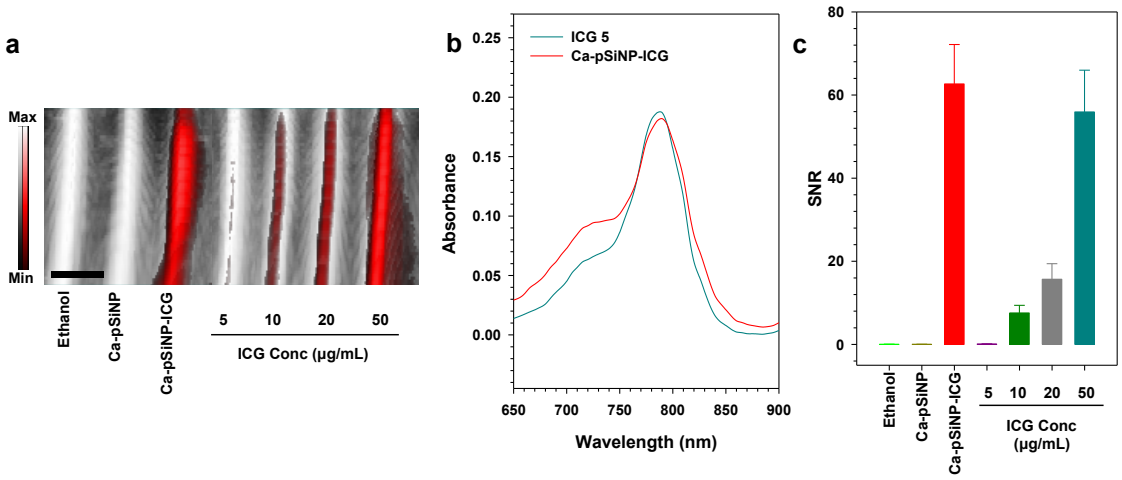

Figure 5.7. Photoacoustic performance of Ca-pSiNP-ICG tested at lower concentrations and compared with controls. (a) Photoacoustic imaging data overlaid on ultrasound image. Tubes contain (from left to right): pure ethanol, Ca-pSiNP (nanoparticles not containing ICG), Ca-pSiNP-ICG (containing total of 5 µg/mL ICG), and free ICG at the concentrations indicated. Solvent for all samples is pure ethanol. Scale bar is 3 mm. (b) UV-Vis absorbance spectra of free ICG (5 µg/mL) and Ca-pSiNP-ICG in ethanol. (c) SNR of photoacoustic signals from (a). SNR was obtained using Image J software.

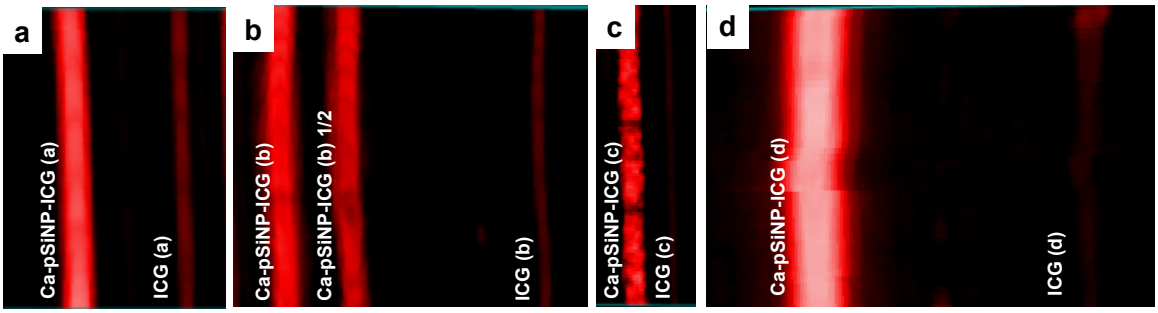

	Set	SNR	abs	SNR/abs	PA efficiency
a	Ca-pSiNP-ICG (a)	100	0.6615	151	16.9
	ICG (a)	15	1.7140	9	1.0
b	Ca-pSiNP-ICG (b)	61	0.3518	173	17.5
	Ca-pSiNP-ICG (b) 1/2	41	0.1945	239	24.2
	ICG (b)	7	0.7416	10	1.0
c	Ca-pSiNP-ICG (c)	77	0.3518	220	17.4
	ICG (c)	5	0.3611	13	1.0
d	Ca-pSiNP-ICG (d)	171	0.4174	410	18.3
	ICG (d)	8	0.3775	22	1.0

Figure 5.8. Replicates comparing PA response of Ca-pSiNP-ICG with free ICG. (a) Image taken from the photoacoustic image of Fig. 5.1f showing the Ca-pSiNP-ICG and ICG 15 µg/mL tubes. (b) Photoacoustic image taken from Fig. 5.11b showing the Ca-pSiNP-ICG and free ICG 10 µg/mL tubes. (c, d) Photoacoustic images of replicate Ca-pSiNP-ICG and free ICG samples. Table at the bottom lists SNR, absorbance, SNR/absorbance ratio and PA efficiency values from samples a-d. The PA efficiency was normalized to the measured value for ICG in each set. SNR was obtained using Image J software. Absorbance was obtained by UV-Vis plate reader using 100 µL volume.

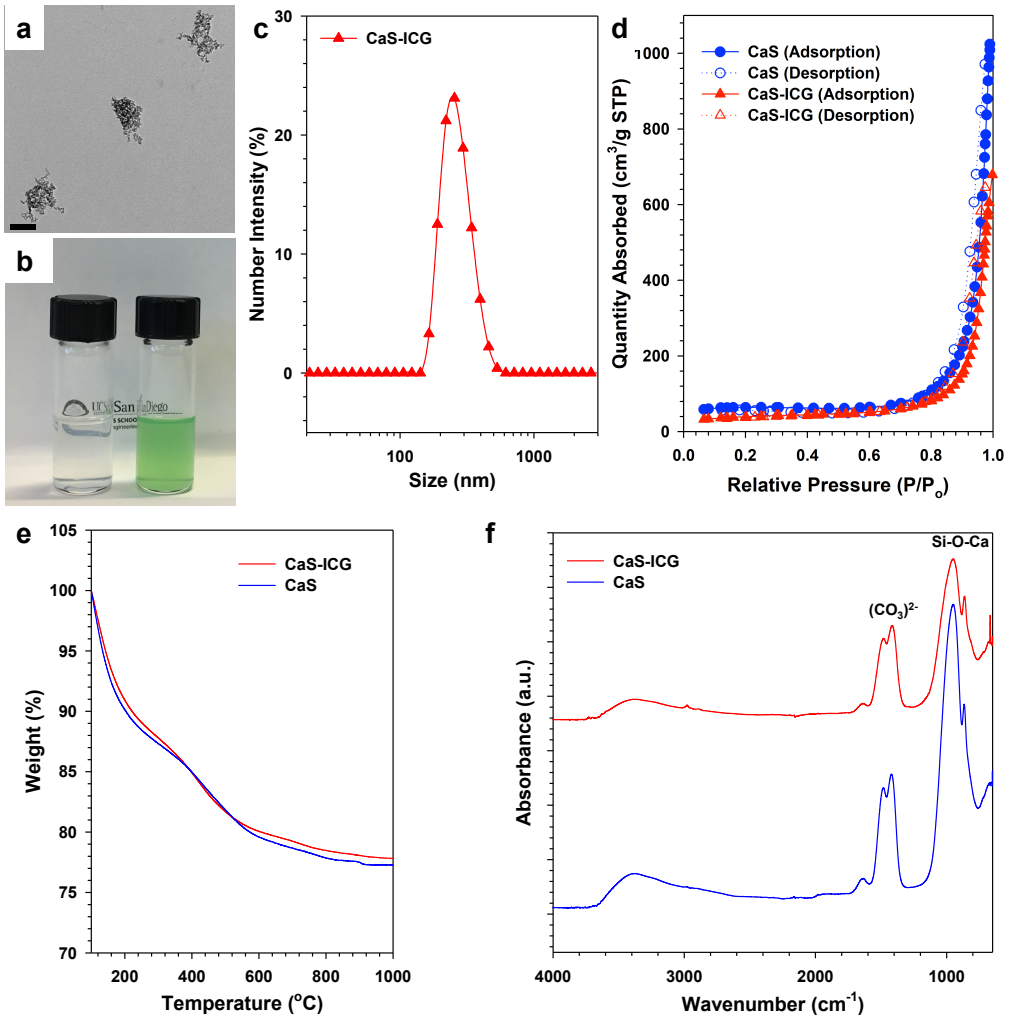

Figure 5.9. (a) Transmission electron microscope (TEM) image of ICG-loaded calcium silicate nanoparticles (CaS-ICG). (b) Photograph of calcium silicate nanoparticles without ICG loading (left) and calcium silicate nanoparticles with ICG loading (right). (c) Size distribution of CaS-ICG in ethanol measured by dynamic light scattering (DLS). (d) Cryogenic nitrogen adsorption-desorption isotherms for CaS and CaS-ICG. (e) TGA data of CaS and CaS-ICG. The particles are fully dried for 4 h in the vacuum oven prior to analysis. The difference of weight change (%) between CaS and CaS-ICG was negligible (< 0.6%). ICG seems to replace some portion of CaS skeleton during loading reaction. (f) ATR-FTIR spectra of CaS-ICG and CaS (top to bottom). Characteristic peaks of ICG (near 1420 cm^{-1}) are not obvious due to the large signals from calcium silicate (Si-O-Ca 950 cm^{-1}, $(CO_3)^{2-}$ 1410-1490 cm^{-1})[38]. Spectra are offset along the y-axis for clarity.

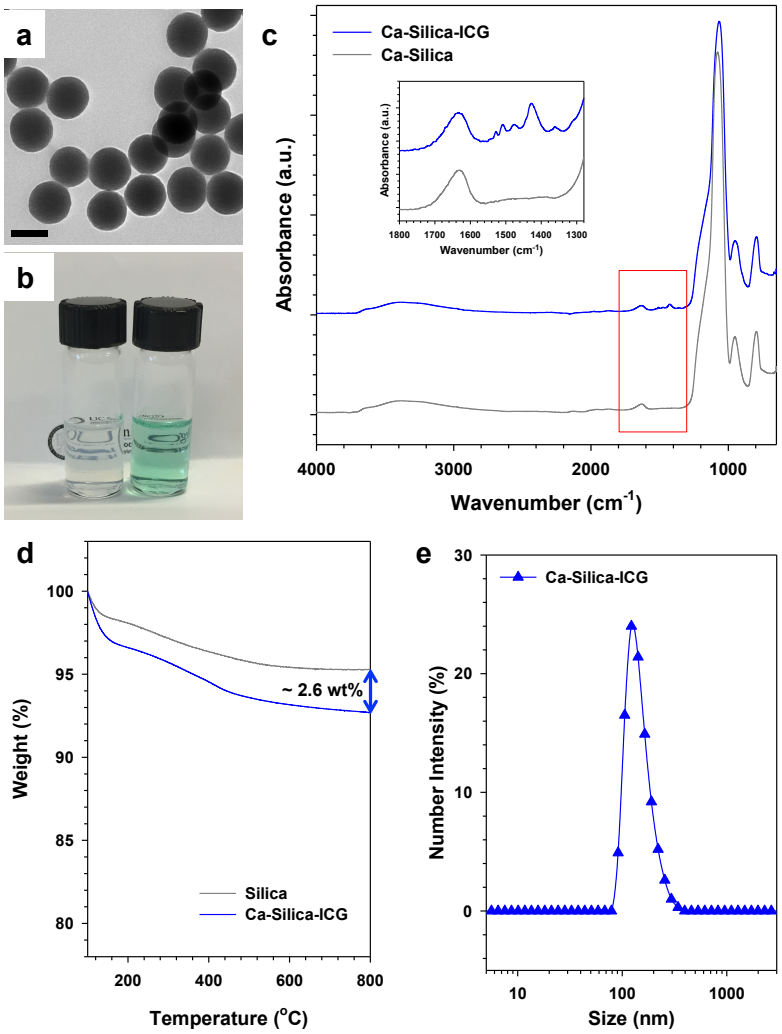

Figure 5.10. (a) Transmission electron microscope (TEM) image of ICG-loaded silica nanoparticles sealed with calcium silicate (Ca-Silica-ICG). (b) Photograph of calcium silicate-coated silica nanoparticles without ICG loading (Ca-Silica, left) and with ICG loading (Ca-Silica-ICG, right). (c) ATR-FTIR spectra of Ca-Silica-ICG and Ca-Silica (top to bottom). Inset is the expanded spectra in the region of 1300-1800 cm^{-1} to clarify the characteristic peaks of ICG (near 1420 cm^{-1}). Spectra are offset along the y-axis for clarity. (d) Size distribution of Ca-Silica-ICG in ethanol measured by DLS. (e) TGA data of Silica and Ca-Silica-ICG. The particles are fully dried for 4 h in the vacuum oven prior to analysis. The weight change (%) is plotted from 100 to 800 °C. The difference of net weight change between Silica and Ca-Silica-ICG is about 2.6 wt%, as indicated in the graph. (e) Size distribution of Ca-Silica-ICG in ethanol measured by DLS.

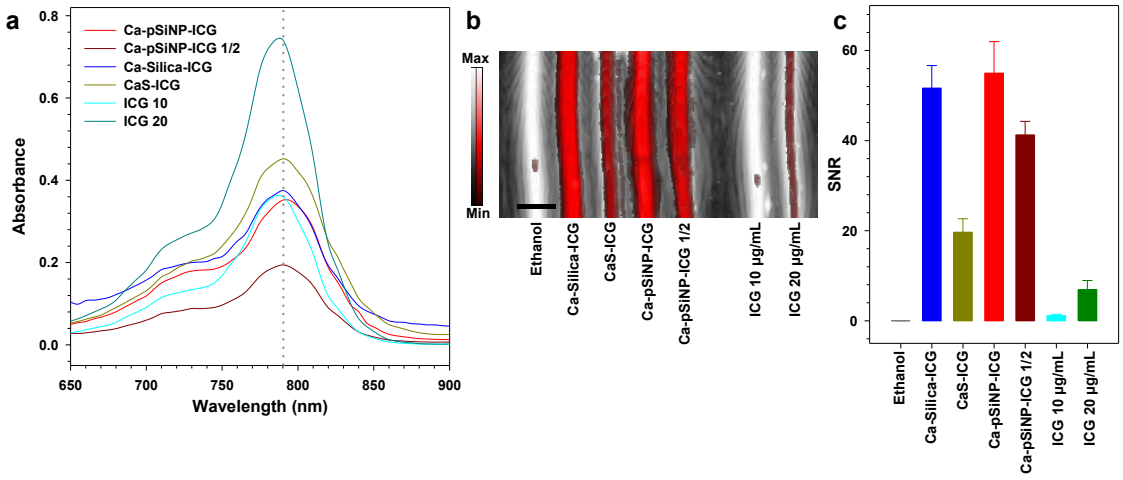

Figure 5.11. (a) UV-Vis absorbance of Ca-pSiNP-ICG, 2 times diluted Ca-pSiNP-ICG (Ca-pSiNP-ICG ½), Ca-Silica-ICG, CaS-ICG, ICG 10 and 20 µg/mL in ethanol. Absorption level at 790 nm (gray dotted line) of 3 different nanoparticles was lower than that of ICG 20 µg/mL, and compatible to ICG 10 µg/mL. (b) Photoacoustic image overlaid on ultrasound image. Each tube contains ethanol, Ca-Silica-ICG, CaS-ICG, Ca-pSiNP-ICG, Ca-pSiNP-ICG ½, ICG 10, and 20 µg/mL. Scale bar is 3 mm. (c) SNR of photoacoustic signals from (b). SNR was obtained using Image J software.

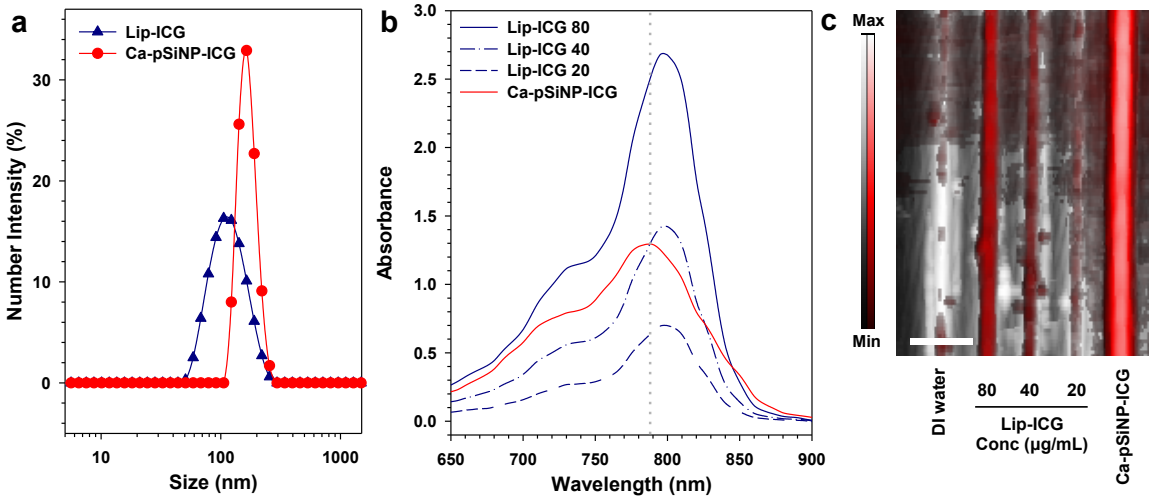

Figure 5.12. Properties of liposomal nanoparticles containing ICG (Lip-ICG), compared with the Ca-pSiNP-ICG construct. (a) Size distribution of Lip-ICG (blue triangles) and Ca-pSiNP-ICG (red circles) measured by dynamic light scattering (DLS). Lip-ICG and Ca-pSiNP-ICG samples were measured in DI water and ethanol, respectively. (b) Optical absorbance spectra of Lip-ICG containing 80, 40, and 20 μg/mL ICG in DI water, and Ca-pSiNP-ICG in ethanol. The Lip-ICG 40 and Ca-pSiNP-ICG formulations showed the same absorbance at l = 788 nm as indicated (gray dotted line). (c) Photoacoustic response of Ca-pSiNP-ICG and Lip-ICG. Photoacoustic image overlaid on ultrasound image with a maximum intensity projection. Each tube contains DI water, liposomal formulations of ICG (Lip-ICG) containing 80, 40, and 20 μg/mL of ICG in DI water, and Ca-pSiNP-ICG in pure ethanol.

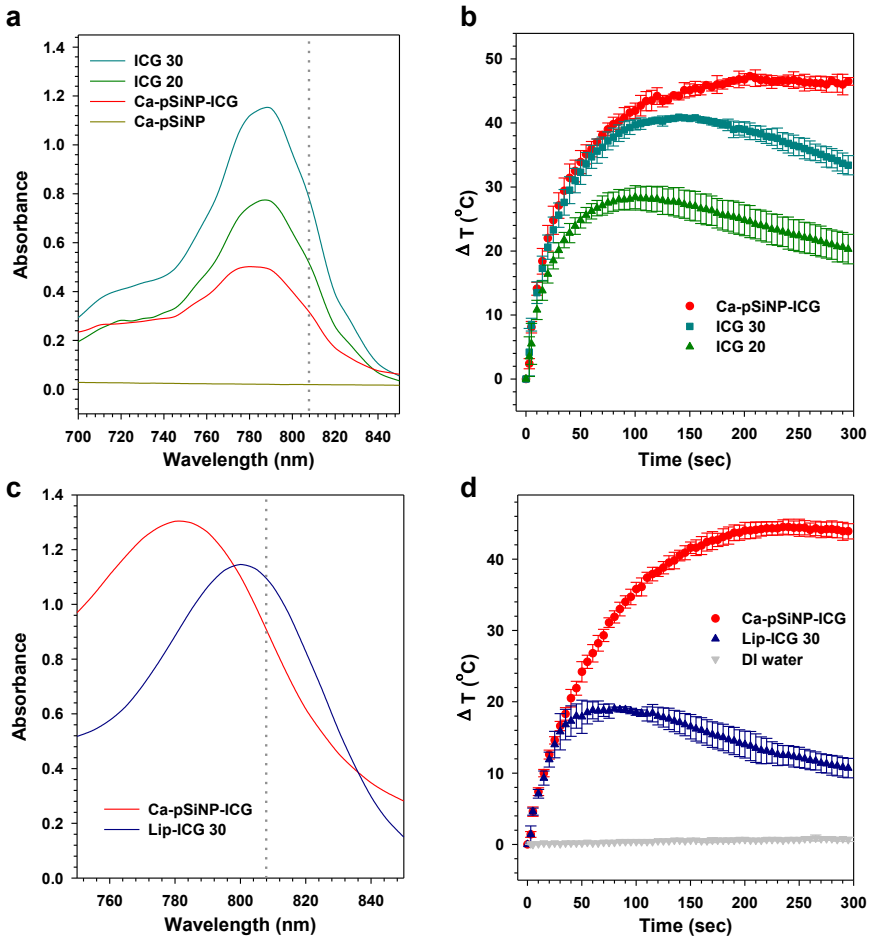

Figure 5.13. Comparison of photostability of ICG and nanoparticle formulations of ICG. (a) Optical absorbance spectra of Ca-pSiNP-ICG, Ca-pSiNP and free ICG at concentrations of 20 and 30 μg/mL, in ethanol (100 μL total volume). The wavelength of excitation by laser irradiation (λ = 808 nm) used in (b) is indicated with the gray dotted line. (b) Temporal temperature profiles measured under steady-state irradiation of the indicated formulations from (a) with (λ = 808 nm) laser light. All samples are in 1:1 (v:v) ethanol:DI water. (c) Optical absorbance spectra of Ca-pSiNP-ICG and Lip-ICG 30 in 20% ethanol (1:4 ethanol:DI water, by volume, (200 μL total volume), and the laser wavelength used in (d) is indicated with the gray dotted line. (d) Temporal temperature profiles measured under steady-state laser irradiation (λ = 808 nm) comparing Lip-ICG with Ca-pSiNP-ICG samples from (c). A pure DI water control is also shown. Nanoparticle samples are in 20% ethanol (1:4 ethanol:DI water, by volume).

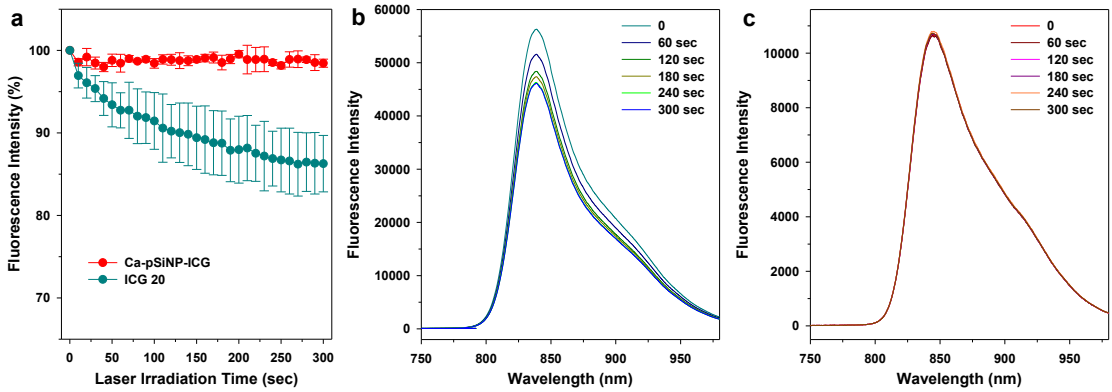

Figure 5.14. Comparison of fluorescence intensity of ICG and Ca-pSiNP-ICG under laser irradiation over time. (a) Normalized fluorescence intensity (integrated over λ_{em} = 800 - 980 nm) from free ICG and from Ca-pSiNP-ICG, obtained under pulsed laser irradiation (tripled YAG-pumped optical parametric oscillator, λ_{ex} = 790 nm, 20 Hz repetition rate, average power = 0.3 mW). Steady state fluorescence spectra were obtained every 10 sec using a QE Pro spectrometer (Ocean Optics) fitted with an 800 nm long-pass emission filter. The initial integrated fluorescence intensity value measured was set as 100% intensity at 0 sec. Fluorescence spectra were acquired every 10 sec, and the integrated intensity was normalized based on the 0 sec value (n = 3). (b, c) Family of raw fluorescence spectra of free ICG (b) and the Ca-pSiNP-ICG formulation (c) obtained during laser irradiation. The temperature increase measured after 300 sec of laser irradiation in this experiment was 7 ± 1 °C for ICG and 21 ± 3 °C for Ca-pSiNP-ICG, measured by infrared thermometer. Optical absorbance measured from both samples before the experiment was equivalent.

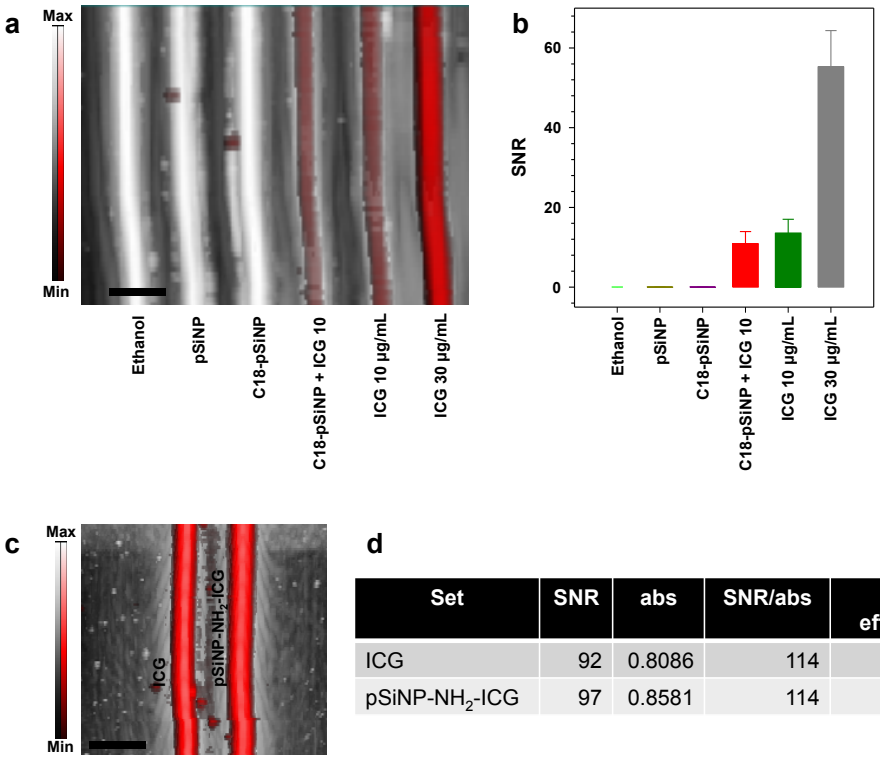

d

Set	SNR	abs	SNR/abs	PA efficiency
ICG	92	0.8086	114	1.0
pSiNP-NH_2-ICG	97	0.8581	114	1.0

Figure 5.15. Photoacoustic response of chemically modified pSiNPs, where the pores have been either blocked by grafting of octadecyl (C18) chains, or modified with amine groups in order to display a net positive surface charge. (a) Photoacoustic image overlaid on ultrasound image. Tubes contain (from left to right): pure ethanol, pSiNP, C18-pSiNP, C18-pSiNP + ICG 10, free ICG 10, and 30 µg/mL. C18-pSiNP + ICG 10 indicates a 1:1 (by volume) mixture of C18-pSiNP (1 mg/mL) and ICG (20 µg/mL); final ICG concentration was 10 µg/mL. ICG 10 µg/mL indicates a 1:1 (by volume) mixture of pure ethanol and ICG (20 µg/mL); final ICG concentration was 10 µg/mL. Scale bar is 3 mm. (b) Signal to noise ratio (SNR) of photoacoustic data from (a). Sample identity as indicated in (a). SNR was obtained using Image J software. (c) Photoacoustic response of amine-functionalized pSiNPs containing electrostatically bound ICG (pSiNP-NH_2-ICG), compared to free ICG. The surface of the pSiNPs was modified using (3-aminopropyl)-dimethylmethoxysilane, and ICG was loaded *via* electrostatic surface interaction. (d) Comparison of the photoacoustic efficiency of free ICG with the electrostatically loaded pSiNP-NH_2-ICG formulation. SNR was obtained from the image of (c) using Image J software. The optical absorbance at $\lambda = 790$ nm is given in "abs", and it was measured from a 100 µL sample volume by plate reader. The "SNR/abs" column reports the ratio of SNR to absorbance at $\lambda = 790$ nm. The "PA efficiency" column gives the relative efficiency of photoacoustic signal generation, which is normalized to the SNR/abs value of free ICG. Within the error of the measurement, the ICG and pSiNP-NH_2-ICG samples showed no significant difference in PA generation efficiency.

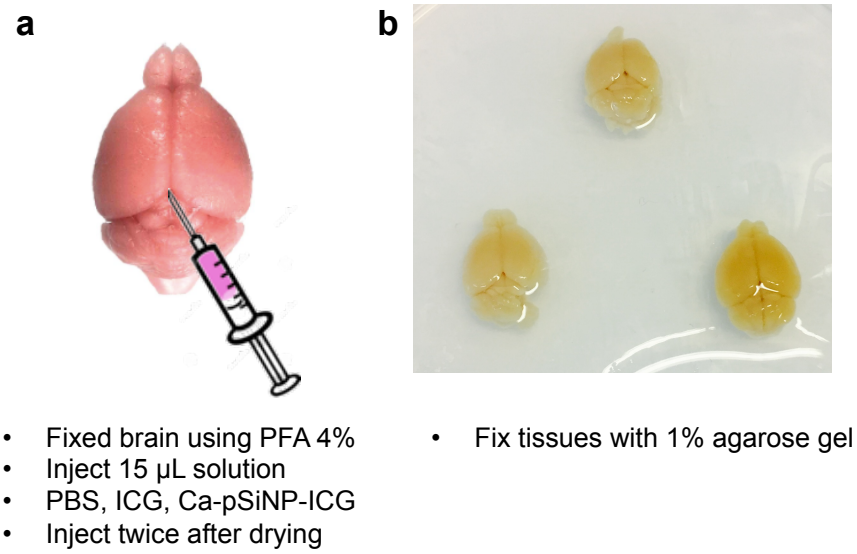

Figure 5.16. Schematic describing *ex vivo* brain preparation for photoacoustic imaging experiments. (a) Aliquots of PBS, ICG, or Ca-pSiNP-ICG were injected at the lambda point of the fixed brain tissue. Sample solutions were injected twice at an interval of 15 min. (b) Photograph of fixed brain tissues in 1% agarose gel.

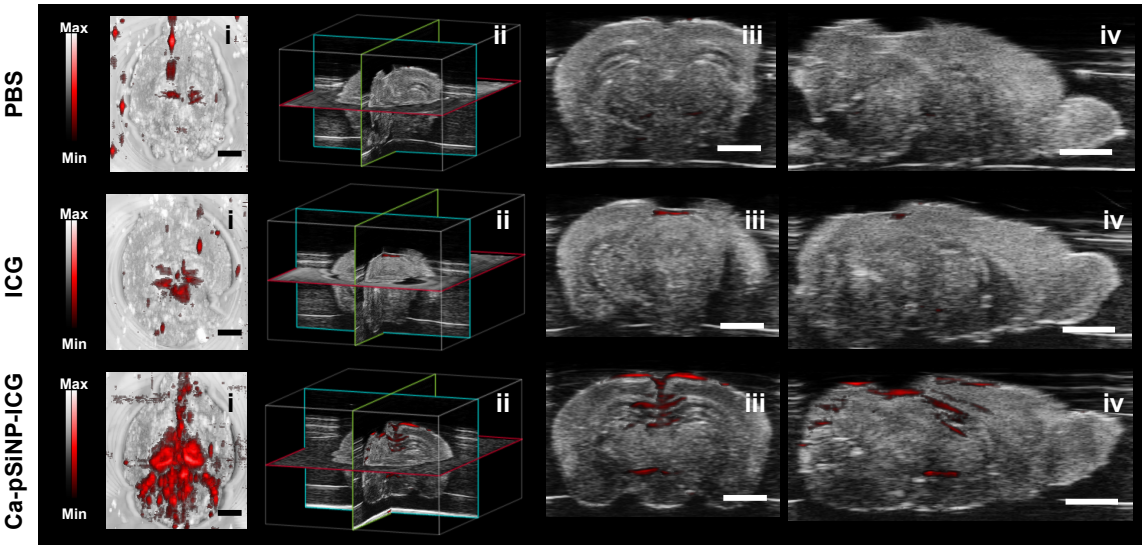

Figure 5.17. Photoacoustic images of fixed mouse brain comparing contrast agents: free ICG vs a comparable quantity of ICG encapsulated in a nanoparticle. Images at the far left are photoacoustic image (red) overlaid on ultrasound image (grayscale) after injection of control (PBS), free ICG, and Ca-pSiNP-ICG, as indicated. Each set of 4 images contain: brain (i) top view, (ii) location of sectioning, (iii) coronal cross-section, and (iv) axial cross-section. Scale bar is 2 mm.

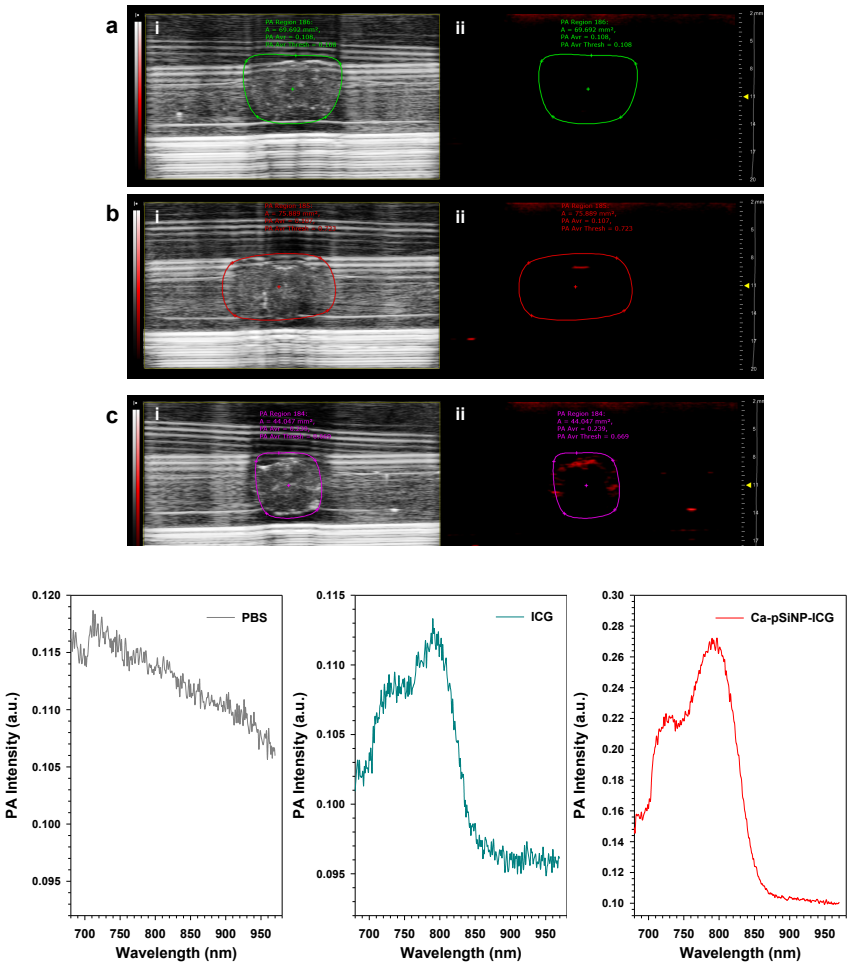

Figure 5.18. Images of brain coronal cross-sections after injection of (a) PBS, (b) free ICG, and (c) Ca-pSiNP-ICG. (i) Ultrasound image and (ii) photoacoustic image. The outlined margin indicates the region of interest for the photoacoustic spectra shown at the bottom (d-f). Photoacoustic spectra of (d) PBS, (e) ICG, and (f) Ca-pSiNP-ICG ICG injected brain tissue, obtained from brain coronal cross-sections in panels a, b, c, respectively.

Chapter 5, in full, is a reprint of the material as it appears in Advanced Materials 2018. Jinyoung Kang, Dokyoung Kim, Junxin Wang, Yunho Han, Jonathan M. Zuidema, Ali Hariri, Ji-Ho Park, Jesse V. Jokerst, Michael J. Sailor. The dissertation author was the primary researcher and author of this material.